Development of Bioplasmonic Platforms for Extracellular Vesicle Capture and Analysis

A thesis submitted to Dublin City University for the award of MSc

By

John O'Sullivan, B.Sc. (Hons.), M.Sc.,

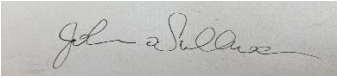Under the Supervision of

Prof. Tia E. Keyes,

School of Chemical Sciences,

Dublin City University, Glasnevin, Dublin 9.

May 2022

Declaration

I hereby certify that this material, which I now submit for assessment on the programme of study leading to the award of MSc, is entirely my own work, and that I have exercised reasonable care to ensure that the work is original, and does not to the best of my knowledge breach any law of copyright, and has not been taken from the work of others save and to the extent that such work has been cited and acknowledged within the text of my work.

Signed: _____

ID No.: ___18213275___

Date: ___04/01/2022___

Acknowledgements

Research Outputs

Posters

"Development of Bio-Plasmonic platforms for Cell and Extracellular Vesicle Capture and Analysis" at the 18th European Conference for Spectroscopy of Biological Molecules, University College Dublin (2019).

"Fabrication of Plasmonic Periodic Array Platforms for Regioselective Exosome Capture and Analysis" at SFI Summit, IPIC, Tyndall Institute Cork (2019).

Short Talks

"Development of Bio-Plasmonic platforms for Extracellular Vesicle Capture and SERS Analysis" at the ICI online Postgraduate Symposium (2020).

"Development of Bio-Plasmonic platforms for Extracellular Vesicle Capture and Analysis" (online) at the DCU Chemistry Day, Dublin City University (2021).

Publications (forthcoming)

"Exosome Capture and SERS; AI Supported Profiling" (*Manuscript in Prep*.) J. P. O'Sullivan *et al.* (2022).

Table of Contents

Glossary of Symbols and Acronyms

α	Polarizability
$\Delta\tilde{v}$	Raman shift
$(d\sigma/d\Omega)$	Differential Raman cross-section per molecule
η	Overall efficiency of the detection system
λ	Wavelength
φ	Phase
A	Area/Adenine
AC	Alternating Current
ACVD	Atherosclerotic Cardiovascular disease
AFM	Atomic Force Microscopy
Ag (/Cl)	Silver (/chloride)
AI	Artificial Intelligence
ALIX	Type of cytoplasmic protein
APTMS	(3-aminopropyl) trimethoxysilane
ATP	Adenosine triphosphate
a.u.	Arbitrary units
Au	Gold
A549	Immortalized-adenocarcinomic lung cell line
B16F10	Melanoma cell line
BODIPY	Dipyrrometheneboron difluoride
BSE	Back scattered electrons
B Z marker	Adjoining junctions of B-DNA to Z-DNA
C	Carbon/ Amino acid Cysteine /Cytosine base
(c)	Cyclic
CD	Cluster of differentiation (in relation to tetraspanin nomenclature)
C_{dl}	Double layer capacitance
CEC	Cardiac endothelial cells
CFM	Confocal fluorescence microscopy
CHMP2a	Charged multi-vesicular body protein 2a
COO^-	Carboxyl group
COOH	Carboxylic acid group

Cr	Chromium
Cu	Copper
CV	Cyclic voltammetry
CVD	Cardiovascular disease
D	Aspartic acid
DLS	Dynamic light scattering
DNA	Deoxyribonucleic acid
D407	Human retinal epithelial cells
E	Electric field / Electric potential / Amino acid glutamic acid
EA.hy926	Hybrid human immortalized umbilical vein endothelial cell line
EBL	Electron beam lithography
EC	Endothelial cells
ECM	Equivalent circle model /Extracellular matrix
EDC	1-Ethyl-3-(3-dimethylaminopropyl)carbodiimide
EDL	Electric double layer
EF	Enhancement Factor
EM	Electromagnetic
EIS	Electrochemical impedance spectroscopy
ELISA	Enzyme linked immunosorbent assays
ESCRT	Endosomal sorting complex required for transport
EV	Extracellular vesicle / Exosome
F	Phenylalanine
f	Frequency of the sinusoidal-wave
FACS	Fluorescence-activated cell sorting
FDTD	Finite-Difference Time Domain
FE-SEM	Field Emission Scanning Electron Microscopy
FIB	Focused Ion Beam
FTIR	Fourier-transform infrared spectroscopy
FTO	Fluorine doped Tin Oxide
G	Glycine/ Guanine
g^4	Electromagnetic enhancement
GM1	monosialotetrahexosylganglioside
GSH	a reduced form of glutathione

H	Hydrogen
HeLa	Oncogenic cervical cell line
HepG2	Tumorigenic hepatic cell line
hi-res	High resolution
HG	Hyperglycaemic (high concentration of glucose treated) Group
HSC	Heat shock cognate
HSP	Heat shock proteins
HuAEC	Human aortic endothelial cardiac cell
HUVEC	Human umbilical vein endothelial cell
I	Intensity / Current
ICAM-1	Intercellular adhesion molecule-1
I_e	Emission current
IG	Immortalized group
IHH	Immortalized hepatic cell line
$ISERS$	Intensity of the signal obtained during SERS measurements
ILV	Intraluminal vesicles
IR	Infrared
Ir	Iridium
K	Lysine
KCl	Potassium chloride
LAMP1	Lysosomal associated membrane protein 1
LDA	Linear discriminant analysis
LO2	Hepatic cell line
LP	Incident laser power
LSPR	Localized Surface Plasmon Resonance
M	Molar(s) (moles per litre)
MCF-7	Oncogenic mammary epithelial cell line
MCF-10A	Healthy mammary epithelial cell line
MCP	Micro contact printing
MEF	Metal Enhanced Fluorescence
MFG-E8	Milk Fat Globule – Epidermal growth factor 8
MHC	Major histocompatability complex (Protein Receptors)
MG	Hypoglycaemic (mannitol treated) Group

miR	Micro-ribonucleic acid
mPEG-SH	Methoxy mercapto polyethylene-glycol
MPTMS	(3-mercaptopropyl) trimethoxysilane
MSCs	Mesenchymal Stem cells
MTT	(3-(4,5-dimethylthiazol-2-yl)-2,5-diphenyltetrazolium bromide
MVB	large multi-vesicular bodies
N	Nitrogen
NX	Number of scattering molecules in the SERS volume
N.A.	Numerical Aperture
NG	Normal (normal concentration of glucose treated) Group
NH_2/NH_3^+	Amine group
NHS	N-hydroxysuccinimide
NIL	Nanoimprint lithography
NP	Nanoparticle
NSL	Nanosphere lithography
NTA	Nanoparticle tracking analysis
O	Oxygen
O. D.	Optical Density
OH	alcohol group/ hydroxide
OsO_4	Osmium tetroxide
P	Dipole moment /Phosphorous/ Amino acid proline
PCA	Principal component analysis
P-Selectin	Type 1 transmembrane protein
PBS	Phosphate buffered saline
Pd	Palladium
PDMS	Polydimethylsiloxane
PEG	Polyethylene-glycol
PC-DFA	Principal component- discriminant function analysis
PLS-DA	Partial least squares- discriminant analysis
PO_2^-	Phosphodiester bond
PS	Polystyrene
Pt	Platinum
R	Arginine

R	Resistance
Rab-GTPase	Rab family of proteins (Part of Ras superfamily)
RAB11B	Rab11b protein (Part of Ras superfamily)
R_{ct}	Charge transfer resistance
RIE	Reactive-ion etching
RNA	Ribonucleic acid
ROS	Reactive oxygen species
R_s	Ohmic resistance of the electrolyte
R6G	Rhodamine 6G
S	Sulphur
S-S	Disulphide bond (in proteins)
s	Second
SAM	Self-assembled monolayer
scPH	Single cell photonics
SE	Secondary electrons
SEM	Scanning Electron Microscopy
SERS	Surface Enhanced Raman Spectroscopy
SERRS	Surface Enhanced Resonance Raman Spectroscopy
SGC7901	Human gastric cancer cell line
SH	Thiol/Sulphydryl/ Mercapto group
Si	Silicon
SMC	Smooth muscle cells
SNAREs	Soluble n-ethylmaleimide sensitive factor attachment protein receptors
SOP	Standard Operating Procedure
SPP	Surface Plasmon Polariton
T	Thiamine
t	Time
TEM	Transmission Electron Microscopy
THF	Tetrahydrofuran
TSG101	Tumour susceptibility gene 101 protein
Tyr	Tyrosine
U	Uracil
V	Volts/ Amino acid valine

V_{acc}	Incident electron-beam
W	Watt (joules per second)/Amino acid tryptophan
X	Magnification power
Y	Tyrosine
Z_{imag}/Z''	Imaginary-impedance
Z_{real}/Z'	Real-impedance
Z_w	Warburg impedance
4,4'-BPY	4,4'-Bipyridine
4-Myp	4-Mercaptopyridine

Abstract

John P. O'Sullivan

Development of Bioplasmonic Platforms for EV capture and Analysis

Exosomes are extracellular vesicles containing proteins, glycoproteins, lipids, integrins, nucleic acids and other cargo. Exosomes are emitted by all cell types and are believed to play a role in inter-cellular signalling. Their sizes range from 30nm-150nm. It is believed that their cargo content can change significantly when their originating cell type becomes diseased and their cargo can be assessed through the use of Raman Spectroscopy. As for many biomolecules, Raman scattering signal intensity is low. To achieve a sufficient Raman signal intensity typically requires samples with a high density of exosomes present. One way to overcome the low signal intensity is to employ Surface Enhanced Raman Spectroscopy. Wherein by capturing exosomes on appropriate SERS substrates upon photon excitation the generation of a plasmonic field significantly enhances Raman intensity by up to 10^{10}, this allows the use of small quantities of label free exosomes thereby making single molecular detection possible.

The primary objective of this thesis involve the fabrication and selective surface modification of Au micro array platforms and subsequent application for label-free exosome capture. Once the functionalization of the Au micro platform has been optimised, the optimised platform is then used for the secondary objective which is to generate a training database of different exosomal populations in collaboration with computer scientists. To generate an effective surface enhanced signal, it is important to drive the analyte to the location of maximum plasmonic field. This is achieved by using Selective Surface modification techniques which is the key achievement of Chapter 3. The exterior of the micro-arrays is selectively modified with an alkane thiol self-assembled monolayer (using micro-contact printing) to prevent exosome adhesion and the interior is modified with a self-assembled (c)-RGDFK peptide monolayer. This particular peptide sequence will promote integrin conjugation, cell and other biomaterial adhesion and will conjugate with any exosome present and allow an effective signal to be generated within the plasmonic field. The Au micro array interiors are also functionalized using thiocholesterol for comparison.

Other key achievements of this thesis are presented in Chapter 4 which involve the application of selectively modified Au micro array platforms. Their array pore interiors are functionalized using both (c)-RGD peptide and thiocholesterol and exosome capture of both types of selectively modified platforms are assessed using two different types of exosome populations. One sourced from immortalized cells and the other from primary cells.

The final outcome of this thesis is presented in Chapter 5. This involves the generation of a training database set of three different types of exosomal sub-populations of primary human aortic endothelial cardiac cells captured exclusively within a (c)-RGD functionalized Au micro array platform and these exosomal sub-populations are subsequently interrogated using Surface Enhanced Raman Spectroscopy and Field Emission Scanning Electron Microscopic techniques.

Chapter 1: Literature Survey

1.01 Introduction

The work presented in this thesis focuses on the fabrication and development of periodic micro-array plasmonic platforms and their application in both capture and SERS analysis of extra-cellular vesicles. This project is a small part of a wider multi-disciplinary collaborative effort between research groups in the Schools of Chemical Sciences, Computing and Biotechnology. The biotechnologist(s) focusing on extensive exosomal-characterisation studies including their size, morphology and roles within diagnostic vascular-therapeutics; The computer-data scientist(s) focusing on multivariate statistical classifications by generating a chemometric algorithm inputted with raw spectral-data supplied by the analytical chemist (myself) in order to produce a training set of data; The primary objective of this thesis, is to develop an exosome capture platform capable of SERS enhancement and the secondary objective is to generate a training database to build a multivariate statistical classification model that can be used to discriminate between different sub-populations of aortic endothelial exosomes.. This was accomplished by applying periodic cavity array substrates, already established as robust and reproducible SERS substrates and selectively chemically-modifying their surfaces to capture and localise exosomes to the region of highest plasmonic enhancement within the pores . These nanovoid platforms are highly versatile for undertaking multimodal analytical and imaging techniques as they can serve as both a working electrode for cyclic voltammetry and electrochemical impedance spectroscopy, and as a SERS substrate for surface enhanced Raman spectroscopic analysis. Simultaneously, using confocal and scanning electron microscopies, their nanowell structures can be further interrogated.

The micro-array platform has many other applications besides exosome capture. In this chapter, the theoretical background to SERS, the main analytical technique used in this thesis, is described. An overview of different types of SERS substrates *(including a sub-section of such functionalized substrates used in cell biological studies)* is also provided and the origin of the Raman signal enhancement on metallic substrates is also outlined. For analytical applications, using uniform array platforms that achieve a reproducible SERS response is very important in exosome-analysis as their Raman signal is quite weak and previous SERS studies carried out in this area did not allow for the achievement of reproducible SERS signal detection, this issue is elaborated in more detail in the last experimental chapter. Background to strategies for capture of biomaterials focusing particularly on exosomes, and other analytical techniques used to further confirm selective-surface modification and exosome capture is also presented here. In the final part of this introduction, a detailed literature survey of exosomes is presented as exosome-capture was the core focus of this thesis and an understanding of their complexity is important to understand why exosomes are so heterogeneous in

nature and thus why their SERS-spectra was quite varied . This complexity highlights the importance of eventually applying AI models to such data

1.1.0   Background to Key Techniques

1.1.1 Raman Spectroscopy

Raman is a non-destructive vibrational spectroscopic technique based on the inelastic photon-scattering phenomenon[1–5]. Raman scattering was first discovered and established experimentally by Sir C.V. Raman in 1928 and it was called the Raman scattering phenomenon[1,2].

Upon laser-excitation from a high powered source, most of the radiation is scattered from the sample by Rayleigh scattering (such that, $\lambda_{incident} = \lambda_{emitted}$). However, $\lambda_{incident}$ promotes the molecule to a very short-lived "virtual (energy) state" from where the molecule relaxes almost instantaneously to a vibrational level higher (Stokes) or lower (anti-Stokes) than the initial ground state of the molecule[4,5].

This causes a change in its molecular-polarizability (α) resulting in an emitted scattered photon of a different wavelength ($\lambda_{emitted}$) from the sample, such that $\lambda_{incident}t \neq \lambda_{emitted.}$ Approximately 1 out of every 10^7 photons[7,8] are inelastically scattered and this low number means the overall Raman signal is quite weak and the low signal-to-noise ratio can prove to be a challenge[3,5,9]. To overcome the weak signal and poor signal-to-noise ratio, high powered lasers are usually used but their use can cause other unwanted effects such as sample degradation.

(1). $\Delta\tilde{v}(cm^{-1}) = \frac{1}{\lambda incident\ (nm)} - \frac{1}{\lambda scattered(nm)}\ x\frac{10^7 nm}{cm}$

1.1.2 Surfaced Enhanced Raman Spectroscopy

SE technology amplifies the weak-signal of Raman scattering. In 1973, the first SERS signal was observed, however it was not understood until 1977[11,12]. Single molecule SERS was observed in 1997[13,14]. The two enhancement mechanisms proposed to explain the SERS effect are electromagnetic and chemical-enhancement.

Chemical enhancement is a non-plasmonic mechansim[15] where in some cases 1 x 10^5 signal enhancement has been reported[16] on metal-substrates. Chemical-surface enhancement occurs when $\lambda_{incident}$ hits the roughened metal-surface causing photon excitation of an electron within the metal promoting it to the fermi energy level state. This excited electronic state results in the formation of a charge-transfer complex between the metal surface and the adsorbed-analyte, this complex causes the promotion of an electron of the adsorbed-analyte to the highest occupied molecular orbital (HOMO). As this electron returns to the ground state, a photon of different frequency is emitted because of this vibrational transition, similar to what occurs during resonance Raman spectroscopy[15]. For non-conductive substrates, charge transfer transitions can occur between: (1) HOMO of the

adsorbed-analyte with the conduction band (CB) edge of the substrate-surface, or; (2) The lowest unoccupied molecular orbital (LUMO) of the adsorbed-analyte with the valence band (VB) of the substrate-surface. Electronic transition states of the adsorbed-analyte from HOMO to LUMO or transitions between VB and CB of the substrate-surface can also contribute to the enhancement of Raman signal by resonance factors that can cause surface enhanced resonance Raman spectroscopy (SERRS)[15–17]. Usually, for successful chemical-SERS enhancement, the adsorbed-analyte must be bonded to the surface.

The **Electromagnetic** enhancement is the strongest contributor to SERS, typically enhancement in the range of 10^6-10^9 [18–20] has been reported and in some cases can reach even higher[13,19,21]. A plasmon is an oscillating wave of electrons created when a photon interacts with the outer valence electrons of a metal[22,23]. EM enhancement arises from the influence of the localised surface plasmon on Raman scattering. **Localised Surface Plasmon Resonance (LSPR)**[24]. The LSPR creates an EM field and this significantly enhances the Raman signal, making the Raman scattering more easily detectible for conventional Raman spectrophotometers [11,21,25,26]. The incident-photons interact with the charge-density oscillations of the conducting electrons on the metal surface creating LSPR(s). SERS detection can be summarised by the following equation: **(2)** $I_{SERS} = Nx \left(\frac{d\sigma}{d\Omega}\right) g^4 \frac{LP}{A} \eta$

Where N_X = the number of scattering molecules within the SERS volume, $(d\sigma/d\Omega)$ = the differential Raman cross-section per molecule, g^4 = electromagnetic enhancement, LP = incident laser power, A = the focus area, and η = the overall efficiency of the detection system (including the collection efficiency of scattered photons, transmission and photon detection efficiency of the spectrophotometer.

Chemical enhancement requires direct bonding between the analyte and the substrate, however EM enhancement does not. Both chemical and EM enhancement contribute to the detected SERS-signal, however it is well established that EM enhancement plays a more prominent role.

1.1.3 SERS substrates

In early studies, there were two main types of SERS substrates explored. The first were colloidal-metal solution(s) or alternatively (electrochemically/chemically) etched foils/wires of Au, Ag, or Cu[27]. SERS substrates are now more routinely fabricated from Au and Ag[28] and can be classified within three distinct categories[27,28]: (1) colloidal-metal NPs (nanoparticles) in suspension; (2) metal-NPs immobilized on solid substrates, and; (3) nano-template platform structures.

1.1.3.1 Colloidal Metal Nanoparticles

Colloidal metal suspensions can be prepared by either chemically or physically[27]. TEM images show these NPs, as spherical to ovoid shaped[29]. There are a wide variety of NP shapes, such as nanorods[30], nanocubes[30,31], nanodiscs[30–32], nanowires[30,31], nanospheres[30,33–35], nanotriangles[30,31,33,34], and nanostars[22,30,33,35]. The main issues with the use of these colloidal substrates is achieving uniform, reproducible signal enhancement and this can vary significantly due to particle-dimensions and shape[29,30,36].

There is considerable variation in strength of EM field enhancement regions due to the metallic nanoparticle shape, size, and aperture and also due to $\lambda_{incident}$ and polarization. The electrical field amplitude is not homogenous throughout the NP. The strongest electric field is typically found along tips and sharp-edges[37,42].

Anisotropic nanostructures such as triangles and rods usually experience larger field enhancement factors than isotropic spherical ones. *Hao et al.*[37] calculated field enhancement factors for similar sized but differing-shaped Ag-NP structures. The maximum EM field value for a 20 nm diameter nanosphere was obtained with a $\lambda_{incident}$ 700 nm laser-source and calculations showed it to be 14-times the applied field. The field enhancement factor was then calculated under the same conditions for Ag nanoprism, nanorod and nanospheroid structures. These anisotropic particles showed greater values than for isotropic-sphericals, approximated as equal to 59.1, 67 and 68.5 respectively.

Aggregation of sphere-shaped Au NPs is necessary to further amplify the SERS signal[33], This shape produced the lowest signal enhancement value[36]. Immobilising these NPs on solid-substrates is one such way of bringing them into close proximity with each other. One way of achieving this involves the use of a 'chemical anchor' to bind Au/Ag-NPs directly onto a quartz platform. *Perón et al.*[38] fabricated such a SERS substrate used for the detection of polycyclic aromatic hydrocarbons in artificial sea-water.

Another method published by *Bibikova et al*[39] uses a dithiol-functionalized PEG to bind metal nanostars onto a thin vapour-deposited Au layer on top of a silica substrate. *Kaminska et al.*[40] used SERS to carry out protein interaction studies and successfully tagged metal-NPs directly to silicon platforms without this intermediate metal-layer by using organosilanes, such as (3-mercaptopropyl) trimethoxysilane (MPTMS) or (3-aminopropyl) trimethoxysilane (APTMS). These compounds can bind directly to silica by silanization of the methoxysilane molecules to the surface and then to the metal-NPs at the opposite end directly after surface-conjugation. However, these irregularly-ordered structures do not allow for uniform, reproducible SERS signals and the chemical methods involved in their synthesis can cause significant spectral background interferences.

Also, from Equation 2, it can be deduced that SERS is a complex multi-factorial process with several influencing parameters, such as the number of adsorbed-analyte molecules, their orientation on the SERS substrate, the enhancement factor, laser power and overall efficiency of the spectrophotometric

system, and to effectively control all of these in order to achieve a highly uniform and reproducible SERS signal can prove quite difficult. The most challenging parameter to control is the number of adsorbed-molecules on the SERS substrate and their location within the plasmon volume.

Therefore, to obtain reproducible SERS-signal intensity, variations of parameters such as particle structure size, shape, inter-particle spacing, and distribution must be kept to a minimum during the substrate-fabrication process, as even slight variations e.g. in inter-particle spacing can strongly influence the amplitude and distribution of the electric field[41]. Structural-variations in fabricated SERS substrates can be also be minimised by constructing uniform, periodic nanostructured array templated-platforms that are presented in the detail in the next sub-section.

1.1.3.2 Immobilised and Periodic SERS Substrates

A 3D-Nanostar Dimer platform (*with a 10nm space underneath the structures for single molecular SERS detection*) was fabricated by *Chirumamilla et al*[43] and a similar substrate was constructed by *Gopalakrishnan et al*[44] (however, their platform was bi-metallic), both studies employed Electron-beam lithography (EBL) with reactive-ion etching (RIE). These fabricated platforms are structurally highly uniform throughout[44] which resulted in excellent, reproducible plasmonic hot-spot generation and localisation throughout the platform and they successfully reported enhancement factor of 4 x 10^{10} for the detection of rhodamine and adenine at extremely low (down to pM concentrations), with SERS signal deviating from no than 10 % from the same sample (reused multiple times[44]). However, EB methods are both costly and time-consuming.

1.1.3.3 Low Cost Lithographic Templated SERS substrates

Nanovoid arrays are widely reported under various names, such as nanoarrays, nanoholes, nanopores, nanocavities and/or nanowells. Due to their plasmonic properties, similar to the metallic nanoparticles previously discussed, their use in SERS studies is becoming increasingly more common. However a key advantage is the negative-curvature of their surfaces allows for analyte-volume capture within their interiors. Nanovoid arrays can be fabricated through variety of lithographic techniques such as NSL(Nano Sphere Lithography)[46,47] and soft NSL[48] which are much less expensive than EBL[23,49] and FIB[50]. NSL still enables successful fabrication of highly uniform SERS array platforms. Moreoever, it also yields reproducible SERS signal-detection. This templated method was used in this thesis to generate nanopore arrays for exosome capture.

Bartlett et al 2004[45] first advanced the use of Au electrodeposition using a 700 nm-polystyrene (PS) sphere(s) monolayer-template. After electro deposition the PS-monolayer can be removed, using THF or other solvents, leaving an intact hexagonally closed-packed array-pore structure. *Keyes et al* have used such SERS-array platforms for assessment of artificial lipid membrane(s)[51–54], oligo-

nucleotide[55] and protein/peptide[56,57] studies. In one such study, lipid-membrane permeation time is determined by the detection of the SERS signal from the bottom of the array pores[55.].

Mallon et al 2010[58] successfully fabricated 5 µM-diameter Au micro-array platforms using the NSL drop-casting method combined with bottom-to-top Au electrochemical deposition. It is this particular NSL-method that was modified here to fabricate the Au micro array platforms presented in this thesis. The void structure contains the plasmonic field specifically within the interior-well of the nanocavity. Both the plasmonic-energy and distribution of plasmon-modes within the array-pores are effectively controlled by array-size, aperture and thickness[47,59,60].

SERS EM factors were determined by *Gimenez et al* 2020[60] and EF_{SERS} (SERS enhancement factor) was calculated to be 7.1×10^3 (on 4,4'-BPY functionalized 1 µm Au array pore-platforms) and EF_{SERS} is further influenced by array dimension-size and $\lambda_{incident}$, this value is lower than the 1.5×10^7 value for 5 µM DRAQ7 reported *by Sakalys et al* 2021[61]. These 1 µm array platforms fabricated by *Gimenez et al* 2020[60] are the same substrates used for exosome capture in this thesis where EF_{SERS} are taken as 1×10^7 as reported. FDTD calculations show the EM field distribution indicate where maximum electric enhancement occurs at normal angle excitation which is ~50% higher than the calculated value at the array-rim[60]. *Bartlett et al*[62] attributed this sizeable variability in enhancement values in nanovoid-templated substrates to Mie plasmon excitations localised with the nanopores. Non-dispersive Mie plasmon resonances in nanovoids activate excitation of intense diffracted-beams within these pores.

Bartlett's theory further explains the location of the plasmonic hot spot within the arrays. Diffuse reflectance spectra on the 1-µm array platform show a plasmonic resonance peak for 1µm diameter Au-arrays around 785 nm[60,63] (See Figure 1.09b), which is why this specific $\lambda_{excitation}$ was chosen. These identical parameters (1µm array dimension-size and λ_{laser} 785 nm) were also used in this thesis for exosome capture and analysis. This NSL fabrication technique costs much less than EB methods and moreover, it is a much faster fabrication method.

1.1.4 Use of SERS substrates in Cell Biological Studies

Large volumes of sample are not necessary for successful single molecular SERS detection. This makes it an ideal analytical tool allowing for biomolecular analysis where production of a large sample volume is not possible. Also the small size(s) of functionalized metallic-NPs allows for cell membrane permeation via endocytosis[64] and intracellular processes can be studied using SERS.

Boca et al 2010[64] used flower shaped Au-NPs functionalized with two Raman active triarylmethane dyes; malachite green oxalate and basic fuchsin (widely used as biocompatible fluorescent biological stains), with the polymer mPEG-SH as capping material. The NPs were tested on D407 (human retinal epithelial) cells with MTT cell-viability assay results displaying low levels of toxicity for

concentrations necessary for SERS analysis. The maintenance of NP SERS signal in combination with fluorescent emission enables their further potential use for combinatorial coding and multiplexed spectral imaging. Moreover, this NP-platform , allowing for future conjugation of target-specific ligands to PEGylated SERS active NPs for *in vivo* tumour and other disease detection using confocal fluorescence and Raman imaging. SERS spectra of the conjugated NPs was carried out *in vitro* using a 633 nm laser source operating at 3 mW power with a 100 X (N.A. = 1.4) oil immersion objective lens on a confocal Raman microscope.

Their functionalized-NP probes proved very effective for *in vitro* SERS signal detection with optical and SERS spectral-profiles remain constant *in vitro* over time proving non-occurrence of intracellular protein-adsorption, and therefore applicable for use in future *in vivo* spectral imaging applications. However, the main drawback is that the NPs cannot be easily retrieved from the cells after completion of studies.

Genova et al 2018[65] eliminated the use of endocytosis of metallic-NP substrates for *in vitro* SERS studies and carried out SERS studies using colloidal Ag and Au-NPs on cell lysates sourced from three different cell lines, a healthy immortalised hepatic cell line (IHH), a tumorigenic hepatic cell line HepG2, and an oncogenic cervical cell line HeLa. Mitotic stages in cell lines were also synchronised (caused by serum media starvation) and these were compared to non-synchronised groups. SERS spectra were also assessed before and after lysate filtration (at 10 kDa to remove proteins in solution thereby preventing protein corona formation on the metallic surface which will impede the SERS signal). Reproducible and consistent EF_{SERS} detection was achieved due to the filtration process however the chosen lysis protocol did not affect EF_{SERS} . SERS analysis were carried out using a 10 X objective lens (0.25 N.A), 785nm laser (operating power 120 mW).

The detected SERS cytosolic spectra varied depending on choice of metallic substrate. Colloidal Ag yielded SERS spectra dominated with intense GSH (a reduced form of glutathione) bands with minor bands attributed to adenine, in contrast to colloidal Au substrates which yielded SERS spectra dominated with by adenine and adenosine bands with little contributions attributed to guanine and GSH. GSH contains multiple NH groups and a SH group which may have more of a bonding affinity to Ag than to Au[66]. Notably, there were no nucleotide rich SERS spectra (expected from cytosolic lysate as it is rich in purine bases) detected from citrate-coated metallic NPs due to charge repelling (the citrate is negatively-charged like the phosphate-bound structures present in the cytosolic lysate)[65]. The colloidal Ag yielded higher EF_{SERS} than Au, however SERS spectra obtained from colloidal Au substrates were able to successfully distinguish. not only the different cell lines but also subtle biochemical changes caused by mitotic synchronisation/serum media starvation. The analyte in question and experimental setup (monitoring a biochemical process versus specific-analyte targeting) dominates the choice (and any necessary surface modifications) of metallic SERS substrates.

The advantage of using cell lysates (over the previously discussed cellular endocytosed method) allows for easy NP retrievability and the additional 10 kPa lysate filtration step removes unwanted larger molecular protein structures (which cannot be removed from intact cells) that will greatly impede SERS signal detection.

SERS is also being employed in the emerging field of single-cell analysis. Single cell analysis is carried out to detect subtle (or pronounced) heterogenic properties within a tissue microenvironment. *Wang et al* 2019[64] successfully designed a SERS active fibre tip containing 4-Mpy (mercaptopyridine) functionalized Ag-NPs. 4-Mpy undergoes various protonation and deprotonation states relative to changes in pH. These altered states result in a change in its characteristic Raman spectrum. The functionalized fibre tip was successfully entered into a single cell and was then able to extra, intra and sub-cellularly detect varying pH levels within different microenvironments. The tip was also calibrated using PBS buffer and successfully re-used. Extra and intra-cellular pH studies were carried out using healthy hepatic LO2 and hepatomic HepG2 cell lines and subcellular studies (i.e. detecting pH levels in the nucleus and other organelles) were carried out using three different oncogenic cell groups; HepG2, MCF-7 and SGC7901. Single Cell heterogeneity was indicated by detection of varied pH values. SERS studies were carried out using a 633 nm laser source (operating power 7 mW) on an optical fibre tip containing 4-Mpy functionalized Ag-NPs on its surface. This platform could have potential diagnostic applications due to the well-established differences in pH values between oncogenic and healthy cell lines[64,67].

The NSL-fabricated Au micro-array pore (presented in forthcoming experimental chapters in this thesis) also has various applications in different biological studies. The LSPR-location within an Au array pore lies within the cavity well[60], therefore it is important to ensure that effective analyte-binding takes place within this region to ensure maximum SERS signal. This can be achieved by selectively-modifying selected-areas of the array with different SAMs (self-assembled monolayers) that can selectively capture analyte within the well whilst inhibiting analyte-adsorption at the top surface[28,68]. Mercaptans are frequently used to achieve this purpose. Au is the prime choice of metal substrate for alkane-thiol functionalization, because it is inert[28,68], robust and stable. It does not oxidise in air and can withstand harsh chemical treatment. Ag is also a suitable SERS substrate, however unlike Au, it readily oxidises in air and can be toxic to cells[28]. For these reasons, Au substrates were used in all studies presented in this thesis. A covalent bond readily forms between the thiol/sulphydyl (R-SH) functional group and Au. This Au-S bond strength is 100kJ/mol which is close to that of an Au-Au bond, which makes it quite stable. The thiol group is deprotonated resulting in the formation of a S radical (thiolate) that forms a covalent bond with the Au atoms (R-S-Au)[69] . The lone pair of electrons on the S of an R-SH group can also form a weak bond to the Au surface (Van Der Waal's forces)[69]. Strong Au-S covalent-bond formation allows for the creation of stable organometallic nanostructures whilst facilitating easy exchange of electrons between the S and Au atoms[69] allowing for effective-production of a LSPR upon hv-excitation[8,24,70,71]. The use of this

metallic surface-modification technique is primarily used to study various biological structures. It primarily involves soaking the substrate in a solution[56,57,72] or alternatively MCP (micro contact printing)[66,73–75], both of these techniques allow for SAM-formation on the substrate-surface.

Adamson et al[72] used selective surface modification (solution deposition) techniques to cause platelet-adhesion on planar Au substrates and studied the changes of surface binding caused by varying the choice of monolayer-functionalization. Their studies showed very little surface binding on an unmodified Au surface and that platelet Au-surface-binding increased approximately 3-fold by using PEG-COO-functionalized surfaces when compared to using a RGD-SAM alone. Also, Platelets conjugating to RGD (the C residue on the linear-peptide-molecule contains a SH group which conjugates to the Au-substrate) or mixed RGD: alkanethiol SAM surfaces were shown to capture platelets in their resting-state. Further, Platelet-RGD conjugation is caused by integrin-RGD recognition.

Adamson et al[56,76] also applied this same regioselective surface modification technique on Au micro array-templated structures to capture and carry out SERS studies on blood platelets captured within 1.6 µm diameter Au-arrays. Results from these studies indicate that selective-surface modification can promote and ensure effective analyte-adsorption to the substrate[72]. It can be seen, comparing SERS intensity that there is a significant increase (almost 4-fold) in Raman count[56] in an Au array structured platform than in a planar Au substrate however, most of the EF_{SERS} is thought to originate from the tops of the array pores so these results may not be directly comparable.

Both of these studies show the benefit of selective surface functionalization to promote maximum and reproducible SERS detection of biological species. Selective surface modification can also be employed to prevent any surface binding within in a specific area in order to ensure analyte-conjugation only occurs within a specific area (i.e. location of plasmonic hot-spot). Another study carried out by *Adamson et al*[57] showed that mercaptooctane-SAM on Au substrates (both planar and array-structured) inhibited surface-binding of both neuroblastoma (an oncogenic cell line) and human blood platelets at all times and an RGD-SAM always promoted surface-binding.

This was the reasoning behind use of mercaptohexane-SAM on the exterior of the Au micro array structures in the present application and an RGD-SAM within the interior of the array structures. This approach was expected to respectively prevent and promote exosome binding at the location of the localised plasmonic hot-spot, which will be shown and discussed in the introduction of Chapter 5.

1.2.0 Background to Other Techniques

1.2.1 Field Emission Scanning Electron Microscopy

FE-SEM, is a microscopic technique, that exploits electrons to create an image under vacuum. FE-SEM technology employs a Field Emitter gun with a sharp tungsten-filament-tip that on exposure to a high electric field (~ 10^{10} V/m near its surface) results in a highly focused electron-beam of ~2 nm in diameter which is approx. 10^3 times smaller than that of a standard SEM. This smaller beam along with a high Field Emission vacuum value (approx. 10^{-8} Torr) results in the production of high resolution microscopic images or alternatively, it can be used to carry out elemental analysis of a solid sample[77,78].

Upon incident of the primary electron beam, the incident-electrons can interact with the sample in various ways and different electron-trajectories can be produced depending on the sample-constituents[76]. Secondary electrons are low energy electrons created by inelastic scattering of primary electrons interacting on the sample's surface.

BSEs (Backscattered electrons) are high-energy electrons caused by elastic-scattering of the primary electron-beam after interacting with the atomic-nuclei present in the sample causing a trajectory of the electron path[79]. BSEs are not limited to the sample-surface; they can be found throughout the sample. The yield of BSEs, that is, the ratio of the number of emitted BSEs versus the amount of primary beam electrons, depends on the element's atomic number, i.e. the higher the atomic number, the brighter the contrast.

Depending on the constituents within the sample, the incident-electrons can be backscattered and emerge on the sample surface, preserving its high energy. Elements, such as the noble metals can deflect incident-electrons more strongly than lighter elements, due to their larger nuclei and heavier atomic mass. Different types of BSE detection-settings are found within different models of electron microscopes, some can detect BSEs emitted from the surface and others can detect BSEs emitted within the sample[77,79,80]. Manipulating these settings allows the microscopist to gain more detailed information about the structure of the sample.

FE-SEM is an invaluable and powerful visual-imaging tool used in molecular biological studies, as surface morphology can be observed in detail down to the nano-metre scale. Typically a biological sample is splutter-coated with either Au, Pt, Pd, Cr, and Ir to prevent any degradation[76,81,82] caused by the high energy electron-beam, with Cr appearing less granular[80] on coated-samples than the other metals, al sample splutter-coating may not always be necessary. The low current emitted typically in the 10-20μA range means that biological structures and surfaces can be easily studied and interrogated in more depth than with conventional SE and TE[80] microscopes.

Sharma et al 2010 [82] successfully imaged exosomes isolated from human-saliva using FE-SEM, the isolated-vesicles were immobilized on UV-cleaned silicon wafer-substrates. Samples were coated with Ir (iridium) for 15 s at a current of 20 mA, and the wafer edges were grounded using Ag-paint. Exosomes were studied under low beam energies (1.5 kV at 3.1 pA). Exosomal morphological structures were quantitated and assessed in great detail, down to the nanoscale. In this thesis, FE-SEM imaging was used to assess exosome capture within the array-pores and FIJI (ImageJ) software was then used to quantitate amount of each sub-group captured per pore.

1.2.2 Electrochemical Impedance Spectroscopy

EIS is a non-destructive electro-spectroscopic technique used to study the interfacial-electrical properties within an electrode system. It involves carrying out frequency domain measurement(s) by applying a low amplitude of sinusoidal perturbations within an electrode system and recording the response[83,84]. A linear response is then assumed due to the use of these low amplitudinal-perturbations

From basic Physics, resistance as a measured-value of an electrical-circuit system's ability to oppose the passage of electrical current through the system. Resistance (R) is governed by Ohm's law, which states that, $R = E$ (potential)$/I$ (current). However, in practice it only applies to an ideal resistor. An ideal resistor demonstrates resistance regardless of alternating current (AC) frequency (Hz) applied, such that I and V (voltage) pass through the resistor in phase. In more complex systems, this set-up does not apply and a phase separation occurs between the applied AC voltage and I reflecting the impedance of the system[85]. Impedance can thus be defined as, the measurement of the phase shift change in AC potential within an electrode-system. A low AC potential is applied to the system in order to produce a pseudo-linear response. A sinusoidal wave function is caused by the applied AC potential and if pseudo linear, the resulting I response will also be sinusoidal at the same frequency, only phase-shifted (Φ)[86–88]. Information from the electrode surface can be gained from the resulting frequency response. EIS measures the I response, where Z (impedance) is influenced by the applied voltage resulting in a perturbation of the sinusoidal wave of a given oscillation. The following equation denotes Z of a system:

$$(3)\ Z(t) = \frac{V(t)}{I(t)} = \frac{V_o Sin(2\pi f t)}{I_o(2\pi f t + \varphi)}$$

In equation 3 above, V_0 and I_0 respectively represent the maximum voltage and current signals applied to the system, f denotes the frequency of the sinusoidal-wave, t represents time, and ϕ, the phase-shift between the $I(t)$ and the $V(t)$ (Voltage-time) functions[83]. The complex impedance plane represents the real and imaginary vectors of the impedance modulus where ϕ is the phase-angle of the phase-shift of the V and I sinusoidal-waves, therefore Z can be considered as a complex value[89].

EIS data can be presented in various formats but is usually analysed using Nyquist or Bode plots. Each plotted-format has its respective advantages/disadvantages. Nyquist plots show Z' on the x-axis versus Z'' on the y-axis. Typically in faradaic impedance, a Nyquist plot consists of a high frequency semi-circular segment which corresponds to the electron-transfer process and a low frequency straight-angled line representing the limited diffusion process[90].

At any given f, both Z' and Z'' components are represented within the point on the spectrum. Total impedance Z, is deduced by the length of the vector from 0 to any given point, and the angle of the vector denotes the phase-shift. Nyquist plots are ideal for studying chemisorption on an electrode system, as the respective physical changes can be immediately observed on the graph. Additional data, such as resistive and capacitive values, must be extracted by fitting to a model circuit to gain further understanding of thickness and overall packing. One disadvantage of Nyquist plots is the lack of f information. To overcome this, Bode plots may be used to supplement analysis, by plotting f in logarithmic scale versus phase-shift[91,92]

There are two electrochemical-cell setups employed to study EIS. The first is a faradaic system which involves a redox probe such as potassium ferrous cyanide dissolved in an electrolyte solution, containing a working metal-electrode and other electrodes (counter and reference). The elements to be included for an equivalent circle model (ECM) are known. A typical ECM for faradaic analysis usually contains a double layer capacitance (C_{dl}), charge transfer resistance (R_{ct}), the ohmic resistance of the electrolyte (R_s) and the Warburg impedance (Z_w) and can be described in more detail using a Randles circuit model[84,93].

The second type of system, known as non-faradaic, the same electrochemical cell setup is used but the electroactive probe is omitted from the electrolyte solution. As there is no redox species present, a faradaic process does not take place and the interfacial-capacitance is usually observed[85,94]. The capacitance value will change with the thickness of the double layer or when surface chemical reactions cause changes to the dielectric constant. Non-faradaic impedance is typically used to study biomimetic protein membrane and phospholipid bilayer[51–53] models because it is non-destructive. It avoids the use of a probe which may interact with and influence the adsorbate. Non-faradaic (i.e. probe free) EIS was used in this thesis as a tool to confirm electrode selective surface modification and to follow exosome capture.

1.3.0 Exosomes

1.3.1 Introduction

Exosomes are heterogenous[95–98] biological nano-sized vesicles consisting of a phospho-lipid bilayer-membrane[99–103] with a thickness of approximately 5 nm[104,105]. They are found in all biological fluids, saliva[106], serum(s)[107], blood plasma[108,109], breast milk[106], urine[110–113], semen[114], amniotic[113,115–118], synovial[97,105,119], epididymal[105,106,116,120,121], broncho-alveolar lavage[106,122] and cerebrospinal fluids[122].

Their diameters range from 30-150 nm [99,121,123–127] with some DLS studies showing a single Gaussian peak around 60 nm[99,122,128] and are either spherical[98,129,130] or cup shaped[99,131–133]. Exosomes are the smallest[118,134] of all extracellular vesicles and are created in the cytosol[121,135] of all eukaryotic cells.

1.3.2 Exosome Structure

Exosomes from different cell lines have been found to carry certain similar structural-surface proteins including Rab-GTPase, SNAREs[120,136], integrins[135,137,138], and various tetraspanins (mainly CD9, CD63, CD31, CD37, CD81 and CD82)[135,139–141], and HSPA8, HSC70, and HSC73). Exosomes do not contain any organelles[105,142], however they do contain nucleic acids and other nuclear material from various organelles including the nucleus[143,144], mitochondrion[97,118,119,129], endoplasmic reticulum[145], and golgi apparatus[145].

Their protein cargo depends on cell type[95,131], it consists of cytoplasmic proteins[128,139,145,146], biomarkers; such as TSG101[95,118,143,144,147–151]; CHMP2a[105,118] (charged multi-vesicular body protein 2a; RAB11B[105,118,152] (Ras-related protein Rab 11B) ALIX[1,34,73] (a typical exosomal marker containing a proline rich region that bioconjugates with the SH_3 domain of c-Src[153], the first identified proto-oncogene[153–155]); and Annexin[53,107,138].

Exosomes also contain cytosol[144,148] and other structures including: MHC I[156] and II[157], flotillin[158], sphingomyelin[118,159] hexosylceramides[118], targeting[95] and adhesion[56] proteins, endosomal[144,150,160] proteins, glycoproteins[158,160] LAMP1[118] and MFG-E8[118], P-selectin[96,131,160] and other integrins[121,161], glycosylphadidylinositol[162] anchored biomolecules such as phosphatidylserine[144], lipids[95,147], lipid rafts[95,144] and carotenoids[110,163]. Exosomes are particularly enriched in cholesterol[95,144] and GM1[164] ganglioside. They also contain numerous other structures[160] (enzymes[97,118,134,165] etc.).

1.3.3 Exosome Formation

E*xo*some formation is known as biogenesis. Biogenesis is a much regulated pathway consisting of three different stages[105,142,166]. It occurs internally within a cell, when intraluminal vesicles called e*ndo*somes fuse within the plasma membrane of the parent cell and then are released from the cells through a process consisting of three different stages[117,118,142,166]:

(1) Endocytic vesicles are formed internally by invagination (inward-budding) of the cell membrane resulting in the creation of an endosome.

(2) Invagination of the endosomal membranes results in the formation of ILVs (intraluminal vesicles)within MVBs (large multi-vesicular bodies). During this process, various proteins are incorporated into the membranal structure and various cytosolic-cargo are also engulfed and captured within the internal structure of these ILVs.

(3) Finally, these large MLVs are transported to the edge of the cell where they fuse with the plasma membrane and are released directly into the tissue micro-enviornment[142,166]. Once they pass through the membrane they are known as exosomes (i.e. extra-cellular vesicles) and this extra-cellular-release is known as exocytosis[117,118].

Different cell types produce varying quantities of exosomes; MSCs produce a large amount[115,178], however much less will be produced by immature dendritic cells[174,179]. *In vitro*, exosome production will increase from pre-confluence to confluence stages, possibly due to cholesterol metabolism[180]. Once full-confluence is reached, contact inhibition is activated, cell metabolism retards and mitosis ceases as cells are entering quiescence[155].

1.3.4 Roles

1.3.4.1 Healthy Tissues

Exosomes play a vital role in cell signalling within the tissue microenvironment[144,148]. By binding to the receptor of a neighbouring cell, an exosome can induce various intra-cellular signalling pathways[56,127,160], caused by effective adhesion and exosomal-cargo delivery (such as new receptors, enzymes and nuclear material)to the target cells[117,121,135]. This adhesive process is carried out with the aid of SNAREs (soluble n-ethylmaleimide sensitive factor attachment protein receptor complexes) and ESCRT[175]. These are large biopolymeric structures contained within exosomes which regulate various cell processes. Such roles include the destruction of obsolete organelles and other molecular structures (apoptosis)[181] and antigen presentation[143]. The specificity of exosome-target cell binding is further regulated by integrins and other adhesion-specific molecules[135].Tetraspanin complexes play a further role in specific exosome target-cell selection *in vitro*[140] and *in vivo*[135] by modifying surface-integrins.

1.3.4.2 Diseased Tissues

In oncogenic-tissue, biogenesis is over-stimulated[153] and the resulting exosomes drive tumour progression by:

(1) *Upregulating angiogenesis* (the formation of new blood vessel network within its microenvironment).

(2) The *creation of a pre-metastatic alcove* and

(3) *Tumour cell migration*[96,182,183]. In the immune system, they activate differentiation of regulatory T-lymphocytes or myeloid cells which suppresses immune responses[184] and also allow pathogenic

propagation by target-cell interactions[156]. In Neurodegeneration, exosomal cargo plays a role in Alzheimer's disease progression[185].

1.3.5 Exosomes in Vascular Biology and Cardio Vascular Disease

1.3.5.1 Diagnostic and Therapeutic Roles of Exosomes

MSCs (Mesenchymal stem cells) are non-hematopoietic stem cells found in bone marrow and were used in breakthrough treatment for myocardial infarction[186]. MSCs have been used extensively in cardiac stem-cell therapy and studies indicate that their therapeutic benefits are mainly due to their secreted exsoomes[187].

Intact MSC-exosomes supplied directly to the myocardial area activated the Akt signalling-pathway[188,189], which increased cell proliferation and prevented adverse myocardial rejection. MSC-exosomes also increased overall cardiac performance and size-proportion, and restored its cellular bioenergetics by acting as a supply of ATP[127]. Moreover, their presence decreased oxidative stress and activated pro-survival signalling pathways and their use in regenerative therapeutics minimised rejection and increased the survival rate of transplanted-MSCs[190–193].

Exosomes play various roles in both disease progression and disease protection, advancement in their studies will further aid in enhancing diagnostic-capabilities and their therapeutic use could help disease treatment

1.4 Other Methods of Exosome Analysis

There are a wide variety of suitable techniques for characterisation of exosomes. These include TEM, SEM, AFM (atomic force microscopy), NTA (nanoparticle-tracking analysis), DLS (dynamic light scattering), resistive pulse sensing, ELISAs (enzyme-linked immunosorbent assays), FACS (fluorescent-activated cell sorting), flow cytometry, and microfluidic and electrochemical biosensors[196,197] and also SERS[198–202] (and a separate section on exosomal SERS studies is discussed in Chapter 5: Introduction).

1.5 Conclusions

This review focused on different SERS substrates in published-literature going from colloidal-metal-NPs in-solution, immobilised-NPs on solid platforms, and finally nanolithographically-fabricated platforms with more emphasis placed on nano-array templated substrates as this was the type of SERS-substrate used throughout this thesis. A section on the applications of differing SERS

substrates used in cell biology was also presented including the use of the SERS micro-array platform for blood platelet capture but progressing this method further by preventing any analyte-adsorption on the array exteriors. The literature survey reveals first that the intensity and location of the EM field on metallic-NP surfaces is influenced by the nanostructure's size, shape and interstitial space(s) between each nanostructure but also by excitation wavelength and its polarization. A review of the published literature on exosomes confirmed how heterogeneous they are in size, morphology, cargo-content and functions (and a comprehensive review of published SERS-exosome literature will be presented in Chapter 5: Introduction). Reproducibility issues can arise in platform design and quality but can also be caused by the SERS technique itself, therefore these influencing parameters must be considered during platform development as exosome amount captured per array pore cannot be controlled. With the intention to use this SERS micro-array platform for exosome capture and analysis, therefore, it is important to thoroughly control the SERS substrate's fabrication-parameters in order to achieve maximum and optimum signal enhancement at all times.

This thesis primarily aims to develop micro-array SERS platforms that are suitable for exosome capture and Raman analysis. A uniform substrate suitable for biocapture and/or analytical applications should allow for high sensitivity and achieve reproducibility of the detected SERS signal.

1.6 References

1   A. N. I. Historic and C. Landmark, *Nat. India*, , DOI:10.1038/nindia.2008.302.

2   C. V RAMAN and K. S. KRISHNAN, *Nature*, 1928, **121**, 501–502.

3   B. D. Patel and P. J. Mehta, 2010, 131–141.

4   S. Bilal, *Encycl. Appl. Electrochem.*, 2014, 1761–1765.

5   P. W. Atkins, T. L. Overton, J. P. Rourke and M. T. Weller, *Shriver and Atkins' Inorganic Chemistry, Fifth Edition*, 2010.

6   C. W. Ferraro, J.R., Nakamoto, K. & Brown, *Introductory Raman spectroscopy.*, Academic Press, 2003.

7   S. Fateixa, H. I. S. Nogueira and T. Trindade, *Phys. Chem. Chem. Phys.*, 2015, **17**, 21046–21071.

8   Z. Starowicz, R. Wojnarowska-Nowak, P. Ozga and E. M. Sheregii, *Colloid Polym. Sci.*, 2018, **296**, 1029–1037.

9   Methods for Improving Signal to Noise Ratio in Raman Spectra, 2018, S. Barton.

10   G. Smith, E. & Dent, *Modern Raman spectroscopy: a practical approach*, (J. Wiley, 2005.

11   M. Fleischmann, P. J. Hendra and A. J. McQuillan, *Chem. Phys. Lett.*, 1974, **26**, 163–166.

12   D. L. Jeanmaire and R. P. VAN Duyne, *J. Electroanal Chem.*, 1977, **84**, 1.

13   S. Nie and S. R. Emory, *Science (80-.).*, 1997, **275**, 1102–1106.

14   K. Kneipp, Y. Wang, H. Kneipp, L. T. Perelman, I. Itzkan, R. R. Dasari and M. S. Feld, *Phys. Rev. Lett.*, 1997, **78**, 1667–1670.

15   J. Kim, Y. Jang, N. J. Kim, H. Kim, G. C. Yi, Y. Shin, M. H. Kim and S. Yoon, *Front. Chem.*, 2019, **7**, 1–7.

16   C. Kuttner, R. P. M. Höller, M. Quintanilla, M. J. Schnepf, M. Dulle, A. Fery and L. M. Liz-Marzán, *Nanoscale*, 2019, **11**, 17655–17663.

17   G. Barbillon, *Nanomaterials*, 2020, **10**, 1–17.

18   R. Pilot, R. Signorini, C. Durante, L. Orian, M. Bhamidipati and L. Fabris, *Biosensors*, , DOI:10.3390/bios9020057.

19   J. P. Camden, J. A. Dieringer, Y. Wang, D. J. Masiello, L. D. Marks, G. C. Schatz and R. P. Van Duyne, *J. Am. Chem. Soc.*, 2008, **130**, 12616–12617.

20   S. Mahajan, J. J. Baumberg, A. E. Russell and P. N. Bartlett, *Phys. Chem. Chem. Phys.*, 2007, **9**, 6016–6020.

21   J. P. Camden, J. A. Dieringer, J. Zhao and R. P. Van Duyne, *Acc. Chem. Res.*, 2008, **41**, 1653–1661.

22   A. La Porta, A. Sánchez-Iglesias, T. Altantzis, S. Bals, M. Grzelczak and L. M. Liz-Marzán, *Nanoscale*, 2015, **7**, 10377–10381.

23   N. A. A. Hatab, J. M. Oran and M. J. Sepaniak, 2008, **2**, 377–385.

24   S. Schlücker, *Angew. Chemie - Int. Ed.*, 2014, **53**, 4756–4795.

25   J. N. Anker, W. P. Hall, O. Lyandres, N. C. Shah, J. Zhao and R. P. Van Duyne, 2008, **7**, 8–10.

26   C. L. Haynes, A. D. McFarland and R. P. Van Duyne, *2005;77(17):338 A-346*, 2005, **77**, 338–346.

27   P. A. Mosier-Boss, *Nanomaterials*, , DOI:10.3390/nano7060142.

28   J. C. Love, L. A. Estroff, J. K. Kriebel, R. G. Nuzzo and G. M. Whitesides, *Self-assembled monolayers of thiolates on metals as a form of nanotechnology*, 2005, vol. 105.

29   G. Herrera, A. Padilla and S. Hernandez-Rivera, *Nanomaterials*, 2013, **3**, 158–172.

30   N. D. Israelsen, C. Hanson and E. Vargis, *Sci. World J.*, 2015, **2015**, 124582.

31   B. Wiley, Y. Sun, B. Mayers and Y. Xia, *Chem. - A Eur. J.*, 2005, **11**, 454–463.

32   M. Li, F. Zhao, J. Zeng, J. Qi, J. Lu and W.-C. Shih, *J. Biomed. Opt.*, 2014, **19**, 111611.

33   F. Tian, F. Bonnier, A. Casey, A. E. Shanahan and H. J. Byrne, *Anal. Methods*, 2014, **6**, 9116–9123.

34   J. Pulit, M. Banach and Z. Kowalski, 2011.

35   F. Benz, R. Chikkaraddy, A. Salmon, H. Ohadi, B. de Nijs, J. Mertens, C. Carnegie, R. W. Bowman and J. J. Baumberg, *J. Phys. Chem. Lett.*, 2016, **7**, 2264–2269.

36   Y. Yang, S. Matsubara, L. Xiong, T. Hayakawa and M. Nogami, *J. Phys. Chem. C*, 2007, **111**, 9095–9104.

37   E. Hao and G. C. Schatz, *J. Chem. Phys.*, 2004, **120**, 357–366.

38   O. Péron, E. Rinnert, M. Lehaitre, P. Crassous and C. Compère, *Talanta*, 2009, **79**, 199–204.

39   O. Bibikova, J. Haas, A. I. López-Lorente, A. Popov, M. Kinnunen, I. Meglinski and B. Mizaikoff, *Analyst*, 2017, **142**, 951–958.

40   A. Kaminska, O. Inya-Agha, R. J. Forster and T. E. Keyes, *Phys. Chem. Chem. Phys.*, 2008, **10**, 4172–4180.

41   J. Ye, F. Wen, H. Sobhani, J. B. Lassiter, P. Van Dorpe, P. Nordlander and N. J. Halas, *Nano Lett.*, 2012, **12**, 1660–1667.

42   J. Krajczewski, K. Kołątaj and A. Kudelski, *RSC Adv.*, 2017, **7**, 17559–17576.

43   M. Chirumamilla, A. Toma, A. Gopalakrishnan, G. Das, R. P. Zaccaria, R. Krahne, E. Rondanina, M. Leoncini, C. Liberale, F. De Angelis and E. Di Fabrizio, *Adv. Mater.*, 2014, **26**, 2353–2358.

44   A. Gopalakrishnan, M. Chirumamilla, F. De Angelis, A. Toma, R. P. Zaccaria and R. Krahne, *ACS Nano*, 2014, **8**, 7986–7994.

45   P. N. Bartlett, J. J. Baumberg, S. Coyle and M. E. Abdelsalam, *Faraday Discuss.*, 2004, **125**, 117–132.

46   P. N. Bartlett, J. J. Baumberg, P. R. Birkin, M. A. Ghanem and M. C. Netti, *Chem. Mater.*, 2002, **14**, 2199–2208.

47   R. M. Cole, J. J. Baumberg, F. J. De Garcia Abajo, S. Mahajan, M. Abdelsalam and P. N. Bartlett, *Nano Lett.*, 2007, **7**, 2094–2100.

48   A. J. Baca, T. T. Truong, L. R. Cambrea, J. M. Montgomery, S. K. Gray, D. Abdula, T. R. Banks, J. Yao, R. G. Nuzzo and J. A. Rogers, *Appl. Phys. Lett.*, , DOI:10.1063/1.3155198.

49   W. Yue, Z. Wang, Y. Yang, L. Chen, A. Syed, K. Wong and X. Wang, *J. Micromechanics Microengineering*, 2012, **22**, 125007.

50   A. G. Brolo, R. Gordon, B. Leathem and K. L. Kavanagh, *Langmuir*, 2004, **20**, 4813–4815.

51   H. Basit, V. Gaul, S. Maher, R. J. Forster and T. E. Keyes, *Analyst*, 2015, **140**, 3012–3018.

52   S. Maher, H. Basit, R. J. Forster and T. E. Keyes, *Bioelectrochemistry*, 2016, **112**, 16–23.

53 J. Robinson, G. B. Berselli, M. G. Ryadnov and T. E. Keyes, , DOI:10.1021/acs.langmuir.0c00035.

54 G. B. Berselli, N. K. Sarangi, S. Ramadurai, P. V Murphy and T. E. Keyes, *ACS Appl. Bio Mater.*, 2019, **2**, 3404–3417.

55 K. W. Kho, G. B. Berselli and T. E. Keyes, , DOI:10.1002/smll.202005815.

56 K. Adamson, E. Spain, U. Prendergast, N. Moran, R. J. Forster and T. E. Keyes, *ACS Appl. Mater. Interfaces*, 2016, **8**, 32189–32201.

57 K. Adamson, E. Spain, U. Prendergast, N. Moran, R. J. Forster and T. E. Keyes, *Langmuir*, 2018, **34**, 715–725.

58 C. T. Mallon, C. Zuliani, T. E. Keyes and R. J. Forster, *Chem. Commun.*, 2010, **46**, 7109–7111.

59 T. A. Kelf, Y. Sugawara, R. M. Cole, J. J. Baumberg, M. E. Abdelsalam, S. Cintra, S. Mahajan, A. E. Russell and P. N. Bartlett, *Phys. Rev. B*, 2006, **74**, 245415.

60 A. V. Gimenez, K. W. Kho and T. E. Keyes, *Nanoscale Adv.*, 2020, **2**, 4740–4756.

61 R. Šakalys, K. W. Kho and T. E. Keyes, *Sensors Actuators, B Chem.*, , DOI:10.1016/j.snb.2021.129970.

62 T. V. Teperik, V. V. Popov, F. J. García de Abajo, T. A. Kelf, Y. Sugawara, J. J. Baumberg, M. Abdelsalem and P. N. Bartlett, *Opt. Express*, 2006, **14**, 11964.

63 C. T. Mallon, K. W. Kho, H. Gartite, R. J. Forster and T. E. Keyes, *Adv. Eng. Mater.*, 2018, **20**, 1–10.

64 J. Wang, Y. Geng, Y. Shen, W. Shi, W. Xu and S. Xu, *Sensors Actuators, B Chem.*, 2019, **290**, 527–534.

65 E. Genova, M. Pelin, G. Decorti, G. Stocco, V. Sergo, A. Ventura and A. Bonifacio, *Anal. Chim. Acta*, 2018, **1005**, 93–100.

66 J. C. Love, L. A. Estroff, J. K. Kriebel, R. G. Nuzzo and G. M. Whitesides, *Self-Assembled Monolayers of Thiolates on Metals as a Form of Nanotechnology*, 2005, vol. 105.

67 G. Hao, Z. P. Xu and L. Li, *RSC Adv.*, 2018, **8**, 22182–22192.

68 T. Wink, S. J. Van Zuilen, A. Bult and W. P. Van Bennekom, *Analyst*, 1997, **122**, 43–50.

69 H. Häkkinen, *Nat. Chem.*, 2012, **4**, 443–455.

70 J. Liang, H. Liu, J. Yu, L. Zhou and J. Zhu, *Nanophotonics*, 2019, **8**, 771–786.

71 R. Forster, T. Keyes and J. Vos, *Interfacial Sopramolecular Assemblies*, John Wiley and Sons, Ltd., 2004.

72 K. Adamson, E. Spain, U. Prendergast, R. J. Forster, N. Moran and T. E. Keyes, *Biomater. Sci.*, 2014, **2**, 1509–1520.

73 C. Crozatier, M. Le Berre and Y. Chen, *Microelectron. Eng.*, 2006, **83**, 910–913.

74 D. Qin, Y. Xia and G. M. Whitesides, *Nat. Protoc.*, 2010, **5**, 491–502.

75 S. Alom Ruiz and C. S. Chen, *Soft Matter*, 2007, **3**, 168–177.

76 M. Malenica, M. Vukomanović, M. Kurtjak, V. Masciotti, S. Dal Zilio, S. Greco, M. Lazzarino, V. Krušić, M. Perčić, I. J. Badovinac, K. Wechtersbach, I. Vidović, V. Baričević, S. Valić, P. Lučin, N. Kojc and K. Grabušić, *Biomedicines*, , DOI:10.3390/biomedicines9060603.

77 C. Rohaida Che Hak, C. T. Foo, N. A. F. Othman, N. A. Shukri, M. S. Ripin, M. Y. Meor

Sulaiman and Y. Abdullah, *Mater. Charact.*, 2015, **47**, 6.

78   Y. Jusman, S. C. Ng and N. A. Abu Osman, *Sci. World J.*, , DOI:10.1155/2014/289817.

79   Nanocomposite coatings based on quaternary metal-nitrogen and nanocarbon systems, 2012, M. Walock..

80   J. Pawley, *Scanning*, 1997, **19**, 324–336.

81   I. Stokroos, D. Kalicharan, J. J. L. Van Der Want and W. L. Jongebloed, *J. Microsc.*, 1998, **189**, 79–89.

82   U. C. Afm, S. Sharma, H. I. Rasool, V. Palanisamy, C. Mathisen, Ḱ. M. Schmidt, D. T. Wong and J. K. Gimzewski, 2010, **4**, 1921–1926.

83   S. Brosel-Oliu, N. Uria, N. Abramova and A. Bratov, *Biosens. - Micro Nanoscale Appl.*, , DOI:10.5772/60741.

84   X. Jiang, Y. Xie, D. Wan, M. Chen and F. Zheng, *Anal. Chim. Acta*, 2019, **1059**, 36–41.

85   A. Janshoff and C. Steinem, *Anal. Bioanal. Chem.*, 2006, **385**, 433–451.

86   A. Sharma, J. K. Bhattarai, S. S. Nigudkar, S. G. Pistorio, A. V. Demchenko and K. J. Stine, *J. Electroanal. Chem.*, 2016, **782**, 174–181.

87   S. Zhu, C; Dong, *Electroanalysis*, 2014, **26**, 14–29.

88   J. Niu and J. Y. Lee, *J. Food Sci.*, 2000, **65**, 780–785.

89   C. Zhu, S. Guo, Y. Fang and S. Dong, *ACS Nano*, 2010, **4**, 2429–2437.

90   B. A. Mei, O. Munteshari, J. Lau, B. Dunn and L. Pilon, *J. Phys. Chem. C*, 2018, **122**, 194–206.

91   F. Yu, X. Dai, T. Beebe and T. Hsiai, *Biosens. Bioelectron.*, 2011, **30**, 165–173.

92   B. Orazem, M. E.; Tribollet, *Electrochemical Impedance Spectroscopy*, Wiley, New Jersey, 2nd edn., 2008.

93   L. Yang and R. Bashir, *Biotechnol. Adv.*, 2008, **26**, 135–150.

94   G. Ertürk and B. Mattiasson, *Sensors* , 2017, 17.

95   N. Ludwig, S. S. Yerneni, B. M. Razzo and T. L. Whiteside, *Mol. Cancer Res.*, 2018, **16**, 1798–1808.

96   J. Rak, *Semin. Thromb. Hemost.*, 2010, **36**, 888–906.

97   X. Yao, W. Wei, X. Wang, L. Chenglin, M. Björklund and H. Ouyang, *Biomaterials*, 2019, **224**, 119492.

98   J. Zhou, S. Ghoroghi, A. Benito-Martin, H. Wu, U. J. Unachukwu, L. S. Einbond, S. Guariglia, H. Peinado and S. Redenti, *Sci. Rep.*, , DOI:10.1038/srep19743.

99   X. Li, L. Liu, J. Yang, Y. Yu, J. Chai, L. Wang, L. Ma and H. Yin, *EBioMedicine*, 2016, **8**, 72–82.

100   Z. Sun, L. Wang, S. Wu, Y. Pan, Y. Dong, S. Zhu, J. Yang, Y. Yin and G. Li, *Anal. Chem.*, 2020, **92**, 3819–3826.

101   I. Perrotta and S. Aquila, *Ultrastruct. Pathol.*, 2016, **40**, 101–106.

102   R. Szatanek, M. Baj-Krzyworzeka, J. Zimoch, M. Lekka, M. Siedlar and J. Baran, *Int. J. Mol. Sci.*, , DOI:10.3390/ijms18061153.

103   E. Hergenreider, S. Heydt, K. Tréguer, T. Boettger, A. J. G. Horrevoets, A. M. Zeiher, M. P. Scheffer, A. S. Frangakis, X. Yin, M. Mayr, T. Braun, C. Urbich, R. A. Boon and S.

Dimmeler, *Nat. Cell Biol.*, 2012, **14**, 249–256.

104 R. Huang, K. Yao, A. Sun, J. Qian, L. Ge, Y. Zhang, Y. Niu, K. Wang, Y. Zou and J. Ge, *Stem Cell Res. Ther.*, 2015, **6**, 1–11.

105 S. Gurunathan, M. Kang, M. Jeyaraj, M. Qasim and J. Kim, *Cells*, 2019, **8**, 307.

106 C. Lässer, V. Seyed Alikhani, K. Ekström, M. Eldh, P. Torregrosa Paredes, A. Bossios, M. Sjöstrand, S. Gabrielsson, J. Lötvall and H. Valadi, *J. Transl. Med.*, 2011, **9**, 1–8.

107 R. B. Koumangoye, A. M. Sakwe, J. S. Goodwin, T. Patel and J. Ochieng, *PLoS One*, , DOI:10.1371/journal.pone.0024234.

108 H. Shin, S. Oh, S. Hong, M. Kang, D. Kang, Y. G. Ji, B. H. Choi, K. W. Kang, H. Jeong, Y. Park, H. K. Kim and Y. Choi, *ACS Nano*, 2020, **14**, 5435–5444.

109 X. Osteikoetxea, A. Balogh, K. Szabó-Taylor, A. Németh, T. G. Szabó, K. Pálóczi, B. Sódar, Á. Kittel, B. György, É. Pállinger, J. Matkó and E. I. Buzás, *PLoS One*, 2015, **10**, 1–16.

110 S. G. Kruglik, F. Royo, J. M. Guigner, L. Palomo, O. Seksek, P. Y. Turpin, I. Tatischeff and J. M. Falcón-Pérez, *Nanoscale*, 2019, **11**, 1661–1679.

111 P. Fernández-Llama, S. Khositseth, P. A. Gonzales, R. A. Star, T. Pisitkun and M. A. Knepper, *Kidney Int.*, 2010, **77**, 736–742.

112 R. Lane, D. Korbie, M. Trau and M. Hill, 2017, **1660**, 111–130.

113 T. Pisitkun and M. A. Knepper, 2012, **77**, 736–742.

114 L. Vojtech, S. Woo, S. Hughes, C. Levy, L. Ballweber, R. P. Sauteraud, J. Strobl, K. Westerberg, R. Gottardo, M. Tewari and F. Hladik, *Nucleic Acids Res.*, 2014, **42**, 7290–7304.

115 R. W. Y. Yeo, R. C. Lai, B. Zhang, S. S. Tan, Y. Yin, B. J. Teh and S. K. Lim, *Adv. Drug Deliv. Rev.*, 2013, **65**, 336–341.

116 J. Conde-vancells, E. Rodriguez-suarez, N. Embade, D. Gil, R. Matthiesen, M. Valle, F. Elortza, S. C. Lu, J. M. Mato and J. M. Falcon-perez, 2008, 5157–5166.

117 G. Raposo and W. Stoorvogel, *J. Cell Biol.*, 2013, **200**, 373–383.

118 M. Colombo, G. Raposo and C. Théry, *Annu. Rev. Cell Dev. Biol.*, 2014, **30**, 255–289.

119 A. T. Jan, M. A. Malik, S. Rahman, H. R. Yeo, E. J. Lee, T. S. Abdullah and I. Choi, *Front. Aging Neurosci.*, 2017, **9**, 1–8.

120 G. Van Niel, I. Porto-Carreiro, S. Simoes and G. Raposo, *J. Biochem.*, 2006, **140**, 13–21.

121 C. Théry, M. Ostrowski and E. Segura, *Nat. Rev. Immunol.*, 2009, **9**, 581–593.

122 T. S. Martins, J. Catita, I. M. Rosa, O. A. B. Da Cruz e Silva and A. G. Henriques, *PLoS One*, 2018, **13**, 1–16.

123 M. Lee, J. J. Ban, W. Im and M. Kim, *Biotechnol. Bioprocess Eng.*, 2016, **21**, 299–304.

124 T. A. Shtam, R. A. Kovalev, E. Y. Varfolomeeva, E. M. Makarov, Y. V. Kil and M. V. Filatov, *Cell Commun. Signal.*, 2013, **11**, 1–10.

125 B. Costa-silva, N. M. Aiello, A. J. Ocean, S. Singh, B. K. Thakur, A. Becker, A. Hoshino, M. T. Mark, H. Molina, J. Xiang, T. Zhang, T. Theilen, G. García-santos, C. Williams, Y. Ararso, Y. Huang and G. Rodrigues, *Nat Cell Biol*, 2018, **17**, 816–826.

126 R. J. Lobb, M. Becker, S. W. Wen, C. S. F. Wong, A. P. Wiegmans, A. Leimgruber and A. Möller, *J. Extracell. Vesicles*, , DOI:10.3402/jev.v4.27031.

127 M. R. Ward, A. Abadeh and K. A. Connelly, *Stem Cells Transl. Med.*, 2018, **7**, 543–550.

128   R. Maroto, Y. Zhao, M. Jamaluddin, V. L. Popov, H. Wang, M. Kalubowilage, Y. Zhang, J. Luisi, H. Sun, C. T. Culbertson, S. H. Bossmann, M. Motamedi and A. R. Brasier, *J. Extracell. Vesicles*, , DOI:10.1080/20013078.2017.1359478.

129   R. A. Kore, J. C. Henson, R. N. Hamzah, R. J. Griffin, A. J. Tackett, Z. Ding and J. L. Mehta, *Sci. Rep.*, 2019, **9**, 1–12.

130   J. M. Noble, L. D. M. Roberts, N. Vidavsky, A. E. Chiou, C. Fischbach, M. J. Paszek, L. A. Estroff and L. F. Kourkoutis, *J. Struct. Biol.*, , DOI:10.1016/j.jsb.2020.107474.

131   M. Y. Xu, Z. S. Ye, X. T. Song and R. C. Huang, *Stem Cell Res. Ther.*, 2019, **10**, 1–11.

132   J. Park and Y. Choi, *Biomed. Eng. Lett.*, 2014, **4**, 258–268.

133   M. K. Jung and J. Y. Mun, 2018, 5–9.

134   C. M. Boulanger, X. Loyer, P. E. Rautou and N. Amabile, *Nat. Rev. Cardiol.*, 2017, **14**, 259–272.

135   S. Rana, S. Yue, D. Stadel and M. Zöller, *Int. J. Biochem. Cell Biol.*, 2012, **44**, 1574–1584.

136   M. Zöller, *Nat. Rev. Cancer*, 2009, **9**, 40–55.

137   B. H. Sung, T. Ketova, D. Hoshino, A. Zijlstra and A. M. Weaver, *Nat. Commun.*, , DOI:10.1038/ncomms8164.

138   C. Théry, A. Regnault, J. Garin, J. Wolfers, L. Zitvogel, P. Ricciardi-Castagnoli, G. Raposo and S. Amigorena, *J. Cell Biol.*, 1999, **147**, 599–610.

139   R. Wubbolts, R. S. Leckie, P. T. M. Veenhuizen, G. Schwarzmann, W. Möbius, J. Hoernschemeyer, J. W. Slot, H. J. Geuze and W. Stoorvogel, *J. Biol. Chem.*, 2003, **278**, 10963–10972.

140   M. E. Hemler, *Annu. Rev. Cell Dev. Biol.*, 2003, **19**, 397–422.

141   Z. Andreu and M. Yáñez-Mó, *Front. Immunol.*, 2014, **5**, 1–12.

142   E. Cocucci and J. Meldolesi, *Trends Cell Biol.*, 2015, **25**, 364–372.

143   A. Bobrie, M. Colombo, G. Raposo and C. Théry, *Traffic*, 2011, **12**, 1659–1668.

144   M. Mathieu, L. Martin-Jaular, G. Lavieu and C. Théry, *Nat. Cell Biol.*, 2019, **21**, 9–17.

145   R. Zhan, X. Leng, X. Liu, X. Wang, J. Gong, L. Yan, L. Wang, Y. Wang, X. Wang and L. J. Qian, *Biochem. Biophys. Res. Commun.*, 2009, **387**, 229–233.

146   V. Luga, L. Zhang, A. M. Viloria-Petit, A. A. Ogunjimi, M. R. Inanlou, E. Chiu, M. Buchanan, A. N. Hosein, M. Basik and J. L. Wrana, *Cell*, 2012, **151**, 1542–1556.

147   Y. Cheng, Q. Zeng, Q. Han and W. Xia, *Protein Cell*, 2019, **10**, 295–299.

148   W. Gao, H. Liu, J. Yuan, C. Wu, D. Huang, Y. Ma, J. Zhu, L. Ma, J. Guo, H. Shi, Y. Zou and J. Ge, *J. Cell. Mol. Med.*, 2016, **20**, 2318–2327.

149   R. Di Santo, S. Romanò, A. Mazzini, S. Jovanović, G. Nocca, G. Campi, M. Papi, M. De Spirito, F. Di Giacinto and G. Ciasca, *Nanomaterials*, , DOI:10.3390/nano11061476.

150   C. April, S. E. E. L. Page, K. Trajkovic, C. Hsu, S. Chiantia, L. Rajendran, D. Wenzel, F. Wieland, P. Schwille, B. Brügger and M. Simons, .

151   S. Stuffers, C. S. Wegner, H. Stenmark and A. Brech, 2009, 925–937.

152   L. Blanc and M. Vidal, *Small GTPases*, 2018, **9**, 95–106.

153   T. Hikita, A. Kuwahara, R. Watanabe, M. Miyata and C. Oneyama, *Sci. Rep.*, 2019, **9**, 1–14.

154   H. Peinado, *Nat. Med.*, 2013, **18**, 883–891.

155   L. Lorencova, T. Bertok, A. Bertokova, V. Gajdosova, S. Hroncekova, A. Vikartovska, P. Kasak and J. Tkac, *ChemElectroChem*, 2020, 1–19.

156   P. Kujala, C. R. Raymond, M. Romeijn, S. F. Godsave, S. I. van Kasteren, H. Wille, S. B. Prusiner, N. A. Mabbott and P. J. Peters, *PLoS Pathog.*, , DOI:10.1371/journal.ppat.1002449.

157   I. M. J. Wolfs, M. M. P. C. Donners and M. P. J. de Winther, *Thromb. Haemost.*, 2011, **106**, 763–771.

158   V. Ciravolo, V. Huber, G. C. Ghedini, E. Venturelli, F. Bianchi, M. Campiglio, D. Morelli, A. Villa, P. Della Mina, S. Menard, P. Filipazzi, L. Rivoltini, E. Tagliabue and S. M. Pupa, *J. Cell. Physiol.*, 2012, **227**, 658–667.

159   R. J. Lakshmi, V. B. Kartha, C. M. Krishna, J. G. R. Solomon, G. Ullas and P. U. Devi, *Radiat. Res.*, 2002, **157**, 175–182.

160   Y. Chen, H. Yuan, Z. Ou and J. Ou, .

161   S. Paone, A. A. Baxter, M. D. Hulett and I. K. H. Poon, *Cell. Mol. Life Sci.*, 2019, **76**, 1093–1106.

162   I. Notingher, C. Green, C. Dyer, E. Perkins, N. Hopkins, C. Lindsay and L. L. Hench, *J. R. Soc. Interface*, 2004, **1**, 79–90.

163   A. Kirby, L. Edwards, D. Sugden and S. Rosenblum, *Res. Dev. Disabil.*, 2010, **31**, 131–139.

164   E. Katz and I. Willner, *Electroanalysis*, 2003, **15**, 913–947.

165   A. J. Ruiz-Chica, M. A. Medina, F. Sánchez-Jiménez and F. J. Ramírez, *J. Raman Spectrosc.*, 2004, **35**, 93–100.

166   N. P. Hessvik and A. Llorente, *Cell. Mol. Life Sci.*, 2018, **75**, 193–208.

167   C. Obregon, B. Rothen-Rutishauser, S. K. Gitahi, P. Gehr and L. P. Nicod, *Am. J. Pathol.*, 2006, **169**, 2127–2136.

168   D. Gruson, S. Bernardini, P. K. Dabla, B. Gouget and S. Stankovic, *Clin. Chim. Acta*, 2020, **509**, 67–71.

169   H. T. Mcmahon and E. Boucrot, 2015, 1065–1070.

170   F. Alcayaga-Miranda, P. L. González, A. Lopez-Verrilli, M. Varas-Godoy, C. Aguila-Díaz, L. Contreras and M. Khoury, *Oncotarget*, 2016, **7**, 44462–44477.

171   S. Zhang, J. Liu, K. Zheng, L. Chen, Y. Sun, Z. Yao, Y. Sun, Y. Lin, K. Lin and L. Yuan, *Vascul. Pharmacol.*, 2021, **136**, 106820.

172   W. Yanan, X. Yingyu, Z. Ao, W. Mingyang, F. Zihan and Z. Junping, *Biomed. Pharmacother.*, , DOI:10.1016/j.biopha.2019.108951.

173   C. Subra, D. Grand, K. Laulagnier, A. Stella, G. Lambeau, M. Paillasse, P. De Medina, B. Monsarrat, B. Perret, S. Silvente-poirot, M. Poirot and M. Record, 2010, **51**, 2105–2120.

174   L. Alvarez-erviti, Y. Seow, H. Yin, C. Betts, S. Lakhal and M. J. A. Wood, *Nat. Biotechnol.*, , DOI:10.1038/nbt.1807.

175   W. M. Henne, H. Stenmark and S. D. Emr, *Cold Spring Harb. Perpectives Biol.*, 2013, **5**, a016766.

176   R. A. Steinman, A. Wentzel, Y. Lu, C. Stehle and J. R. Grandis, *Oncogene*, 2003, **22**, 3608–3615.

177   O. Hayes, B. Ramos, L. L. Rodríguez, A. Aguilar, T. Badía and F. O. Castro, *Anim. Reprod. Sci.*, 2005, **87**, 181–192.

178   T. S. Chen, F. Arslan, Y. Yin, S. S. Tan, R. C. Lai, A. B. H. Choo, J. Padmanabhan, C. N.

Lee, D. P. V. de Kleijn and S. K. Lim, *J. Transl. Med.*, 2011, **9**, 1–10.

179   Y. Tian, S. Li, J. Song, T. Ji, M. Zhu, G. J. Anderson, J. Wei and G. Nie, *Biomaterials*, 2014, **35**, 2383–2390.

180   D. Gal, P. C. MacDonald, J. C. Porter, J. W. Smith and E. R. Simpson, *Cancer Res.*, 1981, **41**, 473–477.

181   C. V. Harding, J. E. Heuser and P. D. Stahl, *J. Cell Biol.*, 2013, **200**, 367–371.

182   J. L. Hood, S. San Roman and S. A. Wickline, *Cancer Res.*, 2011, **71**, 3792–3801.

183   K. Tung, M. Ernstoff, C. Allen and S. Shu, *J. Immunol. Sci.*, 2019, **3**, 4–8.

184   H. G. Zhang and W. E. Grizzle, *Clin. Cancer Res.*, 2011, **17**, 959–964.

185   J. Howitt and A. F. Hill, *J. Biol. Chem.*, 2016, **291**, 26589–26597.

186   M. Madigan and R. Atoui, *Bioengineering*, 2018, **5**, 1–18.

187   Ranganath H. Sudhir et al., *Cell Stem Cell*, 2013, **10**, 244–258.

188   J. Zheng, Y. Y. Zhuo, C. Zhang, G. Y. Tang, X. Y. Gu and F. Wang, *Eur. Rev. Med. Pharmacol. Sci.*, 2020, **24**, 3293–3301.

189   Z. Yan, S. Dutta, Z. Liu, X. Yu, N. Mesgarzadeh, F. Ji, G. Bitan and Y. H. Xie, *ACS Sensors*, 2019, **4**, 488–497.

190   F. Arslan, R. C. Lai, M. B. Smeets, L. Akeroyd, A. Choo, E. N. E. Aguor, L. Timmers, H. V. van Rijen, P. A. Doevendans, G. Pasterkamp, S. K. Lim and D. P. de Kleijn, *Stem Cell Res.*, 2013, **10**, 301–312.

191   C. Ashur and W. H. Frishman, *Cardiol. Rev.*, 2018, **26**, 8–21.

192   P. Gurha, C. Abreu-Goodger, T. Wang, M. O. Ramirez, A. L. Drumond, S. Van Dongen, Y. Chen, N. Bartonicek, A. J. Enright, B. Lee, R. J. Kelm, A. K. Reddy, G. E. Taffet, A. Bradley, X. H. Wehrens, M. L. Entman and A. Rodriguez, *Circulation*, 2012, **125**, 2751–2761.

193   A. G. E. Ibrahim, K. Cheng and E. Marbán, *Stem Cell Reports*, 2014, **2**, 606–619.

194   A. Clayton, J. Court, H. Navabi, M. Adams, M. D. Mason, J. A. Hobot, G. R. Newman and B. Jasani, *J. Immunol. Methods*, 2001, **247**, 163–174.

195   J. Z. Nordin, Y. Lee, P. Vader, I. Mäger, H. J. Johansson, W. Heusermann, O. P. B. Wiklander, M. Hällbrink, Y. Seow, J. J. Bultema, J. Gilthorpe, T. Davies, P. J. Fairchild, S. Gabrielsson, N. C. Meisner-Kober, J. Lehtiö, C. I. E. Smith, M. J. A. Wood and S. E. L. Andaloussi, *Nanomedicine Nanotechnology, Biol. Med.*, 2015, **11**, 879–883.

196   C. Théry, S. Amigorena, G. Raposo and A. Clayton, *Curr. Protoc. Cell Biol.*, 2006, **30**, 3.22.1-3.22.29.

197   R. A. Dragovic, C. Gardiner, A. S. Brooks, D. S. Tannetta, D. J. P. Ferguson, P. Hole, B. Carr, C. W. G. Redman, A. L. Harris, P. J. Dobson, P. Harrison and I. L. Sargent, *Nanomedicine Nanotechnology, Biol. Med.*, 2011, **7**, 780–788.

198   S. Stremersch, M. Marro, B. El Pinchasik, P. Baatsen, A. Hendrix, S. C. De Smedt, P. Loza-Alvarez, A. G. Skirtach, K. Raemdonck and K. Braeckmans, *Small*, 2016, **12**, 3292–3301.

199   J. Park, M. Hwang, B. Choi, H. Jeong, J. H. Jung, H. K. Kim, S. Hong, J. H. Park and Y. Choi, *Anal. Chem.*, 2017, **89**, 6695–6701.

200   J. Carmicheal, C. Hayashi, X. Huang, L. Liu, Y. Lu, A. Krasnoslobodtsev, A. Lushnikov, P. G. Kshirsagar, A. Patel, M. Jain, Y. L. Lyubchenko, Y. Lu, S. K. Batra and S. Kaur, *Nanomedicine Nanotechnology, Biol. Med.*, 2019, **16**, 88–96.

201   B. Hernández, F. Pflüger, S. G. Kruglik and M. Ghomi, *J. Raman Spectrosc.*, 2013, **44**, 827–

833.

202   J. Langer, D. J. De Aberasturi, J. Aizpurua, R. A. Alvarez-puebla, B. Auguie, J. J. Baumberg, G. C. Bazan, S. E. J. Bell and A. Boisen, , DOI:10.1021/acsnano.9b04224.

Chapter 2: Materials and Methods

2.0 Materials and Methods

2.1 Materials

Commercial Au Salt solution was purchased from Technic UK (Lektrachem Ltd). Au Wafers were purchased from Ams Biotechnology (Abington, UK). 1-micron Polystyrene beads were purchased from Polysciences Europe Gmbh (Baden-Wuerttemberg, Germany), (c)-RGDFK peptide powder was purchased from Celtek peptides (USA). Mercaptohexanol, mercaptohexane, sodium dibasic phosphate, EDC 1-ethyl-3-(-3-dimethylaminopropyl) carbodiimide hydrochloride, Sulpho-NHS (N-hydroxysulphosuccinimide), mercaptooctanoic acid, thiocholesterol, D-Mannitol, Glucose and PBS (Phosphate buffered saline) tablets were purchased from Sigma-Aldrich (Wicklow Ireland). Polydimethylsiloxane silicon elastomer (PDMS) was purchased from Dow Corning Gmbh (Wiesbaden, Germany) and prepared according to the supplier's protocol. ExoQuick™ was sourced from Biocat Gmbh (Hiedelberg, Germany) and used according to the manufacturer's instructions.

All Aqueous solutions were prepared using MilliQ water (18mΩ) (Millipore Corp. Bedford, USA).

The BODIPY Cholesterol probe was synthesised by Dr Darragh O'Connor[1], School of Chemical Sciences, DCU.

2.2.0 Methods

2.2.1 Au micro array substrate fabrication

Au micro-array platforms were fabricated using the method previously reported by *Basit et al*[2]. Briefly, PS (polystyrene) beads of 1 μm in diameter were dropcasted onto 15 mm x 8 mm sized silicon wafers containing a 100 nm thick layer of vapour-deposited Au. This dropcasted PS solution was allowed to dry overnight to form a monolayer and a three electrode electrochemical system was set up using the Au coated wafer as the working electrode, platinum wire auxiliary electrode and an Ag/AgCl reference electrode, see Figure 2.01 for schematic of the electrochemical cell setup.

Au was electrodeposited onto the wafer by holding the electrode at a potential (E) of −0.58 V (vs Ag/AgCl reference) in a commercially available Au electrodeposition solution until the electrodeposited Au had grown to the equator of the PS bead-monolayer, i.e. when i_{min} has been reached. This was determined by the lowest current (**i**) reached on the software voltammogram (and this point will be expanded upon in the first experimental chapter). The resulting micro-array platform was then rinsed with deionised water to remove any remaining Au salt/electrolyte from its

surface. The platform was then immersed in THF and sonicated for 10 mins to thoroughly remove the PS-SAM and dried off using N_2 flow to ensure the Au substrate was completely dry. This ensured maximum surface exposure for selective-surface modification and maximized the functionalization process on the substrate's surface.
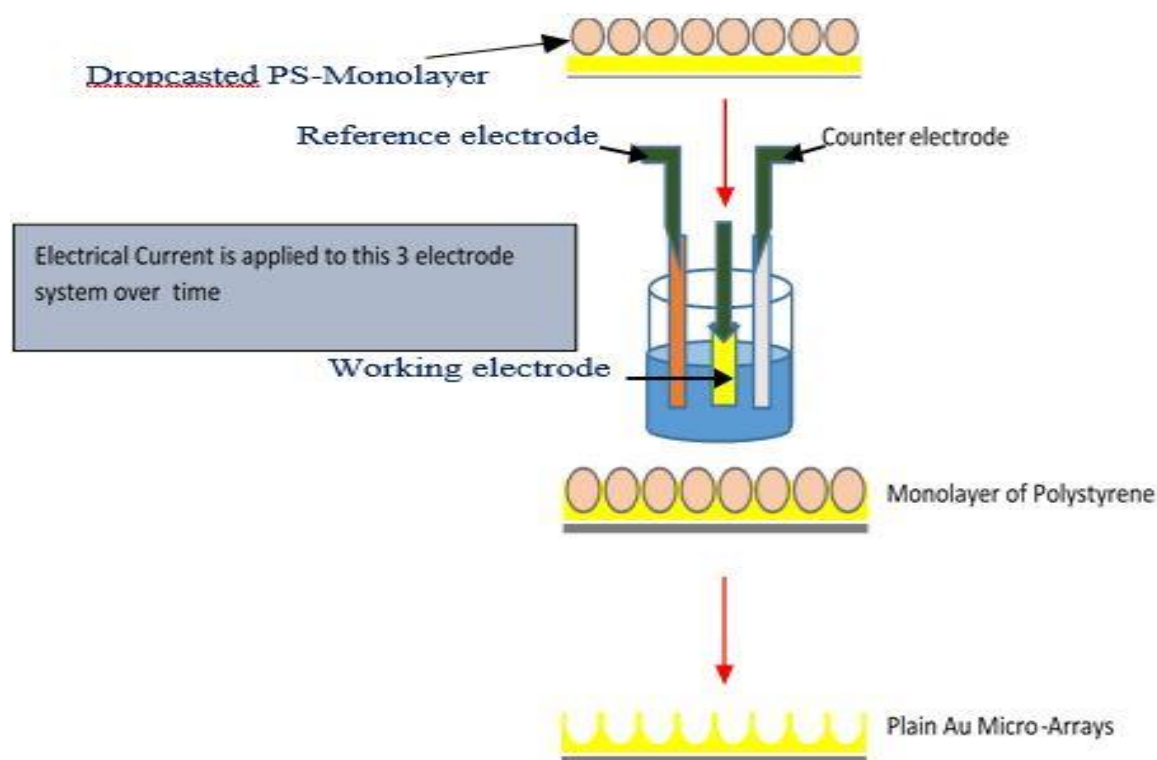
Figure 2.01: Schematic Setup of a 3-electrode electrochemical cell used for bottom to top Au deposition resulting in a micro array platform formation. An electric current is applied to this electrode system over time resulting in bottom to top Au deposition within the inter-sphere spaces of the PS-SAM. This monolayer can be removed after Au deposition has been completed, by sonication in THF revealing a uniform, array-templated structure.

2.2.2 Micro contact printing-stamp fabrication

To make a micro contact printing "stamp"; A modified method previously reported by *Qin et al 2010*[3] was used. 70 µL of 10 mM solution of thiol alcoholic solution (mercaptohexane and/or mercaptohexanol) was aliquoted onto a pre-fabricated PDMS template. After evaporation the template was placed in direct contact with the micro-array platform and this was left for 30 min.

2.2.3 Synthetic modification step of (c)-RGDFK peptide

The (c)-RGDFK peptide was conjugated with a hexyl thiol linker according to EDC Sulpho NHS reaction mechanism outlined in *Hermanson 2013*[4]. The EDC reacts with the Carboxylic acid group creating a sulpho-NHS ester intermediate (an amine nucleophile). An amide bond is then formed with the thiol group on the opposite end of the hexyl chain, see reaction mechanism in Figure 2.02[4].
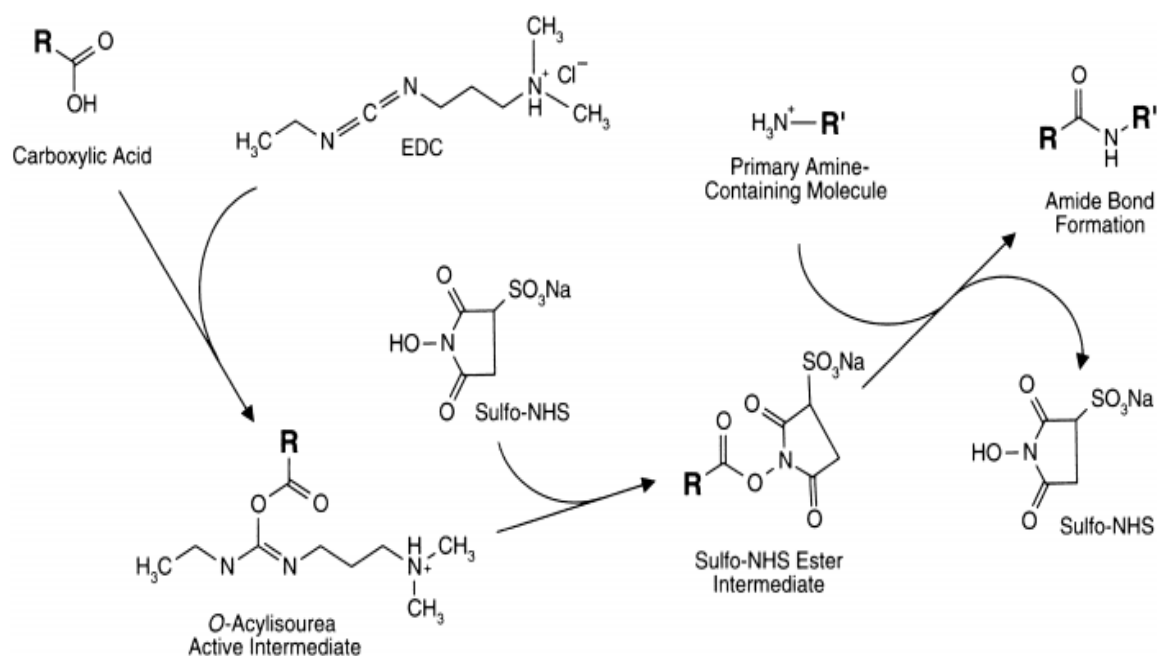
Figure 2.02: EDC Sulpho NHS reaction mechanism. The EDC reacts with the Carboxylic acid group creating an sulpho-NHS ester intermediate (an amine nucleophile). An amide bond is then formed with the thiol group on the opposite end of the hexyl chain. Adapted from[4].

2.2.4 Interior-functionalization of micro arrays

After micro contact printing, the micro-array platform was placed into 1.2 µM solution of SH-(c)-RGDFK solution or 1.25 µM solution of thiocholesterol solution and sonicated for 10 min. After sonication the Au micro array platform was placed in a refrigerator at 4ºC for 48 h incubation.

2.2.5 A$_5$β$_1$ labelling of SH-(c)-RGDFK functionalized micro array interiors

Flourophore-labelled $\alpha_5\beta_1$ integrin was kindly supplied by *Ludger et al.,* (Institute Curie, Paris, France) and was diluted to 0.4 ng/mL. 5 µL of this integrin was aliquoted onto a pre-fabricated RGD functionalised micro-array platform that was previously pre-sonicated with deionised water. This was left to incubate for 24 h in a refrigerator at 4ºC.

2.2.6 Contact-Angle experimental setup for planar Au substrates

All contact angle measurements were carried out using deionised H_2O, that was de-gassed for 10 min using N_2 gas flow. Contact Angle Measurements were carried out in triplicate using FTA 2.0 software.

2.2.7 Zeta Potential Experiments on SH-(c)-RGDFK solution

1.2 µM of SH-(c)-RGDFK was diluted into PBS buffer and 0.5 mL of this solution was aliquoted into a Zeta Potential cell and Zeta Potential measurements were carried out in triplicate.

2.3.0 Cell Culture and Exosome Protocols

2.3.1. Cell Culture Materials

Ea.hy926 immortalized (HuVECs) cell line was sourced from ATCC. Primary Human Aortic Endothelial Cardiac Cells (HuAECs) were sourced from PromoCell's Irish distributor Brennan & Co.

2.3.2 Cell Culture Media

All cell lines were grown using a Growth Medium MV KitC-22120 specifically for exosome studies sourced from Brennan & Co. <u>All cell culture techniques were carried out by Dr Denise Burtenshaw[5]</u>, School of Biotechnology, DCU.

2.3.3 Conditioning of Cell Culture Samples for Exosome Harvesting

Exosomes were sourced from HuVECs and three sub-groups of HuAECs. The three HuAEC sub-groups consisted of a Normal Group (NG), Hyperglycaemic Group (HG) and a Hypoglycaemic Group.

Both cell lines were optimised for short-term growth in 0% serum conditions. This was achieved by lowering serum concentrations by 0.5 % over a period of time (every 24 h until growth in 0 % serum was reached). Once optimised, HuVECs and HuAECs were treated with normal glucose (5 mM, NG) and a further two HuAEC-subgroups were treated with high glucose media (30 mM, HG) and D-Mannitol (5 mM MG) . The conditioned media from each group was harvested every 48 h. A batch of NG, HG and MG conditioned media was collected and pooled for downstream experiments to avoid batch to batch variability. Conditioned media was stored at -80 °C.

2.3.4 Isolation of Exosomes from conditioned cell culture media

Exosome isolation was achieved using ExoQuick™ reagent. Exosomes were isolated as per manufacturer's instructions. All centrifugation steps were performed at 4 °C. Briefly, NG and HG conditioned media was centrifuged at 3,000 x g for 15 min to remove cells and cellular debris. The supernatants were then transferred to a sterile 50 mL tube and appropriate amounts of ExoQuick™ reagent were added to conditioned media. Samples were mixed by inverting, followed by overnight incubation at 4 °C for 24 h. After 24 h, samples were then centrifuged for 1,500 x g for 30 min. The resulting supernatants were removed, and a further centrifugation step was carried out at 1,500 x g for 5 min. The supernatant was then aspirated, and the resulting pellet was re-suspended in distilled H_2O which was then stored at -80 °C.

2.3.5 Exosome labelling Protocol

For the confocal imaging studies, 25 µL of 5 µM of BODIPY Cholesterol was aliquoted into exosome PBS solution and incubated in the refrigerator for 6 h.

2.3.6 Exosome capture Protocol within the Array pore platforms

An SH-(c)-RGDFK functionalized Au micro array platform was sonicated in a 0.4 mL aliquot of PBS buffer. After 10 min sonication, 0.1 mL exosome solution was aliquoted directly into this 0.4 mL solution to allow easy-diffusion of the exosomes into the micro array pores. The prior removal of air-pockets ensured that exosomes were able to successfully bind to the bottom of the pores. This step also ensured that the exosomes remained intact as they were not sonicated in solution as direct sonication may cause exosome rupture. The Au micro array platform containing the exosome solution was then stored for 48 h at 4 ℃ (this ensured that the exosomes did not disintegrate as they are unstable at room temperature[6]). This protocol was used for all EIS, FE-SEM, SERS and CFM studies.

2.4.0 Instrumentation Parameters

2.4.1 Contact Angle

All contact angle measurements were carried out on planar Au substrates using on a Surface Analysis FTA200 Dynamic Contact Angle Analyser.

2.4.2 SEM

All SEM imaging was carried out on unfunctionalized Au micro array platforms using a Hitachi 3400 Scanning Electron Microscope` at 20 kV under various magnifications at a working distance of 10 mm.

2.4.3 Cyclic Voltammetry and Electrochemical Impedance Spectroscopy

All voltammetric measurements were carried out in 1 mM Potassium ferrocyanide Probe with 0.1 M potassium chloride electrolyte in PBS (Phosphate-buffered saline) solution. All EIS measurements were carried out in PBS buffer from 100-1000 kHz. All Voltammetric and EIS measurements were carried out using a CH760e Electrochemical Workstation, with a three-electrode set up: Ag/AgCl reference electrode, platinum wire auxiliary electrode, and the Au platform as the working electrode.

2.4.4 Zeta Potential Measurements

All Zeta Potential experiments were carried out on a Malvern Zetasizer® Nano Series. The software was switched from DLS to Zeta Potential settings.

2.4.5 Confocal and FE-SEM

All Confocal imaging was carried on a Leica STED Super Resolution Microscope using a visible laser diode source, 0.1 % laser power and time delay (of 0.3-1.8 s) settings were used for all confocal imaging studies to exclude scatter from the Au surface. For the labelled $\alpha 5\beta 1$ integrin studies: $\lambda_{excitation}$ was 477 nm and $\lambda_{emission}$ was 577-677 nm. For the BODIPY-cholesterol labelled exosome studies: $\lambda_{excitation}$ was 497 nm and $\lambda_{emission}$ was 520-620 nm.

All FE-SEM imaging was carried out on a Hitachi S5500 Field Emission Scanning Electron Microscope at 1.0 kV at a working distance of 5mm and 20 µA settings. The exosomes were captured in the Au array platforms as described above and imaged under various magnifications without any prior metal-splutter coating nor other chemical treatment.

2.4.6 SERS

All Raman measurements were carried out on a Horiba LabRAM HR spectrophotometer with a 50 X (0.55 N.A.) magnification long distance objective lens from Leica with spectra collected over the range from 200-2000 cm^{-1} using a 785 nm laser excitation source using a 10 % O.D. filter, operating at full power of 60.2 mW. Spectral acquisition was 1 s with 4 s exposure time and 9 frame

accumulations. Prior to analysis, the Raman spectrophotometer was calibrated as per manufacturer's instructions[7] and using the Rayleigh line of a silicon wafer.

For all SERS exosomal studies, XY mapping was pre-set on the software for collecting exosomal spectra across the micro-array platforms. Briefly, the sample stage was pre-set to move in 1-micron increments along the Y axis with the X axis remaining constant (at 0) to collect each spectrum. Approximately 50 exosomal spectra were collected per Au micro-array platform (i.e. one sample). Throughout each entire SERS experimental session, the micro array substrate was kept submerged under deionised H_2O, as captured exosomes cannot be allowed to dry out. All spectra were collected using LabSpec 5.0 Software and baseline corrected and normalised using standard and de-spike settings to remove background noise.

2.5 References

1   D. O'Connor, A. Byrne, C. Dolan and T. E. Keyes, *New J. Chem.*, 2018, **42**, 3671–3682.

2   H. Basit, V. Gaul, S. Maher, R. J. Forster and T. E. Keyes, *Analyst*, 2015, **140**, 3012–3018.

3   D. Qin, Y. Xia and G. M. Whitesides, *Nat. Protoc.*, 2010, **5**, 491–502.

4   G. T. Hermanson, *Bioconjugate Tech.*, 2013, 259–273.

5   Diagnostic Potential of Extracellular Vesicles (EVs) and single cell photonic (scPH) in subclinical Atherosclerosis, 2021, D. Burtenshaw,

6   R. Maroto, Y. Zhao, M. Jamaluddin, V. L. Popov, H. Wang, M. Kalubowilage, Y. Zhang, J. Luisi, H. Sun, C. T. Culbertson, S. H. Bossmann, M. Motamedi and A. R. Brasier, *J. Extracell. Vesicles*, , DOI:10.1080/20013078.2017.1359478.

7   Horiba, LabRAM User Guide, 2005, 1–67.

.

Chapter 3: Selective Surface Modification(s) of Gold micro-array platforms for Exosome Capture

3.0.1 Introduction

The work presented in this chapter focuses primarily on the fabrication and selective surface optimisation methods of the Au micro array platforms only. It is important to ensure that the micro array platforms can be effectively and consistently fabricated and functionalized before involving their application for subsequent exosome capture which is discussed in more detail in Chapter 4. The work presented in this chapter is highly novel involving new techniques that are new to the Keyes Research Group and it is vital to thoroughly validate each part of the fabrication and selective modification process before moving onto the eventual application of the functionalized Au micro array platform which is exosome capture.

Currently in the Keyes Research Group, the principle selective surface modification method(s) of the Au micro array exteriors involve(s) the use of retaining the sphere-monolayer as a protective layer to block micro array pore access and confine monolayer modification to the top of the micro array pores only[1–3], see Figure 3.01 Schematic below for clarification purposes.
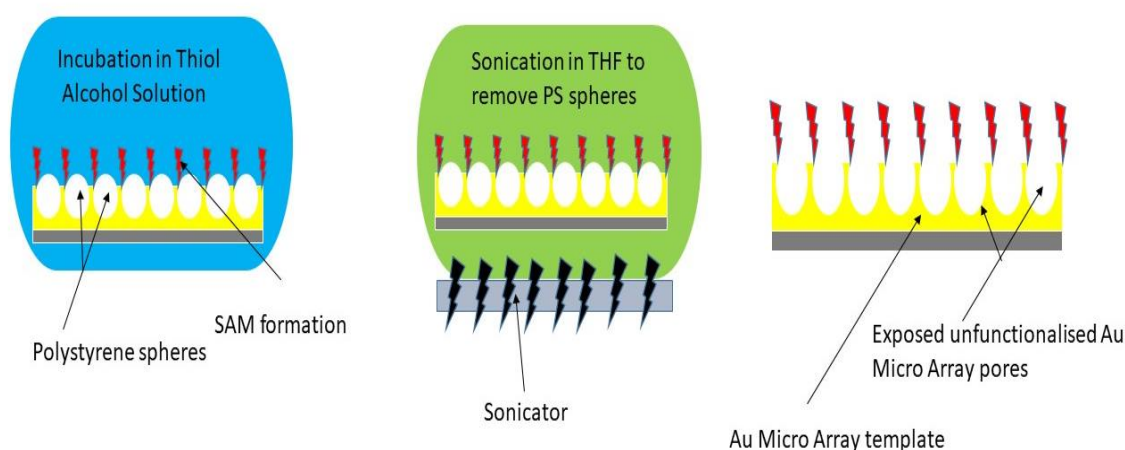
Figure 3.01: Schematic to show traditional selective surface modification incubation method, after Au electrodeposition around the 1-micron PS spheres, the Au micro array platform is placed in a thiol alcoholic solution e.g. mercaptohexanol for 24-hour incubation (with the PS spheres still intact). After 24 h incubation to allow complete SAM formation, the micro array template is then removed and sonicated for at least 10 min in THF solvent. The sonication ensures complete removal of PS within the bottom of the micro array pores.

Mercaptohexanol is also used to form an SAM in lipid-bilayer studies on Au micro array platforms because the OH functional group successfully forms a stable bond to many lipids and areas of interest that are studied within the group include drug permeation[4] and membrane stability studies[5].

Incubation of Au surface in thiol-alcoholic solution is a widely applied method for SAM formation however, a drawback to this technique is the length of required time. It typically takes up to 24 h incubation to form the SAM[1,2], due to need for self-assembly after adsorption which can be a slow process. Another key drawback in the context of the Au micro arrays is removal of the PS spheres (by sonication in THF solvent) after SAM formation. Sonication in such a solvent can also cause partial removal of the SAM. To overcome both of these drawbacks, a new faster technique was employed for selective surface modification called Micro contact printing (MCP).

The work presented in this chapter involves selectively modifying the micro array platforms in ways that have not previously been used by the Keyes Research Group such as micro contact printing.

3.1 Micro Contact Printing

MCP is a one type of soft-lithographical technique that allows for low cost and rapid-functionalization on the molecular level of various Au and other metal substrates[6] thereby dramatically changing their surface properties. This technique was initially developed to create a pattern on Au[7] and first mentioned by *Whitesides et al 1993*[8] but has since been developed to modify other types of surfaces particularly in the biotechnological field[9,10] and in microfluidics[11]. This technique allows for rapid successful surface-functionalization in minutes rather than hours. Suitable platforms for MCP include thin layers of a metal deposited onto silicon, glass, mica and various polymer substrates[6].

MCP involves the utilisation of an elastomeric "stamping" template such as Polydimethylsiloxane (PDMS) whereby the compound of interest is "inked" onto the surface template and the solvent is subsequently allowed to evaporate[9] leaving only the thiolated compound of interest on the PDMS-surface.

Thiolation and supramolecular assembly and of Au previously mentioned in *Forster et al 2004*[12] and *Love et al 2005*[13] allows for rapid formation of a patterned SAM on the Au substrate and the MCP process can potentially be employed in this matter to form thiolated Au substrates.

In this chapter the use of MCP (for 15 and 30 min) was employed to selectively modify the exterior of the micro-array platforms with mercaptohexane and mercaptohexanol to change the surface chemistry rather than the traditional 24-hour incubation method previously used in the Keyes group.

The thiol groups on both mercaptan compounds will covalently bind to the Au surface and the micro-array interiors would remain unmodified at this stage as they do not come into direct contact with the PDMS stamping template. The rationale of this idea is to prevent exosome adhesion on the

exterior of the micro-arrays and to drive the exosomes into the interior for successful bioconjugation. It is also necessary to modify the micro array interiors to ensure effective exosome capture and binding within the location of the plasmonic-hotspot. To achieve this objective, the micro array interiors are functionalized with a SH -(c)-RGDFK using a soaking/incubation step. The rationale for choosing this specific peptide-ligand for Au micro array interior-functionalization is elaborated in more detail in Section 4.3.1.1, Chapter 4.

The micro-array interiors are where maximum surface enhancement and generation of the plasmonic field takes place upon laser excitation; Following surface functionalization of the micro array exteriors by MCP, their interiors were then further selectively-modified using the traditional incubation step using different thiolated compounds to promote exosome conjugation.
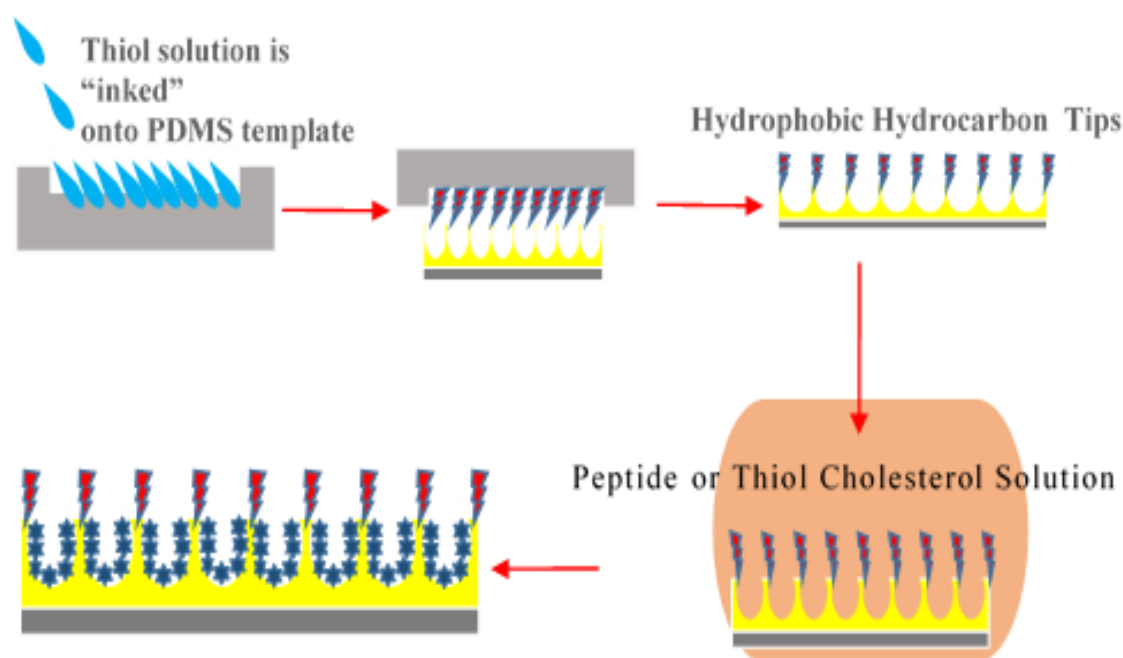
Figure 3.02: Schematic Summary of Micro Contact Printing and Incubation step(s) showing Selective Modifications of both exterior and interior of the micro-array platform. The mercapto-alcoholic solution is inked onto the PDMS stamping-template and allowed to evaporate off under a fume-hood for a number of minutes with only mercaptan compound remaining on the PDMS surface. This PDMS stamping-template is then placed in direct contact with the Au micro array platform for a number of minutes. The stamp is then removed and the micro array platform is then sonicated for 10 min to ensure thorough removal of air-locks within the array pores[1,2] and to ensure that the compound reaches the bottom of the micro array pores where the maximum surface enhancement signal upon photon-excitation occurs[14].

Following modification of the exterior by contact printing the interiors were then further selectively modified (as the top surface is now blocked) using the traditional incubation method with different thiolated compounds to promote exosome conjugation within the Au micro array interiors (See the Schematic in Figure 3.02).

3.2 Materials and Methods

Please refer to Section 2.1, Chapter 2 for the materials used in this chapter.

As methods were varied throughout this chapter, each individual method is described long-side its respective figure.

3.3.0 Results and Discussion

3.3.1 Scanning Electron Microscopy
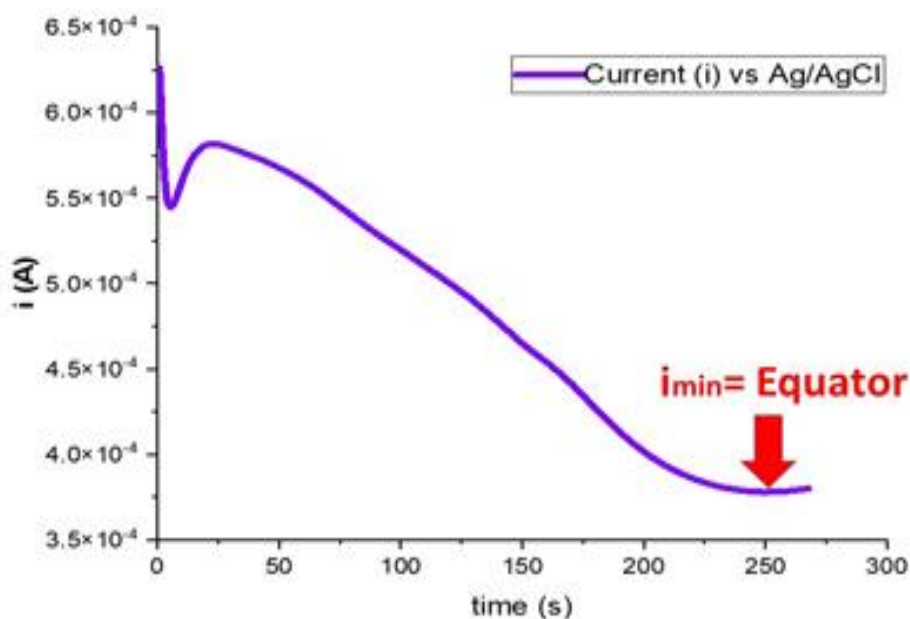
Figure 3.03: Representative (chrono-amperometric) i-t curve obtained during Au electrodeposition around a hexagonally-close-packed 1-micron diameter PS sphere-array monolayer assembled onto the Au/Si substrate until the equator of the PS-sphere monolayer is reached (E=-0.58 V vs. Ag/AgCl) and this point is indicated by i_{min}. The Au micro-array platform was purposely overgrown just beyond of this point to clearly demonstrate that i_{min} has been reached as i will keep increasing beyond this point which will result in complete Au coverage of the PS monolayer. All Au-electrodepositions were carried out within a three-electrode cell set up in a commercially available Au salt solution, Ag/AgCl reference electrode, platinum wire auxiliary electrode and the planar Au platform (with a PS-sphere lithography-deposited monolayer on top) as the working electrode.

The Au micro-array platforms were fabricated using the method previously reported by *Basit et al* 2015[15]. Briefly, polystyrene (PS) beads of 1-micron in diameter were dropcasted onto 15 mm x 8 mm sized silicon wafers containing a 100 nm thick layer of vapour-deposited Au, these beads were allowed to dry overnight to form a PS-sphere monolayer. A three electrode electrochemical system was set in a commercially available Au salt solution, Ag/AgCl reference electrode, platinum wire auxiliary electrode and the planar Au platform (with a PS-sphere dropcasted monolayer template on top) as the working electrode (E=-0.58 V vs. Ag/AgCl).

Au was then electrodeposited between the spaces on the PS beads on the platform until the Au had electrodeposited to the equator of the PS beads- i_{min}. This was determined by the lowest current(i) reached on the software voltammogram (see Figure 3.03). After i_{min} has been reached it can be seen from Figure 3.03 that it is followed by an increase in applied i (if applied i is allowed to continually flow then this will eventually result in complete-coverage of the PS-sphere monolayer).
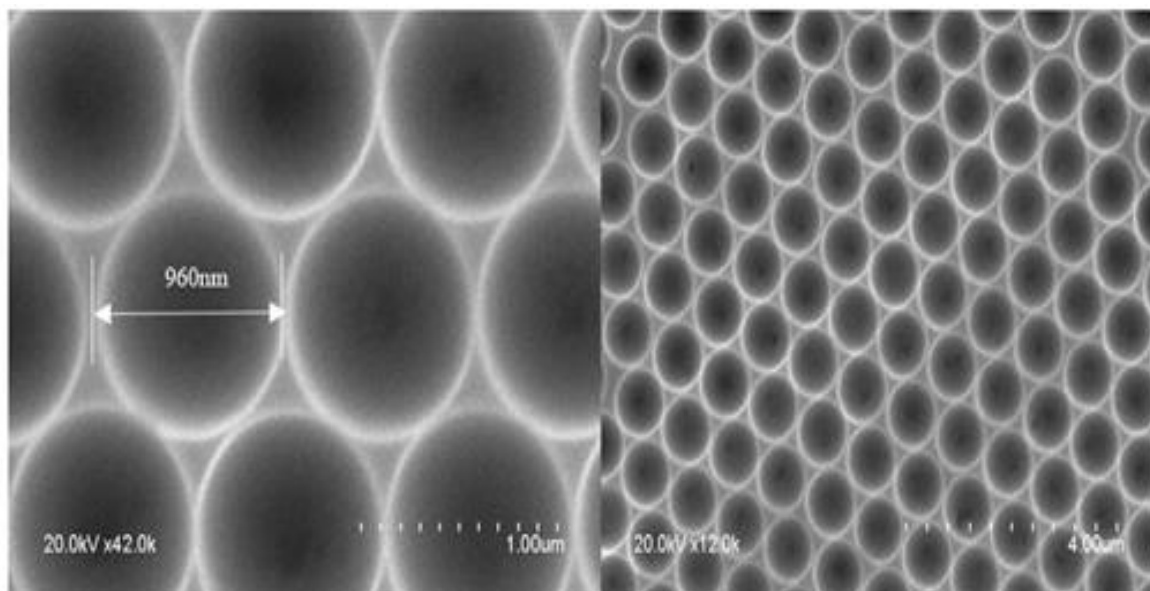
Figure 3.04: SEM Images of 1-micron unfunctionalized Au Micro-Array platform on silicon wafer (after THF sonication) at 20 kV under various magnifications at a working distance of 10 mm. Au was first electrodeposited between the spaces of the PS bead-monolayer from the Au salt solution (electrolyte) until the Au had grown to the equator of the polystyrene beads, this was determined by the start of an increase in the applied current following a decrease and from the shape of the graph on the software (shown in Figure 3.03). The resulting micro-array platform was then rinsed with deionised water to remove any remaining Au salt solution/electrolyte from its surface. The platform was then immersed in THF to remove PS sphere-monolayer and was sonicated for 10 min to ensure thorough complete PS monolayer removal and then dried off using N_2 flow to cause complete THF evaporation within the micro array interiors.

After successful Au electrodeposition the platform was rinsed with deionised H_2O to prevent any Au crystalline formation to occur over the PS-monolayer and then dried under N_2 gas flow, this ensured that no trace of moisture remained on the substrate. Following this step and prior to SEM studies, the Au micro array platform was sonicated for 10 min in THF solution to thoroughly remove the PS monolayer and to ensure complete exposure of the Au micro array pores.

In order to confirm correct formation of the Au micro array platform and to ensure a monolayer of Au deposition had properly formed, SEM measurements were carried out and imaged. It can be seen from the images in Figure 3.04 (above) that the Au micro-arrays form a hexagonally close packed patterned structure on the platform. This platform can then be further selectively modified and functionalized for both exosome capture and subsequent SE Raman spectroscopic analysis.

3.3.2 Contact Angle Measurements on Planar Gold

Many smooth planar metal surfaces display natural hydrophilic properties[16], therefore it was important to assess the hydrophilicity of planar Au substrates both before and after selective-surface modification(s) using MCP to observe any changes in physico-chemical properties. This contact angle experimental set-up (Sessile liquid drop technique) was invented by *Bigelow et al* in 1946[17] and has been significantly improved on since its inception however the actual experimental technique largely remains the same, i.e. involving the controlled deposition of a liquid-droplet (usually H_2O) onto a solid substrate and observing the formed-droplet with a magnifying lens. This controlled liquid-droplet deposition is repeated until the droplet reaches a stable equilibrium caused by the forces arising from the three interfacial phase tensions: solid-liquid, solid-gas and liquid-gas. Taking an image of the droplet on the substrate will then allow the software to accurately calculate the contact angle formed by the solid-liquid interface and the liquid-gas interface.

The hydrophilic or hydrophobic character of the solid substrate is determined by the magnitude of the contact angle, usually in the range of 10° to 40° for a hydrophilic material, above 40° for hydrophobic substrates and above 80° for extremely hydrophobic subtrates[17,18]. During this study, all static contact angle measurements were performed at room temperature.

A <u>clean,</u> planar Au surface typically displays natural hydrophilic properties with θ_{H2O} between 0-40 ° [18]. In this particular experimental study, contact angle analysis (using the sessile drop technique) of a clean, planar, unfunctionalized Au substrate was carried out using deionised H_2O and the natural hydrophilic properties of the planar Au substrate was confirmed to be 40.45° (θ_{H2O}). The next step involved thoroughly drying the planar Au platform under N_2 gas flow to ensure complete H_2O evaporation and then the same planar Au platform was stamped with 10 mM mercaptohexane for 30 min.
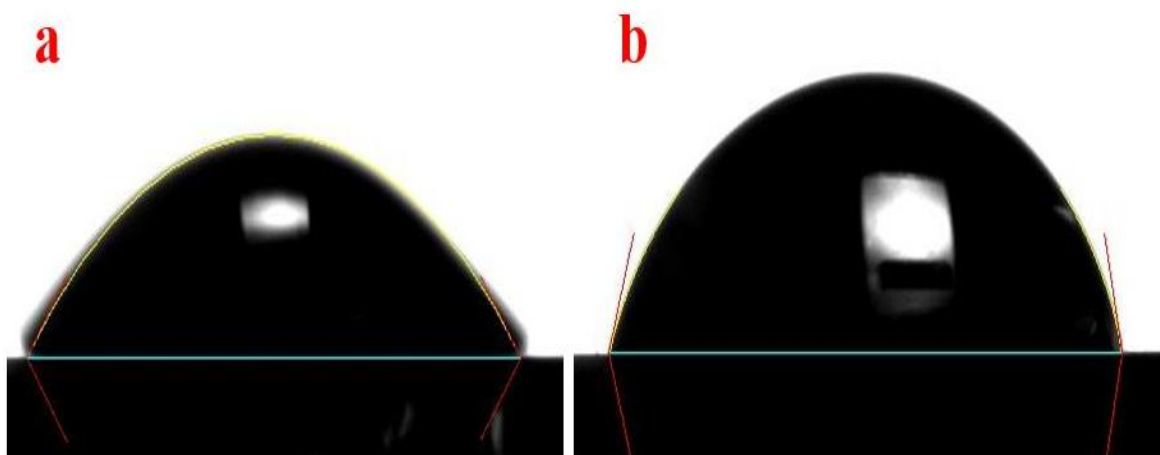
Figure 3.05a (left before MCP) and 3.05b (right after MCP): Sample Contact Angle image(s) taken of a planar Au substrate using the FTA 2.0 software to capture the images and calculate θ_{H2O}. All contact angle measurements were carried out in triplicate using de-gassed deionised H_2O using the Sessile liquid drop technique settings at room temperature. The first Contact Angle measurement on the left was carried out on unfunctionalized planar Au substrate and the contact angle value θ_{H2O} was determined to be 40.45 °. After thorough drying with N_2 gas flow, the same planar Au substrate was stamped with 10 mM mercaptohexane for 30 min and Contact Angle measurement-analysis was repeated under identical conditions, the contact angle value θ_{H2O} in this case was calculated to be 74.81°.

After 30 min MCP with 10 mM mercaptohexane, contact angles were measured under the same identical conditions (using deionised H_2O and the sessile liquid drop technique), θ_{H2O} of the planar functionalized Au substrate was calculated to be 74.81 ° (See Figure 3.05) which is almost a 2-fold increase when compared to the calculated θ_{H2O} (40.45 °) of the unfunctionalized planar Au substrate. It confirms successful Au-Thiol bond formation as thiolates readily form an SAM on an Au surface[12,13]. This further confirms successful thiolation and close-packing on the planar Au substrate with the hydrophobic hexyl chain on the mercaptohexane orientated outwards making the planar Au surface environment now hydrophobic. Clean vapour-deposited Au usually displays a hydrophilic θ_{H2O} of <40 °[18] and the calculated value θ_{H2O} of clean planar Au is very close to published θ_{H2O} value. Contact Angle studies were carried out in triplicate with of which a sample image is illustrated in Figure 3.05 above. Table 1 (below) shows displays the full triplicate results with calculated standard deviation.

Table 1: Triplicate Contact Angle Measurements of Planar Au substrates stamped with 10 mM Mercaptohexane for 30 min, with calculated Mean and Std deviation values.

Contact Angle(°)	Mean(°)	%RSD
74.81	73.97	2.23
72.07		
75.04		

3.3.3.0 Cyclic Voltammetry (CV) and Electrochemical Impedance Spectroscopy (EIS) Studies

3.3.3.1 Planar Au Substrates

To validate the surface modification by the MCP method it was important to assess and establish the best time-frame for optimal MCP on Au platforms and this was achieved using CV studies. EIS studies were then carried out as this is a useful technique to measure the complex impedance of monolayer, which in turn reflects changes of resistance and capacitance to the Au (working) electrode reflecting coverage and leakiness of the film. An important preliminary study was to compare MCP results using different timeframes on the same planar Au substrate (to prevent variation in surface area as the substrates are manually cut) and select the optimum timeframe for MCP by comparison. EIS measures the characteristics of the Au substrate which when extracted from the equivalent circuit give insight into membrane permittivity. A CV of an untreated planar Au platform was carried out in Potassium ferrocyanide Solution, (see Figure 3.06 below) this produces a reversible oxidative-reductive cycle.

Using CV techniques, Potassium ferrocyanide undergoes a reversible 1 electron transfer oxidative-reductive cycle in 100 mM KCl electrolyte solution within the 0-0.6 V range[19] on the Au surface (working electrode system). This particular electrochemical technique was used in this study to compare any changes in the oxidative and reductive peak values of the Potassium ferrocyanide on an unfunctionalized planar Au platform and after 15 min MCP/stamping with 10 mM mercaptohexane, then the thiols were reductively desorbed using 0.1 M KOH solution (this reductive scan mode is shown on Figure 3.10), then the Au substrate was thoroughly dried using N_2 gas flow and the same Au planar substrate was stamped for 30 min. Results from all 3 voltammograms were then compared to assess the optimal time for MCP/stamping. See schematic below Figure 3.06 for clarity step-wise.
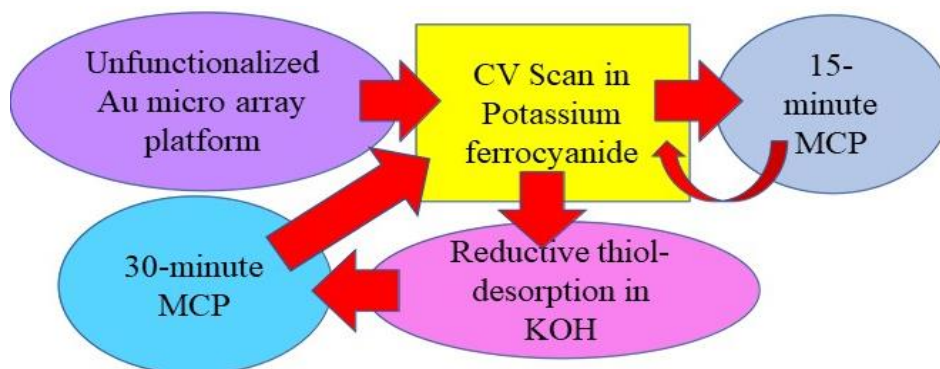
Figure 3.06: Schematic summary to show the CV experimental set up step by step (MCP results are shown in Figure 3.08a and a sample thiol-desorption reductive scan is shown in Figure 3.10) for clarification purposes.

In Figure 3.07a, CV using an unfunctionalized Au micro array platform as the working electrode was carried out ($E_{1/2} = 0.3$ V) at a scan rate (υ) of 50 mV/s in 1 mM $K_3Fe(CN)_6$ in 100 mM KCl electrolyte solution within a three-electrode cell set up, Ag/AgCl reference electrode, platinum wire auxiliary electrode; In the unfunctionalized Au substrate, E_{ox} of the Potassium ferrocyanide was 0.16 V and its respective E_{red} value was -0.24 V (See Figure 3.07a) and there is a large electroactive surface area indicated by the high peak areas determined by the current (**i**) value(s) on the corresponding y-axis; 3 x 10^{-3} A for E_{ox} and -4 x 10^{-3} A for E_{red}. After 15 min MCP with 10 mM mercaptohexane, CV studies were carried out under identical conditions but using the functionalized Au micro array platform as the working electrode. During this second CV scan, E_{ox} of the Potassium ferrocyanide had slightly changed to 0.11 V and the respective reductive value also changed slightly to 0.27 V (a peak to peak separation of 0.16 V) however, there is a dramatic decrease in current (**i**) indicating reduced available electroactive surface area, the peak heights dropped to 1 x 10^{-3} A (new E_{ox} value) and -3 x 10^{-3} A (new E_{red} value). This confirms successful SAM formation after just 15 min MCP. Following this step the SAM mercaptohexane thiol groups were reductively desorbed in 100 mM KOH solution ($E_{1/2} = -0.6$ V)[19] (See Figure 3.10 for sample cyclic voltammogram of reductive desorption removal).

Figure 3.07a (left): CVs of a Planar Au platform. CV studies were carried out on a planar Au substrate before and after stamping for 15 minutes with 10 mM mercaptohexane ($E_{1/2}$ =0.3 V) at a scan rate (υ) of 50 mV/s in 1 mM $K_3Fe(CN)_6$ (Potassium ferrocyanide) in 100 mM KCl electrolyte solution Reductive thiol 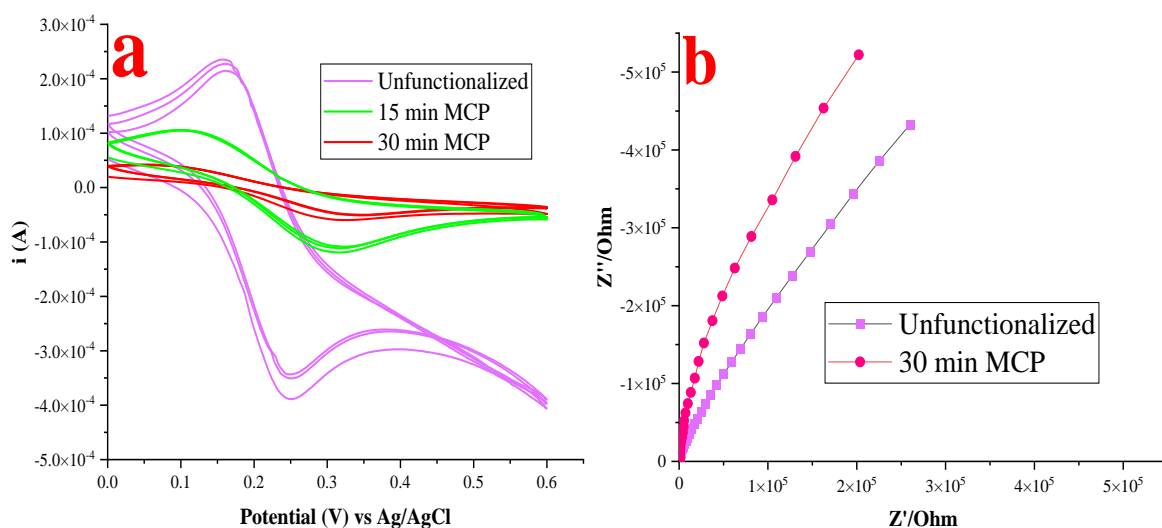de-sorption was carried out in 0.1 M KOH solution, the planar Au platform was thoroughly dried under N_2 gas flow and stamping with 10 mM mercaptohexane was repeated for 30 min and a CV scan was carried out under identical conditions previously described. The probe's oxidative peak was 0.16 V (peak area height 3 x 10^{-3} A) and reductive peak was -0.24 V (peak area height -4 x 10^{-3} A) for the unfunctionalized planar Au substrate (peak separation distance of 0.08 V). After 15 min stamping the probe's E_{ox} value changed to 0.11 V and the E_{red} value changed to -0.27 V (peak separation distance of 0.16 V), their E_{ox} and E_{red} heights dropped to 1 x 10^{-3} A and -3 x 10^{-3} A respectively. After 30 min 10 mM mercaptohexane-stamping the probe's E_{ox} was 0.1 V and its E_{red} changed to -0.32 V (peak separation distance of 0.22 V). There was also another drop in available electroactive surface areas after each step as indicated by the further decrease in E_{ox} and E_{red} height values, 5 x 10^{-4} A and -5 x 10^{-4} A respectively

Figure 3.07b (right): Nyquist Impedance Plot of a Planar Au substrate. Non-faradaic EIS measurements were carried out on an unfunctionalized planar Au platform in 100 mM PBS buffer from 0.1 Hz–10 kHz frequency range with a 0.01 V r.m.s. signal following this the planar Au platform was stamped with 10 mM mercaptohexane for 30 min and EIS measurements were carried out under identical conditions. Both EIS and CV studies were carried out within a three-electrode cell set up, Ag/AgCl reference electrode, platinum wire auxiliary electrode and the planar Au substrate as the working electrode.

EIS studies were carried out on a planar Au platform in 100 mM PBS buffer from 0.1 Hz–10 kHz frequency range with a 0.01 V r.m.s. signal within the same three-electrode cell set up on an unfunctionalized planar Au substrate. Following this the platform was stamped with 10 mM mercaptohexane for 30 min and EIS studies were carried out under identical conditions previously described. This data shows that there was an increase in impedance of the Au electrode cell after stamping which indicated successful Au-Thiol bond formation due to less available electroactive surface as mercaptan compounds readily-form an SAM on an Au surface, this can be seen on the graph because there is an increase in the final -Z_{imag} (on y-axis)[12,13] points from 423.6 kΩ (the unfunctionalized Au platform) to 522.1 kΩ (30 min stamped Au platform) and their respective Z_{real} (on x-axis) points decease from 260 kΩ to 202.3 kΩ indicating in increase in impedance. Similar EIS studies were carried out by *Sharma et al* 2016 using different mercaptan compounds, their studies

also demonstrated that there was an increase in impedance on Au electrode(s) after thiol-functionalization and also impedance shows a further increase as the length of the alkyl chain is increased on the mercaptan compound[20], i.e. the longer aliphatic-chained mercaptans display higher $-Z_{imag}$ (on y-axis) values than shorter aliphatic-chained mercaptans. The increase in impedance after 30 min stamping with mercaptohexane shown here in Figure 3.07b is in agreement with CV measurements carried out (shown in Figure 3.07a) and contact angle measurements shown in the previous sub-section (Refer to Figure 3.05).

Other CV studies were carried out to further investigate if thiolation of the Au substrate had occurred.. Thiol-desorption occurs at -1.1 V in an oxidative H_2SO_4 voltammetric scan[2] and this study can be used to further confirm successful Au substrate-thiolation.
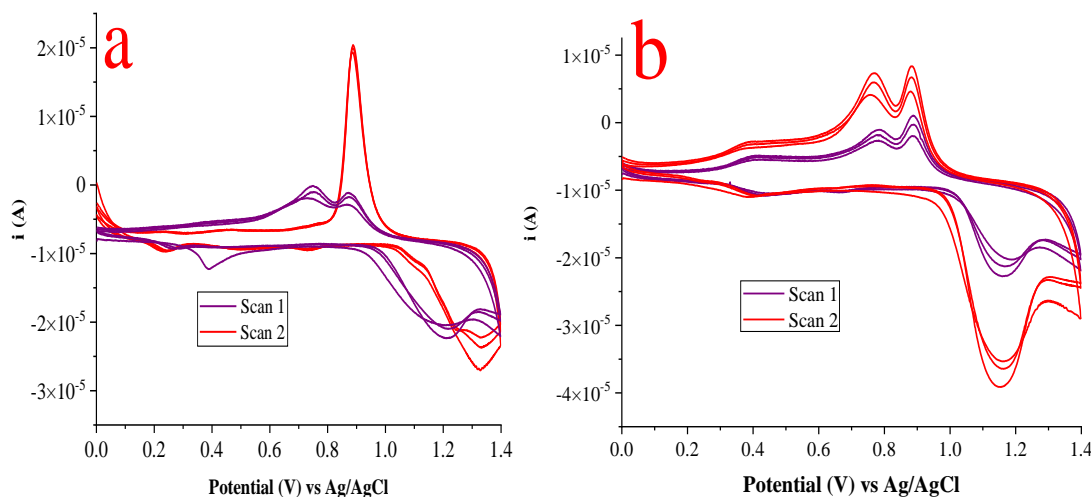
Figure 3.08a (left) and 3.08b (right): CVs of a Planar Au platform at a scan rate (υ) of 50 mV/s ($E_{1/2}$ = 0.7 V) in 100 mM H_2SO_4. This oxidative scan mode was carried on (a) a planar 10mM mercaptohexanol-stamped and (b) a planar 10mM mercaptohexane-stamped Au substrate within a three-electrode cell set up, Ag/AgCl reference electrode, platinum wire auxiliary electrode and the planar Au substrate as the working electrode. 0.4 V and 0.7 V represent distinct Au oxidation-reduction peaks. Inset at -1.1 V peak which is characteristic of thiol-desorption[2] from Au.

Cyclic voltammograms of a Planar Au platform at a scan rate (υ) of 50 mV/s ($E_{1/2}$ = 0.7 V) in 100 mM H_2SO_4. These oxidative-scan modes were carried on a planar 10 mM mercaptohexanol-stamped Au substrate (see Figure 3.08a above) and on a planar 10 mM mercaptohexane-stamped Au substrate (See Figure 3.08b above) within the same three-electrode cell set up as described previously (in Figure 3.07a) to investigate if an Au-O layer around -1.25 V on the electrode surface[21] would develop. Formation of an Au-O layer would indicate absence of a thiolated-SAM on the Au surface. See Schematic of workflow in Figure 3.09.
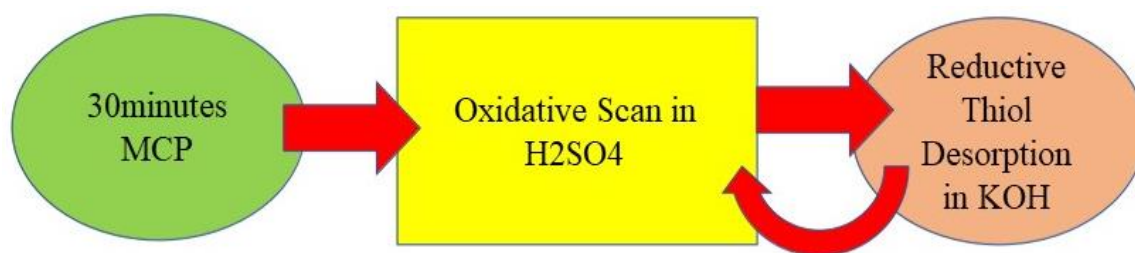
Figure 3.09: Schematic summary to show the CV experimental set up used for results in Figure 3.10 step-by-step.

A CV (reductive mode, $E_{1/2}$ = -0.6 V) scan in 100 mM KOH solution[19] was carried out on both substrates (sample KOH reductive mode scan shown in Figure 3.10 below) to remove the SAM Au-substrate monolayer(s) and after this a final CV was performed under identical voltammetric conditions previously outlined.

In Figures 3.08a and b (above) there is a large change in surface areas when comparing scans 1 and 2 on both voltammograms. 0.4 V and 0.7 V represent distinct Au oxidation-reduction peaks[2]. This E_{ox} peak at 0.4 V is more obvious in 3.08b than 3.08a but this could be due to slight variability in electrode area as both Au substrates as the substrates are manually-cut. The Inset peak at approximately -1.1 V can be observed on scan 1, both voltammograms. This is indicative of thiol-desorption from the Au^2 surface, i.e. thiol reduction has taken place so a thiol-SAM has successfully formed after 30 min of MCP, however this inset reduction peak (-1.1 V) is not present on scan 2 as the thiol-monolayer has been removed following the reductive-desorption scan in 100 mM KOH solution.

The reductive scan range shown in Figure 3.10 (below) was carried out at a scan rate (υ) of 50 mV/s) ($E_{1/2}$ = -0.6 V) in 100 mM Potassium Hydroxide (KOH) solution on a planar 15 min mercaptohexane-stamped Au substrate within the same three-electrode cell set up. This reductive desorption-scan in 100 mM KOH solution permanently-removes any Thiols bonded to the surface of the Au substrate, therefore re-exposing plain Au, i.e. the substrate is defunctionalized and allows subsequent Au substrate-refunctionalization to be carried out.
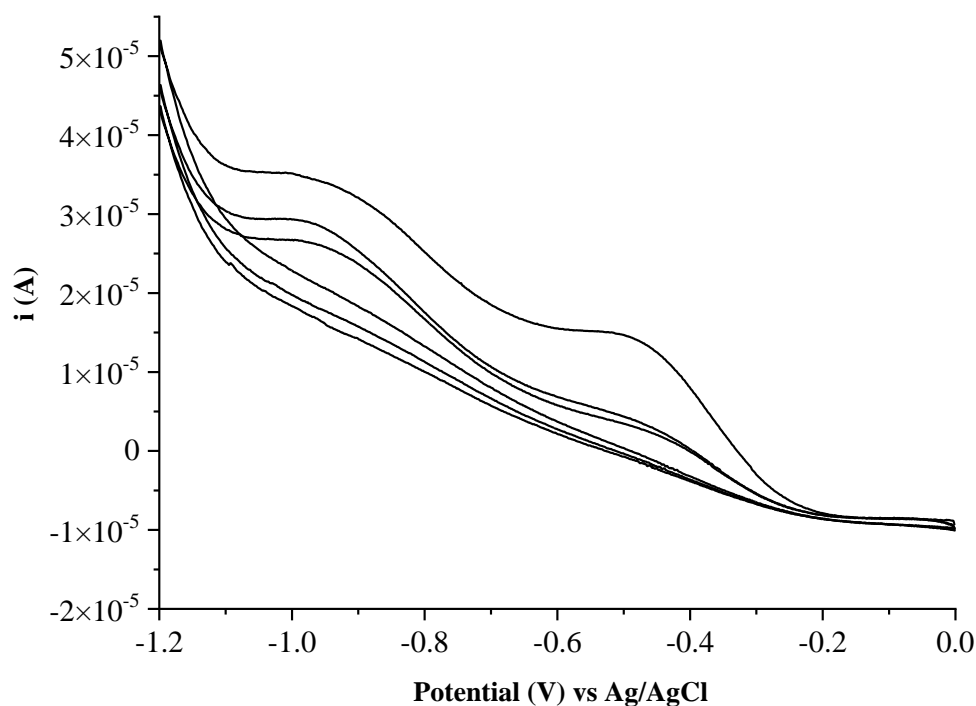
Figure 3.10: Sample CV(s) of reductive scan mode range at a scan rate (v) of 50 mV/s ($E_{1/2}$ = -0.6 V)in 100 mM KOH solution. This reductive-scan mode was carried on a planar mercaptohexane-stamped Au substrate within a three-electrode cell set up, Ag/AgCl reference electrode, platinum wire auxiliary electrode and the planar Au platform as the working electrode. The purpose of this was to de-sorb the thiol SAM from the Au substrate, leaving the Au surface de-functionalized.

3.3.3.2 Au Micro Array Substrates

As the MCP/stamping method had been effectively established on planar Au substrates, it was important to transfer this method onto Au micro array platforms as these platforms have previously been shown to be effective surface enhanced plasmonic substrates[2,4,14] and these selectively modified substrates will be used for extra-cellular vesicle capture and Surface Enhanced Raman Spectroscopic (SERS) analysis.

The same CV technique with Potassium ferrocyanide (described in the previous sub-section for Figure 3.07a) was used in this study to compare any changes in the E_{ox} and E_{red} values before and after 30 min MCP with 10 mM mercaptohexanol and mercaptohexane respectively.
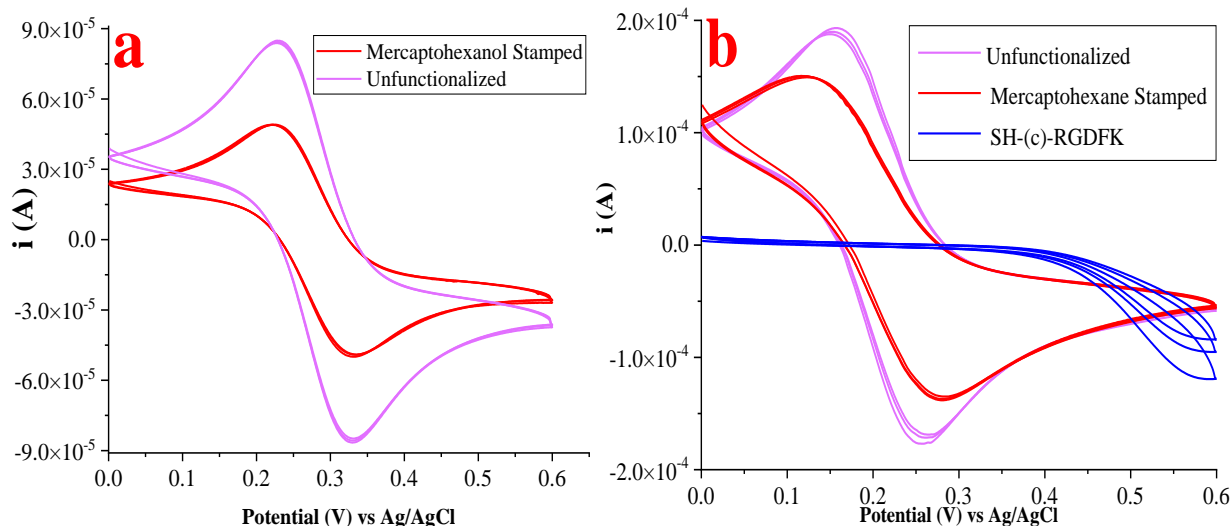
Figure 3.11a (left) and 3.11b (right): CVs of Au micro-array platform(s). CV studies were carried out on a Au micro array substrate before and after 30 min stamping with 10 mM (a) mercaptohexanol and (b) mercaptohexane, $E_{1/2}$ = 0.3 V, at a scan rate of 50 mV/s in 1mM $K_3Fe(CN)_6$ in 100 mM KCl electrolyte solution within a three-electrode cell set up, Ag/AgCl reference electrode, platinum wire auxiliary electrode and the Au micro array substrate as the working electrode. In Figure 3.11a E_{ox} of the Potassium ferrocyanide was 0.23 V and the respective E_{red} was -0.33 V, peak area heights were 8.38 x 10^{-5} A and -8.47 x10^{-4} A respectively. After 30 min MCP, E_{ox} of the Potassium ferrocyanide had slightly changed to 0.21 V and the respective E_{red} was -0.32 V and both respective peak area heights had dropped to 4.89 x10^{-5} A and -4.85 x 10^{-4} A. In Figure 3.11b E_{ox} of the Potassium ferrocyanide was 0.16 V and the respective E_{red} was -0.25 V, respective peak area heights were 1.93 x 10^{-4}A and -1.77 x10^{-4} A. After 30 min MCP with 10 mM mercaptohexane E_{ox} of the potassium ferrocyanide had slightly changed to 0.13 V and the respective E_{red} was -0.27 V, both respective peak area heights had dropped to 1.5 x10^{-4} A and -1.36 x 10^{-4} A. A 3rd step was introduced for this to assess any further electrochemical changes, 1.2 µM SH- (c)-RGDFK incubation for 24 h. After SH-(c)-RGDFK incubation there were no peak values as complete inhibition of the oxidative-reductive cycle of the probe on the Au surface.

In Part 1 using an unfunctionalized Au micro array platform (results shown in Figure 3.11a), E_{ox} of the Potassium ferrocyanide was 0.23 V and the respective E_{red} was 0.33 V. After 30 min MCP with 10 mM mercaptohexanol, CV studies were carried out under the same identical conditions but using the functionalized Au micro array platform as the working electrode. During the second CV scan E_{ox} of the potassium ferrocyanide had slightly changed to 0.21 V and the respective E_{red} also changed slightly to 0.32 V however there is a dramatic decrease in current (**i**) after 30 min MCP using 10 mM mercaptohexanol, which is indicated by the reduced electroactive area when compared to the electroactive area of the unfunctionalized Au micro array electrode, a drop from 8.38 x 10^{-5} A to 4.89 x 10^{-5} A (when comparing both E_{ox} heights), and a drop from -8.47 x 10^{-5} A to -4.85 x 10^{-5} A (when comparing both E_{red} heights) .

For Part 2 (results shown in Figure 3.11b), the same conditions were used as in Part 1 except with the use of 10 mM mercaptohexane instead of mercaptohexanol for MCP and an additional 24 h incubation step with EDC-Sulpho NHS coupled 1.2 µM (c)-RGDFK solution and CV studies were

carried out under previous identical conditions. For the unfunctionalized Au micro array platform, E_{ox} of the Potassium ferrocyanide was 0.16 V and the respective E_{red} was -0.25 V (a peak separation value of 0.09 V), respective peak area heights were 1.93 x 10^{-4} A and -1.77 x10^{-4} A.

After 30 min MCP with 10 mM mercaptohexane, E_{ox} of the Potassium ferrocyanide had slightly changed to 0.13 V and the respective reductive value was -0.27 V (a peak separation distance of 0.14 V). Both respective peak area heights had dropped to 1.5 x10^{-4} A and -1.36 x 10^{-4} A, after SH-(c)-RGDFK incubation there were no peak values recorded. This indicates complete inhibition of the oxidative-reductive cycle of the potassium ferrocyanide probe on the Au micro-array platform indicating no remaining electroactive surface area.

Notably, when comparing peak area values for parts (1) and (2), there is a 40% reduction in peak area for mercaptohexanol, but only 23% reduction for mercaptohexane which indicates that mercaptohexanol forms a more tightly-packed monolayer on the Au surface than mercaptohexane, however mercaptohexane prevents any biocapture[1,2,22] unlike mercaptohexanol which forms the anchoring-scaffold for phospholipid-bilayer[4,5,15,23,24] formation on this same array platform. Exosomes consist of a phospholipid bilayer[25–30] so may bind to the mercaptohexanol bilayer if this particular mercaptan compound is used. The rationale here for using mercaptohexane is to prevent any adhesion outside the array pores and to ensure binding within the LSPR-region within the array interiors[31] only.

For both Parts (1) and (2), the minimal change to peak to peak separation between E_{ox} and E_{red} maxima after 30 min MCP is not surprising as it indicates that there is still unmodified Au surface available within the micro-array platform(s) i.e. it is the resistance of the substrate which is what causes a widening in distance of peak to peak separation. Overall there is little change in resistance because the Au micro array interiors remain unmodified. There is a difference of 0.04 V between the peak separation distances between parts (1) and part (2). Mercaptohexane used in part (2) has a terminal non-polar methyl (CH_3) group and is thus more hydrophobic than mercaptohexanol with its alcohol (OH) terminus used in part (1). This OH group is expected to hydrogen-bond with the ions present in the electrolyte solution and also with the H_2O molecules thus allowing the solution to come into closer contact with the working electrode and increasing wettability. Specifically, in Part (2) the introduction of the SH-(c)-RGDFK incubation step shows complete SAM formation with no remaining available electroactive area on the Au working electrode reflected in absence of electrochemical activity at the modified electrode. This is an important result as it confirmed that tight-packing of mercaptohexane (on the micro-arrays' exterior) blocks access of Potassium ferrocyanide to the electrode surface and further confirmed that the SH-(c)-RGDFK peptide had conjugated within their interiors further blocking Au micro array interior surface access resulting in complete probe oxidative-reductive cycle inhibition.
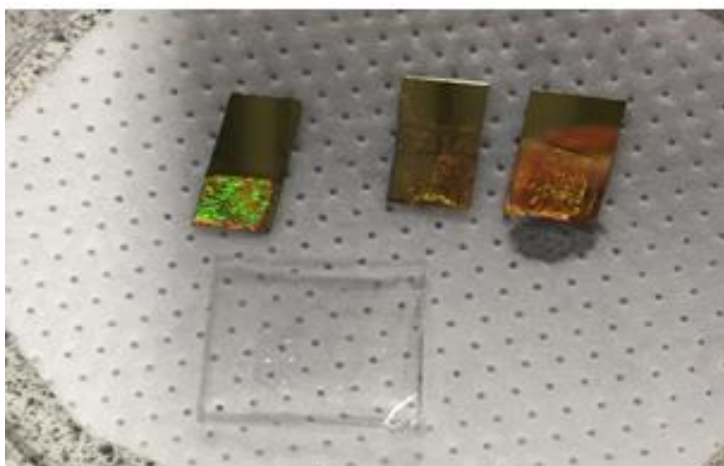
Figure 3.12: Three 1-micron unfunctionalized Au micro array platforms (on top) approximately 15 mm x 8 mm in size after sonication in THF to ensure thorough-removal o PS sphere-monolayer, the opalescence that can be observed in the three 1-micron micro array platforms is indicative of a nano-structured array formation and (on the bottom, below the substrates) a square transparent PDMS template (below the Au platforms) that is used for thiol (mercaptohexanol and mercaptohexane) functionalization (MCP/stamping).

One possible way to improve MCP of the mercaptohexanol on the surface of the Au platform is to plasma-treat (using O_2 plasma) the PDMS template which would allow for the conversion of the top layer hydrophobic siloxane groups to more hydrophilic silanol groups[32], this promotes the orientation of the thiol groups away from the plasma-treated PDMS surface as they will not readily hydrogen bond with the hydrophilic silanol groups[33] and would instead orientate outwards directly facing the planar Au surface.

Another important comparative study to carry out was to repeat the "traditional" incubation (using lithographically-masked micro array pores) or solution deposition method of SAM formation[1–3] that is currently employed within the Keyes Lab group and to compare it with the data shown in Figure 3.13b to assess the effectiveness of MCP as suitable replacement for incubation as only 30 min are required for SAM formation when compared to the 24 h typically required for the lithographically-masked incubation method.

To assess and compare the solution deposition method, CV studies were carried out on an Au micro array platform after Au electrodeposition with the PS bead-monolayer still intact, the Au micro array substrate was then incubated for 24 h in 1 mM Mercaptohexane alcoholic solution for functionalization of the Au micro array exterior. After 24 h incubation the Au micro array platform was removed from solution and CV studies were carried out under identical conditions, the Au platform was then sonicated in THF solvent for 10 min to thoroughly-remove the PS monolayer and to expose the Au micro array surface and cyclic voltammetry was repeated. The last step involved a

further 24 h incubation in 1.2 μM SH-(c)-RGDFK solution and the final CV scan was carried out. CV scans were performed under identical conditions as described for Figures 3.07a and 3.11.
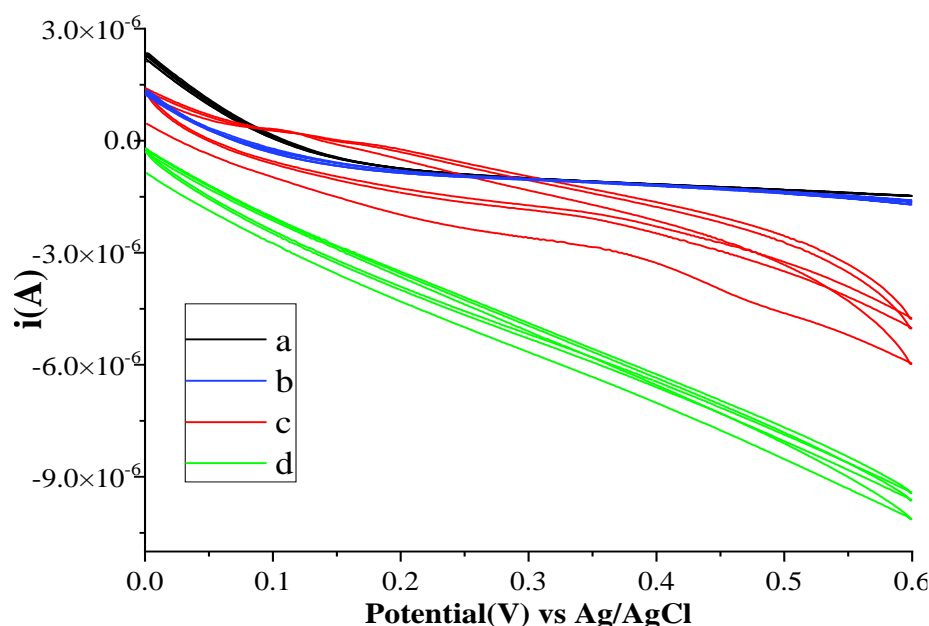

Figure 3.13: Cyclic voltammograms of an Au micro array platform using "Traditional" 24 h incubation (soaking) step method. CV studies were carried out on a Au micro array platform after Au electrodeposition with the PS bead-monolayer still intact, following this the Au micro array substrate was incubated for 24 h in 1mM Mercaptohexane alcoholic solution for functionalization of the micro array exterior. After 24 h incubation the Au micro array platform was removed from solution and voltammetric studies were carried out under identical conditions, the platform was then sonicated in THF solvent for 10 min to thoroughly-remove the PS monolayer and to expose the Au micro array surface and CV was repeated. The last step involved 24 h incubation in 1.2 μM SH-(c)-RGDFK solution and the final CV scan was repeated. CV (E$_{1/2}$ = 0.3 V) was performed at a scan rate (v) of 50 mV/s in 1mM K$_3$Fe(CN)$_6$ in 100 mM KCl electrolyte solution within a three-electrode cell set up, Ag/AgCl reference electrode, platinum wire auxiliary electrode. Legend: a (solid black line), unfunctionalized electrode; b, (solid blue line) mercaptohexane soaked electrode with intact PS sphere monolayer); c (sold red line), Mercaptohexane soaked electrode after PS-SAM removal; d (solid green line), SH-(c)-RGDFK functionalized array interiors.

The voltammograms in both Figures 3.11b and 3.13 are different when compared, however, this is due to a number of factors, the PS spheres still remain in the micro array-interior before mercaptohexane-incubation to prevent any SAM formation within the micro array interiors, this PS-monolayer also prevents any micro array surface exposure to the probe solution. The oxidative reductive cycle of the Potassium ferrocyanide probe is inhibited due to the presence of a PS sphere-monolayer (See Figure 3.13) blocking access to the electrode-surface, the oxidative reductive cycle after PS removal does take place but cannot be easily seen at this scale and the purpose of these overlaid spectra is for comparative purposes only. The only apparent quantitative result in Figure 3.13 is the drop in the initial current (**i**) from 2.26 x 10^{-5} A to 1.24 x 10^{-5} A when comparing the unfunctionalized Au platform voltammetric scan with the thiol-functionalized Au platform scan after 24 h incubation, indicating a slight drop in overlaid peak area(s). There is also a slight increase in the

initial current **(i)** after THF sonication which indicates that the unmodified micro-arrays are now freely-exposed to the probe solution.

In summary, 30 min MCP generates sufficient packing for the purposes of this project because detailed FE-SEM imaging studies (discussed in more detail in Chapter 5) carried out indicate that no exosome-adhesion takes place outside the micro array pores indicating SH-(c)-RGDFK peptide is confined to the interior the micro array platform.

EIS studies on Au micro array substrates were carried out before and after each modification step to compare to the CV data previously shown. Non-faradaic EIS studies were carried out on a Au micro array platform under the same conditions as described for Figure 3.08b with the additional steps of incubation in 1.2 µM SH-(c)-RGDFK peptide solution and then a final incubation step for 6 h in 0.4 ng/mL labelled $\alpha_5\beta_1$ integrin at room temperature. See Schematic of experimental set-up in Figure 3.15 below for clarity.
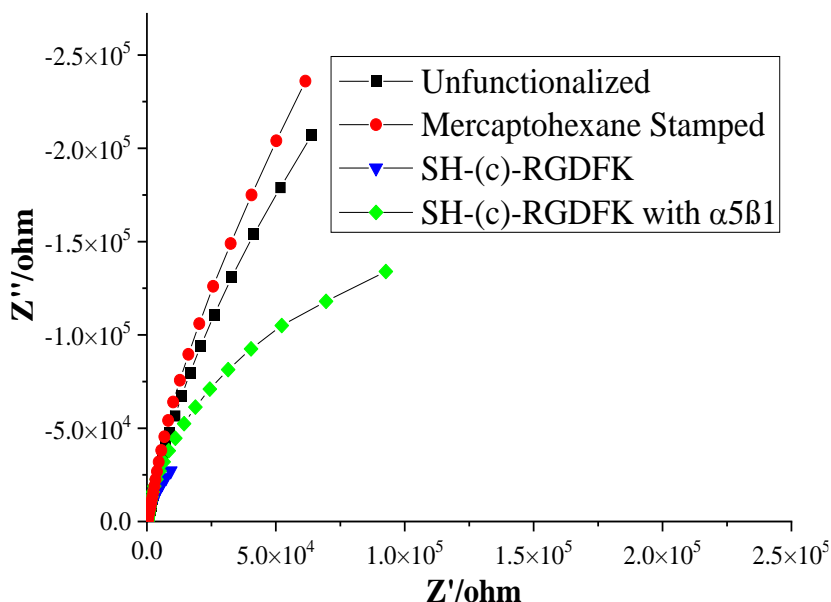
Figure 3.14: Nyquist Impedance Plot(s) of Au micro array platform. Non-faradaic EIS measurements were carried out on an unfunctionalized planar Au platform in 100 mM PBS buffer from 0.1 Hz–10 kHz frequency range with a 0.01 V r.m.s. signal following this the planar Au platform was stamped with 10 mM mercaptohexane for 30 min and EIS measurements were carried out under identical conditions. After this step the micro array platforms were incubated in 1.2 µM SH-(c)-RGDFK for 24 h and EIS studies were carried out under the same conditions. The Au micro array substrate was then incubated in 0.4 ng/mL labelled α5β1 integrin solution for 6 h at room temperature. After this step EIS studies were carried out under identical conditions. All EIS studies were carried out within a three-electrode cell set up, Ag/AgCl reference electrode, platinum wire auxiliary electrode and the planar Au platform as the working electrode.

After previous data on planar Au substrates confirmed MCP as a suitable selective surface technique, it was necessary to assess the MCP-functionalization method on Au micro array platforms by functionalizing their exteriors and then a further step to functionalize the micro array interiors with

SH-(c)-RGDFK solution incubation and assess selective surface modification after each step using the same EIS parameters. In Figure 3.14, an additional step was added, incubation of the SH-(c)-RGDFK modified micro array platform in 0.4 ng/mL labelled-$\alpha_5\beta_1$ integrin solution, this integrin is expected to selectively bind with a RGD sequence[34]. The data is consistent and shows that there was an increase in impedance after 10mM mercaptohexane stamping (indicated by the decrease in final Z_{real} point(s) from 84 kΩ to 24.7 kΩ on the x-axis. Similar findings using thiolated hydrocarbons were reported by *Sharma et al* 2016[20]. Interestingly in Figure 3.14 following SH-(c)-RGDFK incubation there was an increase in Z_{real} from 24.7 kΩ to 161.8 kΩ, this may be due to the charged nature of the amino acids (R-with a + charge and D- with a – charge) within the cyclic peptide chain structure, and the association therefore of mobile ions with the peptide. It also may be that RGD peptide improves wettability of the cavity interior, facilitating and enhancing aqueous filling.
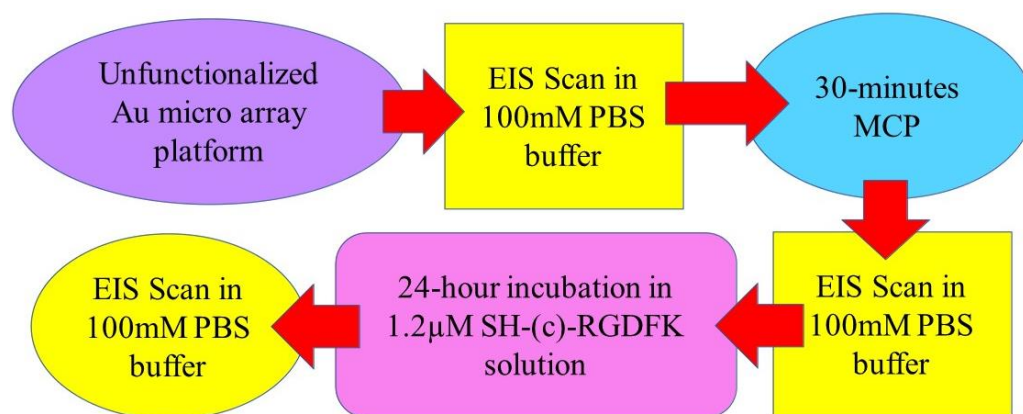
Figure 3.15: Schematic representation of EIS experimental set up using SH-(c)-RGDFK peptide solution for clarification purposes.

Similar findings were reported by *Adamson et al* 2016[2], they used RGD-modified Au micro array platforms for platelet studies and carried out substantial electrochemical work, after the RGD was reductively-desorbed, there was a huge reduction in peak areas on all voltammograms indicating that the charged-polar RGD species may be responsible for increased Au-surface wetting. EIS peptide studies carried out on peptides by *Sanjeev et al* 2019[35] showed that there was a proportional decrease in $-Z_{imag}$ as the peptide concentration was increased, this increased concentration on the electrode may also have increased surface-wettability in their studies. It is likely that the polar nature of peptide species makes them behave differently to non-polar hydrocarbon structures in aqueous solutions. Zeta Potential studies on the SH-(c)-RGDFK solution were carried out in 100mM PBS solution and shown in the next sub-section.

These results confirm the reproducibility of both stages of the selective surface modification process. Following incubation with $\alpha_5\beta_1$ integrin there was a decrease in impedance, this may be due to less-surface area wettability caused by the conjugation $\alpha_5\beta_1$ integrin has conjugated to the RGD-surface.

However, Z_{real} also increased from 91.7 kΩ to 92.7 kΩ which indicates protein-adsorption has taken place within the micro array platform and results in a change in electrode conductivity properties. To confirm that this effect is due to specific RGD recognition and not non-specific binding to the electrode surface, this step was further assessed and imaged using confocal microscopic techniques as the labelled-$\alpha_5\beta_1$ integrin emitted fluorescence ($\lambda_{emission}$) intensity can be surface-enhanced upon laser excitation in the bottom of the micro array pores[14] and is explored in more detail in the next experimental chapter

As the previous set of data shows selective surface modification involving SH-(c)-RGDFK peptide SAM formation within the micro array interiors; Other thiolated compounds were also assessed for selective surface modifications, mainly thiocholesterol. The rationale behind this particular choice of compound is that previous studies carried out by *O'Connor et al* 2019[36] showed that BODPIY cholesterol probes proved effective labelling dyes for liposomes and were also suitable for cell imaging. This BODIPY cholesterol probe will be further assessed as an exosome labelling probe in the next experimental chapter.

Exosomes are also a cellular vesicle and share many similar features to liposomes and one feature they have in common is that they contain sphingomyelin and cholesterol[37,38]. If cholesterol labelling probes can effectively conjugate to exosomes, then a thiocholesterol -SAM may prove to be a suitable alternative to the more expensive (c)-RGDFK peptide which also requires a coupling reaction step for film formation. Thiocholesterol is easily applied directly to the Au micro array platform immediately after dissolving in an organic solvent (THF) and requires no further modification chemically.

For Figure 3.16 (below), non-faradaic EIS studies were carried out under the same conditions as described in Figures 3.06b and 3.14 and the micro array platform was selectively modified as described in Figure 3.14 but with ratio mixtures of thiocholesterol/mercaptohexanol instead of SH-(c)-RGDFK peptide. Each Au micro array platform was incubated in either: (a) 1.25 μM thiocholesterol, ratio mixtures of (b) (70/30)) 1.25 μM thiocholesterol to 1.25 μM mercaptohexanol and/or (c) 50/50 of 1.25 μM thiocholesterol to 1.25 μM mercaptohexanol (See Figures 3.16(a-c) respectively). The rationale for using ratio mixtures of thiocholesterol to mercaptohexanol will be mentioned in discussion of results. See Schematic of experimental set-up in Figure 3.17 for clarification purposes.
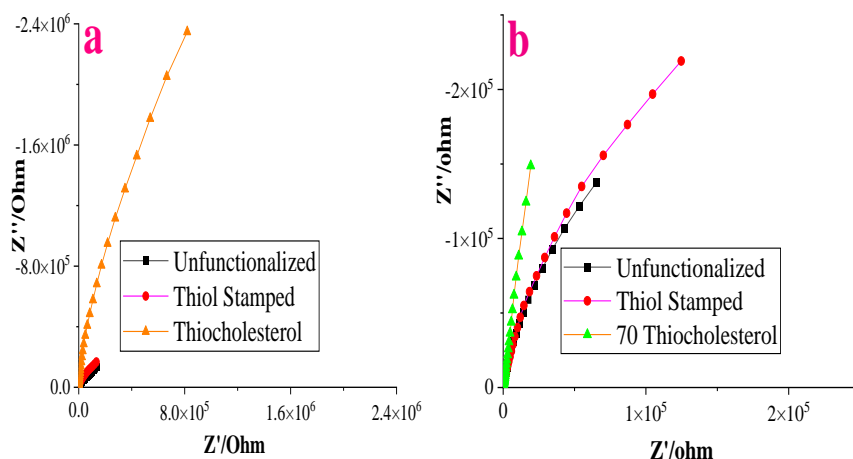
Figures 3.16(a-c): Nyquist Impedance Plot(s) of Au micro array platforms. Non-faradaic EIS measurements were carried out on an unfunctionalized Au micro array platform in 100 mM PBS buffer from 0.1 Hz–10 kHz frequency range with a 0.01 V r.m.s. signal following this the Au micro array substrate was stamped with 10 mM mercaptohexane for 30mins and EIS measurements were carried out under identical conditions. After this step the micro array platforms were incubated in; (a) 1.25 µM thiocholesterol. (b) ratio of 70 1.25 µM thiocholesterol to 30 1.25 µM mercaptohexanol and (c) ratio of 50 1.25 µM thiocholesterol to 50 1.25 µM mercaptohexanol for 24 h. All EIS studies were carried out under the same conditions and within a three-electrode cell set up, Ag/AgCl reference electrode, platinum wire auxiliary electrode and the Au micro array platform as the working electrode.

The data shown in Figures 3.16(a-c) indicate that there was an increase in impedance after 10 mM mercaptohexane-stamping as previously shown indicated by the increase in $-Z_{imag.}$ similar to alkane-thiol studies carried out by *Campuzano et al* 2005[39] and *Sharma et al* 2016[20]. After 24 h 1.25 µM thiocholesterol incubation (Figure 3.16a) and EIS studies was carried out under identical conditions. Following this thiocholesterol incubation-step there was a substantial increase in impedance indicated by the sharp increase in in final $-Z_{imag}$ value from 167.4 kΩ (mercaptohexane-stamped) to 2348 kΩ (thiocholesterol SAM formation). The scale is of an order of magnitude higher when compared to both unfunctionalized ($-Z_{imag}$ 134 kΩ) and mercaptohexane-stamped results. This indicates substantial impedance after thiocholesterol -SAM formation. It further confirms that the majority of the Au electrode surface area is contained within the micro array pores. Cholesterol has a neutral charge and is hydrophobic and extensive EIS studies carried out on cholesterol membranes by *Alobeedallah et al 2018*[40] showed that thick cholesterol-layers on an Au electrode display high levels of impedance and that in contrast, thinner deposited layers of cholesterol layer showed high levels of capacitance, this may indicate that thin layers of cholesterol absorb H_2O. The high level of impedance seen in Figure 3.16a may be due to the formation of a close-packed layer and this thick thiocholesterol layer within the micro-array platform is preventing surface wettability as the Au surface is entirely shielded due to the tight orderly packing. That the last incubation step results in such an intense impedance increase when compared to unfunctionalized and mercaptohexane-

stamped, confirms the second incubation step is very effective in modifying the Au micro-array interior and thus indicates further that this is also an effective route for SH-(c)-RGDFK modification.
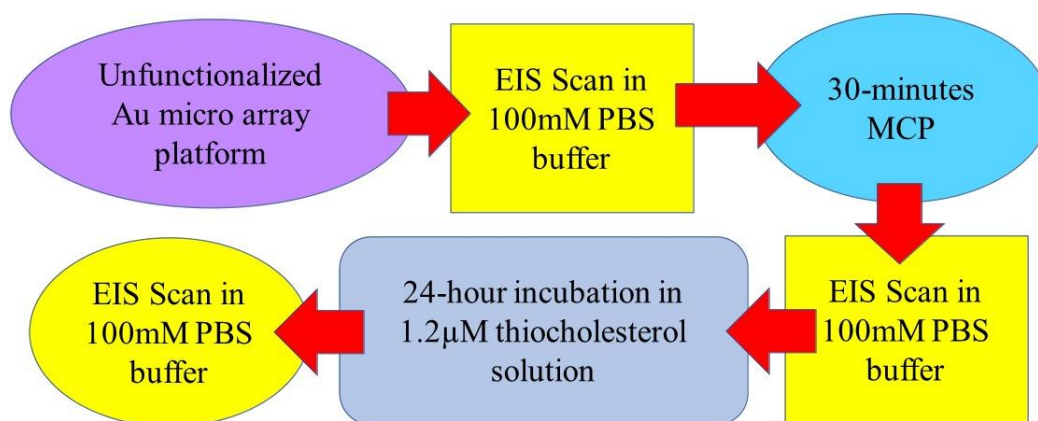
Figure 3.17: Schematic representation of EIS experimental set up using thiocholesterol for clarification purposes.

This intense increase in impedance was the rationale behind the following experimental set-up (results shown in Figures 3.16b and c) where ratio mixture(s) of thiocholesterol to mercaptohexanol were used for Au micro array interior selective modifications to alter the chemical properties of the resulting films. The thiol group on the mercaptan compound would conjugate with the Au surface with the polar OH group facing outwards. This orientation would improve hydrophilicity and prevent over-packing of the thiocholesterol as reported by *Alobeedallah et al 2018*[40]. When the final three -Z_{imag} data points for the thiocholesterol/ thiocholesterol-mercaptohexanol on Figures 3.16a, b, and c (2348 kΩ, 148.8 kΩ and 147.1 kΩ respectively) are compared, there is more one order of magnitude of a difference, this confirms that mixing the thiocholesterol (even with a much smaller concentration) with another mercaptan compound does significantly lower the impedance. Interestingly, the -Z_{imag} data points in both Figures 3.16b and c are very close. This further indicates that the proportional variations did not have any substantial impact.

For studies in this thesis, all exosomes are suspended in PBS buffer (Refer to Section 2.3.6, Chapter 2) and results shown in Figure 3.16a show that the cavities modified with hydrophobic mercaptohexane-exteriors and hydrophobic-thiocholesterol interiors are too hydrophobic for the aqueous PBS solution to effectively fill. It was necessary to try to make the micro array interior-environment slightly more hydrophilic so as to optimise and encourage exosome capture. This was attempted by forming mixed monolayers of thiocholesterol and mercaptohexanol which has been used previously for stable SAM lipid formation on micro array exteriors[4,5]. In microfluidics the use of hydrophilic/hydrophobic patterning is a form of passive-valve system used to induce turbulence

on a microlitre level, when the use of actual pump on that microscale would be impractical[41]. The entire hydrophobic nature of the Au micro array platform may be inhibiting liquid turbulence thus preventing thorough-wetting of the bottom of the micro array pores.

The deposition solution ratio of mixtures of mercaptan compounds do not always result in the same ratio in the SAM formation on the surface. Grazing incidence IR spectroscopic studies carried out by *Nuzzo et al* 1990[43] demonstrates that substituted mercaptan compounds only form densely close-packed high-ordered SAM structures when the terminal functional group (NH2, OH) is relatively small (< 5 Å), IR and Electrochemical studies carried out demonstrated that the orientation of the monolayer is not influenced, however more bulky terminal functional groups (COOH, ferrocene) will decrease the density and the order of SAM formation[.35,36]. A mixed monolayer, indicating random ordering of the two constituents within the formed SAM structure[46]. Thiocholesterol is not an alkyl-chained thiol, rather it contains 4 cycloalkanes which makes it structurally quite bulky when compared to the much shorter and smaller alkyl chained mercaptohexanol. This clearly demonstrates that the use of ratio mixtures will not guarantee the same proportional molar deposition and that adsorption of thiocholesterol will remain almost constant regardless of the molar concentration in solution.

This explains why the results in Figures 3.16b and c are almost identical even though the proportional concentrations are different and this hypothesis further backed up by studies carried out by *Bain et al* 1990[46] that demonstrated that chemisorption of longer chained alkyl thiols than shorter is preferred on an Au substrate. Therefore, proportional-molar deposition of thiocholesterol and alkyl-mercaptoalcohol is not guaranteed as both molecules are so different both structurally and size-wise thereby making phase separation more likely. It is also plausible that the same amount of thiocholesterol will adsorb onto the Au surface regardless of concentration. Reproducibility of exact SAM formation may also prove to be a challenge as slightly different ratios (than the required) may be deposited on the Au surface each time even if the proportional molar-ratio in solution is always kept constant.

It is clear from the three previous sets of results (Figures 3.16a-c) that thiocholesterol readily forms a SAM within the micro array interiors and this is backed up with previously published literature of thiolated Au platforms as suitable plasmonic substrates[12,13] however the suitability of these same thiocholesterol functionalized substrates for successful exosome capture is another matter and their suitability will be assessed in the next experimental chapter.

3.3.4 Zeta Potential Measurements

As all EIS measurements showed an increase in capacitance after SH-(c)-RGDFK functionalization of the Au micro-array platform even though the overall net-charge of the modified (c)- RGDFK is theoretically zero (adding all charges of amino acids together plus taking into account the + charge

loss that occurs to the secondary amine group on the K residue after EDC sulpho-NHS coupling). As peptides are sensitive to changes in pH therefore, it was necessary to determine if any ionisation of the peptide takes place in PBS solution as this is a buffer salt solution at pH 7.4 made up of many charged ions which could potentially affect the overall neutral charge of the peptide. Peptides are affected by minute changes in their pH environment(s).

Zeta Potential measurements were carried out to determine the charge of the SH-(c)-RGDFK peptide in solution using the method outlined in[47]. When a charged particle is dispersed in solution an Electric Double Layer (EDL) conjugates directly onto its surface[48]. This EDL consists of two layers (Stern and Diffuse)[48] shown in Figure 3.18 below.

Table 2: Zeta potential values of 1.2 µM SH-(c)-RGDFK 100 mM PBS solution. 0.75 mL of 1.2 µM (c)-RGDFK peptide in 100 mM PBS solution was aliquoted into a zeta cuvette-cell and the software settings were switched from Dynamic Light Scattering (DLS) to Zeta Potential settings

Zeta Potential (mV)	Mean (mV)	%RSD
-12	-13.14	1.150
-14.3		
-13.1		

0.75 mL of 1.2 µM (c)-RGDFK peptide in 100 mM PBS solution was aliquoted into a Zeta cuvette-cell and the software settings were switched from Dynamic Light Scattering (DLS) to Zeta Potential settings. Results shown in Table 2, above.
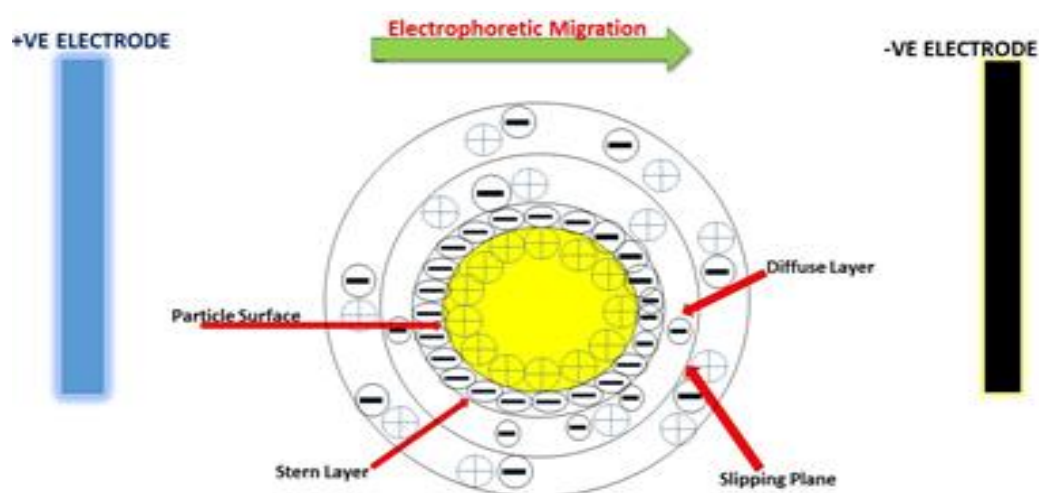

`

Figure 3.18: Schematic showing the Electrophoretic movement of a positively charged particle. The particle electro-osmotically moves to the oppositely-charged electrode. The Zeta Potential is the Electrokinetic Potential value recorded at this slipping plane. Schematic adapted and modified from[48].

Using https://web.expasy.org/compute_pi/ (an online calculator powered by the Swiss Proteomics database[49]), the isoelectric point (pI) of the (c)-RGDFK peptide was calculated to be 5.9. However the (c)-RGDFK used in this study is also thiolated, therefore its pI value may be higher or lower. Zeta Potential measurements in this study have calculated the average charge to be -13.13 mV and, it was also determined that the pH of the solution lies beyond its pI as the peptide molecule has acquired a negative charge[50]. Due to this acquired charge, the peptide will also hydrogen-bond to the polar H_2O molecules (and any charged ions suspended in the PBS buffer solution) thereby increasing Au micro array surface wettability and subsequently allowing the exosomes to come into closer contact with the surface of the SH-(c)-RGDFK functionalized Au micro arrays as exosomes are suspended and incubated in PBS solution to promote biocapture.

3.5 Conclusions

In this chapter fabrication and selective surface modification methods of the Au micro array platform and the characterisation of the substrates were assessed using a variety of analytical techniques. The exterior of the Au micro-array platform was successfully modified using MCP with both mercaptohexanol and the more hydrophobic mercaptohexane. Contact Angle measurements indicated a change in hydrophilic properties of the planar Au substrate after MCP. Non-faradaic EIS results showed an increase in impedance after MCP and CV demonstrated that there was an increase in the peak to peak separation between the E_{ox} and E_{red} of the Potassium ferrocyanide probe indicating increased electrode resistance and also showed a drop in their respective peak-height values indicative of reduced electrode electroactive surface area. Mercaptohexane was concluded to be a better choice for selective surface modification on the Au micro array exteriors as it is more hydrophobic than mercaptohexanol even though according to the CV data, the mercaptohexanol packs better on the Au electrode surface. However, this hydrophobic property is more applicable for the studies undertook for this thesis as it effectively prevents any bio-adhesion on the outside of the micro array pores.

After MCP the Au micro array interiors were successfully selectively-modified using different thiolated compounds EDC Sulpho-NHS modified (c)-RGDFK peptide (to provide an alkyl chain with a thiol terminus to enable Au thiolation) and thiocholesterol (and ratios of thiocholesterol with mercaptohexanol) by incubation in solution.

Using a modified (c)-RGDFK peptide, this regioselective surface functionalization was confirmed using EIS which showed an increase in electrode capacitance after SH-(c)-RGDFK SAM formation, which is attributed to a change in physicochemical properties within the environment of the micro array interiors. Zeta Potential measurements confirmed the slight negative charge of the peptide in the PBS which is attributed to the increase in capacitance. Results from CV measurements showed

that there was complete inhibition of the oxidative-reductive cycle of the Potassium ferrocyanide probe after SH-(c)-RGDFK peptide monolayer formation.

By using thiocholesterol in various ratios to mercaptohexanol to functionalize the micro array interiors after MCP, EIS studies showed that there was a substantial increase in impedance and this is most likely due to the hydrophobic properties of this compound with the highest level of impedance shown on a platform that was modified with 100% thiocholesterol, there was very little difference in results using different ratios of thiocholesterol with mercaptohexanol (70/30 and 50/50 ratios respectively) which suggests that molar ratio concentrations in liquid solution will not necessarily deposit in the same ratio on the surface due to their differences in physicochemical properties.

These functionalized interiors with these different thiol-compounds were then assessed for exosome capture in the following experimental chapter.

3.6 References

1   K. Adamson, E. Spain, U. Prendergast, N. Moran, R. J. Forster and T. E. Keyes, *Langmuir*, 2018, **34**, 715–725.

2   K. Adamson, E. Spain, U. Prendergast, N. Moran, R. J. Forster and T. E. Keyes, *ACS Appl. Mater. Interfaces*, 2016, **8**, 32189–32201.

3   C. T. Mallon, K. W. Kho, H. Gartite, R. J. Forster and T. E. Keyes, *Adv. Eng. Mater.*, 2018, **20**, 1–10.

4   K. W. Kho, G. B. Berselli and T. E. Keyes, , DOI:10.1002/smll.202005815.

5   J. Robinson, G. B. Berselli, M. G. Ryadnov and T. E. Keyes, , DOI:10.1021/acs.langmuir.0c00035.

6   D. Qin, Y. Xia and G. M. Whitesides, *Nat. Protoc.*, 2010, **5**, 491–502.

7   A. Kumar and G. M. Whitesides, *Appl. Phys. Lett.*, 1993, **63**, 2002–2004.

8   G. M. Whitesides, G. S. Ferguson, D. Allara, D. Scherson and A. Ulman, 1993, **3**, 49–65.

9   S. Alom Ruiz and C. S. Chen, *Soft Matter*, 2007, **3**, 168–177.

10   D. Sorg, K. Danowski, V. Korenkova, V. Rusnakova, R. Küffner, R. Zimmer, H. H. D. Meyer and H. Kliem, *Animal*, 2013, **7**, 799–805.

11   C. Crozatier, M. Le Berre and Y. Chen, *Microelectron. Eng.*, 2006, **83**, 910–913.

12   R. Forster, T. Keyes and J. Vos, *Interfacial Sopramolecular Assemblies*, John Wiley and Sons, Ltd., 2004.

13   J. C. Love, L. A. Estroff, J. K. Kriebel, R. G. Nuzzo and G. M. Whitesides, *Self-assembled monolayers of thiolates on metals as a form of nanotechnology*, 2005, vol. 105.

14   B. Jose, R. Steffen, U. Neugebauer, E. Sheridan, R. Marthi, R. J. Forster and T. E. Keyes, *Phys. Chem. Chem. Phys.*, 2009, **11**, 10923–10933.

15   H. Basit, V. Gaul, S. Maher, R. J. Forster and T. E. Keyes, *Analyst*, 2015, **140**, 3012–3018.

16   Y. L. T. Yuan, *Contact Angle and Wetting Properties*, Springer Berlin Heidelberg, 2013, 2013, vol. 51.

17   W. C. Bigelow, D. L. Pickett and W. A. Zisman, *J. Colloid Sci.*, 1946, **1**, 513–538.

18   T. Smith, *J. Colloid Interface Sci.*, 1980, **75**, 51–55.

19   J. Wang, *Analytical Electrochemistry*, 2006.

20   A. Sharma, J. K. Bhattarai, S. S. Nigudkar, S. G. Pistorio, A. V. Demchenko and K. J. Stine, *J. Electroanal. Chem.*, 2016, **782**, 174–181.

21   A. Testolin, S. Cattaneo, W. Wang, D. Wang, V. Pifferi, L. Prati, L. Falciola and A. Villa, 2019, 205–215.

22   K. Adamson, E. Spain, U. Prendergast, R. J. Forster, N. Moran and T. E. Keyes, *Biomater. Sci.*, 2014, **2**, 1509–1520.

23   G. B. Berselli, N. K. Sarangi, S. Ramadurai, P. V Murphy and T. E. Keyes, *ACS Appl. Bio Mater.*, 2019, **2**, 3404–3417.

24   S. Maher, H. Basit, R. J. Forster and T. E. Keyes, *Bioelectrochemistry*, 2016, **112**, 16–23.

25   R. W. Y. Yeo, R. C. Lai, B. Zhang, S. S. Tan, Y. Yin, B. J. Teh and S. K. Lim, *Adv. Drug Deliv. Rev.*, 2013, **65**, 336–341.

26 J. Carmicheal, C. Hayashi, X. Huang, L. Liu, Y. Lu, A. Krasnoslobodtsev, A. Lushnikov, P. G. Kshirsagar, A. Patel, M. Jain, Y. L. Lyubchenko, Y. Lu, S. K. Batra and S. Kaur, *Nanomedicine Nanotechnology, Biol. Med.*, 2019, **16**, 88–96.

27 E. Hergenreider, S. Heydt, K. Tréguer, T. Boettger, A. J. G. Horrevoets, A. M. Zeiher, M. P. Scheffer, A. S. Frangakis, X. Yin, M. Mayr, T. Braun, C. Urbich, R. A. Boon and S. Dimmeler, *Nat. Cell Biol.*, 2012, **14**, 249–256.

28 Y. Chen, H. Yuan, Z. Ou and J. Ou, .

29 M. Colombo, G. Raposo and C. Théry, *Annu. Rev. Cell Dev. Biol.*, 2014, **30**, 255–289.

30 R. Szatanek, M. Baj-Krzyworzeka, J. Zimoch, M. Lekka, M. Siedlar and J. Baran, *Int. J. Mol. Sci.*, , DOI:10.3390/ijms18061153.

31 A. V. Gimenez, K. W. Kho and T. E. Keyes, *Nanoscale Adv.*, 2020, **2**, 4740–4756.

32 P. Rezai and P. R. Selvaganapathy, , DOI:10.1533/9780857096272.1.3.

33 H. J. (Jim) Cleaves, in *Encyclopedia of Astrobiology*, eds. M. Gargaud, R. Amils, J. C. Quintanilla, H. J. (Jim) Cleaves, W. M. Irvine, D. L. Pinti and M. Viso, Springer Berlin Heidelberg, Berlin, Heidelberg, 2011, p. 1668.

34 T. G. Kapp, F. Rechenmacher, S. Neubauer, O. V. Maltsev, E. A. Cavalcanti-Adam, R. Zarka, U. Reuning, J. Notni, H. J. Wester, C. Mas-Moruno, J. Spatz, B. Geiger and H. Kessler, *Sci. Rep.*, 2017, **7**, 1–13.

35 A. Sanjeev, B. Jagannath, Y. Tamrakar, S. Muthukumar and S. Prasad, *Anal. Chim. Acta X*, 2019, **3**, 100029.

36 D. O'Connor, A. Byrne, C. Dolan and T. E. Keyes, *New J. Chem.*, 2018, **42**, 3671–3682.

37 R. Wubbolts, R. S. Leckie, P. T. M. Veenhuizen, G. Schwarzmann, W. Möbius, J. Hoernschemeyer, J. W. Slot, H. J. Geuze and W. Stoorvogel, *J. Biol. Chem.*, 2003, **278**, 10963–10972.

38 X. Osteikoetxea, A. Balogh, K. Szabó-Taylor, A. Németh, T. G. Szabó, K. Pálóczi, B. Sódar, Á. Kittel, B. György, É. Pállinger, J. Matkó and E. I. Buzás, *PLoS One*, 2015, **10**, 1–16.

39 M. Pingarro and E. Fata, 2006, **586**, 112–121.

40 H. Alobeedallah, B. Cornell and H. Coster, *J. Membr. Biol.*, 2018, **251**, 153–161.

41 Y. Feng, Z. Zhou, X. Ye and J. Xiong, 2003, **108**, 138–143.

42 I. Badea, G. L. Radu and G. I. Badea, 2018, 1–6.

43 R. G. Nuzzo, L. H. Dubois and D. L. Allara, *J. Am. Chem. Soc.*, 1990, **112**, 558–569.

44 C. E. D. Chidsey and D. N. Loiacono, *Langmuir*, 1990, **6**, 682–691.

45 T. Kitagawa, H. Matsubara, T. Okazaki and K. Komatsu, *Molecules*, 2014, **19**, 15298–15313.

46 C. D. Bain and G. M. Whitesides, *J. Am. Chem. Soc.*, 1989, **111**, 7164–7175.

47 M. Kaszuba, J. Corbett, F. M. N. Watson and A. Jones, *Philos. Trans. R. Soc. A Math. Phys. Eng. Sci.*, 2010, **368**, 4439–4451.

48 S. Bhattacharjee, *J. Control. Release*, 2016, **235**, 337–351.

49 A. Bairoch and R. Apweiler, 2000, **28**, 45–48.

50 S. Bhatia and R. Dahiya, *Tissue Culture Science*, Elsevier Inc., 2015.

Chapter 4: A Multimodal Study of Extracellular Vesicle Capture in Micro-Array Platforms.

4.1.0 Introduction

As the fabrication and functionalization methods of the Au micro array platform has been confirmed using a variety of analytical techniques in Chapter 3. The aim of this chapter is to use the selectively modified Au micro array platform for exosome capture and a more detailed explanation of the rationale for choosing a (c)-RGD peptide ligand for Au micro array interior functionalization to ensure exosome capture is discussed below in Section 4.3.1.1. The capture of and analysis of exosomes within the functionalized Au micro array platform (presented in this chapter and the next) is very novel and such exosome studies have not been carried out previously by the Keyes Research Group.

Exosome studies carried out are sourced from HUVECs and primary HuAECs so it is important to give a brief background to vascular biology here to gain an understanding of why their exosomal cargo was studied throughout this thesis.

4.1.1 Background to Vascular Biology

The endothelium forms a protective layer that regulates the diffusion of biomolecules and immune cells between the blood and vascular tissues; it controls and regulates several essential physiological functions. A 'normal' (healthy) endothelium will promote various cardio-homeostatic properties such as vascular tone, cell adhesion and SMC proliferation through the regulation of various anticoagulant, anti-thrombotic and anti-inflammatory mechanisms[1].

Atherosclerotic Cardio Vascular Disease (ACVD) is chronic inflammation that occurs in the artery tissues of the cardiovascular system. ACVD can lead to stroke, hypertension, angina or myocardial infarction[2]. It begins at sites where the blood tissue flow has either reduced or developed an oscillatory flow pattern. Curvatures and bifurcations are most prone to plaque deposition[3]. It is initially triggered as a response to injury and/or dysfunction of cardiac endothelial cells (CECs). This CEC layer forms an essential part of the tissue lining of the cardio-vascular network and the subsequent dysfunction and disruption of this lining is considered to play a role in both the activation and progression of atherosclerosis[4,5].

4.1.2 Exosomes in Vascular Biology

Exosomes (Extracellular vesicles) are discussed in detail in Chapter 1: Introduction, refer to Sections 1.4.1 and 1.4.2. Exosomes are heterogeneous[6,7] in nature in both size[8] and cargo-content[9,10] making them highly complex to analyse. In ACVD, cardiac exosomes activate various molecular signalling pathways by activation of specific target molecules which suppresses various inflammatory responses, this results in cardiac regeneration and overall improvement in cardiac function[11,12].Tetraspanins are antigens found on the surface of endothelial exosomes[5,9,13–18] are indicative of overall cardiac health status. Cardiac endothelial exosomes from two different cells types are used in the studies presented in this experimental chapter. These are sourced from human immortalized umbilical vein cells EA.hy926 and primary human aortic endothelial cardiac cells-HuAECs (Normal group).

4.1.3 Background to Endothelial Cell types used in this study

Primary HUVECs are isolated from human umbilical cord endothelial vein tissue[19,20]. This cell line is most frequently used in endothelial cell research and much of the knowledge on endothelial cell processes, various metabolic activities, cardiovascular health (particularly in vasoconstrictive studies) and disease treatments (including anti-hypertensive and atherosclerotic therapeutics) has been a due to experimental work carried out *in vitro* on this specific cell line[20–25] Unfortunately, long-term experimental studies cannot be carried out using the same cell line as they enter senescence after just 10 passages and experimental results can vary significantly across different cell line sources[20]. To create a permanent, robust and standardized cell line, primary HUVECs were fused with the immortalized cell line A549[26] to create a hybrid, immortalized cell line EA.hy926 which has many of properties of the primary cell line but unlike the primary cell line source will perpetually proliferate and are more homogenous so limited cell passages are not a problem[26,27].

Primary HuAECs are isolated and cultured from human ascending and descending aortic tissue and are used in various types of *in vitro* studies including autophagy, free radical generation and response, cardiovascular disease and therapeutics[28–32]. These are not immortalized and passages are limited before entering senescence, however they are real samples from real donors which is an important factor for the AI part of this collaborative project to enable prediction of the origin of an unknown exosome source.

4.1.4 Introduction to Techniques used in This Chapter

In this chapter, the fabrication method described in Chapter 3 for the Au micro array platforms was used, applied and assessed for exosome capture. The Au micro array platform-interiors were

functionalized using SH-(c)-RGDFK peptide and thiocholesterol and these are studied using EIS and SERS techniques both before and after exosome capture for comparison.

As described, EIS was used to confirm a change in the Au electrode-surface properties, the Au micro array platforms are assessed after each stage of the selective surface modification process in the same way as presented in the previous chapter i.e. from unfunctionalized, mercaptohexane-stamped and soaking (*in either SH-(c)-RGDFK peptide or thiocholesterol to functionalize the micro array interiors to promote exosomal-adsorption*) with an additional step after exosomal-solution incubation in order to promote successful exosome binding within the modified micro array pore environment.

Simultaneously using CFM studies where applied, to further confirm successful SH-(c)-RGDFK Au micro array functionalization by using $\alpha_5\beta_1$ integrin as this integrin specifically recognises and binds to a (c)-RGD sequence[33,34]. This is then followed by further CFM studies to confirm successful exosome-labelling using a BODIPY cholesterol probe and subsequent successful capture of labelled EA.hy926 type exosomes within the SH-(c)-RGDFK functionalized micro array pores.

4.2 Materials and Methods

For Materials , please refer to Section 2.1, Chapter 2.

As methods were varied throughout this chapter, each individual method is described long-side its respective figure, and/or referred back to a previous figure (if necessary) to avoid repetition when a method is repeated.

4.3.0 Results and Discussion

4.3.1.0 SERS, Raman Spectroscopy and EIS.

After using chrono-amperometry to fabricate the Au micro array platforms, selective surface modification of the micro array exteriors using MCP and micro array interior-functionalization of the using both SH-(c)-RGDFK peptide and thiocholesterol soaking which were studied using CV and EIS in the previous chapter. Here, the use of SERS (within the Au micro array platform) is undertaken of primary HuAECs (NG).

To establish the SERS method it was necessary to thoroughly-assess the selectively-modified Au micro array platforms using SERS to understand any contributing background signals.

The plasmonic field significantly enhances the weak Raman scattering signal allowing for enhanced signal in the range of 10^4 to 10^{20} in some extreme cases[35–39], please refer to detailed explanation of

SERS theory in Chapter 1: Introduction. Enhancement factors (typically 10^7) on SERS Au micro array platforms have previously been measured by *Bartlett et al*[40] and *Gimenez et al*[41] which is why it was not necessary to measure these factors in this study.
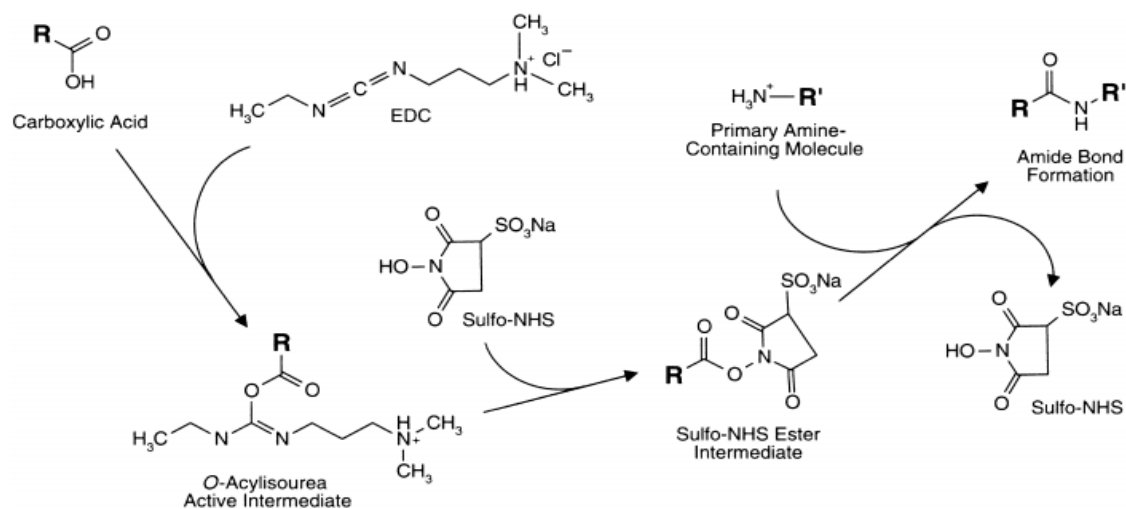
4.3.1.1 (c)-RGD Surface Functionalization

Figure 4.01: EDC Sulpho-NHS reaction mechanism. The EDC reacts with the Carboxylic acid group creating a sulpho-NHS ester intermediate (an amine nucleophile). An amide bond is then formed with the thiol group on the opposite end of the hexyl chain. Adapted from[46].

Studies have shown that the (c)-RGD sequence in fibronectin promotes binding of many biomaterials in a serum-free media[33,34,42]and a (c)-RGD sequence will bind to the integrins present on the surface of exosomes[34,42,43]. This is the rationale for choosing this specific peptide-ligand for Au micro array interior-functionalization. However, there is no thiol functional group terminus present to allow chemisorption to the Au surface in its current molecular structure (c)-RGDFK. Previous RGD SAM studies carried out by *Adamson et al* used a linear GRGDS SAM for biocapture (platelet studies)[44,45]. This linear peptide structure contains a thiol group attached to the Cysteine (C) residue (to enable it to bind and to thiolate the Au surface) however, it is non-cyclic and thus may not effectively conjugate to the exosomal surface-integrins..

In order to be able to use a (c)-RGD SAM structure for Au micro array interior functionalization, an EDC Sulpho-NHS reaction mechanism was carried out on the (c)-RGDFK peptide powder. EDC reacts with a COOH group (on the mercaptooctanoic acid molecule) creating an sulpho-NHS ester intermediate (an amine nucleophile). An amide bond is then formed with the primary NH_3^+ on the Lysine (K) residue[42] with the thiol functional-group attached on the opposite end of this alkyl chain, see Figure 4.01 for the reaction mechanism. This coupling reaction provides the peptide structure with an alkyl-thiol terminus that allows it to chemisorb to the Au surface forming a SH-(c)-RGDFK monolayer within the Au micro array interiors. This SAM could then be used for successful exosome capture.

4.3.1.2 Effective PS-sphere removal

Exosomal SERS-spectra were measured at 1-micron sized array pore by 1-micron sized array pore. The rationale for this first SERS study is to confirm PS-sphere removal after sonication in THF (Please refer back to the fabrication method in the previous chapter).

SERS studies were carried out on an Au micro array platform with the PS sphere monolayer still intact using a 10 % O.D filter and a 785 nm laser source operating at full power of 60.2 mW (See Figures 4.02A and B). Spectral acquisition was: 1 s with 4 s exposure time and 9 frame accumulations. The spectral range was scanned from 200 cm^{-1}-2000 cm^{-1}. Prior to analysis the Raman spectrophotometer was calibrated with a silicon wafer as per manufacturer's instructions[47] and using the Rayleigh line.

In Figure 4.02A (below), one Raman peak is evident at approximately 1000 cm^{-1} also by a weaker peak around 1020 cm^{-1} and two shoulders just before and after 1200 cm^{-1} . All indicate the presence of PS[48]. Both PS[48] and (c)-RGDFK (due to the presence of the distinctive F peak at ~1000 cm^{-1} [49]) have the same distinctive Raman peak at ~1000 cm^{-1}. A Raman spectrum of the pure unmodified (c)-RGDFK powder is shown in Figure 4.03.
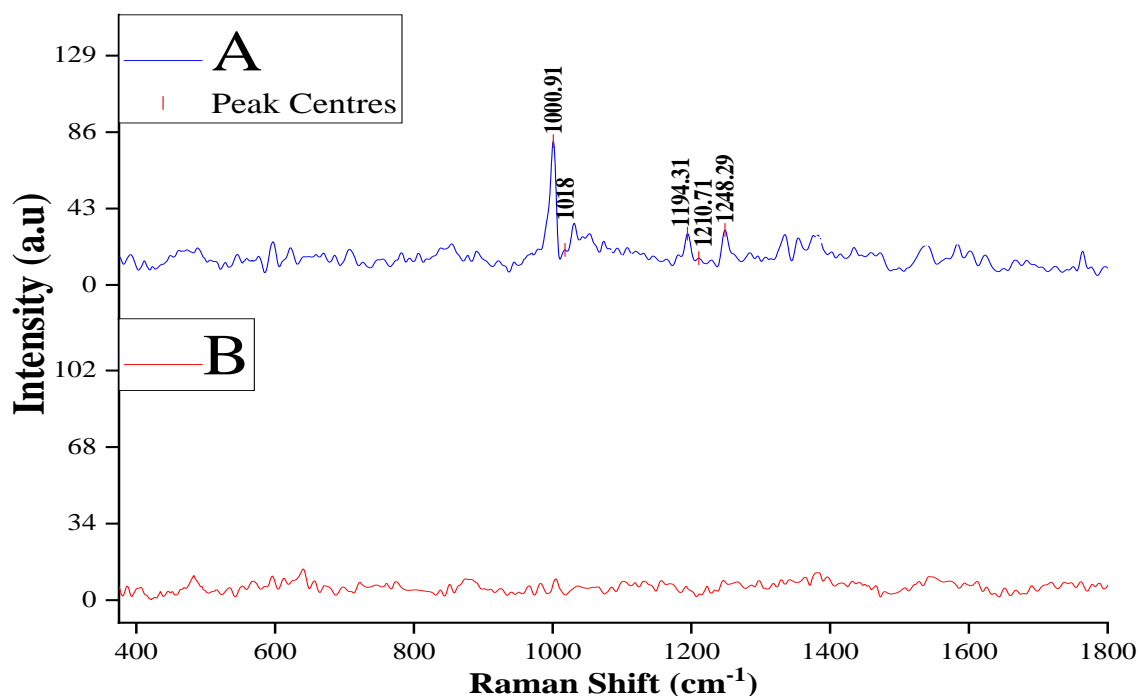
Figures 4.02A and B: SERS Spectra collected on an Au Micro Array platform (all arrays contained ordered pores, 1-micron in diameter) on an Au-silicon platform. 3(A): after Au electrodeposition around the PS monolayer (prior to sonication in THF). 3(B): After THF sonication (to thoroughly-remove the PS monolayer), the micro array substrate was dried to ensure no THF solvent remained in the Au micro array pores. Both studies were carried out using a 785 nm laser with full power of 60.2 mW with a 1 0% O.D. filter. Spectral acquisition was: 1s with 4s exposure time and 9 frame accumulations. Both spectra were baseline corrected and normalised using standard and de-spike settings to remove background noise.

Following sonication in THF for 10 min to thoroughly-remove the PS spheres and drying to ensure that no trace of THF solvent remains the SERS study was repeated. Results in Figure 4.02b appear to show only baseline with no evidence of the PS[50,51]. This result indicates that the 10 min sonication in THF is sufficient to completely remove the PS spheres from the platform. This was further confirmed by examining the Au micro array SEM images shown at the start of the previous experimental chapter and also by viewing the FE-SEM images (both with an intact PS monolayer and without) in the next experimental chapter.

The (c)-RGDFK was characterised by Raman before and after Sulpho-EDC NHS coupling for qualitative confirmation. Raman analysis of pure (c)-RGDFK peptide powder was carried out on a planar Au slide using a 25 % O.D. filter on a 785nm laser operating at full power of 60.2 mW. Spectral acquisition was 1 s with 4 s exposure time and 9 frame accumulations.
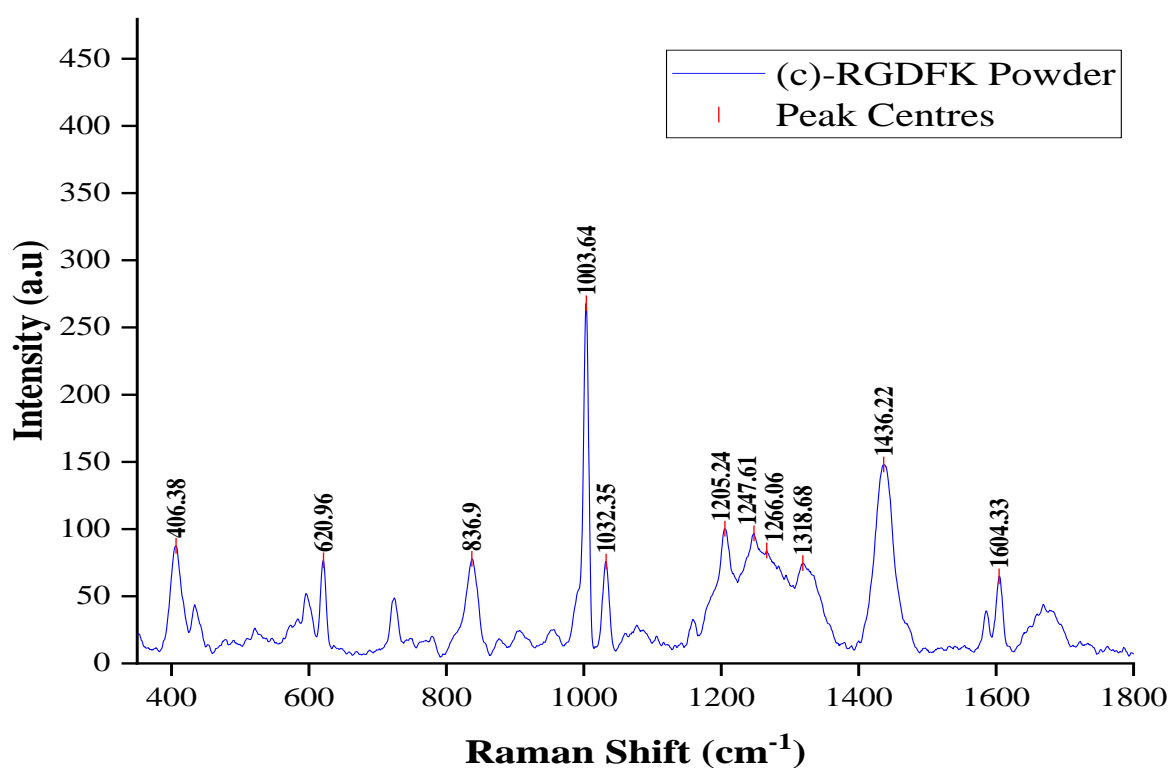
Figure 4.03: Raman spectrum of Pure (c)-RGDFK powder (before the EDC Sulpho-NHS modification step) carried out on a planar Au platform using 25 % O.D. filter on a 785 nm laser source, full working power 60.2 mW. Prior to analysis, the Raman spectrophotometer was calibrated using a silicon wafer as per manufacturer's instructions. Spectral acquisition was: 1 s with 4 s exposure time and 9 frame accumulations. Spectrum was baseline corrected and normalised using standard and de-spike settings to remove background noise.

From literature, six vibrational Raman peaks are expected as characteristic of F at 622 cm^{-1},1004 cm^{-1}, 1031 cm-1, 1207 cm^{-1}, 1586 cm^{-1}, and 1606 cm^{-1} respectively[49]. In Figure 4.03, the distinctive F peak can be observed at ~1003.5 cm^{-1} and in addition to its the other characteristic Raman peaks at 621 cm^{-1}, 1032 cm^{-1}, and 1604 cm^{-1} with the weakest peak around 1589 cm^{-1}. There are other

prominent peaks and shoulders present due to the presence of other amino acids such as Arginine (R).

Both EIS and CV studies confirmed successful SH-(c)-RGDFK functionalization of Au micro array interiors in the previous experimental chapter and successful SH-(c)-RGDFK functionalization was also further confirmed using confocal fluorescence microscopic (CFM) studies shown at the end of this experimental chapter. Here, SH-(c)-RGDFK Au adsorption was also assessed at the micro array using SERS as the spectral-profile of the SH-(c)-RGDFK as described, to confirm adsorption and assess potential contributions to background in exosome spectra.

4.3.1.3 SH-(c)-RGDFK Peptide functionalized Au Micro Array Platforms

The following set of experiments focuses on the use of SH-(c)-RGDFK to functionalize the Au micro array interiors and to perform SERS and EIS studies on these SH-(c)-RGDFK functionalized Au array templated platforms and then to repeat the studies after exosome capture.

An Au micro array platform was first stamped for 30 min with 10 mM mercaptohexane and then incubated for 24 h in 1.2 µM SH-(c)-RGDFK solution. SERS studies were carried out on the SH-(c)-RGDFK functionalized Au micro array platform at varying laser powers; 1 % O.D. filter 10 % O.D. filter and 25 % 785 nm laser with a full power of 60.2 mW. The spectral range was scanned from 200 cm^{-1}-2000 cm^{-1} but the 400 cm^{-1}-1800 cm^{-1} range is shown here as this is the main range of interest. Spectral acquisition was 1 s with 4 s exposure time and 9 frame accumulations. Prior to analysis the Raman spectrophotometer was calibrated using a silicon wafer as per manufacturer's instructions[47] and the Rayleigh line. Please see step-by-step summarised schematic in Figure 4.05 for clarification purposes..
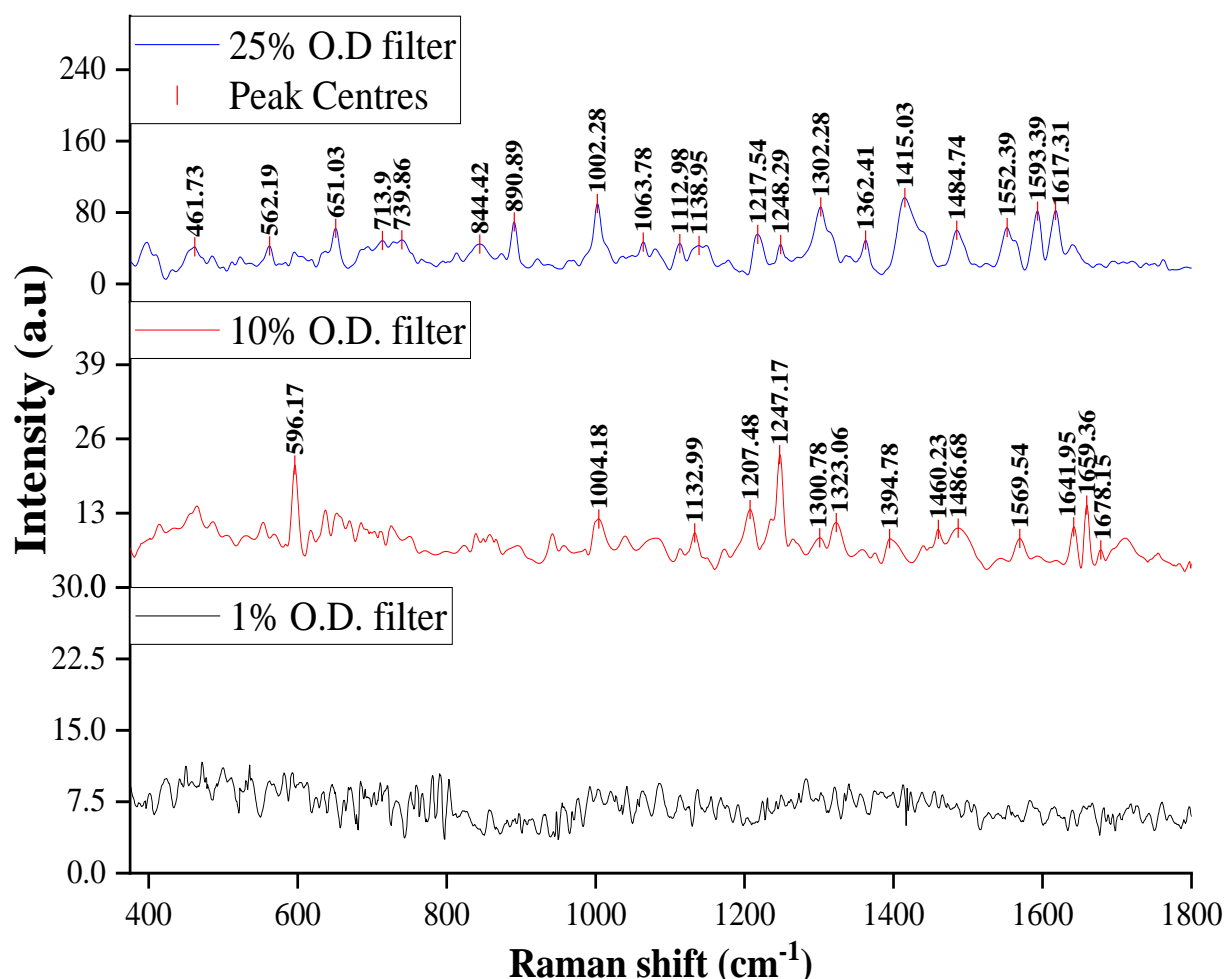
Figure 4.04: Three sample SERS spectra of SH-(c)-RGDFK peptide SAM within the Au micro array platform after 1.2 µM SH-(c)-RGDFK peptide solution incubation for 24 h (the Au micro array platform had been previously stamped with 10 mM mercaptohexane for 30 min prior to peptide solution incubation). SERS studies were carried out using varying laser powers; 1 % O.D. filter (bottom shown in black), 10 % O.D. filter (middle shown in red) and 25 % O.D. filter (top shown in blue), using a 785 nm laser source, full working power at 60.2 mW. Spectral acquisition was 1 s with 4 s exposure time and 9 frame accumulations. All spectra were baseline corrected and normalised using standard and de-spike settings to remove background noise

In Figure 4.04, the SERS spectrum using 1 % O.D. laser power appears to be mainly noise and the spectrum at 10 % is slightly better with 3 small vibrational peaks at 600 cm^{-1}, 1280 cm^{-1} and 1680 cm^{-1} respectively. The spectrum at 25 % O.D. laser power (See Figure 4.04, shown in blue) displays the signature F peak at ~1000 cm^{-1} [49] however, one of the limitations with SERS analysis is the noisy background that is produced by the LSPR[50,51]. The peak ratios have changed in some regions when compared to the (c)-RGDFK peptide powder spectrum shown in Figure 4.03 but this change may be due by the symmetry of the material and lateral packing as well the distance dependence influence of the plasmonic field change the relative intensities Surface stereochemical variations in orientation play a influencing role in SERS[52]. Studies have also shown that molecules close to but not in the plasmonic hotspot can also influence the peak ratios in SERS spectra[48]. That such high 25 % O.D. laser power was required to produce significant intensity in the SH-(c)-RGDFK SERS spectrum

allows for the subsequent, successful SERS spectral-accumulation of exosomes at a lower O.D. laser power without the need to account for or to subtract the SH-(c)-RGDFK background.
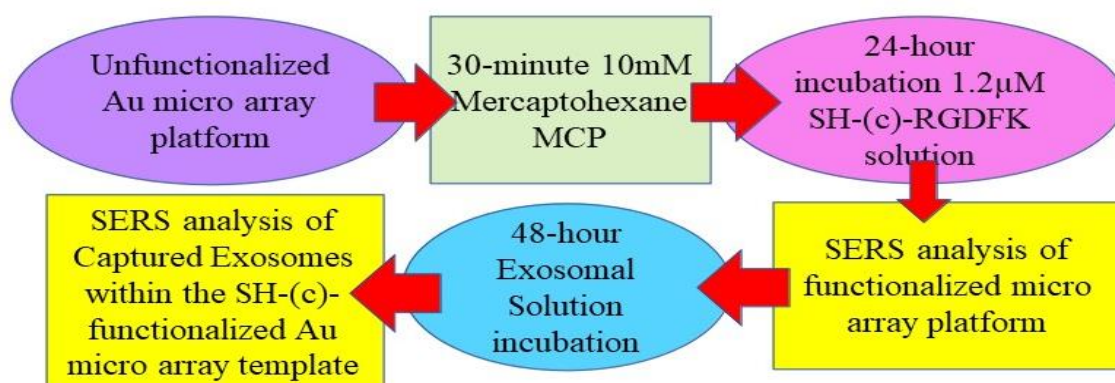
Figure 4.05: Schematic showing SERS analysis experimental workflow for a (c)-RGDFK Au micro array platform used in this study.

Raman spectra using a 1 % O.D. filter setting displayed a poor signal to noise ratio and poor Raman counts and these are not included here but in Appendix B. Next, in order to assess the increase in laser power (from 1 % to 10 % O.D. filter) to improve signal to noise ratio and Raman counts and also, to ensure the platform was kept completely wet at all times to prevent sample degradation, the following studies were carried out. It was also necessary to use this particular exosome type as three populations of these sub-types are studied in more detail in Chapter 5; These HuAECs are primary and not immortalized (making them less homogenous[53]); It is therefore more beneficial to optimise SERS conditions using these particular endothelial exosomes. Exosomes in general are heterogeneous and substantial variations exist depending on their histological source and overall health[5,6].
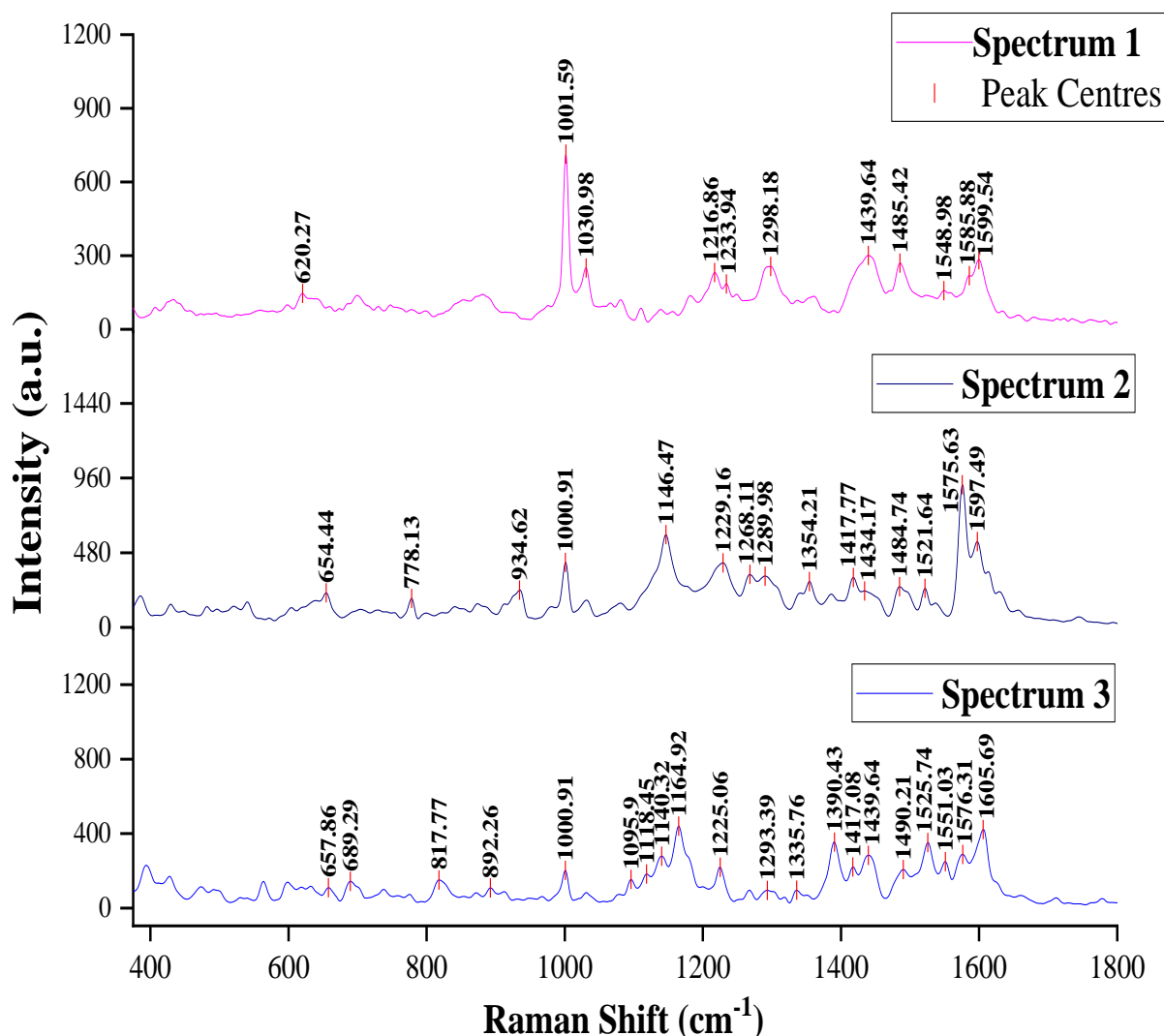
Figure 4.06: Three sample SERS spectra of exosomes sourced from HuAECs (NG) within a SH-(c)-RGDFK modified Au micro array platform. Prior to 24 h 1.2 µM SH-(c)-RGDFK peptide incubation the micro array platform had been previously stamped with 10 mM mercaptohexane for 30 min. 0.5 mL of exosome-solution was incubated in this platform for 48 h at 4 °C. SERS analysis was carried out using 10 % O.D. 785 nm laser at 60 mW full power. Spectral acquisition was 1 s with 4 s exposure time and 9 frame accumulations. All spectra were baseline corrected and normalised using standard and de-spike settings to remove background noise.

A SH-(c)-RGDFK functionalized Au micro array platform was sonicated in a 0.4 mL aliquot of PBS buffer. After 10 min sonication, 0.1 mL exosome solution was aliquoted directly into this 0.4 mL solution to allow easy-diffusion of the exosomes into the micro array pores. The prior removal of air-pockets ensured that exosomes were able to successfully bind to the bottom of the pores. This step also ensured that the exosomes remained intact as they were not sonicated in solution as direct sonication may cause exosome rupture. The Au micro array platform containing the exosome solution was then stored for 48 h at 4 °C (this ensured that the exosomes did not disintegrate as they are unstable at room temperature[54]). SERS analysis was carried out using 10 % O.D. filter on a 78 5nm laser source operating at 60.2 mW full power under the same parameters as previously described. Exosomes are from HuAECs (NG). Please see schematic of experimental workflow in

Figure 4.05 for clarification purposes. SERS analysis was then carried out as previously described with the sample completely submerged in deionised H_2O at all times to prevent degradation and the O.D. filter was changed from 1 % to 10 %.

The spectra in Figure 4.06 are much more complex than the SAM Raman, strongly suggestive of exosome capture. The distinctive F peak is seen at ~1000 cm^{-1} [49]. There is variation in signal intensity but as exosomes from the same cell source are heterogeneous by nature then this is to be expected[6]. Moreover, it is impossible to achieve uniform numbers of exosomes in each micro array pore so variations in exosome quantity per micro array pore may also contribute to the variation in Raman intensity. As previously determined SERS studies carried out (shown in Figure 4.04) the SH-(c)-RGDFK peptide creates a very weak SERS spectrum using a 10 % O.D. laser filter (used in these SERS exosome studies) therefore when using 10 % O.D. laser power the (c)-RGDFK will not cause any interference with the exosome SERS spectra, therefore SH-(c)-RGDFK-functionalization promotes extracellular vesicle capture giving high quality SERS spectra without significant spectral contribution to background.

4.3.1.4 EIS Studies on Exosomes captured within a SH-(c)-RGDFK functionalized Micro-Array Platform.

EIS is a useful method to measure the complex impedance of monolayer, which in turn reflects changes of resistance and capacitance to the gold electrode reflecting coverage and leakiness of the film. (Please refer to Chapter 1 Introduction for more detail on EIS) …

EIS was carried out to further confirm SAM formation and successful exosome capture within the micro array pores. The purpose of this EIS study was not to distinguish exosome type but merely to confirm successful exosome capture and an additional set of repeats can be seen in Appendix B.

Non-faradaic EIS measurements were carried out on an unfunctionalized Au micro array platform in 100 mM PBS buffer from 0.1 Hz–10 kHz frequency range with a 0.01 V applied potential. The SH-(c)-RGDFK micro array platform was fabricated and prepared for exosome capture as previously described in Figures 4.04 and 4.06. Exosomes are sourced from: (A) EA.hy926 shown in Figure 4.08A and, (B) Primary HuAECs (NG) shown in Figure 4.08B. All EIS studies were carried out within a three-electrode cell set up, Ag/AgCl reference electrode, platinum wire auxiliary electrode and the Au micro array platform as the working electrode. Please see Figure 4.07 for clarification of the experimental workflow.
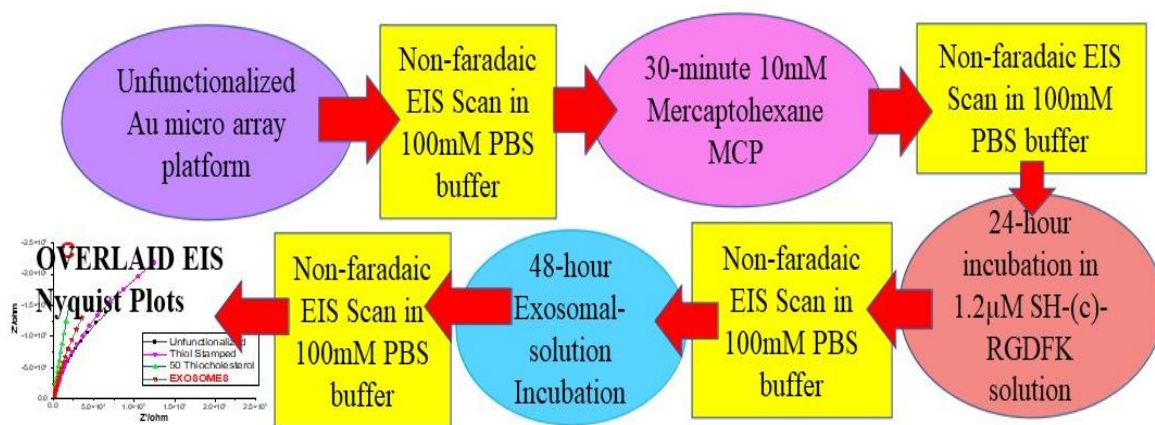
Figure 4.07: Schematic Summary of EIS Experimental workflow showing each stage where an EIS study is preformed; starting from unfunctionalized Au micro array platform study to final exosome capture assessment-study. Each stage where an EIS study is carried out is highlighted in the yellow rectangles.

The absence of a redox-label in a non-faradaic electrochemical system eliminates parameters associated with the electron transfer process of a faradaic system such as charge transfer resistance (R_{ct}) and Warberg impedance. The imaginary impedance (-Z_{imag}) is inversely proportional to the electrical double-layer capacitance[55–58]. Non-faradaic monolayer-peptide EIS studies were carried out by *Tanak et al* 2019[59] and the results outlined in this EIS study are presented and discussed in a similar manner to theirs.
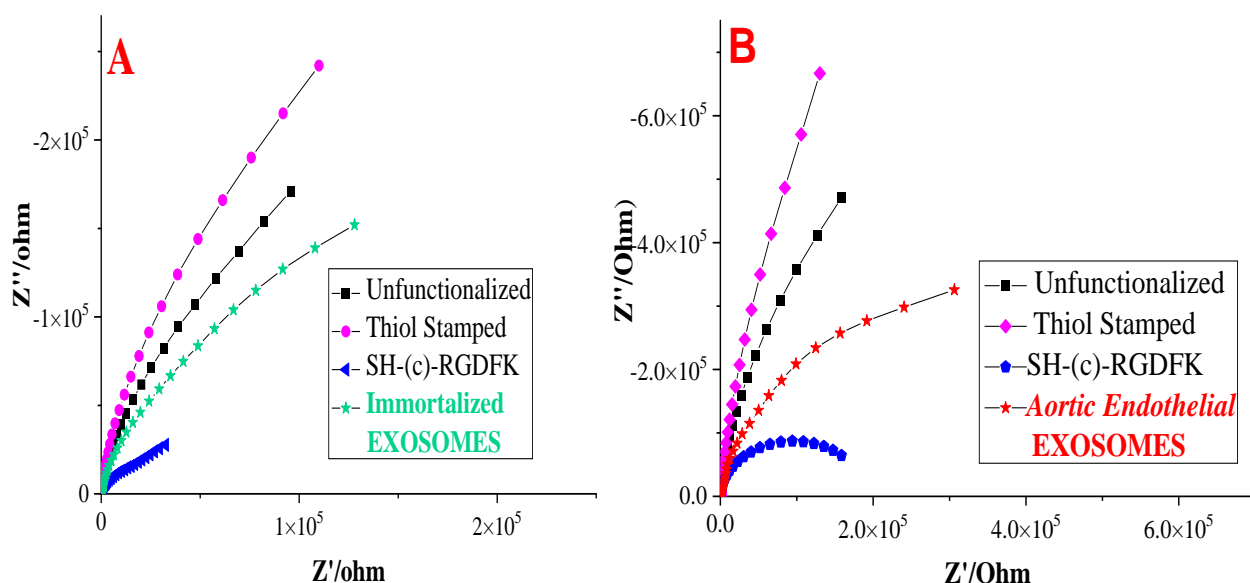
Figures 4.08A and B: Nyquist Impedance Plot(s) of an Au micro array platform(s). Non-faradaic EIS measurements were carried out on an unfunctionalized Au micro array platform in 100 mM PBS buffer from 0.1 Hz–10 kHz frequency range with a 0.01 V applied potential, following this the Au micro array platform was stamped with 10 mM mercaptohexane for 30 min. The Au micro array platforms were then incubated in 1.2 µM SH-(c)-RGDFK peptide solution for 24 h and EIS studies were carried out under the same conditions. This selectively modified platform was incubated in 0.5 mL of exosome-solution for 48 h at 4 ºC. The resulting EIS are shown in green stars in 9A and red stars in 9B. Exosomes are from: (A) Immortalized umbilical vein cells EAhy926. (B) HuAECs (NG). All EIS studies were carried out within a three-electrode cell set up, Ag/AgCl reference electrode, platinum wire auxiliary electrode and the Au micro array platform as the working electrode.

73

Results in Figure 4.08A show, that there was a significant increase in impedance of the Au electrode cell after mercaptohexane-stamping consistent Au-Thiol bond formation due to less available electroactive surface, as mercaptan compounds readily-form a SAM on an Au surface altering the Au electrode resistance. It is important to point out here that the impedance change is less than expected for a fully-packed electrode as the micro array interiors remain unmodified but solution-accessibility to the pores may be reduced by the hydrophobic top surface. As shown in Figure 4.08A there is an increase in the final $-Z_{imag}$ (on y-axis)[60,61] from 171 kΩ (the unfunctionalized Au platform) to 242 kΩ (30 min stamped Au platform) and their respective Z_{real} (on x-axis) points increase slightly from 95.6 kΩ to 110 kΩ also indicating in increase in electrode-impedance. The same trend can be observed in Figure 4.08B, i.e. an increase $-Z_{imag}$ from 471.6 kΩ (the unfunctionalized Au platform) to -666.9 kΩ (30 min mercaptohexane-stamped Au micro array platform). Also, their respective Z_{real} points decrease slightly from 159 kΩ to 130.2 kΩ however, the overall increase in $-Z_{imag}$ also indicates that impedance is increasing. The changes in $–Z_{imag}$ is useful to study how surface binding causes a change in properties of the EDL. Data described above confirms that MCP is chemisorbed and forms monolayers on the Au electrode surface. Similar EIS studies were carried out by *Sharma et al* 2016 using different mercaptan compounds demonstrated that there was an increase in imaginary-impedance on Au electrode(s) after thiol-functionalization and with a further proportional increase as the length of the alkyl chain is increased on the mercaptan compound[62], i.e. the longer aliphatic-chained mercaptans display higher $-Z_{imag}$ values than shorter aliphatic-chained mercaptans.

Following 24 h SH-(c)-RGDFK Au micro array functionalization in Figure 4.08A, interestingly, there was a decrease in both Z_{real} (from 95.6 kΩ to 32.6 kΩ) and $-Z_{imag}$ (from 171 kΩ to 27.7 kΩ). In Figure 4.08B, there was an increase in Z_{real} (from 159.6 kΩ to 185.6 kΩ) and a decrease in $-Z_{imag}$ (from 471.6 kΩ to 64.5 kΩ). Both of these results show an increase in contact-resistance after SH-(c)-RGDFK functionalization. This may be due to the hydrophilic nature of the SH-(c)-RGDFK peptide within the Au micro-array platform attracting the aqueous PBS buffer solution and increasing surface wettability and buffer filling of the pores. Charged-polar RGD species may be responsible for increased Au-surface wetting. Contact angle studies carried out by *Adamson et al* showed decreased contact angle measurements after SAM peptide monolayer formation thereby increasing surface-hydrophilicity[44]. EIS peptide-monolayer studies carried out on peptides by *Sanjeev et al* 2019[63] showed that there was a proportional decrease in $–Z_{imag}$ as the peptide concentration was increased. This increased concentration on the electrode may also have increased surface-wettability in their studies and it is likely that the polar nature of peptide species makes them behave differently to non-polar hydrocarbon structures in aqueous solutions.

Notably, after 48 h incubation in exosome solution, in both sets of EIS studies there is an increase in impedance which indicates successful extracellular vesicle capture. Exosome-binding within the Au micro array interiors is expected to cause increased resistance here, Z_{real} increases from 32.6 kΩ to 128 kΩ and from 185.6 kΩ to 306.2 kΩ and Z_{imag} from 27.7 kΩ to 152 kΩ and from 64.5 kΩ to 355.7

kΩ in both Figures 4.08A and B respectively and may indicate that impedance increases on a SH-(c)-RGDFK functionalized Au micro array platform after exosome capture.

EIS Studies carried out on exosomes by *Sun et al* 2020 shows the same trend, i.e. that imaginary-impedance increases after exosome-adsorption on the Au electrode, the study also showed that imaginary-impedance decreased after monolayer-peptide-functionalization[64]. EIS studies carried out using exosomal miRNA-21 carried out by *Cheng et al* 2020 showed that imaginary-impedance also increased on the electrode surface following this treatment step[65]. The imaginary-impedance increase in surface properties may be due to the RNA and other cargo carried within the exosome as exosomes carry various types of RNA and other types of cargo within their structures[6,7,12,66–70]. Exosome binding within the Au micro array interiors has clearly caused a change in conductivity properties of the Au working electrode. The Nyquist data shows roughly straight lines rising along the y vertical lines the y axis and this is a typical (non-faradaic) response of a case of SAM modified electrode in an inert electrolyte solution. It also reflects capacitor behaviour of the surface-electrode which is due to the Au metal surface acting as one capacitor-plate and the ionic interface at the SAM-electrolyte interface acting as the other capacitor-plate.

4.3.1.5 SERS Studies using Thiocholesterol-functionalization for Exosome capture.

The main drawback with SH-(c)-RGDFK functionalization is that it requires a synthetic step where (c)-RGDFK is treated with EDC Sulpho-NHS coupling reaction to conjugate the mercaptan-alkyl group to the primary amine group on the K residue to permit thiolation of the Au micro array interior environment. Furthermore, while exosomes are expected integrins present on their surface such as CD63[13,71] that will recognise and bind to any (c)-RGD sequence[34], it is possible that this choice of Au surface-functionalization may discriminate against a certain sub-population set that may not have integrin RGD ligand-binding capabilities. An alternative mercaptan-compound thiocholesterol was chosen to functionalize the Au micro array pore interiors and studied as a comparison.

After dissolving in THF, the thiocholesterol is immediately ready for use without any necessary further synthetic modification steps. The rationale behind this particular choice of compound is that previous studies carried out by *O'Connor et al* 2019[72] showed that BODPIY cholesterol probes proved effective labelling dyes for liposomes and were also suitable for cell imaging. Exosomes are also a type of cellular vesicle and share many similar features to liposomes and one feature they have in common is that they are contain a lipid bilayer exterior [68,70]. If cholesterol labelling probes can effectively intercalate to exosomes, then a thiocholesterol-SAM may prove to be a suitable alternative to the more expensive (c)-RGDFK peptide which also requires a coupling reaction step in film formation. Immediately after dissolving in THF, thiocholesterol can be directly applied to the Au micro array platform for thiolation and surface-functionalization. The capacity of cholesterol to bind to exosome is confirmed later, where BODIPY cholesterol probe is assessed as an exosome

labelling probe in the confocal microscopy sub-section at the end of this chapter. Raman spectral analysis of the pure thiocholesterol powder was attempted but it was not successful however SERS and EIS studies were carried out after functionalization of the Au micro array interiors.
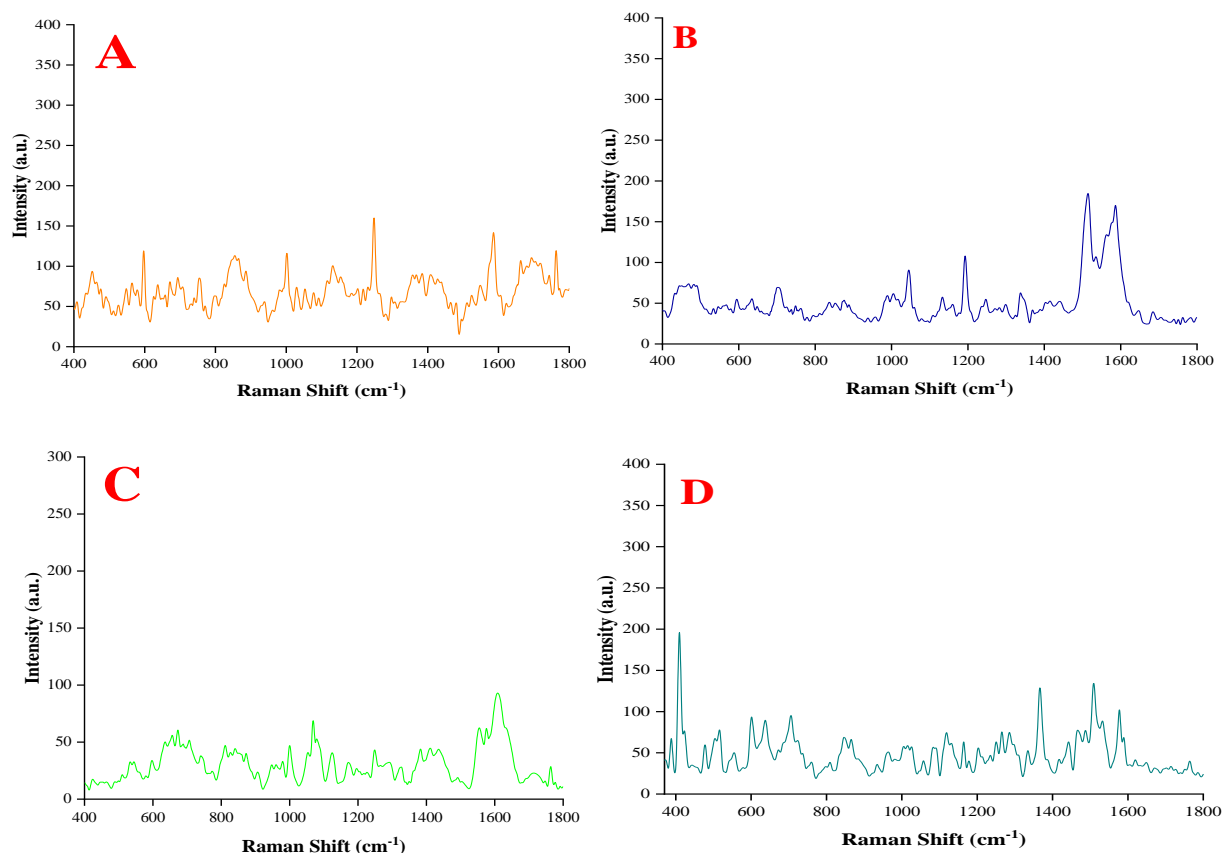
Figures 4.09A, B, C and D: SERS Spectra of (A) 1.25 µM Thiocholesterol, (B) 70/30, (C) 50/50, and (D) 30/70 1.25µM Thiocholesterol to 1.25µM functionalized Au Micro Array platforms. All platforms were incubated in 1.25µM thiocholesterol/ thiocholesterol-mercaptohexanol solution for 24 h. SERS analysis data was collected at 10 % O.D. filter on a 785 nm laser Power source, full working power of 60.2 mW. Spectral acquisition was 1 s with 4 s exposure time and 9 frame accumulations. All spectra were baseline corrected and normalised using standard and de-spike settings to remove background noise.

Four Au micro array platforms were stamped with 10 mM mercaptohexane and then incubated respectively in 1.25 µM thiocholesterol, 70/30, 50/50 and 30/70 ratio mixtures 1.25 µM thiocholesterol to 1.25 µM mercaptohexanol solution for 24 h. SERS studies were carried on these thiocholesterol/thiocholesterol-mercaptohexanol functionalized micro-array pores before assessment of exosome capture. Results are shown in Figures 4.09A-D. Please see simplified schematic set-up in Figure 4.10 for clarification purposes
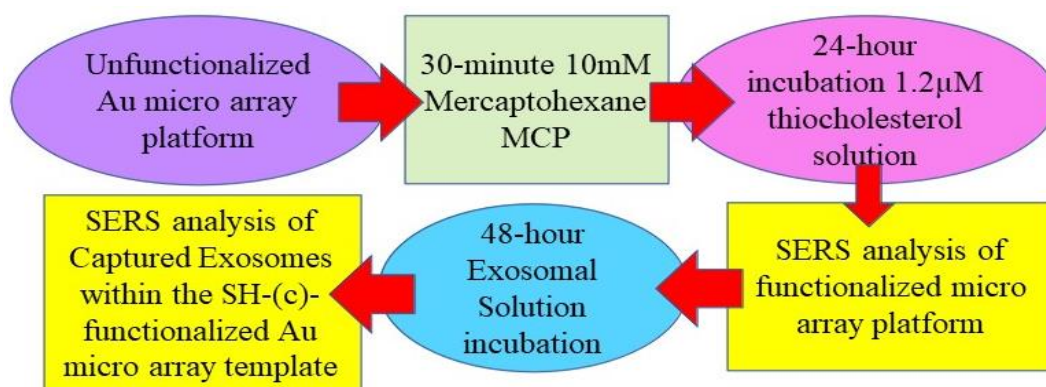
Figure 4.10: Schematic showing SERS analysis experimental set-up within a thiocholesterol functionalized Au micro array platform used in this study.

Figures 4.09A-D display the best thiocholesterol spectra obtained. The distinctive steroid-ring stretch (between 700 cm^{-1}-1050 cm^{-1})[73] are much more prominent in Figures 4.09B and C than in Figures 4.09A and D. It is most likely that the thiocholesterol formed a tightly-packed monolayer (in Figure 4.09A) repelling the H$_2$O and preventing it from coming into direct contact with the plasmonic Au surface which may also have contributed to the low Raman count. The slight improvement in Raman count in Figures 4.09B and C may be due to the presence of the OH group on the mercaptohexanol. The hydrophobic SH group covalently binds to the Au Substrate leaving the OH group facing outwards and its polar charge creates an electric dipole moment charge between the H$_2$O molecules[74]. The spectrum shown in Figure 4.10D is similar to that shown in Figure 4.10A.

The thiocholesterol functionalized Au micro array platforms were prepared for exosome capture in the same manner as previously outlined in Figure 4.06.

In Figure 4.11A below, Resulting SERS spectra all have similar peaks at 600 cm^{-1}, 1000 cm^{-1}, 1250 cm^{-1} and 1770 cm^{-1} respectively however, the rest of the spectra are quite poor. The metallic-background noise is apparent in all three exosome-spectra and overall SERS intensity is quite low. This further suggests that the hydrophobicity of the micro-array interior is preventing the H$_2$O from coming into direct contact with the plasmonic field thereby making sufficient SERS signal detection an issue. It is also possible that thiocholesterol is too large a molecule suitable for surface-functionalization for biocapture. The site of conjugation with extracellular vesicles may be located too far from the LSPR. It may also pack too tightly to the surface of the Au platform and completely-shield the plasmonic-field.

In Figure 4.11B, the resulting spectra are quite complex but all three spectra shown display peaks at around 700 cm^{-1} and 1100 cm^{-1} which is indicative of a steroid ring stretch[73]. There are more peaks between 1000-1400 cm^{-1} on Spectrum 3B which may indicate the presence of fatty acids[73,75], phospholipids[76], and amide III[75]when compared to the three spectra shown in Figure 4.11A.
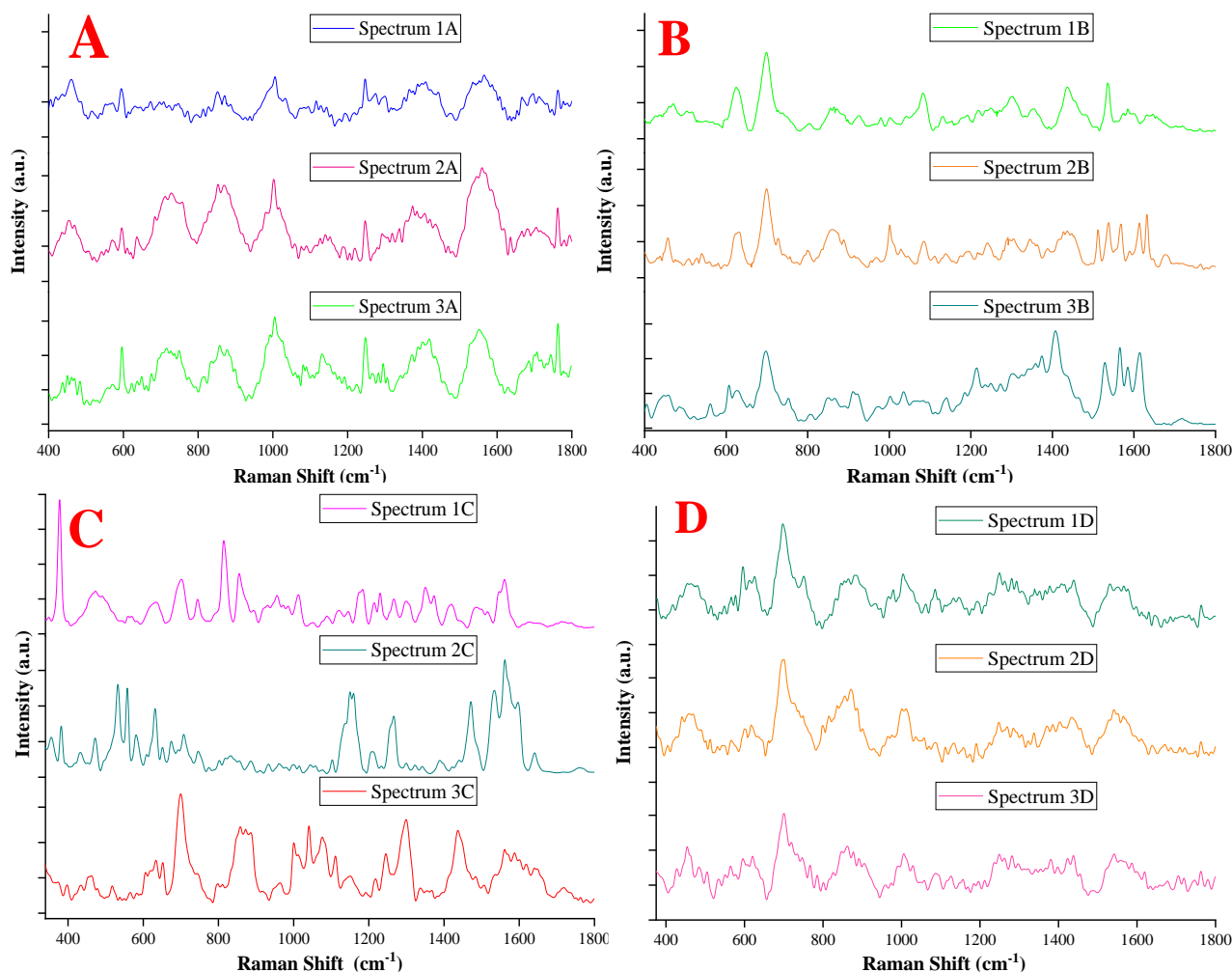
Figures 4.11A-D: SERS spectrograms, each containing 3 representative SERS spectra of exosomes captured within array platforms functionalized with deposition-solutions containing respectively; (A) 1.25 µM thiocholesterol, (B) 70/30, (C) 50/50 and (D) 30/70 ratio mixtures of 1.25 µM thiocholesterol to 1.25 µM mercaptohexanol. Exosomes are from primary HuAECs, All SERS analysis was carried out using a 10% O.D. Filter on a 785 nm laser power source, full power at 60.2 mW. Spectral acquisition was 1 s with 4 s exposure time and 9 frame accumulations. All spectra were baseline corrected and normalised using standard and de-spike settings to remove background noise.

In Figure 4.11C after exosome incubation there is a variation in SERS spectra which indicates heterogeneity. This heterogeneous property is a distinct exosome characteristic and has been published across various studies and disciplines, such as DLS and others[6,77].On Spectrum 1C , the main identifiable peaks are: 816 cm^{-1} indicative of the PO$_2^-$ stretch of nucleic acids[78], 1008 cm^{-1} indicates the presence of F[79] and/or a polysaccharide ring[78] and the presence of W is indicated by the characteristic peak at 1560 cm^{-1} [80]. On Spectrum 2C, the main identifiable peaks are: 548 cm^{-1} which is a cholesterol peak[81], 624 cm^{-1} which indicates C-C twisting of F[82–84], 705 cm^{-1} is a C-S stretch indicating the presence of M[85] , C-N protein stretch is indicated by the presence of the peak at 1157 cm^{-1} [86], C=N stretching is indicated by the peak at 1471 cm^{-1} [79], the presence of W is indicated by the peak at 1560 cm^{-1} [80] and the 1600 cm^{-1} peak indicates the presence of an Amide I protein vibration [86–88]. On Spectrum 3C, the main identifiable peaks are: 705 cm^{-1} is the C-S stretch of M[85] , 1003cm^{-1} is the distinctive peak of F [49,79] 1043 cm^{-1} indicates the presence of P found in collagen[89], 1243 cm^{-}

^{1} indicates the presence of Amide III[84,87], 1294 cm^{-1} indicates a methylene twist[90]. It is clear from these identifiable peaks that some exosome-adsorption took place within the micro-array pores. In Figure 4.11D, Spectra 1D-3D resemble spectra illustrated in A and B, it is likely that exosome capture here was quite poor and may have not occurred.

As exosomes are suspended in aqueous PBS solution, the hydrophobic environment may be too strong and repel the PBS solution and prevent the extracellular vesicles from coming into close enough contact with the Au surface in order to promote conjugation. The thiocholesterol may also bind to a sub population of exosomes that are less Raman active. Overall, there may also be less exosome-cholesterol binding than exosomes with SH-(c)-RGDFK as (c)-RGD structures on fibronectin have been shown to bind to exosomal-surface integrins[33,34].

4.3.1.6 EIS Studies of Thiocholesterol Modified Au Micro Array Platforms

To further assess exosome capture using thiocholesterol and thiocholesterol/mercaptohexanol-functionalized Au micro array platforms, non-faradaic EIS studies were carried out after each stage of the selective-modification process from unfunctionalized, mercaptohexane-stamped, thiocholesterol/thiocholesterol-mercaptohexanol micro array interior-functionalization and subsequent exosome capture.

In Figures 4.12A-D, non-faradaic EIS measurements were carried out as previously described for Figure 4.08. Following this, the Au micro array platform was stamped with 10 mM mercaptohexane for 30 min. The micro array platforms were incubated in: (A) 1.25 µM thiocholesterol, (B)-(D) ratio mixtures of 70 1.25 µM thiocholesterol: 30 1.25 µM mercaptohexanol, 50 1.25 µM thiocholesterol: 50 1.25 µM mercaptohexanol and 30 1.25 µM thiocholesterol: 70 1.25 µM mercaptohexanol respectively for 24 h. The Au micro array platforms were prepared for exosome capture in the same way at outlined in Figure 4.06. Please see Schematic of experimental set-up shown in Figure 4.14 for clarification purposes.
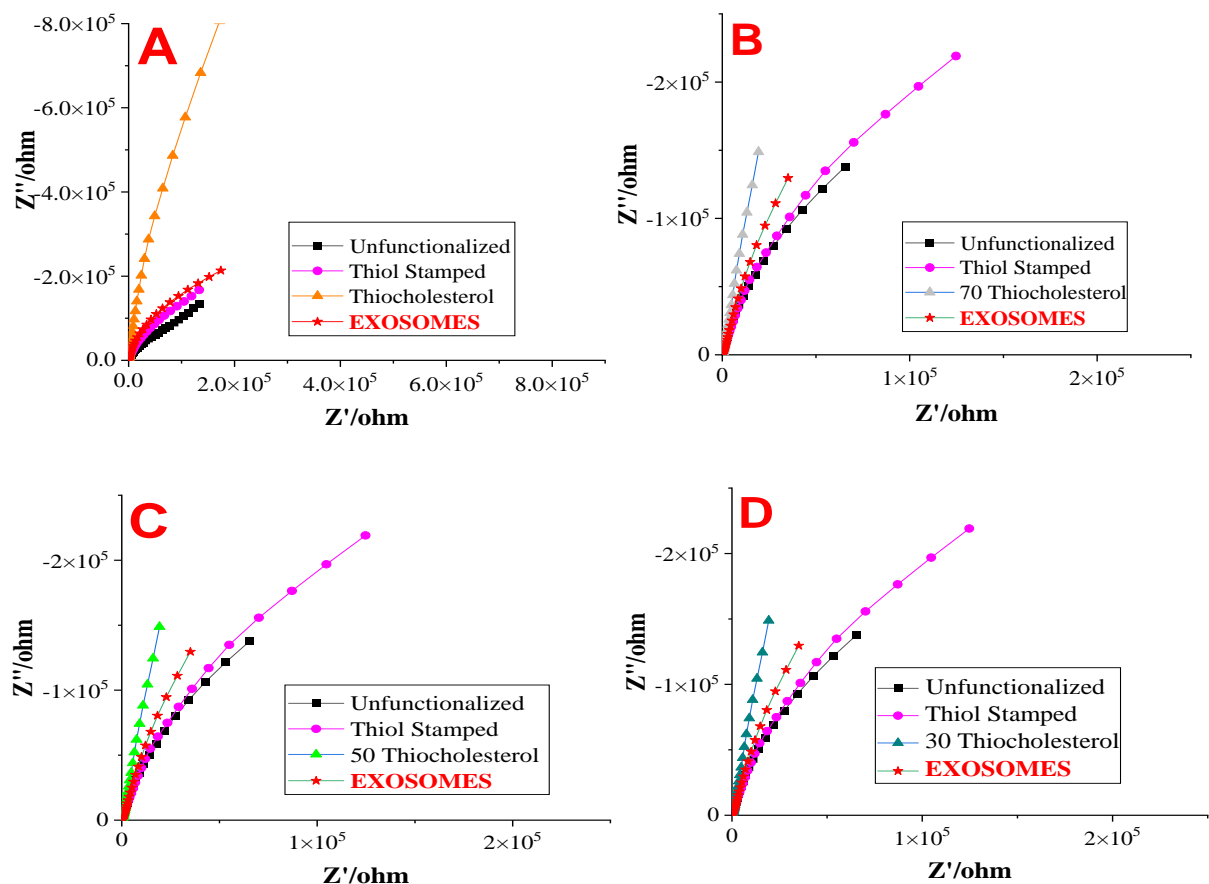
Figures 4.13A-D: Nyquist Impedance Plot(s) of Au micro array platform(s). Non-faradaic EIS measurements were carried out on unfunctionalized Au micro array platform(s) in 100 mM PBS buffer from 0.1 Hz–10 kHz frequency range with a 0.01 V applied potential, following this the Au micro array platform was stamped with 10 mM mercaptohexane for 30 min. The Au micro array platforms were incubated in: (A) 1.25 μM thiocholesterol, and ratio mixtures of 70/30, 50/50, and 30/70 1.25 μM thiocholesterol to 1.25 μM mercaptohexanol in (B), (C) and (D) respectively. These selectively modified platforms were then incubated in 0.5 mL of exosome-solution for 48 h at 4 ºC. Successful exosome capture shown in red stars. All EIS studies were carried out within a three-electrode cell, with Ag/AgCl reference electrode, platinum wire auxiliary electrode and the Au micro array platform as the working electrode. Exosomes are from HuAECs (NG).

The absence of a redox-label in a non-faradaic electrochemical system eliminates the main parameters associated with the electron transfer process of a faradaic system such as charge transfer resistance (R_{ct}) and Warberg impedance by becoming infinite, therefore in this non-faradaic electrochemical system the imaginary impedance ($-Z_{imag}$) is inversely proportional to the electrical double-layer capacitance[55–58]. Non-faradaic protein-monolayer EIS studies were carried out by *Tanak et al* 2019[59] and the results outlined in this section are presented and discussed in a similar manner as theirs.

In Figures 4.13A-D, following the thiocholesterol incubation-step there was a substantial increase in imaginary-impedance indicated by the sharp increase in in final $-Z_{imag}$ value from 167.4 kΩ (mercaptohexane-stamped) to 2348 kΩ (thiocholesterol SAM formation) this change is an order of magnitude higher when compared to both unfunctionalized ($-Z_{imag}$ 134 kΩ) and mercaptohexane-stamped results, most likely due to the tight-packing of the cholesterol-monolayer on the Au micro array surface interior. After 48 h exosome-solution incubation, Z_{real} decreased to 174.2 kΩ and $-Z_{imag}$ decreased to 213.4 kΩ (one order magnitude of a decrease) which indicates a substantial decrease in

imaginary-impedance as there is a significant change in Au surface-physicochemical properties due to the deposition of the exosomes and their cargo. Cholesterol has a neutral charge[91] and the peptides and other cargo have charges as they are polar.
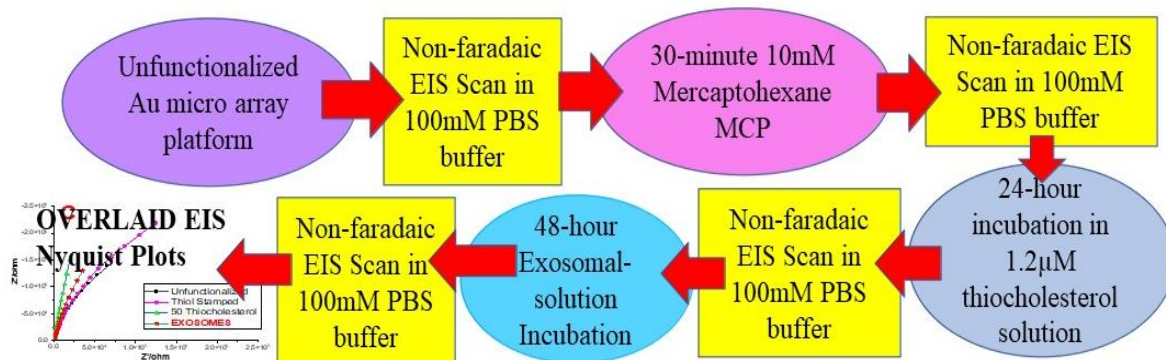

Figure 4.14: Schematic Summary of EIS Experimental workflow for clarification purposes showing each stage where an EIS study is preformed; starting from unfunctionalized Au micro array platform study to final exosome capture assessment-study. Each stage where an EIS study is carried out is highlighted in the yellow rectangles

For the 48 h incubation step, exosomes are suspended in aqueous PBS buffer solution and the optical medium used for SERS studies is deionised H_2O. The thiocholesterol SAM significantly altered the interior micro array environment by making causing an increase in impedance. It was therefore necessary to attempt to optimise its surface chemistry by making it less hydrophobic and to observe if there was an improvement in exosome capture as evidenced by increased SERS signal intensity. This was attempted by varying the ratios of thiocholesterol and mercaptohexanol in the deposition solution. 1.25 µM thiocholesterol and 1.25 µM mercaptohexanol, 70 thiocholesterol: 30 mercaptohexanol, 50 thiocholesterol: 50 mercaptohexanol and 30 thiocholesterol: 70 mercaptohexanol respectively, were applied and the impact on EIS are shown in Figures 16b-d. Mercaptohexanol has a thiol group on one end terminus which will covalently bond to the Au surface[61] and an OH functional group end terminus which is more polar, it will readily hydrogen-bond with itself and other molecules such as H_2O[74]. This hydrophilic functional group is expected to orientate facing outwards making the micro array interior environment less hydrophobic. The less hydrophobic environment should allow for greater wettability of the Au micro-array platform, promote exosome capture and may improve SERS spectra.

The data in Figures 4.13B-D show that after 10 mM mercaptohexane-stamping there was an increase in Z_{real} values. This value increased from 65.6 kΩ to 123.2 kΩ, from 65.5 kΩ to 123.6 kΩ, and from 65.2 kΩ to 123.3 kΩ in Figures 16B, C and D respectively. Their respective -Z_{imag} values all increased from 137.8 kΩ to 219.4 kΩ, 137.6 kΩ to 219.2 kΩ, and 137.8 kΩ to 219.1 kΩ).This trend shows that there was an increase in imaginary-impedance after MCP which indicates successful Au-Thiol bond formation and a characteristic of successful chemisorption and SAM formation on the electrode

surface ; It is similar to alkane-thiol studies carried out by *Campuzano et al* 2005[92] and *Sharma et al* 2016[62].

 Following 24 h 1.25 µM thiocholesterol-mercaptohexanol incubation, their respective Z_{real} values decreased to 19.5 kΩ, 19.45 kΩ, and 19.38 kΩ, and respective $-Z_{imag}$ increased to 146.7 kΩ, 147.1 kΩ and 147.3 kΩ indicating that there was a further increase in impedance. Cholesterol has a neutral charge and is hydrophobic and extensive EIS studies carried out on cholesterol membranes by *Alobeedallah et al* 2018 showed that thick cholesterol-layers on an Au electrode display high levels of impedance[91] which may be due to the tight-packing of the thiocholesterol.

It is interesting to note that there is substantially lower imaginary-impedance (over one order in magnitude less) in Figures 4.13B-D than in Figure 4.13A which indicates than the micro array environment in A is much more resistant. Also the data shown in Figures 4.13B, C and D. are quite similar, even though the ratios of thiocholesterol to mercaptohexanol vary. This trend is similar to alkane-thiol studies carried out by *Campuzano et al* 2005[92] and *Sharma et al* 2016[62] which showed an increase in imaginary-impedance after thiol-surface functionalization with a proportional increase in imaginary-impedance value as the alkyl chain length was increase. Following 24 h 1.25 µM thiocholesterol-mercaptohexanol incubation, Z_{real} decreased to 19.3 kΩ and $-Z_{imag}$ decreased to 148 kΩ. The Nyquist data shows roughly straight lines rising along the y vertical lines the y-axis and this is a typical (non-faradaic) response of a case of SAM modified electrode in an inert electrolyte solution, and reflects capacitor behaviour of the surface-electrode. This is due to the Au metal surface acting as one capacitor plate and the ionic interface at the SAM-electrolyte interface acting as the other capacitor plate.

Ratio mixtures of mercaptan compounds in deposition-solution do not always result in the same ratio of SAM formation on the Au electrode-surface. Grazing incidence IR spectroscopic studies carried out by *Nuzzo et al* 1990[93] demonstrates that substituted mercaptan compounds only form densely close-packed high-ordered SAM structures when the terminal functional group (such as NH_2, OH) is relatively small (< 5 Å), IR and electrochemical studies carried out demonstrated that the orientation of the monolayer is not influenced, however more bulky terminal functional groups (such as COOH, ferrocene) will decrease the density and the order of SAM formation and also, chemisorption of longer chained alkyl thiols than shorter is preferred on an Au substrate [63,94–96]. As thiocholesterol is not an alkyl-chained thiol, rather it contains 4 cycloalkanes within its molecular-structure, one of which is where the thiol group is attached and not on the terminus of its alkyl branch which makes it structurally quite bulky when compared to the much shorter and smaller alkyl chained mercaptohexanol. Therefore, the use of molar ratio mixtures of thiocholesterol with another alkyl-mercaptoalcohol will not guarantee the same proportional molar deposition and that chemisorption of thiocholesterol will remain almost constant regardless of the molar concentration in solution. It explains why the results in Figures 16B-D are almost identical. Therefore, the required ratio molar

deposition of thiocholesterol and alkyl-mercaptoalcohol is not guaranteed as both molecules are so different structurally and size-wise making phase separation more likely.

After 48 h exosome-solution incubation, their respective Z_{real} values increased to 35.13 kΩ, 35.28 kΩ, and 35.3 kΩ, and respective -Z_{imag} decreased to 129.4 kΩ, 129.57 kΩ and 129.6 kΩ which indicates a decrease in impedance due to a significant change in Au surface-physicochemical properties caused by surface-deposition of the exosomes and their cargo. Cholesterol has a neutral charge[91] and the peptides and other cargo are not neutral as they are polar. No published data could be found using an Au electrode with a cholesterol-monolayer functionalized surface for exosome capture but published data clearly shows an increase in impedance after exosome capture when compared to unfunctionalized, alkanethiol and peptide-functionalized electrodes[62,64,65,92,96,97].

4.3.1.7 Exosome Capture Study on an Unfunctionalized Au Micro Array Platform

In order to assess if exosome binding had taken place without selective surface modification of the Au micro array interiors, an unfunctionalized Au micro array platform was incubated with exosome solution; An important control-study to assess if any non-selective exosome binding will take place within the micro array pores further confirming the successful selective surface modification process in both this and in the previous experimental chapter. Moreover, it further confirms that functionalization of Au substrates is necessary for effective SERS studies to promote surface adsorption which is the location of LSPR[98].
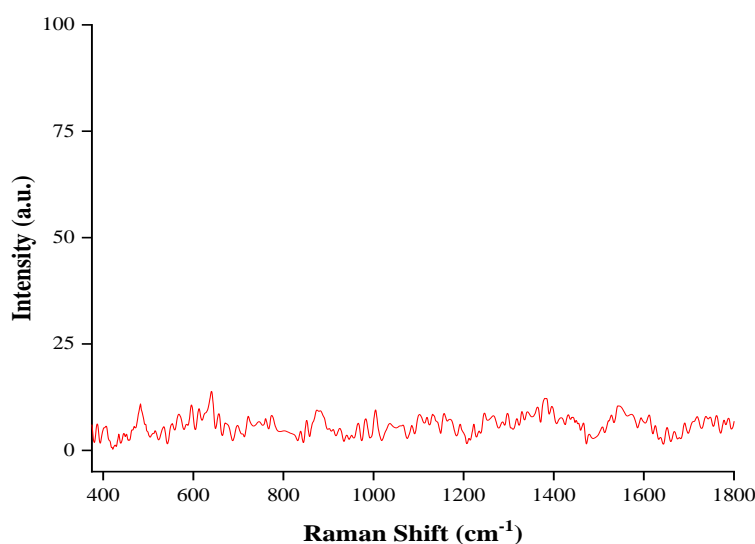
Figure 4.15: Sample SERS spectrum of exosomes from EA.hy926 cells incubated within an unfunctionalized Au micro array platform to assess if any non-selective binding takes place within the micro array interiors. SERS analysis was carried out using 10 % O.D. filter on a 785 nm laser power source, full working power of 60.2 mW.

Refer to Figure 4.02 for the preparation of the unfunctionalized Au micro array platform and to Figure 4.06 for preparation of exosome capture. It is evident from Figure 4.15 that that no exosome

capture occurred within the unfunctionalized micro array interiors. It further demonstrates the requirement of functionalizing the micro array interiors, the location of the LSPR[98], with either SH-(c)-RGDFK and/or thiocholesterol to ensure effective exosome capture. Figure 4.15 is very similar to Figure 4.02B shown previously.

4.3.2 Confocal Fluorescence Microscopy

The rationale for the following set of experiments is to visually assess selective surface modification using (c)-RGDFK within the Au micro-array platform interior by using of fluorophore-labelled $\alpha_5\beta_1$ integrin, this integrin specifically recognises and binds to a (c)-RGD sequence[33,34] and then to study exosome capture within the Au micro array interior environment by using BODIPY-cholesterol labelled exosomes for fluorescence detection and confocal imaging.

In CFM, the sample is first labelled with a flourophore-probe with a known specific excitation wavelength ($\lambda_{excitation}$) and emission wavelength ($\lambda_{emssion}$) range and these settings are programmed into the CFM software[99]. The high-intensity laser beam at $\lambda_{excitation}$ is directed to the flourochrome-labelled sample using a dichroic mirror. The photons hit the sample inducing fluorescence, and the emitted fluorescence ($\lambda_{emssion}$) from the flourochrome-labelled sample travels directly through the dichroic mirror to the confocal pinhole to the photomultiplier detector. The confocal pinhole aperture omits all the out-of-focus radiation from the upper and lower plane of the focus. It only allows radiation through that comes directly through the focal plane. Now multiple images from the different focal planes are collected by the computer software, and finally the three-dimensional image is constructed[100,101].

Figure 4.16: Schematic showing experimental set-up using $\alpha_5\beta_1$ incubation for confocal fluorescence microscopic studies as further confirmation of successful SH-(c)-RGDFK functionalization.

Refer to Figure 4.03 for the preparation of the Au micro array platform. This unfunctionalized micro array platform was then incubated in 1 mL aqueous solution containing 0. 4 ng/mL labelled $\alpha_5\beta_1$ integrin for 24 h in a refrigerator at 4 °C before CFM imaging studies were carried out with 0.1 % laser power using a 100 X oil immersion objective lens, $\lambda_{excitation}$ was 477 nm and $\lambda_{emission}$ was 577-677 nm. Time delay (of 0.3-1.8 s) was used to exclude scatter from the Au surface. Results shown in Figures 4.17A, B and C. Refer to Figure 4.16 (above) for clarity of the experimental set-up.
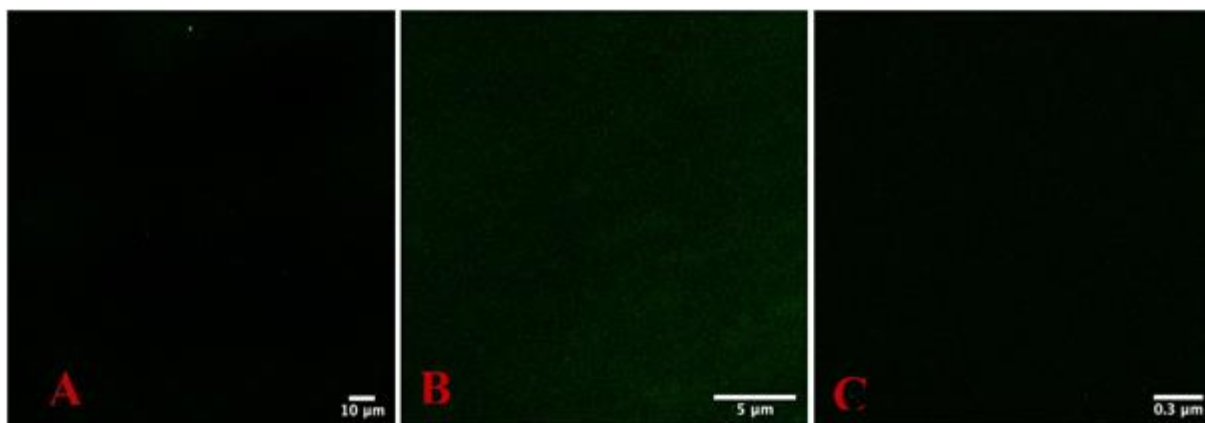
Figures 4.17A-C: Confocal fluorescence images under various magnifications of an unfunctionalized Au micro array platform incubated with labelled $\alpha_5\beta_1$ integrin. The unfunctionalized Au micro array platform was sonicated in 1 mL deionised H_2O for 10 min to ensure thorough-removal of air-pockets at the bottom of the Au micro array pores. The Au micro array platform was then incubated in 1 mL aqueous solution containing 0. 4 ng/mL labelled $\alpha_5\beta_1$ integrin for 24 h in a refrigerator at 4 ºC before CFM imaging studies were carried out. Time delay (of 0.3-1.8 s) was used to exclude scatter from the Au surface. All confocal imaging was carried out using 0.1 % Laser power. $\lambda_{excitation}$ was 477 nm and $\lambda_{emission}$ was 577-677 nm.

It can be seen in Figures 4.17A-C that labelled $\alpha_5\beta_1$ integrin did not bind to any significant degree to the unfunctionalized Au micro array interiors as no fluorescence can be observed in the images above. There is some background noise in Figure 4.17B but no evidence of fluorescence.

Next, in order to confirm if labelled-$\alpha_5\beta_1$ integrin will non-selectively-conjugate to any other compound and to further confirm its specific-binding to a (c)-RGDFK peptide sequence the following studies were carried out.

An Au micro array platform was stamped with 10 mM mercaptohexane for 30 min and the micro array platform was incubated in 1.2 µM mercaptohexanol alcoholic solution for 24 h. After selective surface modification, the completely-functionalized Au micro array platform was sonicated in 1 mL deionised H_2O for 10 min. The Au micro array platform was then incubated for 24 h in 1 mL aqueous solution containing 0. 4 ng/mL labelled $\alpha_5\beta_1$ integrin in a refrigerator at 4 ºC before CFM imaging studies were carried out. All confocal imaging was carried out using 0.1 % laser power. $\lambda_{excitation}$ was 477 nm and $\lambda_{emission}$ was 577-677 nm. Time delay (of 0.3-1.8 seconds) was used to exclude scatter from the Au surface. Results are shown in Figures 4.18A, B and C.
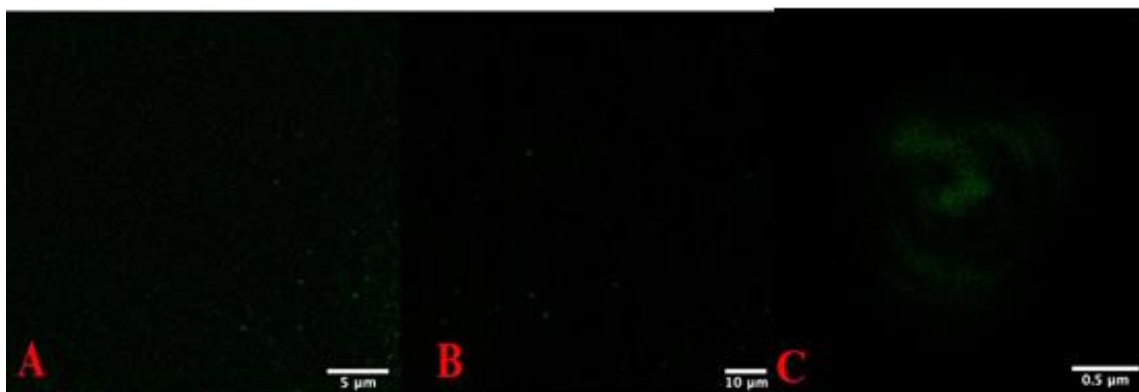
Figures 4.18A, B, and C: CF images under various magnifications of a functionalized Au micro array platform. An Au micro array platform was stamped with 10 mM mercaptohexane for 30 min. The micro array substrate was then incubated in 1 mM mercaptohexanol alcoholic solution for 24 h. After selective surface modification, the functionalized Au micro array platform was sonicated in 1 mL deionised H_2O for 10 min. The Au micro array platform was then incubated for 24 h in 1 mL aqueous solution containing 0. 4 ng/mL labelled $\alpha_5\beta_1$ integrin in a refrigerator at 4 ºC before CFM imaging studies were carried out. All confocal imaging was carried using 0.1% laser power, $\lambda_{excitation}$ was 477 nm and $\lambda_{emission}$ was 577-677 nm and. Time delay (of 0.3-1.8 s) was used to exclude scatter from the Au surface.

In Figures 4.18A-C, slight areas of fluorescence can be observed within the micro array structures. This may be due to weak hydrogen-bonding between the $\alpha_5\beta_1$ integrin and the outward-facing OH group on the mercaptohexanol however the fluorescence signal is not uniform throughout the whole array platform so non-selective $\alpha_5\beta_1$-mercaptohexanol conjugation did not occur in this case.

Refer to Figure 4.04 for the SH-(c)-RGDFK functionalization-steps of the Au micro array platform. The Au micro array platform was then incubated in labelled $\alpha_5\beta_1$ integrin solution as described above. All confocal imaging was carried out using 0.1 % laser power. $\lambda_{excitation}$ was 477 nm and $\lambda_{emission}$ was 577-677 nm. Time delay (of 0.3-1.8 s) was used to exclude scatter from the Au surface. Results are shown in Figures 4.19A-C.

In Figures 4.19A-C (below) distinct fluorescent hexagonal-closed packed patterns can be observed in the images indicating that SH-(c)-RGDFK functionalization is present only within the micro-array interior(s) and furthermore that the $\alpha_5\beta_1$ integrin recognised and associated with SH-(c)-RGDFK SAM. The 1-micron micro-arrays are much larger than the scale shown in the image; The brightness at the cavity bottom is greatest- this is due to both metal enhanced flourescence and the reflectance/focusing effects of the cavity structure wells in the micro-arrays. This location is where the LSPR is expected to be strongest producing a clear Surfaced Enhanced Fluorescence signal. This finding is in excellent agreement with other published literature on fluorescence from micro arrays[99]
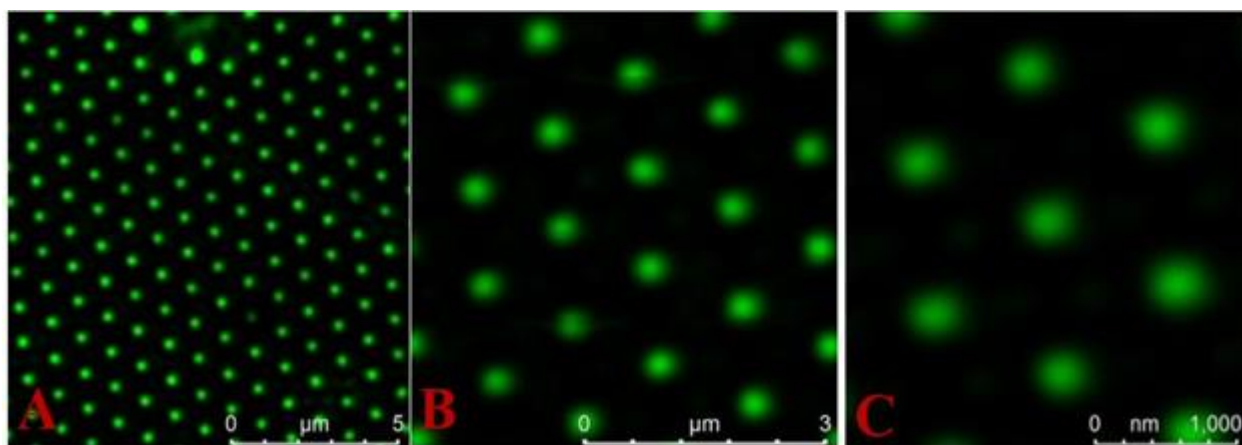
Figures 4.19A-C: CFM images under various magnifications of a SH-(c)-RGDFK functionalized Au micro array platform after incubation with labelled $\alpha_5\beta_1$ integrin. After selective-surface modification, the Au micro array platform was then incubated for 24 h in 1 mL aqueous solution containing 0. 4 ng/mL labelled $\alpha_5\beta_1$ integrin in a refrigerator at 4 ºC before CFM studies were carried out. All confocal imaging was carried out using 0.1 % laser power. $\lambda_{excitation}$ was 477 nm and $\lambda_{emission}$ was 577-677 nm. Time delay (of 0.3-1.8 s) was used to exclude scatter from the Au surface.

These results further confirm that mercaptohexane-stamping has functionalized the array pore exteriors limiting SH-(c)-RGDFK modification only to the micro array interior environment. These results also further confirm that the MCP technique as a suitable alternative to the traditional incubation soaking method for selective surface modification as no fluorescence can be seen outside of the array pores.

Flow cytometry and nanoparticle track analysis are some of the main techniques used in exosome study and characterization these techniques involve the use of fluorescent-probes[77]. Liposomes were labelled and imaged *in vitro* by *O'Connor et al* 2018[72] and as liposomes and exosomes share many similar characteristics, e.g. both vesicles contain a lipid-bilayer exterior [70,102]. The rationale for the next series of CFM imaging studies was to use this liposome-labelling probe and apply it to assess if exosome labelling could also be achieved and subsequently imaged within the functionalized Au micro array platform.

In Figure 4.20 below, 25 µL of 5 µM of BODIPY Cholesterol was aliquoted into exosome (PBS) solution and incubated in a refrigerator at 4 ºC for 6 h to prevent their degradation[54,103]. 250 µL of the BODIPY cholesterol-stained exosomal solution was aliquoted onto a glass-slide and a cover-slip was placed on top before any CFM-imaging studies were carried out, see schematic (Part 1) in Figure 4.21 (below) for clarification purposes. $\lambda_{excitation}$ was 497 nm and $\lambda_{emission}$ was 520-620 nm with 0.1 % laser Power.
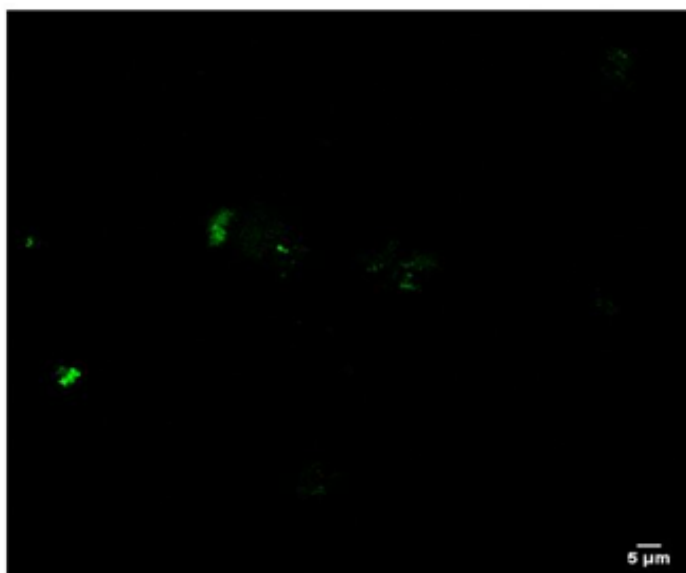
Figure 4.20 CFM image of BODIPY cholesterol-stained exosomes. Exosomes were sourced from Immortalized Umbilical Vein Cells EA.hy926. 25 µL of 5 µM of BODIPY Cholesterol was aliquoted into the exosome solution and incubated in a refrigerator at 4 ºC for 6 h to prevent their degradation[54,103]. 250 µL of stained exosome solution was aliquoted onto a glass-slide and a cover-slip was placed on top before carrying out any CFM imaging studies. CFM imaging was carried. $\lambda_{excitation}$ was 497nm and $\lambda_{emission}$ was 520-620 nm with 0.1 % laser power.

It can be observed in Figure 4.20 (above), clear patches of fluorescence on the glass slide and, that after 6 h incubation, the BODIPY cholesterol probe successfully labelled the exosomes present in solution. This is indicated by the clear fluorescence images obtained using the detected $\lambda_{emission}$ range of the probe. However, as exosome sizes typically range from 30-150 nm in diameter [66,104–106], even though their small size does not allow for resolution in this particular experimental set up. It can also be observed that exosome aggregation has taken place in solution.
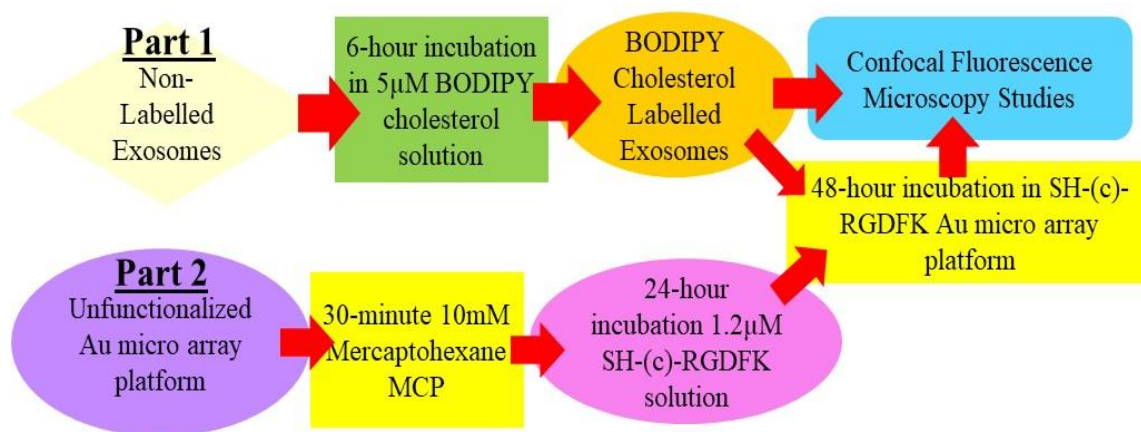
Figure 4.21: Schematic Summary to show experimental workflow for labelled exosomes CFM studies. Part 1 involved labelling the exosomes and imaging them on a glass slide using CFM. Part 2 involved incubating these labelled-exosomes within a SH-(c)-RGDFK functionalized Au micro array platform and carrying out CFM imaging studies on the labelled exosomes within the platform to confirm successful exosome capture.

As BODIPY cholesterol probe labels exosomes, the BODIPY-cholesterol labelled exosomes were then incubated within a SH-(c)-RGDFK functionalized Au micro array platform in order to understand if biocapture/ exosome adhesion occurs at the array interiors. This is a very important control-study to confirm and reinforce both the SERS and EIS spectral data shown earlier in this chapter.
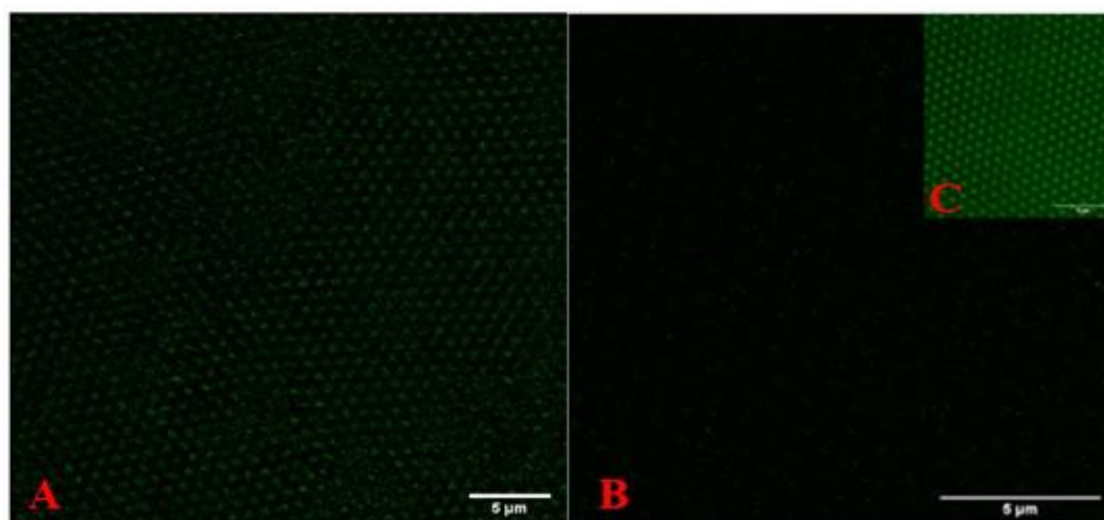
*Figures 4.22A, B (**both with time delay from 0.3 to 1.8 seconds) to exclude scatter from Au micro array surface) and Figure 4.23C (top right, without time delay)** to show the Au micro array platform background: Confocal fluorescence images of BODIPY cholesterol stained exosomes captured within a SH-(c)-RGDFK functionalized Au micro array platform. Exosomes are from EA.hy926. CFM imaging was carried out using 0.1 % laser power, $\lambda_{excitation}$ was 497nm and $\lambda_{emission}$ was 520-620nm.*

In part 1: The exosome-labelling was carried out as described above for Figure 4.20.

In part 2: Please refer to Figures 4.04 and 4.06 for the SH-(c)-RGDFK functionalization and exosome incubation procedures. CFM imaging was carried out using 0.1 % laser power, $\lambda_{excitation}$ was 497 nm and $\lambda_{emission}$ was 520-620 nm. Exosomes were from EA.hy926. CFM studies were carried out with time delay from 0.3 to 1.8 s to exclude scatter from the Au surface in both Figures 4.22A and B and without time delay to expose the Au surface shown in Figure 4.23C. Both Figures 4.22B and C are the same image with the time delay setting switched on/off.

One of the drawbacks of using a lustrous, metallic surface such as Au is the strong reflectance background, and one way to overcome this is to use the time delay function on the software so that the scattering/reflectance signal does not reach the signal-detector and subsequently allows for successful $\lambda_{emission}$ detection. This scattering can be seen in Figure 4.22C where the hexagonally close-packed pattern of the Au micro array platform can be observed.

It can be seen in Figures 4.22A and 4.22B that exosome capture has occurred within the Au micro array platform(s) as this is confirmed by successful $\lambda_{emission}$ detection, there appears to be more extracellular vesicle capture in A than B as the fluorescence on the image is more intense. It is possible that quantity of exosomes may vary in each array pore platform and their sizes will also affect the detected fluorescence signal. Exosome sizes range from 30-150 nm in diameter[66,104–106], no further resolution can be achieved in this case due their small sizes, nonetheless this is an important control in that confirms biocapture within the Au micro array platform. In Chapter 5, the use of FE-SEM will be employed to improve on this resolution where the exosome-structures can be seen more closely.

4.4 Conclusions

Successful (c)-RGDFK peptide Au micro array functionalization and exosome capture was confirmed in this experimental chapter using Raman, SERS, EIS and CFM studies.

Raman spectra of the pure (c)-RGDFK powder was successfully obtained and SERS studies after SH-(c)-RGFK functionalization of the Au micro array interiors both showed the distinctive F peak at ~1000 cm^{-1}. Successful SH-(c)-RGDFK modification of the Au micro array interior was further confirmed using a fluorophore-labelled $\alpha_5\beta_1$ integrin which selectively binds to a (c)-RGD sequence using CFM studies. These same CFM studies further demonstrated successful selective SH-(c)-RGDFK functionalization within the Au micro array interior environment only, as no fluorescence could be obtained on the micro array exterior environment. The selective binding of $\alpha_5\beta_1$ integrin specifically to SH-(c)-RGDFK was further confirmed using CFM studies. No fluorescent images could be obtained showing conjugation of $\alpha_5\beta_1$ integrin either within an unfunctionalized Au micro array platform or within a mercaptohexanol-functionalized micro array platform.

Successful exosome capture using two different exosome types (EA.hy926 and primary HuAEC types) within a SH-(c)-RGDFK functionalized Au micro array platform was confirmed using SERS, EIS and CFM studies. The steps leading to optimisation of SERS were described and it was found that 10 % O.D. laser filter gave best balance of intensity and stability. Clearer and more heterogeneous spectra were obtained using 10 % power and by ensuring that the micro array platform was completely submerged in H_2O throughout the studies to prevent drying-out and degradation of the sample caused by heat emitted by the LSPR.

 EIS studies from each stage of the selective modification process demonstrated successful exosome capture shown by an increase in imaginary-impedance after SH-(c)-RGDFK functionalization. EA.hy926 type exosomes were first successfully labelled with a liposome-labelling BODIPY cholesterol probe and their subsequent capture within the SH-(c)-RGDFK functionalized Au micro array platform was also confirmed using CFM studies. SERS studies further confirmed that no exosome binding took place within any unfunctionalized Au micro array interiors. This further reinforces the necessity of SAM selective functionalization within the Au micro array interior in order to promote successful exosome adsorption.

Using thiocholesterol-functionalized micro array interiors as suitable exosome-binding substrates produced varied results. EIS studies seemed to show successful exosome-conjugation within all thiocholesterol-functionalized interiors shown by a decrease in imaginary-impedance after exosome-thiocholesterol binding however, SERS studies on arrays containing proportional ratio mixtures of 70/30 and 50/50 thiocholesterol to mercaptohexanol and seemed to produce the best spectra before and after exosome solution incubation. Exosome binding was shown to be quite poor in both pure thiocholesterol and 30/70 thiocholesterol to mercaptohexanol functionalized micro array platforms. This is indicated by the poor spectra obtained using these functionalized array platforms both before and after exosome solution incubation. One drawback of the EIS technique is that it only confirms a change in relative electrode-surface properties of the sum of the entire system. It doesn't allow any further interrogation. Therefore, in this study, it not a suitable stand-alone technique.

SERS studies on exosomes captured within SH-(c)-RGDFK functionalized Au micro array platforms are significantly better and more reproducible than thiocholesterol-functionalized platforms. SH-(c)-RGDFK functionalized micro array platforms will be used to build the training dataset that is discussed in the next experimental chapter.

4.4 References

1   P. Rajendran, T. Rengarajan, J. Thangavel, Y. Nishigaki, D. Sakthisekaran, G. Sethi and I. Nishigaki, *Int. J. Biol. Sci.*, 2013, **9**, 1057–1069.

2   M. Mudau, A. Genis, A. Lochner and H. Strijdom, *Cardiovasc. J. Afr.*, 2012, **23**, 222–231.

3   I. M. J. Wolfs, M. M. P. C. Donners and M. P. J. de Winther, *Thromb. Haemost.*, 2011, **106**, 763–771.

4   Y. Zhang, M. Yu and W. Tian, *Cell Prolif.*, 2016, **49**, 3–13.

5   S. Paone, A. A. Baxter, M. D. Hulett and I. K. H. Poon, *Cell. Mol. Life Sci.*, 2019, **76**, 1093–1106.

6   J. Kowal, G. Arras, M. Colombo, M. Jouve, J. P. Morath, B. Primdal-Bengtson, F. Dingli, D. Loew, M. Tkach and C. Théry, *Proc. Natl. Acad. Sci. U. S. A.*, 2016, **113**, E968–E977.

7   C. Théry, A. Regnault, J. Garin, J. Wolfers, L. Zitvogel, P. Ricciardi-Castagnoli, G. Raposo and S. Amigorena, *J. Cell Biol.*, 1999, **147**, 599–610.

8   J. Park and Y. Choi, *Biomed. Eng. Lett.*, 2014, **4**, 258–268.

9   G. Van Niel, I. Porto-Carreiro, S. Simoes and G. Raposo, *J. Biochem.*, 2006, **140**, 13–21.

10   H. Peinado, *Nat. Med.*, 2013, **18**, 883–891.

11   R. Shah, T. Patel and J. E. Freedman, *N. Engl. J. Med.*, 2018, **379**, 958–966.

12   R. Huang, K. Yao, A. Sun, J. Qian, L. Ge, Y. Zhang, Y. Niu, K. Wang, Y. Zou and J. Ge, *Stem Cell Res. Ther.*, 2015, **6**, 1–11.

13   Z. Andreu and M. Yáñez-Mó, *Front. Immunol.*, 2014, **5**, 1–12.

14   N. P. Hessvik and A. Llorente, *Cell. Mol. Life Sci.*, 2018, **75**, 193–208.

15   A. Shaimardanova, V. Solovyeva, D. Chulpanova, V. James, K. Kitaeva and A. Rizvanov, *Neural Regen. Res.*, 2020, **15**, 586–596.

16   S. Saeedi, S. Israel, C. Nagy and G. Turecki, *Transl. Psychiatry*, , DOI:10.1038/s41398-019-0459-9.

17   W. Gao, H. Liu, J. Yuan, C. Wu, D. Huang, Y. Ma, J. Zhu, L. Ma, J. Guo, H. Shi, Y. Zou and J. Ge, *J. Cell. Mol. Med.*, 2016, **20**, 2318–2327.

18   L. Lorencova, T. Bertok, A. Bertokova, V. Gajdosova, S. Hroncekova, A. Vikartovska, P. Kasak and J. Tkac, *ChemElectroChem*, 2020, 1–19.

19   R. C. M. Siow, *Methods Mol. Biol.*, 2012, **806**, 265–274.

20   E. A. Jaffe, R. L. Nachman, C. G. Becker and C. R. Minick, *J. Clin. Invest.*, 1973, **52**, 2745–2756.

21   T. Osanai, K. Magota, M. Tanaka, M. Shimada, R. Murakami, S. Sasaki, H. Tomita, N. Maeda and K. Okumura, *Hypertension*, 2005, **46**, 1140–1146.

22   D. J. Medina Leyte, M. Domínguez Pérez, I. Mercado, M. T. Villarreal Molina and L. Jacobo Albavera, *Appl. Sci.*

23   J. Zheng, Y. Y. Zhuo, C. Zhang, G. Y. Tang, X. Y. Gu and F. Wang, *Eur. Rev. Med. Pharmacol. Sci.*, 2020, **24**, 3293–3301.

24   N. Kang, J. H. Lee, W. W. Lee, J. Y. Ko, E. A. Kim, J. S. Kim, M. S. Heu, G. H. Kim and Y. J. Jeon, *Environ. Toxicol. Pharmacol.*, 2015, **39**, 764–772.

25   W. Li, Y. Li, Y. Zhao and L. Ren, *Artif. Cells, Nanomedicine Biotechnol.*, 2020, **48**, 107–

115.

26   C. J. S. Edgell, C. C. McDonald and J. B. Graham, *Proc. Natl. Acad. Sci. U. S. A.*, 1983, **80**, 3734–3737.

27   K. Ahn, S. Pan, K. Beningo and D. Hupe, *Life Sci.*, 1995, **56**, 2331–2341.

28   S. Karger, Y.-D. Chen, T. Zhang, F. Tian, J. Wang, J. Jing and S.-S. Zhou, *Cell Physiol Biochem*, 2015, **37**, 1369–1378.

29   B. L. Vaisman, T. G. Vishnyakova, L. A. Freeman, M. J. Amar, S. J. Demosky, C. Liu, J. A. Stonik, M. L. Sampson, M. Pryor, A. V. Bocharov, T. L. Eggerman, A. P. Patterson and A. T. Remaley, *Biomed Res. Int.*, , DOI:10.1155/2015/607120.

30   M. Riederer, M. Lechleitner, H. Köfeler and S. Frank, *Arch. Physiol. Biochem.*, 2017, **123**, 249–253.

31   K. L. Macnaul and N. I. Hutchinson, *Biochem. Biophys. Res. Commun.*, 1993, 196, 1330–1334.

32   J. L. Zweier, R. Broderick, P. Kuppusamy, S. Thompson-Gorman and G. A. Lutty, *J. Biol. Chem.*, 1994, **269**, 24156–24162.

33   M. Nagae, S. Re, E. Mihara, T. Nogi, Y. Sugita and J. Takagi, *J. Cell Biol.*, 2012, **197**, 131–140.

34   T. G. Kapp, F. Rechenmacher, S. Neubauer, O. V. Maltsev, E. A. Cavalcanti-Adam, R. Zarka, U. Reuning, J. Notni, H. J. Wester, C. Mas-Moruno, J. Spatz, B. Geiger and H. Kessler, *Sci. Rep.*, 2017, **7**, 1–13.

35   W. J. Cho, Y. Kim and J. K. Kim, *ACS Nano*, 2012, **6**, 249–255.

36   A. K. Misra, S. K. Sharma, L. Kamemoto, P. V. Zinin, Q. Iu, N. Hu and L. Melnick, *Appl. Spectrosc.*, 2009, **63**, 373–377.

37   S. Fateixa, H. I. S. Nogueira and T. Trindade, *Phys. Chem. Chem. Phys.*, 2015, **17**, 21046–21071.

38   J. P. Camden, J. A. Dieringer, Y. Wang, D. J. Masiello, L. D. Marks, G. C. Schatz and R. P. Van Duyne, *J. Am. Chem. Soc.*, 2008, **130**, 12616–12617.

39   K. Bagga, D. F. Brougham, T. E. Keyes and D. Brabazon, *Phys. Chem. Chem. Phys.*, 2015, **17**, 27968–27980.

40   R. M. Cole, S. Mahajan, P. N. Bartlett and J. J. Baumberg, *Opt. Express*, 2009, **17**, 13298.

41   A. V. Gimenez, K. W. Kho and T. E. Keyes, *Nanoscale Adv.*, 2020, **2**, 4740–4756.

42   B. H. Sung, T. Ketova, D. Hoshino, A. Zijlstra and A. M. Weaver, *Nat. Commun.*, , DOI:10.1038/ncomms8164.

43   C. Lee, R. Carney, K. Lam and J. W. Chan, *J. Raman Spectrosc.*, 2017, **48**, 1771–1776.

44   K. Adamson, E. Spain, U. Prendergast, N. Moran, R. J. Forster and T. E. Keyes, *ACS Appl. Mater. Interfaces*, 2016, **8**, 32189–32201.

45   K. Adamson, E. Spain, U. Prendergast, N. Moran, R. J. Forster and T. E. Keyes, *Langmuir*, 2018, **34**, 715–725.

46   G. T. Hermanson, *Bioconjugate Tech.*, 2013, 259–273.

47   A. Introduction, 2005, 1–67.

48   J. Langer, D. J. De Aberasturi, J. Aizpurua, R. A. Alvarez-puebla, B. Auguie, J. J. Baumberg, G. C. Bazan, S. E. J. Bell and A. Boisen, , DOI:10.1021/acsnano.9b04224.

49   B. Hernández, F. Pflüger, S. G. Kruglik and M. Ghomi, *J. Raman Spectrosc.*, 2013, **44**, 827–833.

50   E. Burstein, E; Chen, Y; Lundquist, S; Tosatti, *Solid State Commun.*, 1979, **29**, 567–570.

51   T. E. Furtak and J. Reyes, *Surf. Sci.*, 1980, **93**, 351–382.

52   S. Abdali and E. W. Blanch, *Chem. Soc. Rev.*, 2008, **37**, 980–992.

53   A. R. Baydoun, *Princ. Tech. Biochem. Mol. Biol. Sixth Ed.*, 2005, 71–102.

54   R. Maroto, Y. Zhao, M. Jamaluddin, V. L. Popov, H. Wang, M. Kalubowilage, Y. Zhang, J. Luisi, H. Sun, C. T. Culbertson, S. H. Bossmann, M. Motamedi and A. R. Brasier, *J. Extracell. Vesicles*, , DOI:10.1080/20013078.2017.1359478.

55   J. S. Daniels, *Electroanalysis*, 2008, **19**, 1239–1257.

56   A. Bogomolova, E. Komarova, K. Reber, T. Gerasimov, O. Yavuz, S. Bhatt and M. Aldissi, *Anal. Chem.*, 2009, **81**, 3944–3949.

57   F. Lisdat and D. Schäfer, *Anal. Bioanal. Chem.*, 2008, **391**, 1555–1567.

58   E. Katz and I. Willner, *Electroanalysis*, 2003, **15**, 913–947.

59   A. S. Tanak, B. Jagannath, Y. Tamrakar, S. Muthukumar and S. Prasad, *Anal. Chim. Acta X*, 2019, **3**, 100029.

60   R. Forster, T. Keyes and J. Vos, *Interfacial Sopramolecular Assemblies*, John Wiley and Sons, Ltd., 2004.

61   J. C. Love, L. A. Estroff, J. K. Kriebel, R. G. Nuzzo and G. M. Whitesides, *Self-assembled monolayers of thiolates on metals as a form of nanotechnology*, 2005, vol. 105.

62   A. Sharma, J. K. Bhattarai, S. S. Nigudkar, S. G. Pistorio, A. V. Demchenko and K. J. Stine, *J. Electroanal. Chem.*, 2016, **782**, 174–181.

63   A. Sanjeev, B. Jagannath, Y. Tamrakar, S. Muthukumar and S. Prasad, *Anal. Chim. Acta X*, 2019, **3**, 100029.

64   Z. Sun, L. Wang, S. Wu, Y. Pan, Y. Dong, S. Zhu, J. Yang, Y. Yin and G. Li, *Anal. Chem.*, 2020, **92**, 3819–3826.

65   W. Cheng, J. Ma, P. Cao, Y. Zhang, C. Xu, Y. Yi and J. Li, *Talanta*, 2020, **219**, 121242.

66   C. Théry, M. Ostrowski and E. Segura, *Nat. Rev. Immunol.*, 2009, **9**, 581–593.

67   C. M. Boulanger, X. Loyer, P. E. Rautou and N. Amabile, *Nat. Rev. Cardiol.*, 2017, **14**, 259–272.

68   X. Osteikoetxea, A. Balogh, K. Szabó-Taylor, A. Németh, T. G. Szabó, K. Pálóczi, B. Sódar, Á. Kittel, B. György, É. Pállinger, J. Matkó and E. I. Buzás, *PLoS One*, 2015, **10**, 1–16.

69   M. Y. Xu, Z. S. Ye, X. T. Song and R. C. Huang, *Stem Cell Res. Ther.*, 2019, **10**, 1–11.

70   R. Wubbolts, R. S. Leckie, P. T. M. Veenhuizen, G. Schwarzmann, W. Möbius, J. Hoernschemeyer, J. W. Slot, H. J. Geuze and W. Stoorvogel, *J. Biol. Chem.*, 2003, **278**, 10963–10972.

71   G. Raposo and W. Stoorvogel, *J. Cell Biol.*, 2013, **200**, 373–383.

72   D. O'Connor, A. Byrne, C. Dolan and T. E. Keyes, *New J. Chem.*, 2018, **42**, 3671–3682.

73   E. B. Hanlon, R. Manoharan, T. W. Koo, K. E. Shafer, J. T. Motz, M. Fitzmaurice, J. R. Kramer, I. Itzkan, R. R. Dasari and M. S. Feld, *Phys. Med. Biol.*, , DOI:10.1088/0031-9155/45/2/201.

74 I. Badea, G. L. Radu and G. I. Badea, 2018, 1–6.

75 Z. Yan, S. Dutta, Z. Liu, X. Yu, N. Mesgarzadeh, F. Ji, G. Bitan and Y. H. Xie, *ACS Sensors*, 2019, **4**, 488–497.

76 R. J. Lakshmi, V. B. Kartha, C. M. Krishna, J. G. R. Solomon, G. Ullas and P. U. Devi, *Radiat. Res.*, 2002, **157**, 175–182.

77 R. Szatanek, M. Baj-Krzyworzeka, J. Zimoch, M. Lekka, M. Siedlar and J. Baran, *Int. J. Mol. Sci.*, , DOI:10.3390/ijms18061153.

78 W. T. Cheng, M. T. Liu, H. N. Liu and S. Y. Lin, *Microsc. Res. Tech.*, 2005, **68**, 75–79.

79 Dieter Naumann, *Infrared Spectrosc. New Tool Med.*, 1998, **3257**, 245–257.

80 D. P. Lau, Z. Huang, H. Lui, C. S. Man, K. Berean, M. D. Morrison and H. Zeng, *Lasers Surg. Med.*, 2003, **32**, 210–214.

81 H. P. Chiang, R. Song, B. Mou, K. P. Li, P. Chiang, D. Wang, W. S. Tse and L. T. Ho, *J. Raman Spectrosc.*, 1999, **30**, 551–555.

82 N. Stone, C. Kendall, J. Smith, P. Crow and H. Barr, *Faraday Discuss.*, 2004, **126**, 141–157.

83 N. Stone, C. Kendall, N. Shepherd, P. Crow and H. Barr, *J. Raman Spectrosc.*, 2002, **33**, 564–573.

84 H. Schulz and M. Baranska, *Vib. Spectrosc.*, 2007, **43**, 13–25.

85 G. Shetty, C. Kendall, N. Shepherd, N. Stone and H. Barr, *Br. J. Cancer*, 2006, **94**, 1460–1464.

86 J. W. Chan, D. S. Taylor, T. Zwerdling, S. M. Lane, K. Ihara and T. Huser, *Biophys. J.*, 2006, **90**, 648–656.

87 R. K. Dukor, *Handb. Vib. Spectrosc.*, , DOI:10.1002/0470027320.s8107.

88 S. Sigurdsson, P. A. Philipsen, L. K. Hansen, J. Larsen, M. Gniadecka and H. Christian Wulf, *IEEE Trans. Biomed. Eng.*, 2004, **51**, 1784–1793.

89 C. J. Frank, R. L. McCreary and D. C. B. Redd, *Anal. Chem.*, 1995, **67**, 777–783.

90 Z. Huang, H. Lui, D. I. McLean, M. Korbelik and H. Zeng, *Photochem. Photobiol.*, 2005, **81**, 1219.

91 H. Alobeedallah, B. Cornell and H. Coster, *J. Membr. Biol.*, 2018, **251**, 153–161.

92 M. Pingarro and E. Fata, 2006, **586**, 112–121.

93 R. G. Nuzzo, L. H. Dubois and D. L. Allara, *J. Am. Chem. Soc.*, 1990, **112**, 558–569.

94 C. E. D. Chidsey and D. N. Loiacono, *Langmuir*, 1990, **6**, 682–691.

95 T. Kitagawa, H. Matsubara, T. Okazaki and K. Komatsu, *Molecules*, 2014, **19**, 15298–15313.

96 C. D. Bain and G. M. Whitesides, *J. Am. Chem. Soc.*, 1989, **111**, 7164–7175.

97 D. Fang, D. Zhao, S. Zhang, Y. Huang, H. Dai and Y. Lin, *Sensors Actuators, B Chem.*, 2020, **305**, 127544.

98 B. Jose, R. Steffen, U. Neugebauer, E. Sheridan, R. Marthi, R. J. Forster and T. E. Keyes, *Phys. Chem. Chem. Phys.*, 2009, **11**, 10923–10933.

99 P. Dey, *Basic Adv. Lab. Tech. Histopathol. Cytol.*, , DOI:10.1007/978-981-10-8252-8.

100 R. L. Price and W. G. Jerome, *More basic confocal microscopy: A tutorial*, 2003, vol. 9.

101 B. Jose, R. Steffen, U. Neugebauer, E. Sheridan, R. Marthi, R. J. Forster and T. E. Keyes,

Phys. Chem. Chem. Phys., 2009, **11**, 10923–10933.

102   M. Hasan, S. Hama and K. Kogure, *Sci. Rep.*, 2019, **9**, 1–12.

103   M. Lee, J. J. Ban, W. Im and M. Kim, *Biotechnol. Bioprocess Eng.*, 2016, **21**, 299–304.

104   R. J. Lobb, M. Becker, S. W. Wen, C. S. F. Wong, A. P. Wiegmans, A. Leimgruber and A. Möller, *J. Extracell. Vesicles*, , DOI:10.3402/jev.v4.27031.

105   M. R. Ward, A. Abadeh and K. A. Connelly, *Stem Cells Transl. Med.*, 2018, **7**, 543–550.

106   X. Li, L. Liu, J. Yang, Y. Yu, J. Chai, L. Wang, L. Ma and H. Yin, *EBioMedicine*, 2016, **8**, 72–82.

Chapter 5: Analysis of Extra Cellular Vesicles using SERS and FE-SEM techniques

5.0 Introduction

Chapter 3 focused on the successful fabrication and selective surface modification techniques of Au micro array platforms, and in Chapter 4 these functionalized micro array platforms were studied in great detail using SERS both before and after exosome capture to understand spectral background noise. The use of CFM in Chapter 4 although confirming successful exosome capture, did not allow any further interrogation of their morphology, here this limitation is overcome by the use of FE-SEM techniques. Results from FE-SEM studies carried out on 2 groups of exosomes (HuAECs and HUVECs) captured within the functionalized Au micro array platform are presented in this chapter. Also in Chapter 4, it was also determined that using 10 % O.D. laser filter produced a much better SERS signal than a 1% O.D. laser filter. As the SERS method had now been optimised, here in Chapter 5 the more detailed SERS study of three sub-groups of HuAEC exosomes (NG, HG and MG) are presented here.

The primary aim of this chapter is a more detailed, in-depth study of three sub-groups of HuAECs (NG, HG and MG) exosomes and this is achieved using SERS and FE-SEM techniques. The secondary aim of this chapter (and this thesis) involves passing on all SERS spectra data to computer scientists who will carry out multivariate statistical classification analysis on these results. This point be further discussed in Chapter 6 as future work.

5.0.1 Spectral Data of Exosomes in combination with Multivariate Statistical Classification and Chemometric techniques

There are a growing number of Raman and SERS studies on exosomes. Spectral data from their vesicle-cargo (containing biomarkers[1–6]) offers a distinct advantage of discerning the various cell-signalling[7,8] and cross-talk[9] processes taking place within the tissue micro-environment, this data may provide clear, diagnostic insight into overall histological health-status when combined with chemometric methods as signals are complex and heterogenous. Blood, urine and other bio-fluids are complex, impure matrices requiring correct determination of purification choice, often with lengthy-purification steps[10] to access key biomarkers before accurate diagnostic analysis can be carried out however exosomes can be easily isolated and purified from a patient's sample giving much easier access to their biomarker-cargo which can then undergo analysis.

In *in vitro* studies, the use of multivariate statistical classification in combination with large sets of spectral data is becoming more common. SERS is particularly attractive over Raman due to the weak Raman scattering of the key components of exosomes, which can lead to sensitivity issues. One of the earliest SERS studies was by *Stremersch et al*[11] who were successfully able to discriminate AuNP-coated exosomes (isolated and re-suspended in solution) sourced from 2 different cell-lines (B16F10-melanoma and healthy red blood corpuscles) using SERS and PLS-DA.

One of the first chemometric studies was carried out by *Park et al*[12] who demonstrated that PCA of their SERS data was able to successfully distinguish exosomes sourced from healthy and cancerous lung cells. PC-DFA of SERS data carried out by *Carmicheal et al*[13] successfully differentiated exosomes sourced from healthy and cancerous pancreatic cells, and this was successfully-applied to pancreatic cancer profiling of serum-purified exosomes for oncogenic mutations. *Yan et al 2019*[14] performed PCA on SERS spectra of exosomes isolated from four different sources and were able to successfully discriminate between the different populations.

Ferreira et at 2019[15] carried out SERS studies on exosomes sourced from MCF-10A (non-tumorigenic) mammary epithelial and MDA-MB-231 (oncogenic) mammary cell cultures. The resulting SERS spectra were then further analysed using PCA. Combining PCA with heterogenic exosomal SERS-data, they were able to distinguish the healthy vs the cancerous groups with 95% confidence.

Shin et al 2020[16] used a machine learning algorithm. They inputted SERS spectra of exosomes sourced from normal and lung cancer cell lines and found that their algorithm could determine their origin with an accuracy of 95%. Moreover, their multivariate statistical model predicted that sanguine exosomes (isolated from plasma) sourced from 90.7% of cancer patients had higher similarity to lung cancer cell exosomes than to the healthy controls. This similarity increased o the progression of cancer. Not only is the use of multivariate statistical classification tools able to distinguish diseased-exosomal-Raman spectra from healthy, it can further indicate disease stage and progression. In a biomedical lab setting, this could have enormous diagnostic potential for the analyst.

5.0.2 Spectroscopic analysis in combination with Multivariate Statistical Classification Tools in Vascular Biology

Numerous review articles have been published linking exosomes with CVD[17–20] and *Zheng* et al[21] showed that exosome-mediated transfer of miR-155 between SMCs and ECs caused endothelial injury and induced atherosclerosis in cardiac cells.

In vascular biological studies, *Molony et al*[22] successfully differentiated spectral signatures of MSCs and their myogenic progeny from their nuclei using Raman spectroscopy and PCA. Using FTIR and Raman spectroscopy with PCA fed LDA, they further discriminated undifferentiated stem cells from

their myogenic and osteogenic progenies and subsequently quantitated this discrimination by showing which cell type(s) showed the greatest similarities.

Multivariate statistical classification combined with spectroscopic-analyses is proving to be a powerful diagnostic tool which could be used not only to enable to provide accurate diagnosis of CVD but also, to further determine its underlying-cause within the tissue environment.

If early disease detection and diagnosis can be performed by routine analysis of exosomes through the use of SERS with Multivariate statistical classification tools, then the outcome is a better prognosis maximising any treatment by preventing disease progression and premature death.

Surveying published literature, cancer research seems to be the main focus of the vast majority of SERS- multivariate statistical and chemometric studies involving exosomes. Also, across previous SERS studies where roughened surfaces or colloidal metal substrates were used, there are significant issues in such substrates in achieving uniformity in enhancement and response. *Keyes et al*[23–28] and *Bartlett et al*[29–31] have reported highly uniform arrays with solid SERS performance made from pore arrays that can be selectively modified to capture exosomes so we demonstrate here for the first time that this approach works, we discuss the Raman method used to yield good SERS signals from primary HuAEC-exosomes and provide preliminary conclusions from an AI-chemometrics method that demonstrates reliable discrimination even though the exosomal-spectra visually appear to be very heterogeneous.

5.0.2 Background to Experimental Setup

Three sub-groups of exosomes sourced from primary HuAECs, (NG, HG and MG) are studied using SERS. The NG is treated with 5mM glucose and mimics a healthy aortic-cardiac cell-line. For the HG, HuAECs are treated with 30 mM glucose, which causes the onset of CVD in aortic-endothelial tissue[32–34], the MG are treated with 5 mM D-Mannitol, an osmotic-control reagent to glucose[35].

5.1.0 Materials and Methods

5.1.1 Materials

For Materials, please refer to Section 2.1, Chapter 2.

5.1.2.0 Methods

5.1.2.1 Surface Functionalization and Exosome Capture Methods

An Au micro array platform was stamped with mercaptohexane for 30 min and then incubated in 1.2 µM SH-(c)-RGDFK peptide solution for 24 h. After this step, the SH-(c)-RGDFK functionalized micro array platform was sonicated for 10 min in 0.4 mL of PBS solution to ensure thorough-removal of any air-pockets within the micro array pores as micro array studies have shown that this step is necessary for optimum SERS enhancement, the location of LSPR is located at the bottom of these array pores[36]. After this step, 0.1 mL exosome solution was aliquoted directly into this 0.4 mL solution to allow easy-diffusion into the micro array pores, the prior removal of air-pockets ensured that exosomes were able to effectively bind to the bottom of the pores. This step also prevented any exosome rupture, as they were not sonicated in solution. This Au micro array platform was then incubated for 48 h at 4 °C (to prevent exosome-degradation as they are unstable at room temperature[37]) to promote biocapture.

5.1.2.2 FE-SEM Instrumentation Settings for Exosome Studies

Incident electron beam (V_{acc}) settings was set to 1 kV. The sample-stage was set at a working distance of 5 mm. Emission current (I_e) settings were 20 µA.

5.1.2.3 SERS Instrumentation Settings for Exosome Studies

SERS analysis was carried out using 10 % O.D. filter on a 785 nm laser power source, full working power of 60.2 mW. The spectral range was scanned from 200 cm^{-1}-2000 cm^{-1} but the 400 cm^{-1}-1800 cm^{-1} range is shown here as this the spectral range of interest. Spectral acquisition was 1 s with 4 s exposure time and 9 frame accumulations. Prior to analysis the Raman spectrophotometer was calibrated using a Silicon wafer as per manufacturer's instructions[38] and using the Rayleigh line.

5.1.2.4 ImageJ Exosome Counting

Exosome counting was carried out on ImageJ software using the automatic particle analysis setting. The image was first converted to a binary (black and white) image. The edge of the micro array was determined manually using an outlined circular shape. A "threshold" range is set and pixels in the image whose value lies in this range are converted to black. The software then counted the black particles as exosomes.

5.2.0 Results and Discussion

5.2.1.0 FE-SEM

Typically in FE-SEM studies (*immediately prior to imaging*), a biological sample is sputter-coated with either Au, Pt, Pd or Cr, with Cr appearing less granular on coated-samples than the other metals[39]. Exosomes captured within the micro array platforms presented in this chapter were not sputter-coated nor stained for imaging purposes. Studies carried out by *Wu et al* 2015[2] found that the best FE-SEM images came from freshly-prepared exosomes captured within their copper grid substrates immediately prior to undertaking imaging-studies.

There were a number of FE-SEM studies carried out on non-functionalized array pores to further determine pore size etc. For the narrative-flow purposes of this sub-section and this chapter, this data has been placed in Appendix C.

CFM imaging studies (refer to CFM sub-section 4.3.2 in the previous experimental chapter) although confirming exosome capture within the array platform, did not allow further interrogation of exosome size and morphology within the array pores. FE-SEM imaging studies using unlabelled exosomes were carried out which allowed detailed probing of the internal structures of the array pore interiors after exosome capture.

5.2.1.1 Primary HuAECs-Normal Group (NG)

Primary HuAECs (NG) were treated with 5 mM glucose. Please see Schematic summary of experimental workflow in Figure 5.01 for clarification purposes for results shown in Figures 5.02B-E.
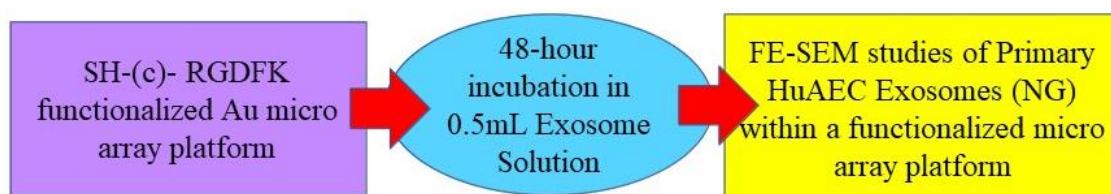

Figure 5.01: Schematic of FE-SEM experimental set-up of exosomes from primary HuAECs -NG.

For Figure 5.02A, an unfunctionalized micro array platform was imaged after the PS SAM template was removed by sonication in THF solvent, before any selective surface modification process was carried out.

In Figure 5.02A, the array platform was imaged under identical experimental parameters as B-E, this purpose was to show the smooth interiors of the array pores and that the roughness in the array interiors shown in B-E is exosome material and that exosome capture within the array pores has taken place. In Figures 5.02B-E, it can be seen that exosomes have been successfully captured within the array pore platforms. Their sphere-like shapes can be clearly seen B and C (below) respectively and their sizes range from 50-150 nm which fall within the shapes[40,41] and range(s)[42–44] that have previously been reported. In C below one of the sizes was calculated to be 113 nm and some aggregation took place (488 nm in size) also shown in in Figure 5.02C. Exosomes in Figure5.02D appear to be slightly cup-shaped and appear as clear as if TEM-negative staining technique[44] had been used. Their heterogenous sizes and shapes can easily be observed in Figures 5.02B-E below. From literature, tumour derived exosomes captured on a silica-functionalized substrate and imaged using negative-staining TEM[44] appear similar to images presented in Figures 5.02B-E.
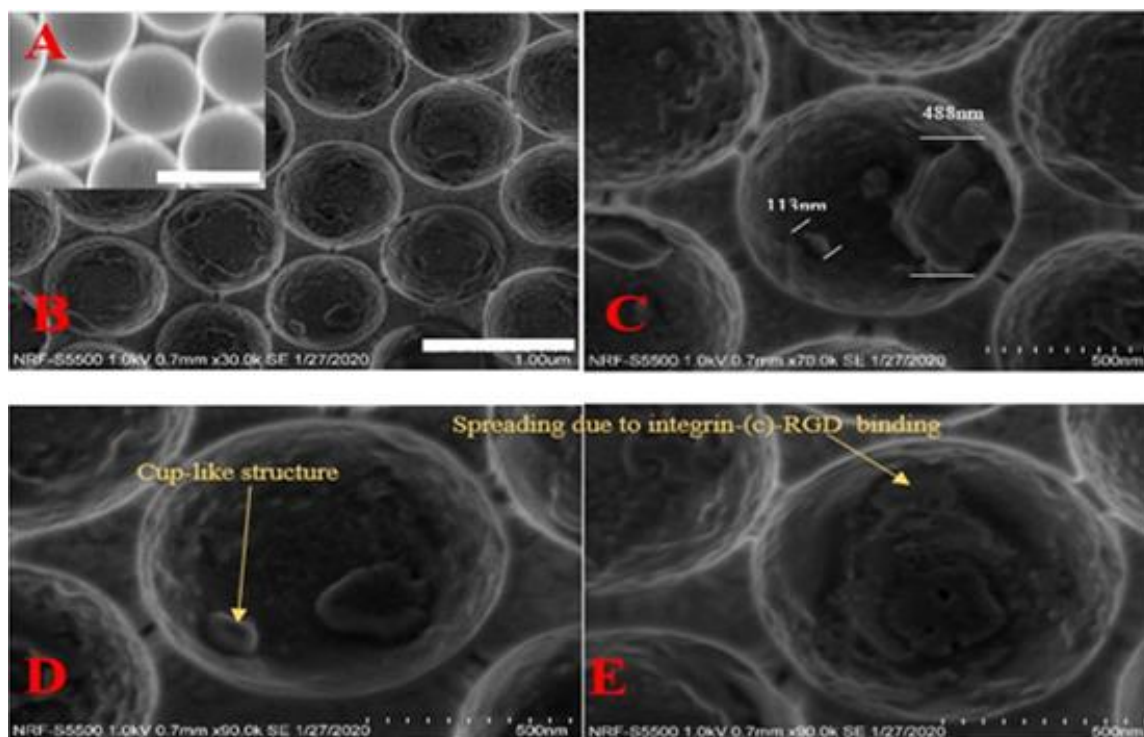
Figures 5.02A-E: FE-SEM (using various magnifications) images of (A) plain, unmodified arrays before exosome capture and, (B-E of exosomes) captured within a SH-(c)-RGDFK-functionalized Au micro array platform. Exosomes are from primary HuAECs -NG. Incident electron beam (V_{acc}) settings was set to 1kV. The sample-stage was set at a working distance of 5mm. Emission current (I_e) settings were 20μA. Scale bars: White solid, 1μm; White dashed, 500nm.

Also in Figure 5.02E (above), the exosomes appear to have spread along the surface of the array pore-interiors and this is likely due to surface integrin-binding[45–48] caused by integrin (c)-RGD interactions[49]. This spreading within the array pores may also cause exosomes to appear slightly larger than their spherical size(s). Exosomal aggregation can be observed in all images above and this feature has previously reported by *Wu et al* 2015[2] and *Wang et al* 2017[50].

The main differences between published images (shown in this chapter) and the images presented in Figures 5.02B-E (above) is the wide heterogeneity in morphological structures, exosomal spreading is more apparent in the array pores (Figure 5.02E above). Exosomes were counted in 10 sample array pores using FIJI (ImageJ) software and there is slight variation in amount of exosomes captured within different pores ranging from 44 to 120 with a mean of 74 exosomes captured per array pore (See Table 3 below).

ImageJ software has many in-built analytical features specifically for microscopists, such as particle size and particle count analysis. There are currently nine threshold settings, of which one must be pre-selected for particle analysis. All of these were individually assessed and the "Contrast" threshold setting was deemed to be the most suitable as other thresholds gave particle counts between 20,000-40,000 per array which is an unrealistic calculation, given both the sizes of the exosomes (30-150 nm), the array-pore surface area, and further by visually assessing the images. There are a few sample binary images of the threshold setting used to count exosome amount per array pore in Appendix C.

Table 3: Exosome amount captured per array-pore, counted using FIJI (ImageJ) software. Exosomes are from primary HuAECs -NG.

Exosome Number per Array Pore	Mean
53	74
44	
49	
73	
42	
98	
91	
120	
117	
52	

The circularity parameter range values were selected to exclude any polygon[51] shaped pixels that may be counted as particles by the software as exosomes are either ovoid/spherical/cup shaped. The obvious morphological and numerical variations in Figures 5.02B-E (above) and moreover, exosomal spreading/surface coverage in E (which is further supported by the EIS data shown in the previously in Section 4.3.1.4, Chapter 4), would also explain why there was considerable variation in Raman count and spectra between each sample as the sample-stage moved along to capture a different spectrum (this sample-stage step will be further explained in the upcoming SERS results sub-section).

5.2.1.2 Primary HuAECs -Hyperglycaemic Group (HG)
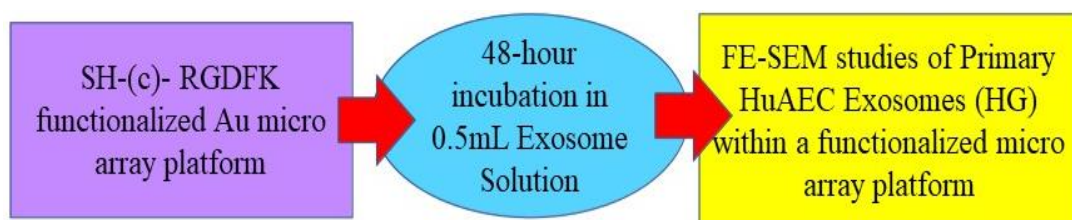
Figure 5.03: Schematic of FE-SEM experimental set-up of exosomes from primary HuAECs -HG.

Next, FE-SEM imaging studies were carried out for the Hyperglycaemic Group. HuAECs-HG are treated with 30 mM glucose to cause hyperglycaemic-induced oxidative stress. This "stress" causes the production of ROS at cellular level that has been linked to activation of many cell-signalling pathways and to the onset of many CVDs[32–34]. It was therefore important to image and study exosomes from this sub-group and to compare results from the NG.
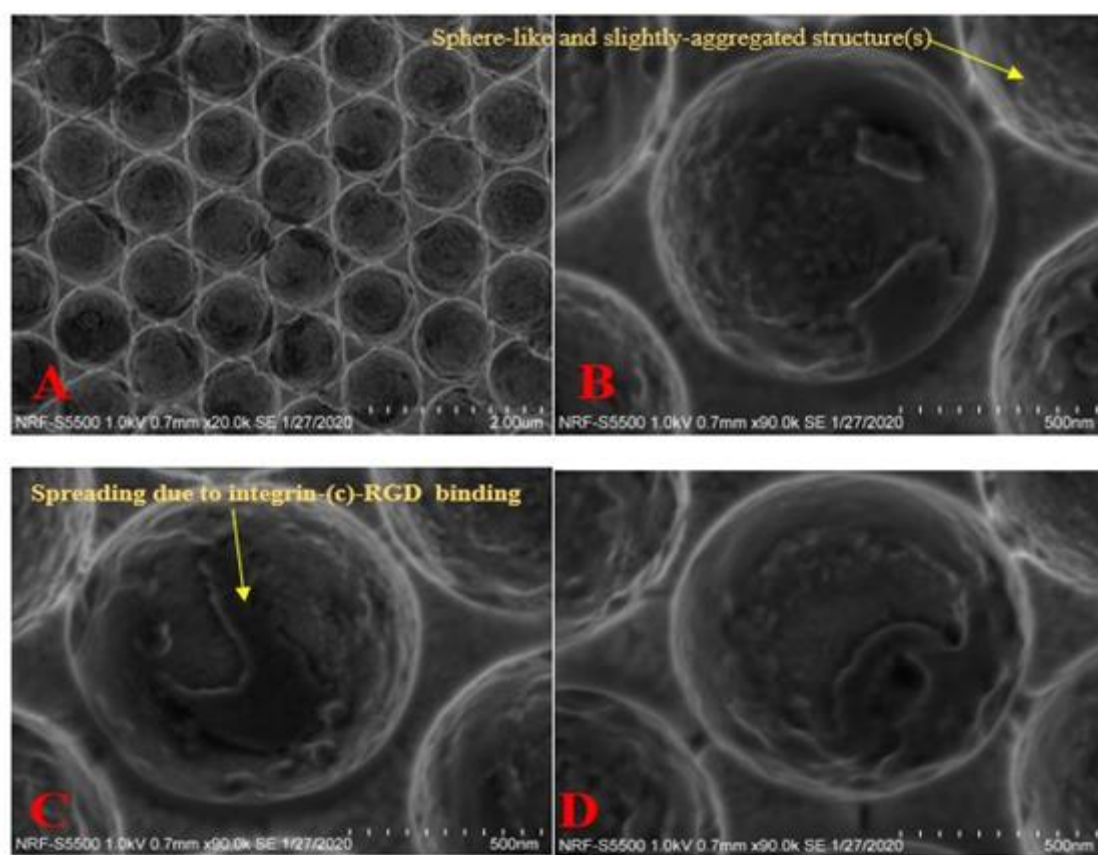
Figures 5.04A-D: FE-SEM (using various magnifications) images of exosomes from primary HuAECs-HG captured within a SH-(c)-RGDFK-functionalized Au micro array platform. Incident electron beam (V_{acc}) settings was set to 5 kV. The sample-stage was set at a working distance of 5 mm. Emission current (I_e) settings were 20 μA.

See Schematic summary of experimental workflow in Figure 5.03 (above) for clarification purposes.

In Figures 5.04A-D above, the exosome shapes are much harder to discern and compared to some published literature, some sphere shapes can be seen in B and compared to SEM images published by *Kore et al* 2019[52]. Notably, when compared to the NG (shown previously in Table 3), there is slightly more exosome-capture within the array pores. Exosomes captured per array pore ranges from 52 to 156 with a mean of 96 exosomes captured per pore (See Table 4), when compared to 74 (the mean of the NG, shown in Table 3), there is 30% more capture in the HG. The greater vesicle capture per pore explains why the Raman count was consistently higher for the HG than the NG. The HG-exosomes overall may be a smaller in size than the normal-exosomes which may also account for more vesicles captured per pore.

Table 4: Exosome amount captured per array-pore, counted using FIJI (ImageJ) software. Exosomes are from primary HuAECs -HG.

Exosome Number per Array Pore	Mean
152	96
85	
78	
82	
79	
86	
52	
100	
93	
156	

In primary HuAECs, it is most likely that high level of glucose treatment has activated the p38 MAP kinase TGF-β-stimulated VEGF cell-signalling-pathway ad other metabolic dysfunctional responses[53-55] causing a structural physico-chemical change on the exocytosed-exosomal surfaces. *Natarajan et al*[56] showed that hyperglycaemic conditions induced increased VEG-F expression in vascular endothelial smooth muscle cells causing increased cell-growth (and also the onset of CVD). It is therefore likely that hyperglycaemic conditions also cause an increase in exosome production in cell tissues meaning there are higher quantities present in the isolated pellet[5] after ultra-centrifugation.

The (c)-RGD peptide sequence is present in many extracellular matrix (ESM) proteins and several integrins recognise this specific ligand[57,58]. The (c)-RGD ligand binds to the recognition site on the β subunit of a recognised-integrin, with the R residue electrostatically-interacting with one or two D

residues of the α-subunit[49,59]. Exosomes have integrins present on their surfaces[45,48,60–64], and their cargo contents are involved in various inter and intra cell-signal pathways mainly by integrin-receptor binding to a neighbouring cell[7,48,61,65–67]. Expression of ICAM-1 in monocyte and endothelial exosomes is also increased following high glucose treatment, this mechanism triggers inflammatory responses[68]. It is therefore likely that these hyperglycaemic-exosomes may also contain a higher concentration of (c)-RGD binding integrins than normal-exosomes which would explain both the increased binding and spreading within the array pores.

5.2.1.3 Primary HuAECs -Hypoglycaemic Group (MG)

Next, FE-SEM imaging studies were carried out for the Hypoglycaemic Group: HuAECs are treated with 5 mM D-Mannitol, an osmotic-control reagent for glucose concentrations[35] frequently used in *in vitro* molecular biology studies as a comparative to any glucose treatment studies to negate the effects of osmotic shock that is caused by glucose, as mannitol is not metabolised. It was therefore important to image and study exosomes from this sub-group and to compare results from the NG and HG. See Schematic summary of experimental workflow in Figure 5.05 (below) for clarification purposes.
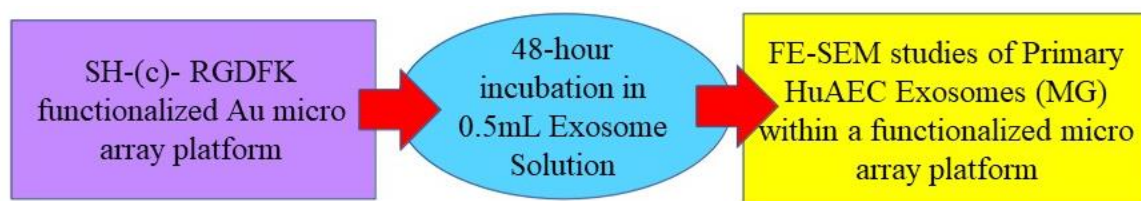
Figure 5.05: Schematic for FE-SEM experimental set-up of exosomes sourced from primary HuAECs-MG.

In Figures 5.06A-D below, exosome capture can be seen within the array pore interiors. Their sphere-like shapes can be clearly seen in D below, and their sizes range from 50-150 nm which fall within the shapes[40,41] and range(s)[42–44] that have previously been reported. SEM and TEM Images published by *Zhou et al 2016*[69] display the same spherical structures and sizes and also shows slight aggregation of extracellular vesicles.

Also in Figures 5.06A-D below, the exosomes appear to have spread along the surface of the array pore-interiors and this may be due to surface integrin-binding[45–48]caused by integrin and (c)-RGD[49] interactions. Exosomal aggregation can be observed in all images above and this feature has previously reported by *Wu et al 2015*[2] and *Wang et al 2017*[50].
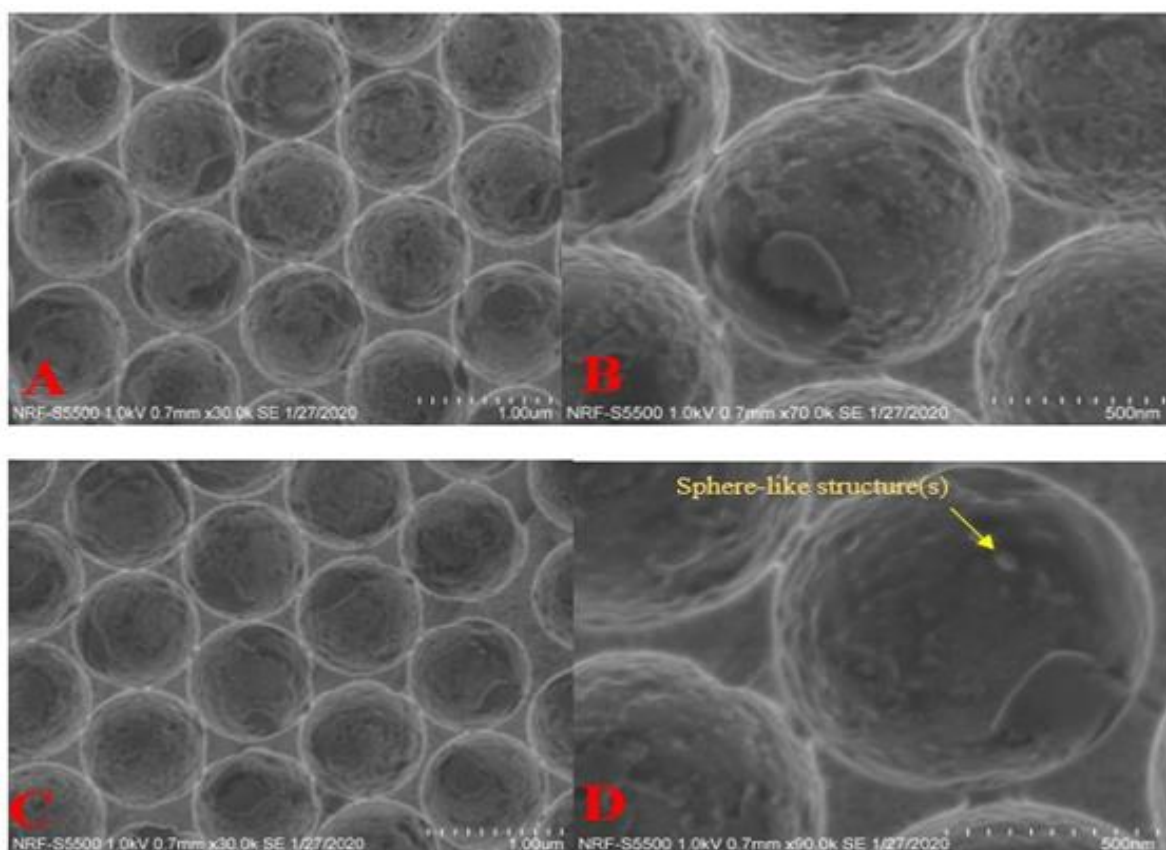
Figures 5.06A-D: FE-SEM (using various magnifications) images of exosomes captured within a SH-(c)-RGDFK-functionalized Au micro array platform. Exosomes are from primary HuAECs-MG.

Mannitol is cell-impermeable saccharide frequently used in *in vitro* studies as a comparative osmotic-control to glucose treatment[70]. However, it can act as a ROS scavenger[35,70] and its presence within the ECM can activate various signalling pathways, which can induce apoptosis in endothelial cells[71–74]. It is therefore likely that its presence will influence exocytosed hypoglycaemic-exosomes resulting in a lower production rate.

From Table 5 (below), vesicle amount per pore ranges from 22 to 59 with a mean of 43 exosomes captured per array pore. This mean (when compared to the other 2 sub-groups) is 42% lower than that for the NG (74 vesicles per array pore, from Table 3) and 55% lower than that of the HG (96 per array pore, from Table 4). It is possible that mannitol is impacting exosomal-exocytosis or affecting level of (c)-RGD recognising-integrins on the exosomal surface when compared to the NG, however it further indicates that high levels of glucose-treatment does have a significant effect on exocytosed exosomes.

Table 5: Exosome amount within 10 micro array pores counted using FIJI (ImageJ) software. Exosomes are sourced from primary HuAECs-MG.

Exosome Number per Array Pore	Mean
152	96
85	
78	
82	
79	
86	
52	
100	
93	
156	

SEM images from both the normal-exosomes and hypoglycaemic-exosomes are more similar when compared to the hyperglycaemic-exosomes, however the lower mean of 43 (Table 5, MG) when compared to 74 (Table 3, NG) explains why the Raman count of this cell sub-group was consistently slightly lower than the other 2 groups as there was a slightly lower amount of captured exosomes per pore. It is clear that mannitol has a modest effect on an exosome population.

5.2.1.4 Immortalized HUVECs, EA.hy926 – Immortalized Group (IG)

By carrying out further FE-SEM studies, the EA.hy926 cell line was used to compare results to the three previous cell sub-groups. This cell line was selected because many *in vitro* comparative studies are carried out using it to compare to primary endothelials to understand many cardiovascular functions and therapeutics on a molecular level[75].
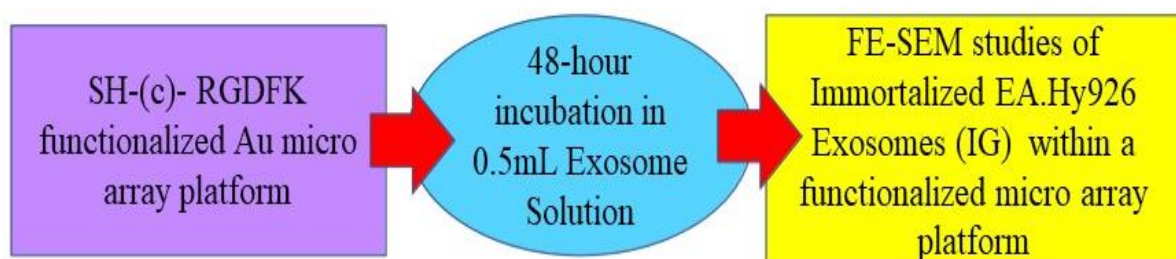
Figure 5.07: Schematic of FE-SEM experimental workflow of human immortalized EA.hy926 exosomes -IG.
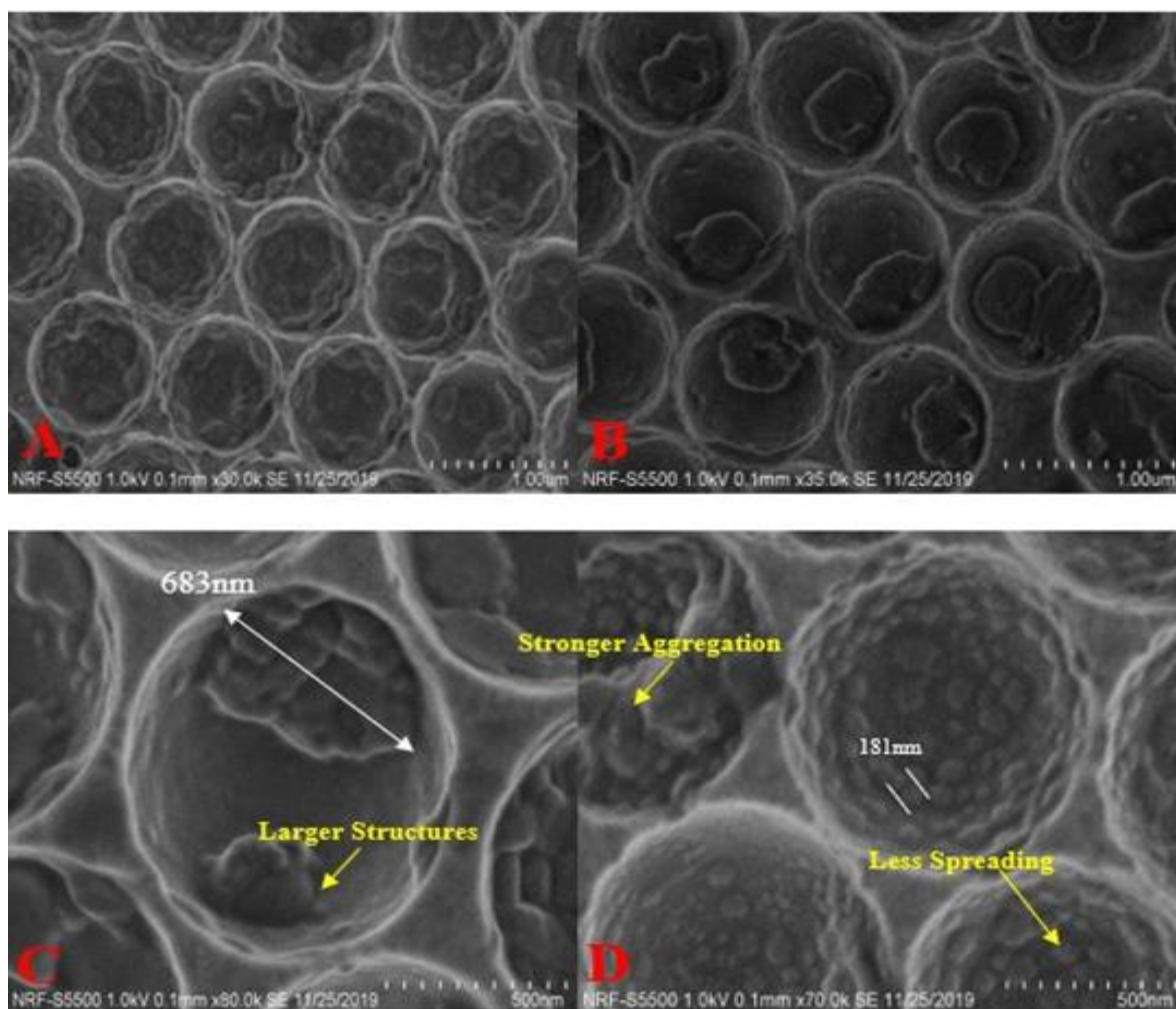
Figures 5.08A-D: FE-SEM (using various magnifications) images of exosomes (immortalized EA.Hy926) captured within a SH-(c)-RGDFK-functionalized Au micro array platform.

See Schematic summary of experimental workflow in Figure 5.07 for clarification purposes.

It can be observed that exosomes were captured within the array pore interiors shown in Figures 5.08A-D above. Less exosomal-surface spreading has taken place when compared to the three previous sets of FE-SEM results (Figures 5.02, 5.04 and 5.06) which may also suggest lower levels of integrin are present at the membrane interface. Exosome size(s) seem larger (around 181 nm in size) in Figures 5.08 than that reported by *King et al* 2012[8], *Wu et al* 2015[2] and *Wang et al* 2017[50]. Their larger diameters are more consistent with TEM-imaging data of exosomes sourced from a mammary-fibrocystic cell line published by *Noble et al* 2020[76]. DLS Studies carried out on two different exosomal populations by *Stremersch et al*[11] showed that average exosome size varied by up to 30% between both groups (0.12 µm versus O.17 µm sizes respectively). It is evident that cell origin, health and other influencing factors will affect the size of the average exocytosed-exosome.

Table 6: Exosome amount within 10 array pores using FIJI (ImageJ software). Exosomes are from human immortalized EA.hy926 cells -IG.

Exosome Number per Array Pore	Mean
18	20
11	
8	
23	
24	
20	
30	
15	
17	
30	

In Table 6 (above), exosome capture number ranged from 8 to 30 with a mean amount of 20 exosomes captured per array pore. Extensive exosomal-aggregation can be observed in Figure 5.08D (above) may have taken place during the incubation process[67,77]. Exosomal fusion is caused by specific aggregation-inducing proteins in various pathological diseases such as Parkinson's[77]. It is possible that EA.hy926 may behave more like exosome from a diseased cell and may also contain a higher concentration of proteins that lead to the observed aggregation.

The immortalized HuVEC cell line *EA.hy926* was created by fusing primary HuVECs with the immortalized-adenocarcinomic lung cell line *A549*[78]. This hybrid cell line has more chromosomes and is more homogenous than standard, primary HuVEC lines[78–80] which may further explain why this exosome group behaves differently to the three primary endothelial sub-groups.

When comparing the mean values in Table 6 (IG) and Table 3 (NG) values are 20 and 74 respectively, there is 73% less exosomal-binding within the array pore interiors. It is possible that EA.hy926 may have less (c)-RGD recognising surface-integrins than that of a primary cell line, which may further explain why there is significantly less binding within the array pore interiors.

5.2.2.0 SERS

To collect SERS spectra and to maximise spectra collection across the whole substrate surface, automated XY mapping was employed. Whereby (See schematic in Figure 5.09) the software is programmed to move the sample-stage in 1-micron increments, the 785 nm laser-beam is first focused into an array pore and the detector collects the spectral data as the sample stage moves along the y-axis in a straight line with the x-axis remaining constant ($= 0$) . The resulting spectrum is then split (and saved) into the various spectra obtained during this process.

Movasaghi et al. published two comprehensive review articles, gathering and compiling relevant Raman and FTIR spectral peak values (of particular relevance to biomedical scientists) into one source, *Raman Spectroscopy of Biological Tissues (2007)*[81] and *FTIR Spectroscopy of Biological Tissues (2008)*[82]. The referenced-sources from both of their reviews were subsequently used to interpret exosomal SERS data by *Zhang et al*[83] and exosomal FTIR data by *Di Santo et al*[84]. The same rationale is applied here for identification of main Raman bands and also using some references from *Stremersch et al* [11] and illustrations other published papers are also used for identification and comparative purposes.
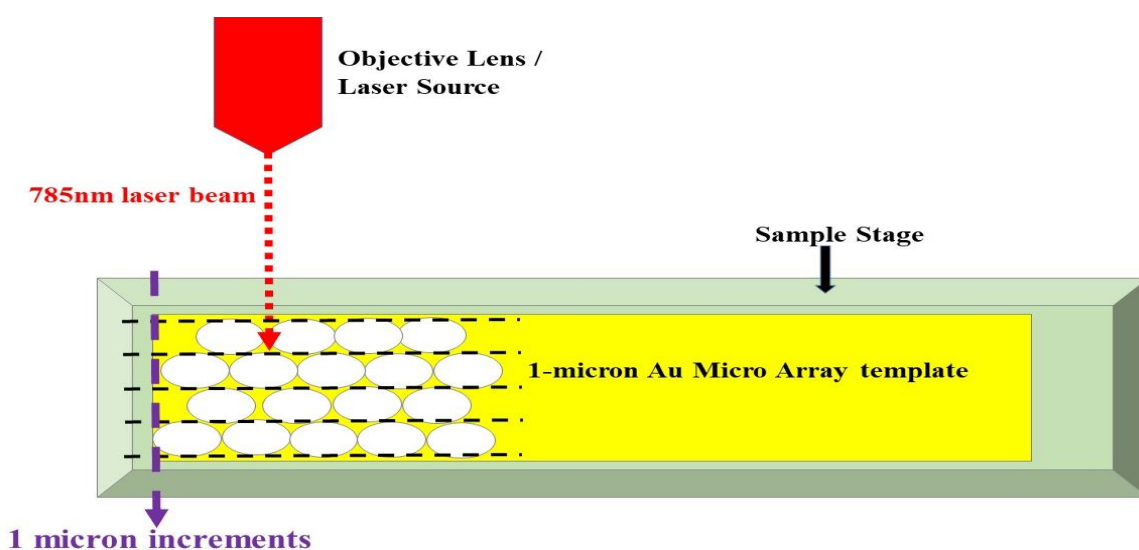
Figure 5.09: Schematic to show XY mapping settings used for all SERS studies presented in this chapter. The sample stage was pre-set to move in 1-micron increments (25 increments per run and 2 runs per Au micro array platform making a total of 50 SERS spectra) along the y-axis only with the x-axis remaining constant. This set-up ensured that each SERS spectra was collected from a different area on the array platform at all times.

Representative Raman spectra of each exosome type (taken from across different array platforms) are graphed and presented in this chapter to display the heterogeneity and similarities found within exosomal-SERS spectra. SERS spectra were not analysed manually in great detail here to determine each peak/band. However, for the purposes of this experimental chapter, sample spectra are discussed and important regions/peaks within the Raman spectrum are identified. In Appendix C, there are additional 12 overlaid spectral graphs of each sub-group. The graphs presented in this chapter represent the most common and representative spectra from hundreds of each sub-group.

5.2.2.1 Primary HuAECs -NG
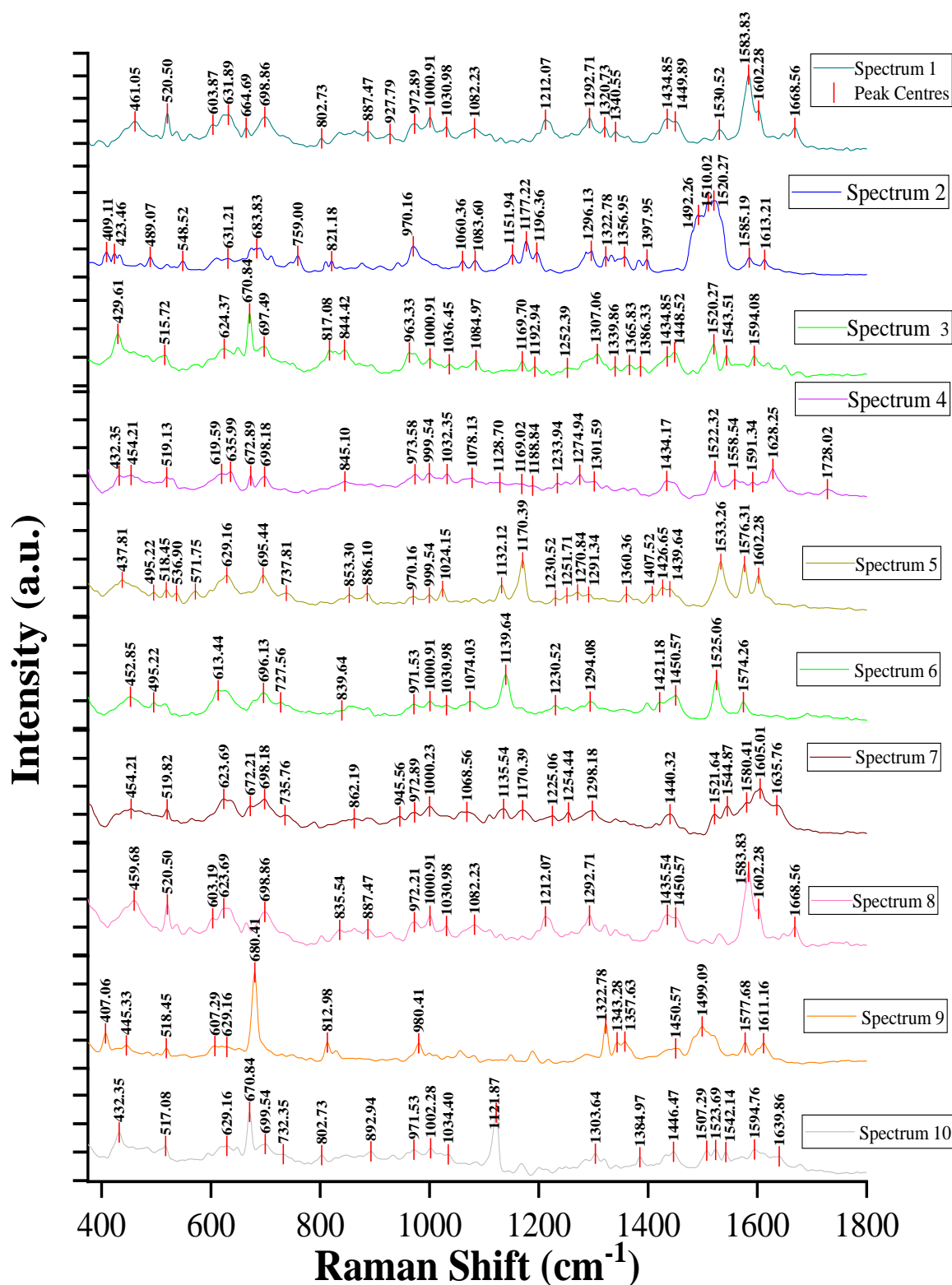
Figure 5.10: Ten representative SERS spectra of exosomes from primary HuAECs-NG within a SH-(c)-RGDFK functionalized Au micro array platform. All SERS analysis data was collected at 10 % O.D. Filter on a 785 nm Laser Power source, full power at 60.2 mW. Spectral acquisition was 1 s with 4 s exposure time and 9 frame accumulations. All spectra were baseline corrected and normalised using standard and de-spike settings to remove background noise. Please refer to table 7 for the presumed origin of the main peaks. A comprehensive table containing all main peaks from all above spectra can be seen in Appendix C.

Table 7: Main peak/band areas of SERS spectra illustrated in Figure 5.10 (above). Legend: v, stretching; δ, deformation; ρ, rocking; b, bending; sc, scissoring; tw, torsion.

Raman Shift (cm-1)	Corresponding Spectrum on Figure 5.10	Presumed Origin	References
407-495	1, 2, 4-6, 8-10	Glycogen Fingerprint Region.	85.
453/4	4, 6, 7	Tw (Ring) of a phenyl group.	86.
516-537	1,3,5,7,8, 10	v (S-S) in protein.	11, 87
519	4, 5, 9	Phosphatidylinositol.	88.
603-738	1-10	Nucleotide structures(s).	89.
620-624	3,4, 8	aromatic ring tw (C-C) , most likely due to F.	90-93.
821-39	2, 6, 8	v (C-C) of amino acid P and/or its derivative hydroxyproline; Also v (PO43-).	94,95.
886/7	1, 5, 8	ρ (CH2) in protein.	11,96,97.
972	1, 7, 8, 10	C-C backbone (indicative of collagen).	98.
1000-1003	1, 3-8, 10	Amino acid F, also aromatic v (C-C).	91,99.
1030- 1036	1, 3, 6, 8, 10	F residues within collagen.	100,101.
1060-1078	2, 6 -8	v (PO2-) (in DNA/RNA)/ Chain v (C-C) (lipids)/ v (C-O) and v (C-C) in carbohydrates.	90.
1132-1152	4-6	v (C-C)-lipids, fatty acids.	11,102,103.
1170	3, 5, 7	b (C-H) in-plane of amino acid Y.	92,93.
1188-1196	4-6	Anti-symmetric phosphate vibrations.	100.
1212-1294	1,4-8	Amide III v (C-N) and b (N-H)/ Alternatively indicative of nucleotide structures.	89,90,99,102.
1427-1446	1, 3-5, 8, 10	Sc (CH2 in lipid b (CH2) of proteins and lipids G, A bases (in DNA and/or RNA) δ(CH) in DNA/RNA, proteins, lipids and carbohydrates)	90,104.
1448/1450	1, 3, 9	v(C-H) in proteins (collagen) or lipids	104,90.
1520-1533	1-7, 10	Carotenoid -C=C-	102.
1542-1594	3, 4, 9, 10	Amide carbonyl group vibrations and aromatic hydrogens	105.
1611-1653	2, 7, 9	Amino Acid Y/ Amide I band of proteins due to v (C=O)/ Amide carbonyl group vibrations and aromatic hydrogens	89,105-107.
1668	1, 8, 10	Amide I band (protein)	108.

Please see Schematic summary of experimental workflow on Figure 5.11 for clarification purposes.

A table containing the complete list of all main peaks can be viewed in Appendix C.
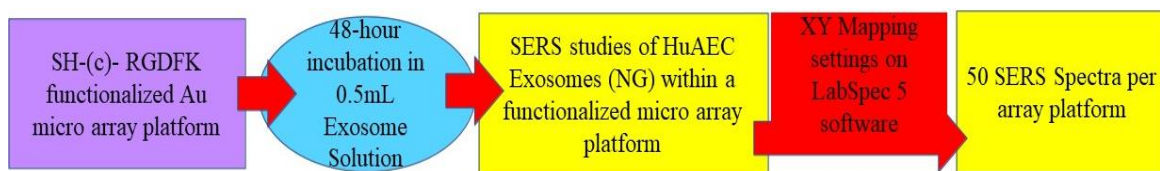
Figure 5.11: Schematic of SERS experimental-workflow of exosomes sourced from primary HuAECs (Normal Group).

From Figure 5.10 (above), all exosomal SERS spectra appear to be fairly heterogeneous, particularly in terms of relative peak intensity however many of the main peaks are common to the spectra and the key peaks are tabulated in Table 7 (above) and these results are then compared to published results.

From Table 7, all spectra (except 9) display vibrational-peaks between 500-550 cm^{-1} which is indicative of a ν (S-S) protein, the same band was also reported in exosomal SERS studies carried out by *Stremersch et al* 2016[11]. Spectra 1-3 and 5-8 display broad bands within the nucleotide regions beyond 700 cm^{-1} and 1579 cm^{-1} respectively which was also reported by *Stremersch et al* 2016[11] and *Kruglik et al* 2019[109]. This indicates that these exosomes are enriched with purine bases and other nuclear material.

Spectra 3,4 and 8 (from Figure 5.10 above) display the first F band between 620-624 cm^{-1} is also reported by *Kruglik et al* 2019[109]. All spectra display the second-distinctive narrow F peak (~1000cm^{-1}) also reported by, *Kerr et al* 2014[110], *Park et al* 2017[12] and *Kruglik et al* 2019[109]. The third F peak just beyond 1600 cm^{-1} can be seen in most spectra shown in Figure 5.10 above, however it is not listed as a main peak and also slightly overlaps with a prominent Amide I band. Spectra 1 and 4-8 all display an Amide III band (from 1212-94c m^{-1}) which was also reported by both *Stremersch et al* 2016[11] and *Kruglik et al* 2019[109] within similar spectral regions. Amide I (1611-53cm^{-1}) vibrations were also reported by *Kruglik et al* 2019[109] in exosome spectra.

Notably in Figure 5.10, all spectra except 8 and 9 appear to be rich in carotenoids (from 1520-1533 cm^{-1}), *Stremersch et al* 2016[11] and *Kruglik et al* 2019[109] also reported the presence of carotenoids within the same spectral region. The additional bands between 1132-1152 cm^{-1} in spectra 4-6 may also further indicate the presence of carotenoids as this is a fatty-acid/lipid feature, also these peaks are close to the region of the second carotenoid-peak published by *Kruglik et al* 2019[109]. The exosome membrane originates from the plasma-membrane during biogenesis[111–114] and, carotenoids are either imbedded in this membrane and are also present in high amounts of the Golgi apparatus[115] (one of the organelles where exosomal cargo originates[116]).

The variation in absolute Raman intensity is most likely due to variation in quantity of exosome captured per array pore as reflected in the FE-SEM sub-section. One peak that shows up as much more prominent in the NG than in other two groups is the distinctive phosphatidylinositol[88] peak at 519 cm^{-1} which is found in the exosomal membrane. The presence of this peak suggests that

exosomes from this group may have a slightly different composition within their membranal structure the other two sub-groups.

5.2.2.2 Primary HuAECs -HG

Please see Schematic summary of experimental workflow on Figure 5.12 (below) for clarification purposes. A table containing the complete list of all main Raman peaks can be viewed in Appendix C.
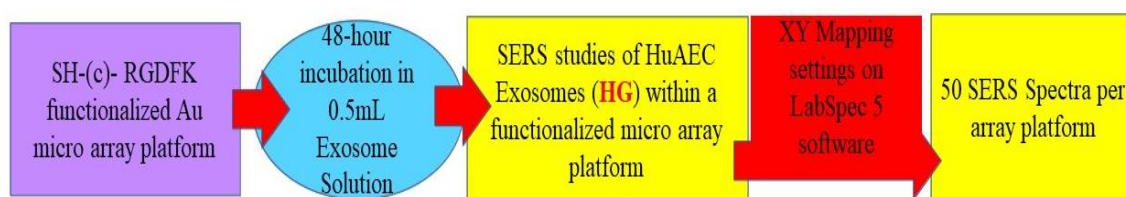
Figure 5.12: Schematic of SERS-experimental workflow on exosomes sourced from primary HuAECs (Hyperglycaemic Group) for clarification purposes
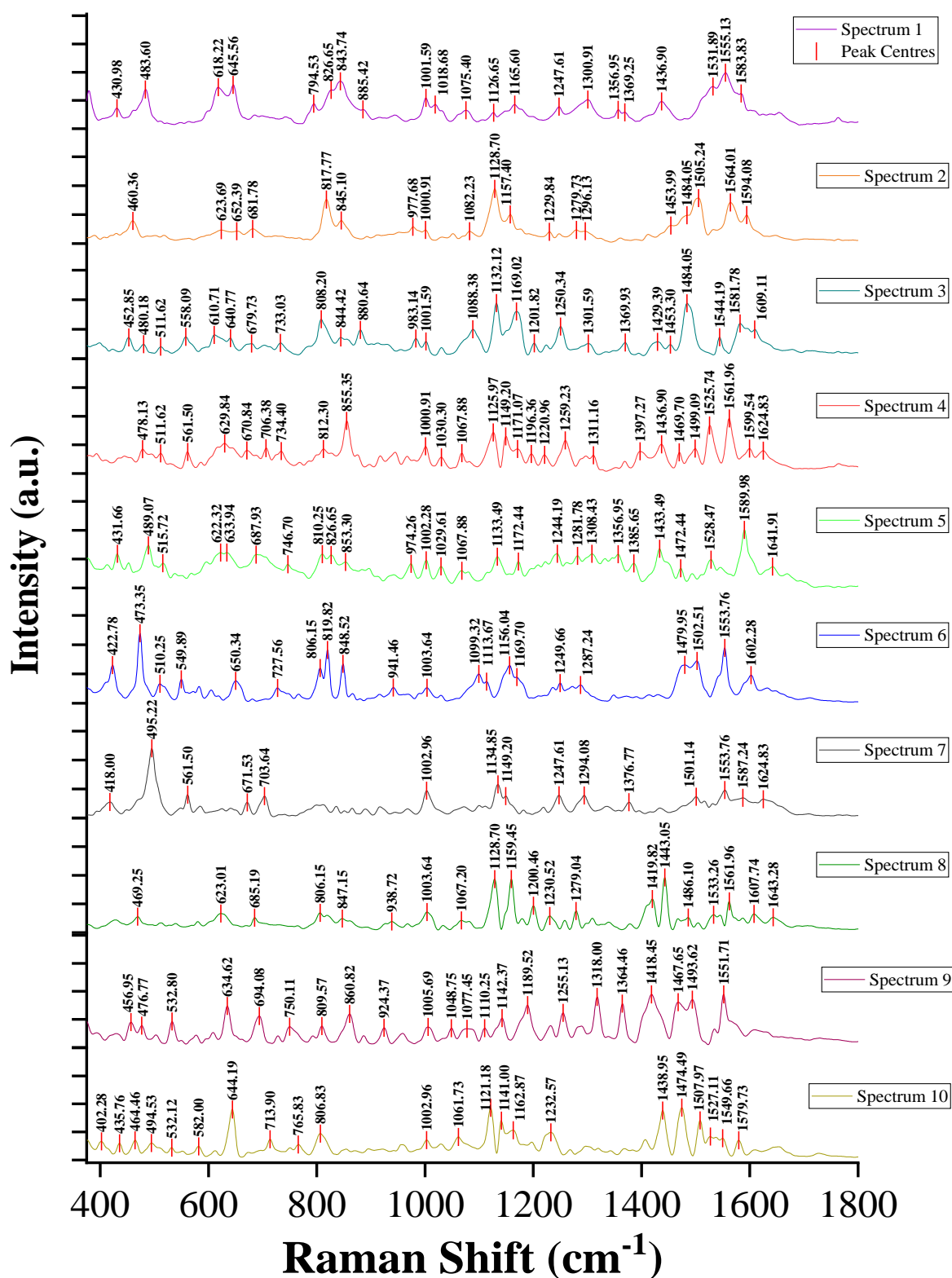
Figure 5.13: Ten representative SERS spectra of exosomes from primary HuAECs (Hyperglycaemic Group) within a SH-(c)-RGDFK functionalized Au micro array platform. Spectral acquisition was 1 s with 4 s exposure time and 9 frame accumulations. All SERS analysis data was collected at 10 % O.D. Filter on a 785 nm laser power source, full power at 60.2 mW. Spectral acquisition was 1 s with 4 s exposure time and 9 frame accumulations. All spectra were baseline corrected and normalised using standard and de-spike settings to remove background noise.. Please refer to table 8 for the presumed origin of the main peaks. A comprehensive table containing all main peaks from all above spectra can be seen in Appendix C.

From Table 8 below, all spectra (except 1, 2, 7 and 8) display vibrational-peaks between 500-550 cm^{-1} indicative of a ν(S-S) protein, the same band was also reported in exosomal SERS studies carried out by *Stremersch et al* 2016[11]. All areas display broad bands within the nucleotide regions from 634 cm^{-1}-700 cm^{-1} another band between 1544-1594 cm^{-1} which was also reported by *Stremersch et al* 2016[11] and *Kruglik et al* 2019[109].

Table 8: Main peak/band areas of SERS spectra in Figure 5.13. Legend: ν, stretching; δ, deformation; ρ, rocking; b, bending; sc, scissoring and; tw, torsion.

Raman Shift (cm^{-1})	Corresponding Spectrum on Figure 5.13	Presumed Origin	References
402-562	1-10	Glycogen Fingerprint Region.	85.
510-550	3, 4, 5, 6, 9, 10	ν (S-S) in protein.	11,87.
618-624	1, 2, 5, 8	aromatic ring tw (C-C), most likely due to F.	89-93.
634-795	1-10	Nucleotide structure(s).	89.
808-812	3, 4, 5, 9	Phosphodiester (Z-marker).	95.
844-861	1, 2, 3, 8, 9	Polysaccharide structure/ Protein/ Carbohydrate fingerprint region.	117.
1001-1006	1-10	aromatic ring ν (C-C), usually Amino Acid F.	91,99,101.
1067/8	4, 5, 8	Amino acid P (in collagen)	98.
1062-1077	1, 9, 10	Symmetric ν (PO$_2^-$) in DNA/RNA)/ Also indicative of ν (C-C) in lipids	90,118.
1129-1132	2, 3, 8	skeletal ν(C-C) of acyl backbone in lipids.	11,101,103,119.
1110-1159	5, 7, 9, 10	Amide III.	88.
1150-1157	2, 4, 6	Carotenoid structure(s)/ In-plane vibrations of conjugated =C-C=.	115,120,121.
1163-1172	3, 4, 5, 6, 10	Y (specifically in collagen type I)/ δ(C-H) in F and/or Y.	11,92,93,97, 101,122.
1231-1282	1, 5, 7, 8, 10	Amide III (arising from coupling of ν(C-N) and b(N-H).	89,90,99,107.
1250-1259	3, 4, 6, 9	ν(NH$_2$) in G and C bases/ Amide III protein vibrations.	95,98.
1357-1364	1, 5, 9	G base (in the N$_7$ form, B,Z-marker)	95.
1429-1480	3, 5, 6, 8, 10	Sc (CH$_2$) in lipids)/ B (CH$_2$) in proteins & lipids/ G and A bases in DNA, RNA/ δ(C-H) in DNA/RNA, proteins, lipids and/or carbohydrates.	90,123.
1484-1492	2, 3, 6, 8, 9	Amide II vibrations due to a coupling of ν (C-N) & in-plane b (N-H)	107.
1528-1533	1, 5, 9, 10	Carotenoid -C=C-	92,120
1544-1594	1-10	Amide carbonyl group vibrations and aromatic hydrogens/ Amide II vibrations/ COO$^-$ vibrations Nucleotide bases	105,107,109,124.
1582/1587/1602	3, 6, 7	δ(C=C) in F	101,122.
1625-1643	5, 7, 9	Amino Acid Y/ Amide I band of proteins due to ν(C=O)/ Amide carbonyl group vibrations and aromatic hydrogens	86,101,105-107.

Lee et al 2018[125] attributed sharper peaks between 700-800 cm^{-1} to the presence of lactic acid within exosomal-cargo. As hyperglycaemic conditions *in vitro* often induce an hypoxic response causing the production of many ROS[8,52,126–129], it is therefore possible that the sharp peaks between 700-800 cm^{-1} in Figure 5.13 (Spectra 3, 4, 6, and 7). are also due to the presence of both lactic acid and nucleotide structures

From Figure 5.13 above, Spectra 3,4 and 8 display the first F band between 620-624 cm^{-1}, also reported by *Kruglik et al* 2019[109] and *Lee et al* 2018[125]. The broad general protein band between 844-861cm^{-1} (shown in Spectra 1-3,8 and 9) may further indicate the presence of Y as it corresponds to data published by *Lee et al* 2018[125]. All spectra (displayed in Figure 5.13 above) display the second-distinctive narrow F peak (~1000 cm^{-1}) also reported by *Kerr et al* 2014[110], *Park et al* 2017[12], *Lee et al* 2018[125], and *Kruglik et al* 2019[109]. The third F peak just beyond 1600 cm^{-1} can be seen in most spectra, however it is not listed as a main peak. An Amide III band (from 1231-1282 cm^{-1}) which was also reported by *Stremersch et al* 2016[11] and *Kruglik et al* 2019[109] within similar spectral regions can be seen on Spectra 1, 5, 7, 8 and 10 in Figure 5.13 (above).

To compare to the previous group. There was a much higher Raman count in this HG than the NG. This greater absolute signal intensity was consistent across spectral-data collected across from multiple array platforms. FE-SEM data shown in the previous sub-section shows that there are on average more exosomes captured per array pore in the HG than the other two sub-groups. The higher quantities captured per array pore explain the higher Raman count. Similar to the NG (shown previously in Figure 5.14), all spectra (except 3 and 7) appear to be rich in carotenoids (from 1150-1157 and 1528-1533cm^{-1} respectively), within similar regions previously published *Stremersch et al* 2016[11], *Lee et al* 2018[125] , and *Kruglik et al* 2019[109].

Notably, there are two main differences between Figures 5.13 (above) and 5.10 (shown previously); One, more prominent band in Figure 5.13 is Amide II (from 1484-1492cm^{-1} on Spectra 2, 3, 6, 8 and 9). There is also a second Amide III band (from 1110-1159 cm^{-1}) on Figure 5.13 (Spectra 5, 7, 9 and 10) that is absent on Figure 5.10. Both of these Amide bands found in exosomal Raman studies carried out by *Lee et al* 2018[125]. As these bands are not present in the NG, this suggests that the protein cargo has significantly changed in the HuAECs following a high concentration (30 mM) of glucose treatment.

5.2.2.3 Primary HuAECs- MG
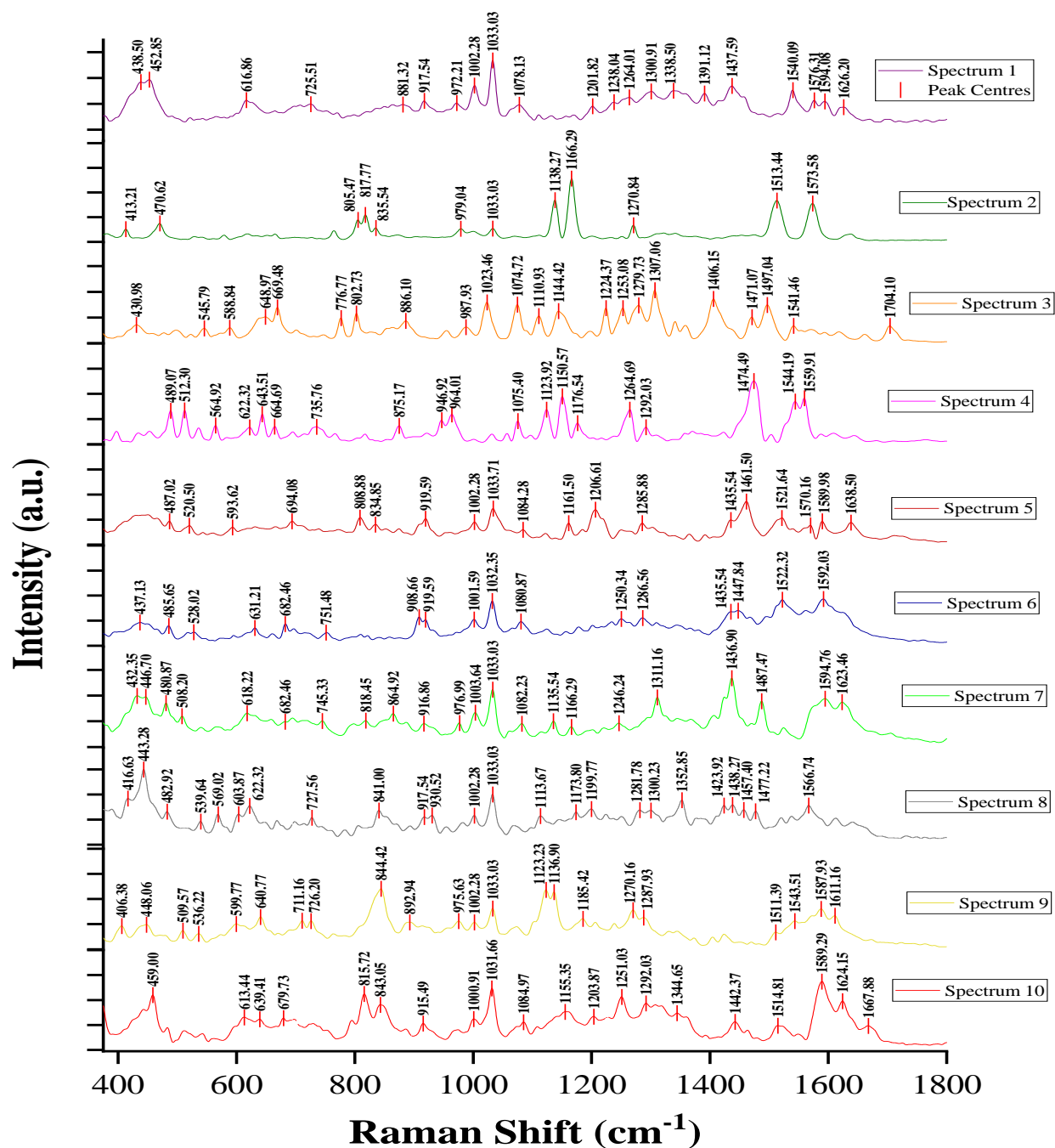
Figure 5.14: Ten sample SERS spectra of exosomes from primary HuAECs -MG within a SH-(c)-RGDFK functionalized Au micro array platform. All SERS analysis data was collected at 10 % O.D. Filter on a 785 nm laser power source, full power at 60.2 mW. Spectral acquisition was 1 s with 4 s exposure time and 9 frame accumulations. All spectra were baseline corrected and normalised using standard and de-spike settings to remove background noise. A comprehensive table containing all main peaks can be seen in Appendix C.

Please see Schematic summary of experimental workflow in Figure 5.15 (below) for clarification purposes. A table containing the complete list of all main peaks can be viewed in Appendix C.

Table 9: Main peak/band areas of SERS spectra in Figure 5.14
Legend: ν, stretching; δ, deformation; ρ, rocking; b, bending; sc, scissoring and; tw, torsion.

| Raman Shift (cm^{-1})	Corresponding Spectrum on Figure 5.14	Presumed Origin	References
406-599	1-10	Glycogen Fingerprint Region.	85.
447/453	1, 7, 9	tw(phenyl ring).	86.
508-546	3-9	ν (S-S) in protein structures.	11,87.
604-777	3-10	Nucleotide structure(s)	89.
803-808	2, 3, 5	General Protein band.	85.
816-818	2, 7, 10	ν (C-C) in collagen.	98.
841-845	8-10	Polysaccharide structure(s).	85.
916/7	7, 8, 10	Ribose Vibration	89.
918-920	1, 5, 6	ν (C-C) in Amino Acid P and/or its derivative Hydroxyproline/ Glycogen and lactic acid	92,94,101,130.
909-947	4, 6, 8	General Protein band .	87.
1001-4	1, 5-10	Amino acid F, also aromatic ν(C-C).	91,98,99, 101,122.
1032-1034	1, 2, 5-10	F residues within collagen.	100,101.
1075-1078	1, 3, 4	PO$_2^-$ stretching (in DNA/RNA)/ Chain st (C-C) in lipids/ ν (C-O), ν (C-C) in carbohydrates,	90.
1114-1200	2-4, 7-10	ν(C-C) in lipids/fatty acids/ Amide III.	11,87,88,102.
1162-1166	2, 5, 7	Y (specifically in collagen type I).	92,93,101.
1202-1338	1, 4, 5, 7, 8, 10	Amide III ν (C-N) and in-plane b (N-H))/ Alternatively indicative of nucleotides	89,90,99, 102,107.
1250-1253	6, 8, 10	NH$_2$ in G and C bases	95.
1287-1292	4, 6, 9, 10	C base	95.
1436-1442	5-7, 10	Sc (CH$_2$) in lipids B (CH$_2$) in proteins and lipids G, A bases (in DNA and/or RNA) δ(CH) in DNA/RNA & proteins, lipids and carbohydrates.	90.
1438	1, 6, 8	δ(CH$_2$)	119,131.
1540-1595	1, 3-10	Amide carbonyl group vibrations and aromatic hydrogens/ Amide II vibrations/ COO$^-$ vibrations.	105,107,124.
1623-1639	5, 7, 10	Amino Acid Y/ Amide I band of proteins due to ν (C=O)/ Amide carbonyl group vibrations and aromatic hydrogens.	89,101,105,107.
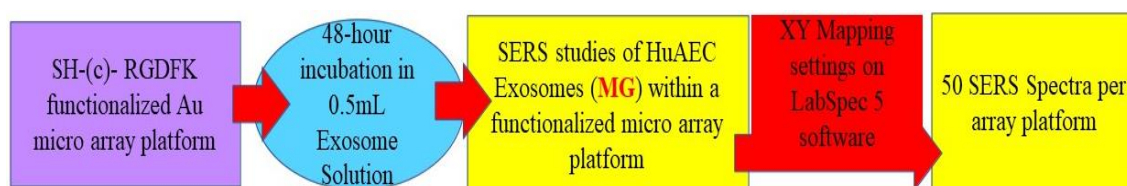
Figure 5.15: Schematic of SERS-experimental workflow on exosomes sourced from primary HuAECs -MG for clarification purposes.

The same ν (S-S) protein, nucleotide structures and F peaks/bands outlined in the two previous sub-groups are also present in Table 8 and Figure 5.14 above. The main identifiable difference between this sub-group from is the peak around 916 cm⁻¹, a distinctive ribose vibration and can be seen on Spectra 7, 8, and 10 on Figure 5.20 and Table 9 (above). Its presence suggests that there is more nucleic acid content within this sub-group. RNA material was previously identified from the colorectal carcinomic cell line by *Zheng et al* 2018[132].

Similar to the HG, there are two Amide III bands present in the MG. The first Amide III band can be observed from 1114-1200 cm⁻¹ on Spectra 2-4, and 7-10 and the second from 1202-1338 cm⁻¹ can be seen on Spectra 1, 4 ,5, 7, 8 and 10 respectively on Figure 5.14. Both of these bands were also reported within similar spectral regions by *Stremersch et al* 2016[11] and *Kruglik et al* 2019[109]. The second Amide III band listed above in Table 8 (1202-1338cm⁻¹) is much broader than the same band in Table 7 (1212-1294 cm⁻¹) this may be due to the presence of nucleotides/purine bases in some spectra (as reported in this spectral region in studies carried out by *Kerr et al* 2014[110]) , there is some overlapping within this spectral-region denoting various protein and nucleic acid structures.

It is therefore likely that there is more nucleic acid material present in the MG than in the previous two sub-groups as there are spectral peaks found within the spectral-region that are not found in the previous 2 sub-groups. An Amide I band (1623-1639 cm⁻¹) can be seen on Spectra 5, 7 and 10 and these vibrations were also reported in exosomal spectra by *Kruglik et al* 2019[109]. There is an Amide II band (from 1540-1595 cm⁻¹) present on Spectra 1 and 3-10 (see Figure 5.14 above) that is also found the HG (refer to Figure 5.10 shown previously). This same protein band was also reported in exosomal studies carried by *Lee et al* 2018[125]. Notably, there are much less carotenoids present in this group than in the previous two sub-groups. On Figure 5.14 above, it is only present as a major peak on Spectra 5 and 6 at 1522cm⁻¹.

The Raman count for this sub-group was consistently much lower and, FE-SEM studies shown the previous sub-section showed that there was less capture of the hypoglycaemic-exosomes within the array pores than the other two sub-groups. It is likely that mannitol treatment is having a subtle effect on the resulting exosomal-cargo.

In Summary a total of 1165 spectra on 24 samples, 915 spectra on 20 samples and a further 865 spectra on 18 samples were collected for the NG, HG, and MG respectively and some additional representative spectra can be found in Appendix C.

5.3 Conclusions

FE-SEM studies confirmed successful exosome capture within the array pore platforms mediated by recognition of cavity immobilised RGD peptides. ImageJ/FIJI software was used to assess exosome capture of four different groups sourced from two different cell lines. Results showed that three sub-

groups of exosomes all sourced from primary HuAECs were captured in greater quantities, with those following glucose treatment recording the highest number of exosome-capture per array pore, followed by the normal and the mannitol treated sub-groups respectively.

The lowest extent of capture within the array pores were recorded for the exosomes sourced from the hybrid, immortalized Ea.hy926 cell line. This suggests that primary HuAEC-exosomes have more (c)- RGD-ligand-binding integrins than the Ea.Hy926-exosomes. The use of a peptide even though highly effective in exosome capture may be a disadvantage in terms of biasing the outcome by selectively capturing some exosome sub-populations which may have a higher binding affinity to the chosen peptide and potentially certain sub-populations which do not conjugate to the peptide (or even repelled)may be excluded

The selective surface modification capture approach used to conjugate exosomes within the micro-array interior environment was a success, as high quality, SERS spectra was consistently obtained. This capture approach by using selective surface modification was a success, as high quality SERS spectra were consistently obtained. Extensive SERS studies were carried out on the three sub-groups of HuAEC-exosomes (NG, HG and MG respectively) in order to build up a training-set-database in collaboration with the School of Computing Applications, DCU.

 SERS results showed that the highest Raman count was consistently recorded for the glucose treated group than the other two groups, these results were consistent with the FE-SEM data outlined above where these exosomes showed the greatest capture rate.

Even though, these cell sub-groups were not sourced from pathological tissue-samples, they were merely treated with reagents. Glucose is mainly used to simulate the onset of CVD, as its presence in high quantities can induce the production of various ROS within the cell, triggering various molecular biochemical inflammatory pathways, yet there is still considerable spectral variation in each exosomal-subgroup. The main difference(s) in SERS-results seem to suggest that the NG contains more phospholipid cargo than the other two sub-groups; The HG contains higher amounts of lactic acid and more protein cargo than the other two sub-groups and; The MG appears to contain more nuclear material within their cargo than in the other two sub-groups.

It is evident that the approach applied here exploiting pore capture surfaces with recognition moieties as SERS substrates, may prove to be an invaluable tool in providing effective diagnostic-insight at a molecular level within human biological samples, especially in combination with suitably-optimised uniform substrates which are consistent in providing both reproducible surface enhancement and signal responses. Separately, applying AI models with the approach described here can show distinction between subtle effects in exosome treatments and going forward, this analytical technique could be applied with AI-machine learning capabilities (and other multivariate statistical classification techniques) for analysis of a patient's biological sample in order to determine overall

health-status and also, to detect any subtle metabolic-biochemical changes over time that may be indicative of disease onset.

5.4 References

1   L. Lorencova, T. Bertok, A. Bertokova, V. Gajdosova, S. Hroncekova, A. Vikartovska, P. Kasak and J. Tkac, *ChemElectroChem*, 2020, 1–19.

2   Y. Wu, W. Deng and D. J. Klinke, *Analyst*, 2015, **140**, 6631–6642.

3   P. Fernández-Llama, S. Khositseth, P. A. Gonzales, R. A. Star, T. Pisitkun and M. A. Knepper, *Kidney Int.*, 2010, **77**, 736–742.

4   J. Z. Nordin, Y. Lee, P. Vader, I. Mäger, H. J. Johansson, W. Heusermann, O. P. B. Wiklander, M. Hällbrink, Y. Seow, J. J. Bultema, J. Gilthorpe, T. Davies, P. J. Fairchild, S. Gabrielsson, N. C. Meisner-Kober, J. Lehtiö, C. I. E. Smith, M. J. A. Wood and S. E. L. Andaloussi, *Nanomedicine Nanotechnology, Biol. Med.*, 2015, **11**, 879–883.

5   R. J. Lobb, M. Becker, S. W. Wen, C. S. F. Wong, A. P. Wiegmans, A. Leimgruber and A. Möller, *J. Extracell. Vesicles*, , DOI:10.3402/jev.v4.27031.

6   R. A. Dragovic, C. Gardiner, A. S. Brooks, D. S. Tannetta, D. J. P. Ferguson, P. Hole, B. Carr, C. W. G. Redman, A. L. Harris, P. J. Dobson, P. Harrison and I. L. Sargent, *Nanomedicine Nanotechnology, Biol. Med.*, 2011, **7**, 780–788.

7   C. Théry, M. Ostrowski and E. Segura, *Nat. Rev. Immunol.*, 2009, **9**, 581–593.

8   H. W. King, M. Z. Michael and J. M. Gleadle, *BMC Cancer*, , DOI:10.1186/1471-2407-12-421.

9   Z. Boussadia, J. Lamberti, F. Mattei, E. Pizzi, R. Puglisi, C. Zanetti, L. Pasquini, F. Fratini, L. Fantozzi, F. Felicetti, K. Fecchi, C. Raggi, M. Sanchez, S. D'Atri, A. Carè, M. Sargiacomo and I. Parolini, *J. Exp. Clin. Cancer Res.*, 2018, **37**, 1–15.

10   A. Saito, *Contrib. Nephrol.*, 2010, **166**, 100–111.

11   S. Stremersch, M. Marro, B. El Pinchasik, P. Baatsen, A. Hendrix, S. C. De Smedt, P. Loza-Alvarez, A. G. Skirtach, K. Raemdonck and K. Braeckmans, *Small*, 2016, **12**, 3292–3301.

12   J. Park, M. Hwang, B. Choi, H. Jeong, J. H. Jung, H. K. Kim, S. Hong, J. H. Park and Y. Choi, *Anal. Chem.*, 2017, **89**, 6695–6701.

13   J. Carmicheal, C. Hayashi, X. Huang, L. Liu, Y. Lu, A. Krasnoslobodtsev, A. Lushnikov, P. G. Kshirsagar, A. Patel, M. Jain, Y. L. Lyubchenko, Y. Lu, S. K. Batra and S. Kaur, *Nanomedicine Nanotechnology, Biol. Med.*, 2019, **16**, 88–96.

14   Z. Yan, S. Dutta, Z. Liu, X. Yu, N. Mesgarzadeh, F. Ji, G. Bitan and Y. H. Xie, *ACS Sensors*, 2019, **4**, 488–497.

15   N. Ferreira, A. Marques, H. Águas, H. Bandarenka, R. Martins, C. Bodo, B. Costa-Silva and E. Fortunato, *ACS Sensors*, 2019, **4**, 2073–2083.

16   H. Shin, S. Oh, S. Hong, M. Kang, D. Kang, Y. G. Ji, B. H. Choi, K. W. Kang, H. Jeong, Y. Park, H. K. Kim and Y. Choi, *ACS Nano*, 2020, **14**, 5435–5444.

17   H. Wang, Y. Xie, A. M. Salvador, Z. Zhang, K. Chen, G. Li and J. Xiao, *Curr. Atheroscler. Rep.*, 2020, **22**, 1–9.

18   W. Yanan, X. Yingyu, Z. Ao, W. Mingyang, F. Zihan and Z. Junping, *Biomed.*

Pharmacother., , DOI:10.1016/j.biopha.2019.108951.

19   Y. Chen, H. Yuan, Z. Ou and J. Ou, .

20   W. Gao, H. Liu, J. Yuan, C. Wu, D. Huang, Y. Ma, J. Zhu, L. Ma, J. Guo, H. Shi, Y. Zou and J. Ge, *J. Cell. Mol. Med.*, 2016, **20**, 2318–2327.

21   B. Zheng, W. na Yin, T. Suzuki, X. hua Zhang, Y. Zhang, L. li Song, L. shuang Jin, H. Zhan, H. Zhang, J. shui Li and J. kun Wen, *Mol. Ther.*, 2017, **25**, 1279–1294.

22   C. Molony, J. McIntyre, A. Maguire, R. Hakimjavadi, D. Burtenshaw, G. Casey, M. Di Luca, B. Hennelly, H. J. Byrne and P. A. Cahill, *Biochim. Biophys. Acta - Mol. Cell Res.*, 2018, **1865**, 343–353.

23   B. Jose, C. T. Mallon, R. J. Forster and T. E. Keyes, *Phys. Chem. Chem. Phys.*, 2011, **13**, 14705–14714.

24   B. Jose, R. Steffen, U. Neugebauer, E. Sheridan, R. Marthi, R. J. Forster and T. E. Keyes, *Phys. Chem. Chem. Phys.*, 2009, **11**, 10923–10933.

25   C. T. Mallon, C. Zuliani, T. E. Keyes and R. J. Forster, *Chem. Commun.*, 2010, **46**, 7109–7111.

26   C. T. Mallon, R. J. Forster and T. E. Keyes, *Chem. Commun.*, 2011, **47**, 7605–7607.

27   K. W. Kho, G. B. Berselli and T. E. Keyes, , DOI:10.1002/smll.202005815.

28   R. Šakalys, K. W. Kho and T. E. Keyes, *Sensors Actuators, B Chem.*, , DOI:10.1016/j.snb.2021.129970.

29   R. M. Cole, J. J. Baumberg, F. J. De Garcia Abajo, S. Mahajan, M. Abdelsalam and P. N. Bartlett, *Nano Lett.*, 2007, **7**, 2094–2100.

30   S. Mahajan, J. J. Baumberg, A. E. Russell and P. N. Bartlett, *Phys. Chem. Chem. Phys.*, 2007, **9**, 6016–6020.

31   R. M. Cole, S. Mahajan, P. N. Bartlett and J. J. Baumberg, *Opt. Express*, 2009, **17**, 13298.

32   X. Li, Y. Rong, M. Zhang, X. L. Wang, S. A. LeMaire, J. S. Coselli, Y. Zhang and Y. H. Shen, *Biochem. Biophys. Res. Commun.*, 2009, **381**, 660–665.

33   A. Manea, S. A. Manea, A. Todirita, I. C. Albulescu, M. Raicu, S. Sasson and M. Simionescu, *Cell Tissue Res.*, 2015, **361**, 593–604.

34   D. Burtenshaw, M. Kitching, E. M. Redmond, I. L. Megson and P. A. Cahill, *Front. Cardiovasc. Med.*, 2019, **6**, 1–18.

35   A. B. El-Remessy, G. Abou-Mohamed, R. W. Caldwell and R. B. Caldwell, *Investig. Ophthalmol. Vis. Sci.*, 2003, **44**, 3135–3143.

36   B. Jose, R. Steffen, U. Neugebauer, E. Sheridan, R. Marthi, R. J. Forster and T. E. Keyes, *Phys. Chem. Chem. Phys.*, 2009, **11**, 10923–10933.

37   R. Maroto, Y. Zhao, M. Jamaluddin, V. L. Popov, H. Wang, M. Kalubowilage, Y. Zhang, J. Luisi, H. Sun, C. T. Culbertson, S. H. Bossmann, M. Motamedi and A. R. Brasier, *J. Extracell. Vesicles*, , DOI:10.1080/20013078.2017.1359478.

38   Horiba, LabRAM User Guide, 2005, 1–67.

39   I. Stokroos, D. Kalicharan, J. J. L. Van Der Want and W. L. Jongebloed, *J. Microsc.*, 1998, **189**, 79–89.

40   H. G. Zhang and W. E. Grizzle, *Clin. Cancer Res.*, 2011, **17**, 959–964.

41   R. Szatanek, M. Baj-Krzyworzeka, J. Zimoch, M. Lekka, M. Siedlar and J. Baran, *Int. J. Mol. Sci.*, , DOI:10.3390/ijms18061153.

42   X. Osteikoetxea, A. Balogh, K. Szabó-Taylor, A. Németh, T. G. Szabó, K. Pálóczi, B. Sódar, Á. Kittel, B. György, É. Pállinger, J. Matkó and E. I. Buzás, *PLoS One*, 2015, **10**, 1–16.

43   V. Luga, L. Zhang, A. M. Viloria-Petit, A. A. Ogunjimi, M. R. Inanlou, E. Chiu, M. Buchanan, A. N. Hosein, M. Basik and J. L. Wrana, *Cell*, 2012, **151**, 1542–1556.

44   M. K. Jung and J. Y. Mun, 2018, 5–9.

45   C. Lee, R. Carney, K. Lam and J. W. Chan, *J. Raman Spectrosc.*, 2017, **48**, 1771–1776.

46   M. Nagae, S. Re, E. Mihara, T. Nogi, Y. Sugita and J. Takagi, *J. Cell Biol.*, 2012, **197**, 131–140.

47   T. G. Kapp, F. Rechenmacher, S. Neubauer, O. V. Maltsev, E. A. Cavalcanti-Adam, R. Zarka, U. Reuning, J. Notni, H. J. Wester, C. Mas-Moruno, J. Spatz, B. Geiger and H. Kessler, *Sci. Rep.*, 2017, **7**, 1–13.

48   S. Rana, S. Yue, D. Stadel and M. Zöller, *Int. J. Biochem. Cell Biol.*, 2012, **44**, 1574–1584.

49   K. E. Gottschalk and H. Kessler, *Angew. Chemie - Int. Ed.*, 2002, **41**, 3767–3774.

50   Z. Wang, R. Zhang, P. Huang, C. Chen, H. Li, P. Li, D. Quinn, M. Dao, S. Suresh, M. Wu, Y. Ouyang, Z. Wang, R. Zhang, P. Huang, C. Chen, H. Li and P. Li, *Proc. Natl. Acad. Sci. U. S. A.*, 2020, **117**, 28525.

51   T. Ferreira and W. Rasband, *Image J user Guid.*, , DOI:10.1038/nmeth.2019.

52   R. A. Kore, J. C. Henson, R. N. Hamzah, R. J. Griffin, A. J. Tackett, Z. Ding and J. L. Mehta, *Sci. Rep.*, 2019, **9**, 1–12.

53   Z. Irshad, M. Xue, A. Ashour, J. R. Larkin, P. J. Thornalley and N. Rabbani, *Sci. Rep.*, 2019, **9**, 1–14.

54   F. Cosentino, K. Hishikawa, Z. S. Katusic and T. F. Lüscher, *Circulation*, 1997, **96**, 25–28.

55   T. Yamamoto, O. Kozawa, K. Tanabe, S. Akamatsu, H. Matsuno, S. Dohi and T. Uematsu, *J. Cell. Biochem.*, 2001, **82**, 591–598.

56   R. Natarajan, W. Bai, L. Lanting, N. Gonzales and J. Nadler, *Am. J. Physiol. - Hear. Circ. Physiol.*, 1997, **273**, 2224–2231.

57   D. G. Stupack and D. A. Cheresh, *J. Cell Sci.*, 2002, **115**, 3729–3738.

58   E. Ruoslahti, *Annu. Rev. Cell Dev. Biol.*, 1996, **12**, 697–715.

59   J. P. Xiong, T. Stehle, R. Zhang, A. Joachimiak, M. Frech, S. L. Goodman and M. A. Arnaout, *Science (80-.).*, 2002, **296**, 151–155.

60   M. E. Hemler, *Annu. Rev. Cell Dev. Biol.*, 2003, **19**, 397–422.

61   C. Théry, A. Regnault, J. Garin, J. Wolfers, L. Zitvogel, P. Ricciardi-Castagnoli, G. Raposo and S. Amigorena, *J. Cell Biol.*, 1999, **147**, 599–610.

62   R. Wubbolts, R. S. Leckie, P. T. M. Veenhuizen, G. Schwarzmann, W. Möbius, J. Hoernschemeyer, J. W. Slot, H. J. Geuze and W. Stoorvogel, *J. Biol. Chem.*, 2003, **278**, 10963–10972.

63   J. Song, X. Chen, M. Wang, Y. Xing, Z. Zheng and S. Hu, *Sci. Rep.*, 2014, **4**, 4–9.

64   Y. Tian, S. Li, J. Song, T. Ji, M. Zhu, G. J. Anderson, J. Wei and G. Nie, *Biomaterials*, 2014, **35**, 2383–2390.

65   G. Raposo and W. Stoorvogel, *J. Cell Biol.*, 2013, **200**, 373–383.

66   L. Zitvogel, G. Regnault, Armelle; Lozier, Anne; Wolfers, Joseph; Flament, Caroline; Tenza, Danielle; Ricciardi-Castagnoli, Paola; Raposo and S. Amigorena, *Nat. Med.*, 1998, **4**, 594–600.

67   X. Yao, W. Wei, X. Wang, L. Chenglin, M. Björklund and H. Ouyang, *Biomaterials*, 2019, **224**, 119492.

68   T. Sáez, P. de Vos, J. Kuipers, L. Sobrevia and M. M. Faas, *Immunobiology*, 2019, **224**, 325–333.

69   J. Zhou, S. Ghoroghi, A. Benito-Martin, H. Wu, U. J. Unachukwu, L. S. Einbond, S. Guariglia, H. Peinado and S. Redenti, *Sci. Rep.*, , DOI:10.1038/srep19743.

70   Ç. Karasu, *Eur. J. Pharmacol.*, 2000, **392**, 163–173.

71   A. M. Malek, G. G. Goss, L. Jiang, S. Izumo and S. L. Alper, *Stroke*, 1998, **29**, 2631–2640.

72   A. Farkas, E. Szatmári, A. Orbók, I. Wilhelm, K. Wejksza, P. Nagyoszi, P. Hutamekalin, H. Bauer, H. C. Bauer, A. Traweger and I. A. Krizbai, *J. Neurosci. Res.*, 2005, **80**, 855–861.

73   D. C. Hess, E. Howard, C. Cheng, J. Carroll and D. W. Hill, *Stroke*, 2000, **31**, 1179–1186.

74   H. J. Kwak, S. J. Lee, Y. Lee and C. H. Ryu, 2000, **1**, 2317–2324.

75   D. King, M. D. Glynn, S. Cindric, D. Kernan, T. O'Connell, R. Hakimjavadi, S. Kearney, T. Ackermann, X. M. Berbel, A. Llobera, U. Simonsen, B. E. Laursen, E. M. Redmond, P. A. Cahill and J. Ducrée, *Sci. Rep.*, 2019, **9**, 1–14.

76   J. M. Noble, L. D. M. Roberts, N. Vidavsky, A. E. Chiou, C. Fischbach, M. J. Paszek, L. A. Estroff and L. F. Kourkoutis, *J. Struct. Biol.*, , DOI:10.1016/j.jsb.2020.107474.

77   J. Howitt and A. F. Hill, *J. Biol. Chem.*, 2016, **291**, 26589–26597.

78   C. J. S. Edgell, C. C. McDonald and J. B. Graham, *Proc. Natl. Acad. Sci. U. S. A.*, 1983, **80**, 3734–3737.

79   K. Ahn, S. Pan, K. Beningo and D. Hupe, *Life Sci.*, 1995, **56**, 2331–2341.

80   A. R. Baydoun, *Princ. Tech. Biochem. Mol. Biol. Sixth Ed.*, 2005, 71–102.

81   Z. Movasaghi, S. Rehman and I. U. Rehman, *Appl. Spectrosc. Rev.*, 2007, **42**, 493–541.

82   Z. Movasaghi, S. Rehman and I. U. Rehman, *Appl. Spectrosc. Rev.*, 2008, **43**, 134–179.

83   H. Zhang, A. C. Silva, W. Zhang, H. Rutigliano and A. Zhou, *PLoS One*, 2020, **15**, 1–16.

84   R. Di Santo, S. Romanò, A. Mazzini, S. Jovanović, G. Nocca, G. Campi, M. Papi, M. De Spirito, F. Di Giacinto and G. Ciasca, *Nanomaterials*, , DOI:10.3390/nano11061476.

85   I. R. M. Ramos, A. Malkin and F. M. Lyng, *Biomed Res. Int.*, , DOI:10.1155/2015/561242.

86   H. Schulz and M. Baranska, *Vib. Spectrosc.*, 2007, **43**, 13–25.

87   H. J. Yvon, *Horiba Jobin Yvon, Raman Appl. Note*, 2017, 1–2.

88   R. J. Lakshmi, V. B. Kartha, C. M. Krishna, J. G. R. Solomon, G. Ullas and P. U. Devi, *Radiat. Res.*, 2002, **157**, 175–182.

89   J. W. Chan, D. S. Taylor, T. Zwerdling, S. M. Lane, K. Ihara and T. Huser, *Biophys. J.*, 2006, **90**, 648–656.

90   I. Notingher, C. Green, C. Dyer, E. Perkins, N. Hopkins, C. Lindsay and L. L. Hench, *J. R. Soc. Interface*, 2004, **1**, 79–90.

91   E. Ó Faoláin, M. B. Hunter, J. M. Byrne, P. Kelehan, M. McNamara, H. J. Byrne and F. M. Lyng, *Vib. Spectrosc.*, 2005, **38**, 121–127.

92   N. Stone, C. Kendall, J. Smith, P. Crow and H. Barr, *Faraday Discuss.*, 2004, **126**, 141–157.

93   N. Stone, C. Kendall, N. Shepherd, P. Crow and H. Barr, *J. Raman Spectrosc.*, 2002, **33**, 564–573.

94   N. J. Kline and P. J. Treado, *J. Raman Spectrosc.*, 1997, **28**, 119–124.

95   A. J. Ruiz-Chica, M. A. Medina, F. Sánchez-Jiménez and F. J. Ramírez, *J. Raman Spectrosc.*, 2004, **35**, 93–100.

96   I. Tatischeff, E. Larquet, J. M. Falcón-Pérez, P. Y. Turpin and S. G. Kruglik, *J. Extracell. Vesicles*, , DOI:10.3402/jev.v1i0.19179.

97   C. Lee, R. P. Carney, S. Hazari, Z. J. Smith, A. Knudson, C. S. Robertson, K. S. Lam and S. Wachsmann-Hogiu, *Nanoscale*, 2015, **7**, 9290–9297.

98   C. J. Frank, R. L. McCreary and D. C. B. Redd, *Anal. Chem.*, 1995, **67**, 777–783.

99   R. Malini, K. Venkatakrishna, J. Kurien, K. M. Pai, L. Rao, V. B. Kartha and C. M. Krishna, *Biopolymers*, 2006, **81**, 179–193.

100   P. G. L. Andrus and R. D. Strickland, *Biospectroscopy*, 1998, **4**, 37–46.

101   W. T. Cheng, M. T. Liu, H. N. Liu and S. Y. Lin, *Microsc. Res. Tech.*, 2005, **68**, 75–79.

102   G. Shetty, C. Kendall, N. Shepherd, N. Stone and H. Barr, *Br. J. Cancer*, 2006, **94**, 1460–1464.

103   L. Tirinato, F. Gentile, D. Di Mascolo, M. L. Coluccio, G. Das, C. Liberale, S. A. Pullano, G. Perozziello, M. Francardi, A. Accardo, F. De Angelis, P. Candeloro and E. Di Fabrizio, *Microelectron. Eng.*, 2012, **97**, 337–340.

104   Kaminaka K; Yamazaki H; Ito T et al, *J. Raman Spectrosc.*, 2001, **32**, 139–141.

105   B. R. Wood, M. A. Quinn, B. Tait, M. Ashdown, T. Hislop, M. Romeo and D. McNaughton,

Biospectroscopy, 1998, **4**, 75–91.

106 S. Sigurdsson, P. A. Philipsen, L. K. Hansen, J. Larsen, M. Gniadecka and H. Christian Wulf, *IEEE Trans. Biomed. Eng.*, 2004, **51**, 1784–1793.

107 R. K. Dukor, *Handb. Vib. Spectrosc.*, , DOI:10.1002/0470027320.s8107.

108 R. Agarwal, P. Tandon and V. D. Gupta, *J. Organomet. Chem.*, 2006, **691**, 2902–2908.

109 S. G. Kruglik, F. Royo, J. M. Guigner, L. Palomo, O. Seksek, P. Y. Turpin, I. Tatischeff and J. M. Falcón-Pérez, *Nanoscale*, 2019, **11**, 1661–1679.

110 L. T. Kerr, L. Gubbins, K. Weiner Gorzel, S. Sharma, M. Kell, A. McCann and B. M. Hennelly, *Biophotonics Photonic Solut. Better Heal. Care IV*, 2014, **9129**, 91292Q.

111 N. P. Hessvik and A. Llorente, *Cell. Mol. Life Sci.*, 2018, **75**, 193–208.

112 S. Stuffers, C. S. Wegner, H. Stenmark and A. Brech, 2009, 925–937.

113 M. Colombo, G. Raposo and C. Théry, *Annu. Rev. Cell Dev. Biol.*, 2014, **30**, 255–289.

114 M. Mathieu, L. Martin-Jaular, G. Lavieu and C. Théry, *Nat. Cell Biol.*, 2019, **21**, 9–17.

115 G. J. Puppels, H. S. P. Garritsen, J. A. Kummer and J. Greve, *Cytometry*, 1993, **14**, 251–256.

116 R. Zhan, X. Leng, X. Liu, X. Wang, J. Gong, L. Yan, L. Wang, Y. Wang, X. Wang and L. J. Qian, *Biochem. Biophys. Res. Commun.*, 2009, **387**, 229–233.

117 I. R. M. Ramos, A. Malkin and F. M. Lyng, *Biomed Res. Int.*, , DOI:10.1155/2015/561242.

118 L. Chiriboga, P. Xie, H. Yee, V. Vigorita, D. Zarou, D. Zakim and M. Diem, *Biospectroscopy*, 1998, **4**, 47–53.

119 C. Krafft, L. Neudert, T. Simat and R. Salzer, *Spectrochim. Acta - Part A Mol. Biomol. Spectrosc.*, 2005, **61**, 1529–1535.

120 A. Mahadevan-Jansen and R. R. Richards-Kortum, *J. Biomed. Opt.*, 1996, **1**, 31–70.

121 E. B. Hanlon, R. Manoharan, T.-W. Koo, K. E. Shafer, J. T. Motz, M. Fitzmaurice, J. R. Kramer, I. Itzkan, R. R. Dasari and M. S. Feld, *Phys. Med. Biol.*, 2000, **45**, R1–R59.

122 Z. Huang, A. McWilliams, H. Lui, D. I. McLean, S. Lam and H. Zeng, *Int. J. Cancer*, 2003, **107**, 1047–1052.

123 D. P. Lau, Z. Huang, H. Lui, C. S. Man, K. Berean, M. D. Morrison and H. Zeng, *Lasers Surg. Med.*, 2003, **32**, 210–214.

124 R. A. Shaw and H. H. Mantsch, *J. Mol. Struct.*, 1999, **480–481**, 1–13.

125 W. Lee, A. Nanou, L. Rikkert, F. A. W. Coumans, C. Otto, L. W. M. M. Terstappen and H. L. Offerhaus, *Anal. Chem.*, 2018, **90**, 11290–11296.

126 S. Zhang, J. Liu, K. Zheng, L. Chen, Y. Sun, Z. Yao, Y. Sun, Y. Lin, K. Lin and L. Yuan, *Vascul. Pharmacol.*, 2021, **136**, 106820.

127 P. Kucharzewska, H. C. Christianson, J. E. Welch, K. J. Svensson, E. Fredlund, M. Ringnér, M. Mörgelin, E. Bourseau-Guilmain, J. Bengzon and M. Belting, *Proc. Natl. Acad. Sci. U. S. A.*, 2013, **110**, 7312–7317.

128   K. J. Svensson, P. Kucharzewska, H. C. Christianson, S. Sköld, T. Löfstedt, M. C. Johansson, M. Mörgelin, J. Bengzon, W. Ruf and M. Belting, *Proc. Natl. Acad. Sci. U. S. A.*, 2011, **108**, 13147–13152.

129   J. Zheng, Y. Y. Zhuo, C. Zhang, G. Y. Tang, X. Y. Gu and F. Wang, *Eur. Rev. Med. Pharmacol. Sci.*, 2020, **24**, 3293–3301.

130   J. Binoy, J. P. Abraham, I. H. Joe, V. S. Jayakumar, G. R. Pettit and O. F. Nielsen, *J. Raman Spectrosc.*, 2004, **35**, 939–946.

131   S. Koljenović, T. B. Schut, A. Vincent, J. M. Kros and G. J. Puppels, *Anal. Chem.*, 2005, **77**, 7958–7965.

132   W. Zheng, W. Huang, J. Chen, J. Zhou, X. Xu, G. Xu, R. Chen and G. Wang, *Int. J. Clin. Exp. Med.*, 2018, **11**, 12991–13002.

Chapter 6: Final Conclusions and Future Work

This thesis set out to develop novel exosome capture plasmonic surfaces .and successfully demonstrate RGD as a useful capture surface that can be regioselectively applied to the cavity interior hotspots. The SH-(c)-RGDFK modified Au micro array interiors proved to be an effective ligand (after undergoing EDC Sulpho-NHS coupling step) for successful exosome capture as it yielded consistent, reproducible SERS spectra.

6.1 Final Conclusions

Chapter 1 (Introduction) focused on Raman and SERS including SERS substrates. SERS substrates are becoming more common in biological studies due to the small volume required for single molecular SERS detection and can be used to test for a specific analyte and also to monitor pH levels within a biological system. The desired experimental outcome needs to be considered when choosing a suitable metallic substrate as different analytes have more affinities with certain metals. The literature survey also revealed that the main issues with SERS substrates are the reproducibility of signal enhancement and detection and these issues can be overcome by using micro array platforms which allow achievement of reproducible SERS signal and detection.

Chapter 3 saw the successful fabrication and selective surface modification of Au micro array platforms. Confirmation of micro array pore formations were confirmed visually using SEM. The micro array pores were then successfully modified exteriorly with mercaptohexanol and mercaptohexane using MCP and interiorly with SH-(c)-RGDFK peptide and thiocholesterol using a soaking method. These functionalization steps were confirmed using CV and EIS.

Chapter 4 employed the same fabrication and substrate-functionalization methods used in Chapter 3 and the SH-(c)-RGDFK and thiocholesterol functionalized Au micro array platforms were assessed for exosome capture. CFM was also used to further confirm SH-(c)-RGDFK Au micro array functionalization through the use of a labelled $\alpha_5\beta_1$ integrin which specifically recognises and binds to a (c)-RGD sequence. Successful exosome capture was confirmed using EIS, SERS and CFM with SH-(c)-RGDFK functionalized array platform giving more consistent, reproducible SERS results than thiocholesterol functionalized array platforms Ea,hy926 exosomes were successfully labelled with a BODIPY-Cholesterol and were successfully captured within a SH-(c)-RGDK functionalized array pore platform which was visually confirmed using CFM. However the LOD of the fluorophore-labelled probe and the small sizes of extracellular vesicles did not allow for further study of exosome morphology.

In Chapter 5, SH-(c)-RGDFK functionalized array platforms were solely employed for exosome capture and a new imaging method FE-SEM was chosen that would allow for further interrogation and study of both extracellular vesicle size and morphology. 4 sub-groups of unlabelled exosomes

from two different cell types were imaged, an immortalized Ea.hy926 -IG cell line and three sub-groups of primary HuAECs, the NG treated with 5mM of glucose, the HG treated with 30mM glucose and the MG treated with 5mM of mannitol. ImageJ was used to calculate the amount of exosomes captured per array pore with the HG showing the most captured per pore and the IG showing the least amount captured per pore.

Extensive SERS analysis of the three primary HuAEC sub-groups (NG, HG, and MG) was carried out and a training set of spectral-data of these sub-groups was successfully generated in collaboration with Prof. Mark Roantree and Mr Dinh Cuong, School of Computing Applications, DCU.

The observed SERS exosome spectra while highly heterogeneous, particularly in terms of relative intensity of contributing peaks showed the following notable differences and similarities, key difference(s) seem to suggest that the NG contains more phospholipid cargo than the other two sub-groups; The HG contains higher amounts of lactic acid and more protein cargo than the other two sub-groups and; The MG appears to contain more nuclear material within their cargo than in the other two sub-groups. It appears that treating cells with reagents *in vitro* will have an effect on resulting exosomal cargo.

6.2 Future Work

In Chapter 5, 10 representative spectra of each HuAEC exosome sub-group were presented from a total of: 1165 spectra of HuAEC exosomes-NG collected from 24 samples, 915 spectra of HuAEC exosomes-HG collected from 20 samples, and a further 865 spectra of HuAEC exosomes-MG collected from 18 samples, and some additional representative spectra from these datasets can be found in Appendix C. This is quite a large dataset and it will be used as a training database set for computer scientists to carry out multivariate statistical classification which would then further allow the blind testing of the machine-learning algorithm with exosome samples of unknown origins to see if the algorithm can correctly predict the origin of a spectrum.

SERS has many advantages, as an its application allows for the detection of the presence of a lipid, nuclear material and/or a protein/peptide structure, it has now been established by SERS that treating HuAECs with different reagents has an effect on resulting exosomal cargo, however, a disadvantage of SERS is that it does not allow any further identification of these structures. This limitation could be overcome by carrying out proteomic and RNAomic studies on the NG, HG and MG exosomes in order to gain further insight and understanding of the differences between their contained cargo.

 A good comparative study would be to carry out DLS studies and compare results from multiple batches of NG and HG isolated exosomes to assess if there is any overall difference in mean size of exosome sub-population. Two other control-studies would be to carry out the same DLS studies on exosomes sourced from primary HuVEC and A549 cell lines and compare with results shown in

Figures 5.10 and Table 5. Results from these experimental studies would further determine if primary cell lines have more integrin-binding capabilities than immortalized. Simultaneously DLS[1], Flow Cytometric[2] and NTA[3,4] studies on exosomes sourced from primary HuAECs, HuVECs, EA.hy926 and A549 cell lines would further highlight any substantial difference(s) in mean size(s) between immortalized and primary groups.

Successful application of the functionalized Au micro array platform could be employed in a number of areas. Keeping it in its current format with SH-(c)-RGDFK modified array interiors, fully-diseased HuAECs groups could be studied *in vitro* and *in vivo* for comparison. Biomedical samples from patients could also be taken and studied on the array platform, giving its further application considerable diagnostic potential. Analyses of exosomes from other primary endothelial cell groups could also be further carried out. The functionalized array platform could be applied for the study of exosomes sourced from a variety of MSCs in order to gain more insight to their contained cargo.

Alternative integrin-ligand interactions, particularly those integrins overexpressed on pathological exosomal surfaces could also be utilised to study and gain further understanding of their contained cargo. Also the application of a highly specific ligand which selectively interacts an integrin found only on a distinctive exosomal sub-population, yet to be thoroughly researched, would allow for more selective capture within the array-pore platform. This would allow for further study in both SERS and FE-SEM areas.

It is evident that the use of selectively modified Au micro array platforms has enormous potential in its current functionalized format and could prove to be even more versatile by undergoing further selective modification(s) which would allow for specifically targeting distinctive exosomal sub-population.

6.3 References

1   R. Maroto, Y. Zhao, M. Jamaluddin, V. L. Popov, H. Wang, M. Kalubowilage, Y. Zhang, J. Luisi, H. Sun, C. T. Culbertson, S. H. Bossmann, M. Motamedi and A. R. Brasier, *J. Extracell. Vesicles*, , DOI:10.1080/20013078.2017.1359478.

2   A. Clayton, J. Court, H. Navabi, M. Adams, M. D. Mason, J. A. Hobot, G. R. Newman and B. Jasani, *J. Immunol. Methods*, 2001, **247**, 163–174.

3   R. A. Dragovic, C. Gardiner, A. S. Brooks, D. S. Tannetta, D. J. P. Ferguson, P. Hole, B. Carr, C. W. G. Redman, A. L. Harris, P. J. Dobson, P. Harrison and I. L. Sargent, *Nanomedicine Nanotechnology, Biol. Med.*, 2011, **7**, 780–788.

4   M. Logozzi, D. Mizzoni, D. F. Angelini, R. Di Raimo, M. Falchi, L. Battistini and S. Fais, *Cancers (Basel).*, , DOI:10.3390/cancers10100370.

Appendices

Appendix A

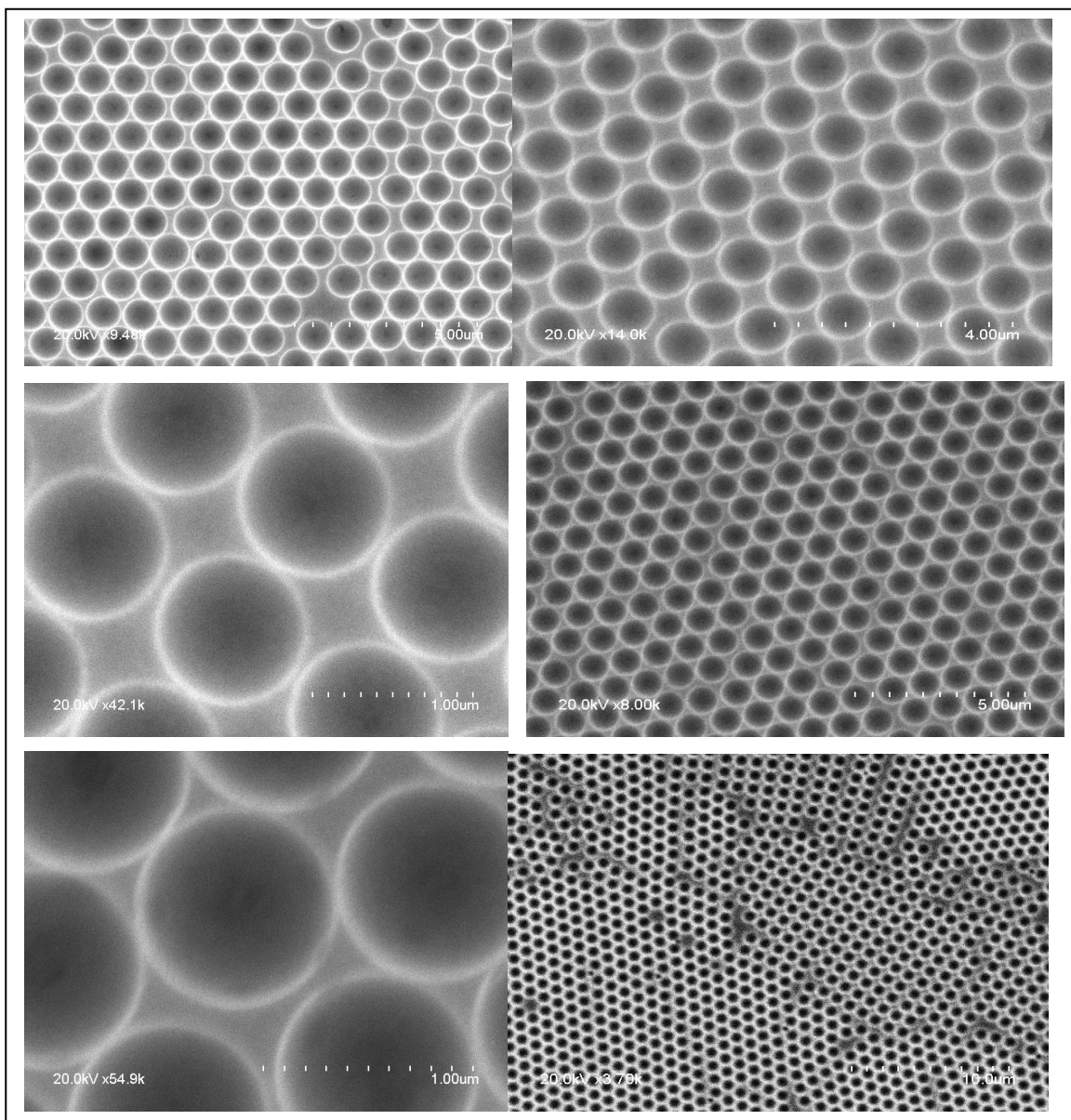### A.1 Additional SEM Images of Au Micro Array pore platforms

Figure S1.01: Additional Scanning Electron Images of 1-micron unfunctionalized Au Micro-Array platform on silicon wafer (after THF sonication) at 20kV under various magnifications at a working distance of 10 mm. Au was first electrodeposited between the spaces of the PS bead-monolayer from the Au salt solution (electrolyte) until the Au had grown to the equator of the polystyrene beads, this was determined by the start of an increase in the applied current following a decrease and from the shape of the graph on the software (See Figure 3.03, Chapter 3). The resulting micro-array platform was then rinsed with deionised water to remove any remaining Au salt solution/electrolyte from its surface. The platform was then immersed in THF to remove PS sphere-monolayer and was sonicated for 10 min to ensure thorough complete PS monolayer removal and then dried off using N_2 flow to cause complete THF evaporation within the micro array interiors.

Refer to Figure 3.04, Chapter 3 for experimental details. The purpose here is to show additional SEM images of the array pore platforms after sonication in THF solvent to remove the PS template.
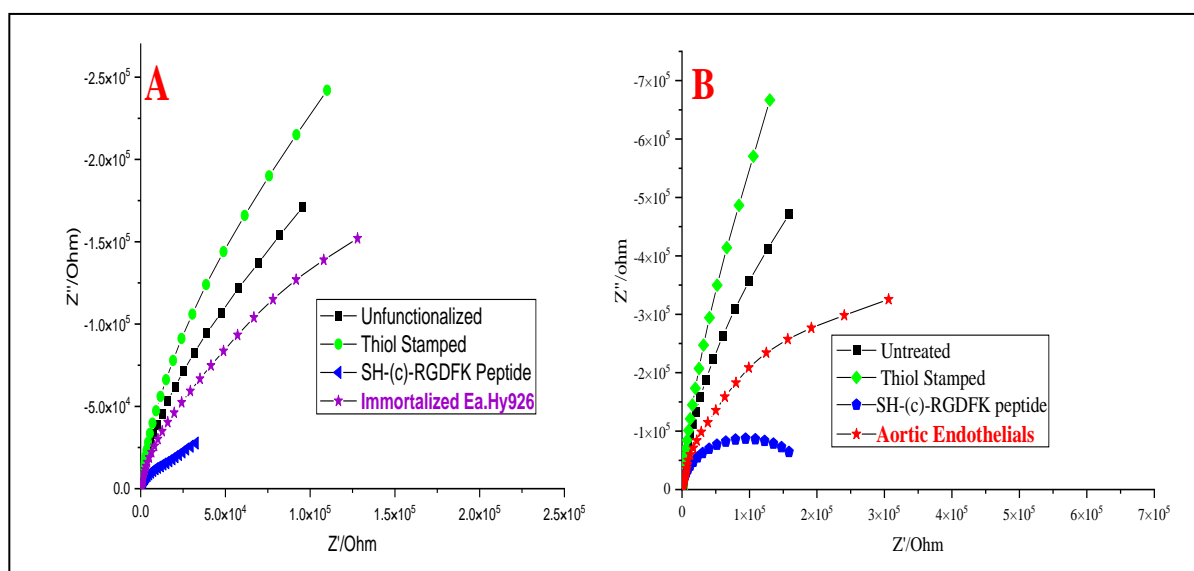
A.2 Additional EIS Data
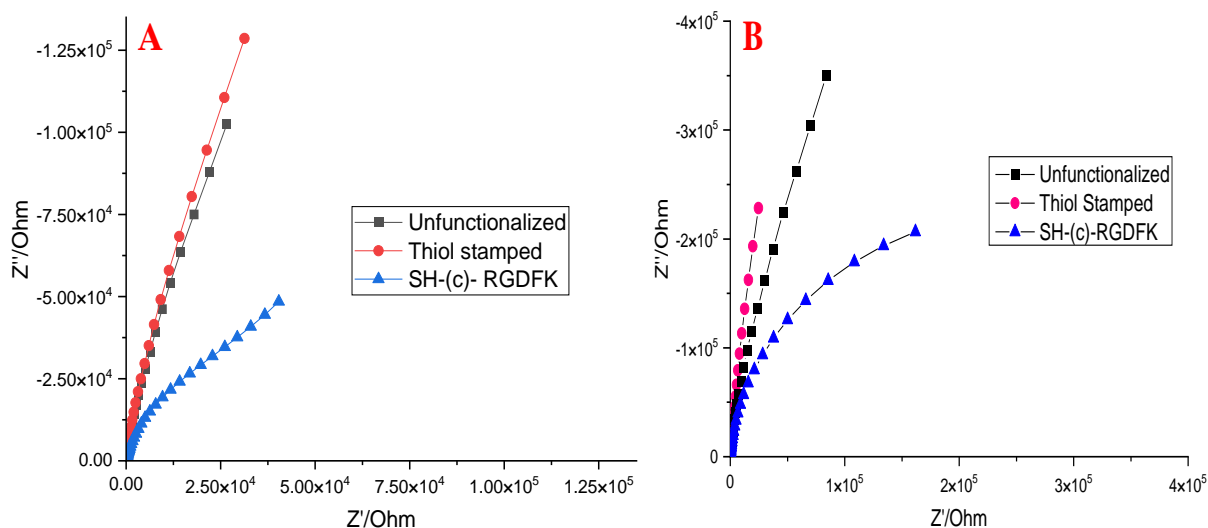
Figures S1.02A and B: Additional Nyquist Impedance Plot(s) of Au micro array platforms. Non-faradaic EIS measurements were carried out on an unfunctionalized planar Au platform in 100 mM PBS buffer from 0.1 Hz–10 kHz frequency range with a 0.01 V r.m.s. signal following this the planar Au platform was stamped with 10 mM mercaptohexane for 30 min and EIS measurements were carried out under identical conditions. After this step the micro array platforms were incubated in 1.2 µM SH-(c)-RGDFK for 24 h and EIS studies were carried out under the same conditions.. All EIS studies were carried out within a three-electrode cell set up, Ag/AgCl reference electrode, platinum wire auxiliary electrode and the planar Au substrate as the working electrode.

Refer to Figure 3.14 in Chapter 3 for the experimental procedure. The purpose here is to show additional EIS Nyquist plots of the array pore platforms to show that the SH-(c)-RGDFK functionalized Au micro array platforms did not give the exact same response under identical experimental parameters but peptide-functionalization was studied in great depth

Appendix B

B.1 Supplementary EIS Results

Figures S2.01A and S2.01B: Additional Nyquist Impedance Plot(s) of an Au micro array platform(s). Non-faradaic EIS measurements were carried out on an unfunctionalized Au micro array platform in 100 mM PBS buffer from 0.1 Hz–10 kHz frequency range with a 0.01 V applied potential, following this the Au micro array platform was stamped with 10 mM mercaptohexane for 30min. The Au micro array platforms were then incubated in 1.2 μM SH-(c)-RGDFK peptide solution for 24 h and EIS studies were carried out under the same conditions. This selectively modified platform was incubated in 0.5 mL of exosome-solution for 48 h at 4 ºC. The resulting EIS are shown in purple stars in A and red stars in B. Exosomes are from: (A) Immortalized umbilical vein cells EAhy926. (B) HuAECs (Normal group). All EIS studies were carried out within a three-electrode cell set up, Ag/AgCl reference electrode, platinum wire auxiliary electrode and the Au micro array platform as the working electrode.

Refer to Figures 4.08A and B, Chapter 4 for the experimental procedures used for Figures S2.01 above. The purpose of displaying the above Figures is to show the peptide response is slightly different after each study (as for Figures S1.01A and B shown previously), however exosome response after surface deposition is the same.

B.2 Supplementary SERS results

SERS studies were carried out after incubation of the Au micro array modified with SH-(c)-RGDFK with exosomes. SERS spectra were compared to SH-(c)-RGDFK modified Au

micro array interiors shown in Chapter 4 to determine if exosome capture had occurred within the micro array interiors.
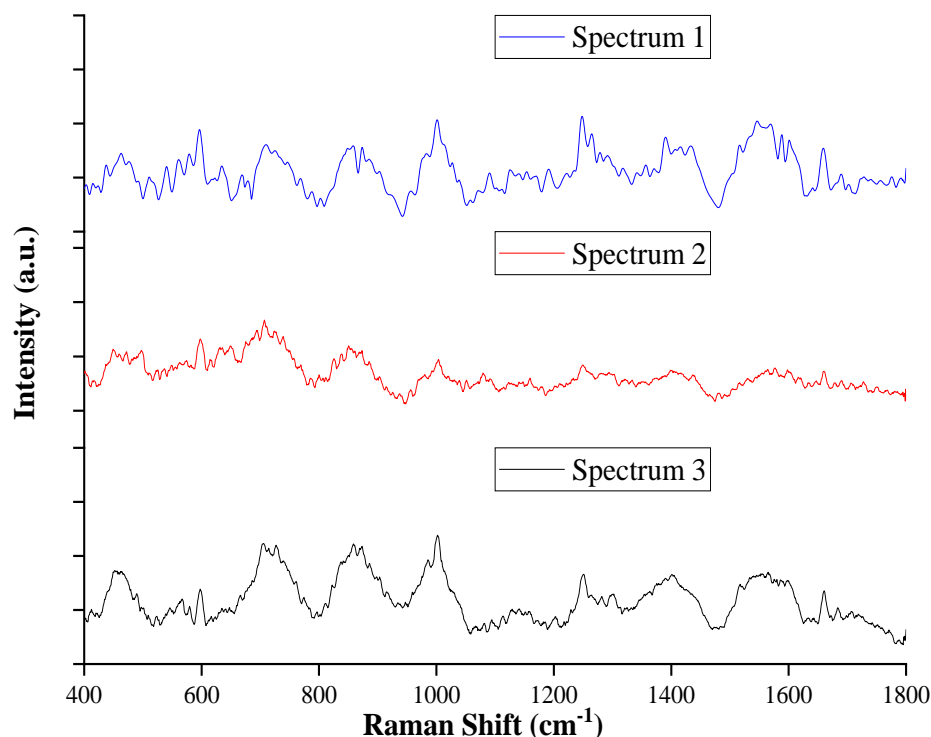

Figure S.2.02: Three sample SERS spectra of exosomes sourced from human immortalized umbilical vein cells-EA.hy926 captured within a SH-(c)-RGDFK modified Au micro array platform. was incubated in 0.5 mL of exosome solution for 48 h in a refrigerator at 4 °C. SERS analysis was carried out using a 1 % O.D. filter on a 785 nm laser source operating at full power of 60.2 mW. Spectral acquisition was 1 s with 4 s exposure time and 9 frame accumulations. All spectra were baseline corrected and normalised using standard and de-spike settings to remove background noise.

The same experimental procedure was carried out as per Figure 4.06, Chapter 4, except that the O.D. filter used for Figure S2.02 above was 1 % instead of 10 % and exosomes used were human immortalized Ea.hy926 and not primary HUVECs. The signal-to-noise ratio in the resulting-spectra above were quite high. From these results, it was decided to use a 10 % O.D. filter instead to improve signal-to-noise ratio.

Appendix C

C.1 Supplementary FE-SEM Results
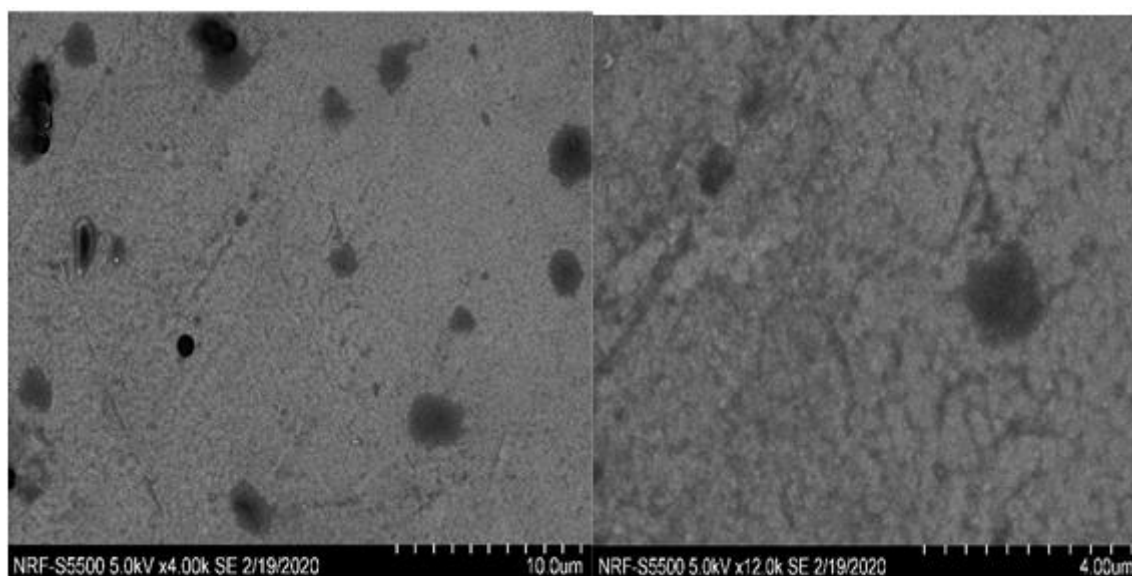
Figure S3.01: FE-SEM (using various magnifications) images of an Au micro array template (after Au electrodeposition around the 1-micron diameter PS-monolayer) on an Au-silicon wafer. Incident electron beam (V_{acc}) settings was set to 5 kV. The sample-stage was set at a working distance of 5 mm. Emission current (Ie) settings were 20 μA.

The purpose of these images is to show the PS template before sonication in THF solvent. This is to further understand the fabrication step method of the Au micro array platform and the importance of the sonication step in solvent. After sonication in THF solvent, the unmodified Au micro array platforms can be seen in Figure S3.02 below.
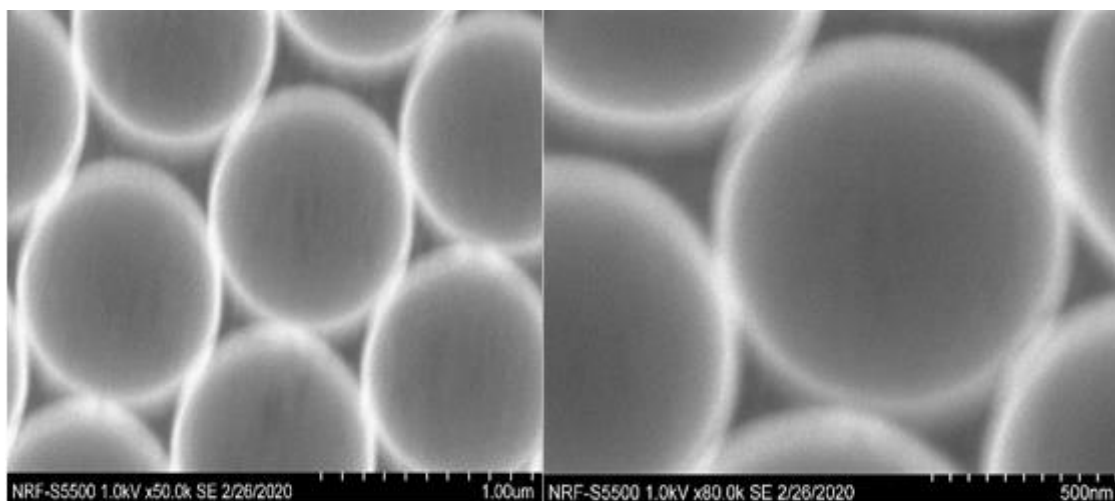
Figure S3.02: FE-SEM (using various magnifications) images of an Au micro array platform on an Au silicon wafer after sonication in THF solvent to remove the PS template. Prior to FE-SEM studies, the platform was incubated in 0.5 mL 100 mM PBS for 48h. Incident electron beam (V_{acc}) settings were set to 1 kV. The sample-stage was set at a working distance of 5 mm. Emission current (I_e) was set to 20 µA.

The rationale of this experiment was not to take pristine images of unmodified array pores. The purpose of this experimental study was to image plain, unmodified array pores under the same parameters used to image exosomes. Firstly to demonstrate the smoothness of the array pore interiors and secondly to show that the spreading within the pores after exosome incubation is due to RGD ligand-exosomal integrin binding.
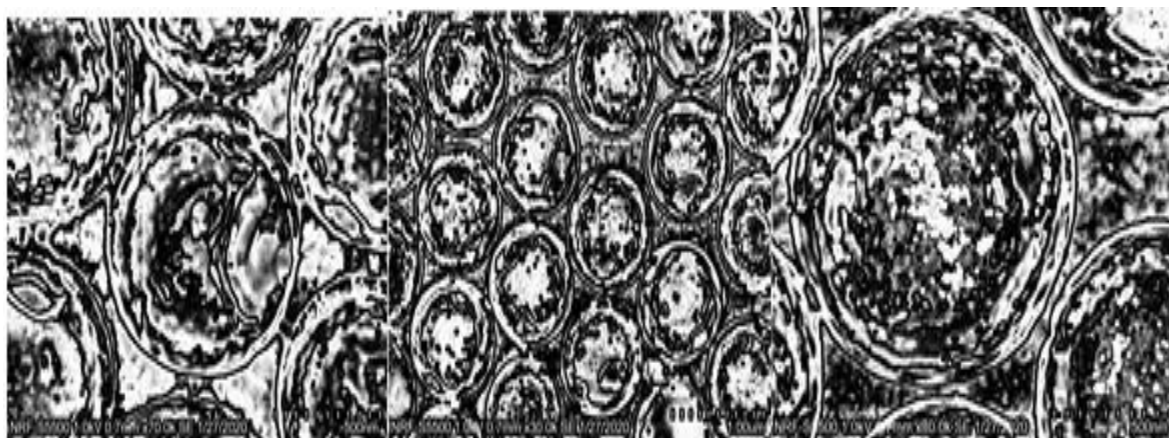
Figure S3.03 Three representative FE-SEM images (under various magnifications from Chapter 5) edited with the "contrast" threshold setting on ImageJ software that was used to count the particles within the array pores. The area within an array pore was outlined and all white particles were counted as particles by the software. Black areas were classed as background.

The purpose of these images is to show how the ImageJ software works by changing the contrast settings on an image which is the converted into a binary image which can then be further analysed

using the software settings. And also justify the "Contract" threshold (discussed in Chapter 5) used to count exosomes within the array pores. was to image plain, unmodified array pores under the same parameters used to image exosomes. Firstly to demonstrate the smoothness of the array pore interiors and secondly to show that the spreading within the pores after exosome incubation is due to RGD ligand-exosomal integrin binding.

C.2 Tabulated Data from Chapter 5 Containing All Assigned Major Peaks

Table S1: All assigned major peaks of primary HuAEC-NG exosomes from Figure 5.10, Chapter 5.

Raman Shift (cm^{-1})	Corresponding Spectra on Figure 5.10, Chapter 5.	Presumed Origin
407-495	1,2,4-6, 8-10	Glycogen Fingerprint Region
429, 548	2, 3	Cholesterol
453/4	4, 6, 7	Ring torsion of a phenyl group
516-537	1,3,5,7,8, 10	S-S stretching (protein)
519	4, 5, 9	Phosphatidylinositol
572	5	Amino acid W/ C and G bases
603-7	1, 3,	Nucleotide conformation
614	6	Cholesterol ester
620-4	3,4, 8	aromatic ring C-C twist, most likely due to F
632-672	1-5, 7-10	ν(C-S) *gauche* in amino acid M
680-699	1-3, 4-8	Nucleotide conformation
700-38	5, 10	ν(C-S) *trans* (amino acid M)
728	6	C-C stretching in amino acid P (collagen assignment)
735	8	C-S stretch
759	2	Amino Acid W
803	1, 10	Uracil-based ring breathing mode
813	9	Distinct peak for RNA/ C-C stretching (in collagen)
817	3	C-C stretching in collagen
821-39	2, 6, 8	(C-C) stretch of amino acid P and/or its derivative hydroxyproline; Also a PO_4^{3-} vibration
844/5	3, 4	Polysaccharide structure
853	5	Ring breathing mode of Y/ C-C stretch of P ring/ Glycogen
862	7	General Protein band
886/7	1, 5, 8	ρ(CH_2) (in protein)

892	10	ν (C-C) skeletal backbone
928	1	ν(C-C) stretching probably in amino acids P & V (protein band)
963	3	Unassigned mode in protein structures/ CH'$_{2,6}$ out-of-plane bending
970	2, 5	Phosphate monoester groups of phosphorylated proteins and/or cellular nucleic acids
945, 980	7, 9	General Protein band
972	1, 7, 8, 10	C-C backbone (collagen assignment)
974	4	Ribose vibration
1000-1003	1, 3-8, 10	Amino acid F, also aromatic C-C stretching
1024	5	Glycogen
1030- 1036	1, 3, 6, 8, 10	F residues within collagen
1032	4	CH_2 CH_3 bending (in phospholipids) / ν(C-C) (in polysaccharides)
1060-1078	2, 6 -8	PO_2^- stretching (in DNA/RNA)/ Chain C-C stretching (lipids)/ C-O, C-C stretching (carbohydrates)
1078	4	ν(C-C) or ν(C-O) in phospholipids/ Pronounced symmetric phosphate stretch/ C-C or C-O lipid stretch/ C-C or PO_2^- nucleic acid stretch
1082	1, 8	Carbohydrate residues of collagen/ Also indicative of nucleic acids
1084	2	Symmetric PO_2^- stretching of DNA
1085	3	PO_4^{3-} groups in nucleic acids
1122	10	(C-N) stretch (protein assignment) (C-C) stretching mode of lipids & protein
1128	4	C-N stretching (proteins)/ C-O stretching (carbohydrates)
1132-1152	4-6	ν(C-C)-lipids, fatty acids
1152	2	Carotenoid
1169	4	Y in collagen type I
1170	3, 5, 7	C-H in-plane bending mode of amino acid Y
1177	2	C and G bases (in DNA/RNA)
1188-1196	4-6	Anti-symmetric phosphate vibrations
1212-94	1,4-8	Amide III(C-N stretching and N-H bending vibrations)/ Alternatively indicative of nucleotides
1252	3, 5	G and C bases/ C-O$_4$ aromatic stretch
1255	7	General Lipid band
1271	5	Amide III / C=C (in fatty acids)
1291	5	C base

D

1293	1, 8	Amide III and/ or C base
1296	2	$\delta(CH2)$ in lipids
1298	7	CH bending
1301	4	Triglycerides (fatty acids) (54) $tw(CH_2)$ in lipids
1304	10	$\delta(CH_2)$ in lipids/ A and C bases
1307	3	C-N asymmetric stretching (e.g., protein)/ $CH_3\,CH_2$ twisting (e.g., lipid)
1321	1	G (DNA/RNA) and/or $\delta(CH)$ in protein
1323, 1357	2, 9	G base
1340	1, 3	Collagen assignment/ Nucleic acid modes
1343	9	CH_3, CH_2 wagging in collagen assignment
1360	5	W
1365	3	Amino Acid W
231	3, 10	CH_3 band
1398	2	C=O symmetric stretch/ $\delta(CH_2)$
1408	5	$\nu(C=O)O^{2-}$ (in amino acids D and E)
1421	6	Deoxyribose, (B,Z-marker) A, G (ring breathing modes of the DNA/RNA bases)
1427-46	1, 3-5, 8, 10	CH_2 scissoring vibrations (lipid band) CH_2 bending mode of proteins and lipids G, A bases (in DNA and/or RNA) $\delta(CH)$ in DNA/RNA & proteins, lipids and carbohydrates)
1440	5, 7	$\delta(CH_2)$, also indicative of cholesterol
1448/50	3, 1, 9	$\nu(C-H)$ in proteins (collagen) or lipids
1451	6, 8	CH_2CH_3 deformation (collagen assignment)
1492-9	2, 9	Amide II/ $NH3^+$
1507	10	C base
1510	2	A base (ring breathing mode)
1520-1533	1-7, 10	Carotenoid -C=C-
1544	3,7	Amide II Protein
1558	4	Amino acid W/ $\nu(C-N)$ and $\delta(N-H)$ in amide II protein/ $\nu(C-C)$ porphyrin
1574-6	5, 6	Nucleic Acid bases A and G
1580	7	C-C stretching
1584	1, 8	C=C bending mode of F
1585	2	Olefinic C=C stretch (protein assignment)/ F, or its derivative hydroxyproline.

E

1542-1594	3, 4, 9, 10	Amide carbonyl group vibrations and aromatic hydrogens
1602	1, 8	δ(C=C) in F
1605	7	C base/ aromatic C-C stretch of phenyl group/ Also indicative of F,Y, C=C (protein vibration)
1611-1653	2, 7, 9	Amino Acid Y/ Amide I band of proteins due to C=O stretching/ Amide carbonyl group vibrations and aromatic hydrogens
1626	4	Cα=Cα stretch Amide C=O stretching absorption for the β-form polypeptide films
1668	1, 8, 10	Amide I band (protein)
1728	4	ν(C=O)OH (in amino acids D and E)

Table S2: All assigned major peaks of primary HuAEC-HG exosomes from Figure 5.13, Chapter 5.

Raman Shift (cm^{-1})	**Corresponding Spectra on Figure 5.13, Chapter 5**	**Presumed Origin**
418	7	Cholesterol
402-562	1-10	Glycogen Fingerprint Region
453	3	Ring torsion of a phenyl group
476-478	4, 9	Polysaccharides
481	3	DNA
484	1	Glycogen
510-550	3, 4, 5, 6, 9, 10	S-S stretching (protein)
611	3	Cholesterol
618-624	1, 2, 5, 8	aromatic ring C-C twist, most likely due to F
630	4	Glycerol
634-652	2-6, 9, 10	ν(C-S) *gauche* in amino acid M
646	1	C-C twisting mode of W
671-694	2-5, 7-9	Nucleotide conformation
704-714	4, 7	ν(C-S) *trans* (in amino acid methionine)/ Nucleotide conformation
728, 766,	6, 10	C-C stretching in collagen/ Amino Acid P

733	3	Phosphatidylserine
765-795	1, 4, 5, 9, 10	Nucleotide conformation
806/7	8, 10	General Protein band
808-812	3, 4, 5, 9	Phosphodiester (Z-marker)
818	2	C-C stretching in collagen
820	6	Protein band/ Structural tumorigenic protein modes
827	1, 5	Amino acid P, hydroxyproline and/or Y/ also $\nu(PO_2^-)$ in nucleic acids
844-861	1, 2, 3, 8, 9	Polysaccharide structure/ Protein/ Carbohydrate fingerprint region
849	6	C-C stretch of amino acid P or its derivative hydroxyproline
853	5	Ring breathing mode of Y/ C-C stretch of ring in amino acid P
855	4	ν(C-C) in amino acids P and/or Y, δ(CCH) ring breathing in F (olefinic protein assignment)/ C-C stretching in Y, P and/or hydroxyproline (collagen assignment)
881	3	δ(ring) of W
885	1	Disaccharide (cellobiose)/ (C-O-C) skeletal mode
924-939	8, 9	ν(C-C), stretching-most likely due to amino acids P & V
941	6	Polysaccharide band
974	5	Ribose vibration
978	2	C-C stretching in β-sheet protein structures/ =CH bending (in lipids)
983	3	C-C stretching β-sheet (proteins)/ =CH bending (in lipids)
1001-1006	1-10	C-C aromatic ring stretching Amino Acid F
1019	1	Stretching C-O in ribose
1030	4, 5	F found in collagen
1049	9	Glycogen
1067/8	4, 5, 8	Proline (in collagen)
1062-1077	1, 9, 10	Symmetric PO_2^- stretching (in DNA/RNA)/ Also indicative of C-C stretching (in lipids)/
1082	2	Carbohydrate residues of collagen/ Nucleic acids
1088	3	C-C stretch/ PO_2^- stretch
1099	6	protein ν(C-N)
1114	6	lipid ν(C-C)
1121	10	Strong Ribose (C-O) band

1126	4	C-N protein stretching vibration (72)
1127	1	ν_{22} (porphyrin half ring)/ C-C stretch (in either lipid or protein)/ Also, ν(C-N) in protein
1129-1132	2, 3, 8	skeletal ν(C-C) of acyl backbone in lipid
1110-1159	5, 7, 9, 10	Amide III
1150-1157	2, 4, 6	Carotenoid/ In-plane vibrations of conjugated =C-C=
1163-1172	3, 4, 5, 6, 10	Y (specifically in collagen type I)/ δ(C-H) vibrations in F and/or Y
1190-1196	4, 9	Anti-symmetric phosphate stretching vibrations
1200	8	Nucleic acids and phosphates/ Aromatic ν(C-O) and ν(C-N)
1202	3	Amide III(C-N) stretching and (N-H)bending vibrations)/ Alternatively indicative of nucleotides
1221	4	Amide III (β-sheet)/ T and A bases in DNA/RNA/ =CH bending (in lipids)
1230	2	Antisymmetric phosphate stretching vibrations
1231-1282	1, 5, 7, 8, 10	Amide III (arising from coupling of C-N stretching & N-H bonding)
1250-1259	3, 4, 6, 9	ν(NH_2) in G and C bases/ Amide III protein vibrations
1279	8	Amide III (α-helix)
1280-1294	2, 7	Amide III (α-helix)/ Amide III and CH_2 wagging vibrations from G backbone & P side-chains/ Collagen/ Nucleic acids and phosphates
1287	6	PO_4^{3-} groups in nucleic acids
1296	2	CH_2 scissoring vibration (lipid band) CH_2 bending mode of proteins & lipids/ G, A bases (DNA, RNA) / Also due to δ(C-H) in DNA/RNA, proteins, lipids and/or carbohydrates.
1301	1	Triglycerides, CH_2 twisting and C-H vibrations in lipids
1302	3	δ(CH_2) twisting, wagging, and/or bending of collagen and phopholipids (protein or lipid assignment)/ Amide III (protein)/ Also indicative of Methylene bending mode (a combination of proteins & phospholipids)
1308	5	asymmetric C-N stretching in asymmetric aromatic amines
1311	4	CH bending
1318	9	G Base (B,Z-marker)

1357-1364	1, 5, 9	G base (in the N_7 form, B,Z-marker)
1369	1	G base/ TRP (protein)/ porphyrins/ lipids
1370	3	The strongest saccharide band
1377	7	lipid ν(C-C)
1386	5	CH bending
1397	4	C=O symmetric stretch
1418	9	ν(C=O)$^-$ in amino acids D and E
1429-1480	3, 5,6, 8, 10	CH_2 scissoring-vibration in lipids)/ CH_2 bending mode of proteins & lipids/ G and A bases in DNA, RNA/ δ(C-H) in DNA/RNA, proteins, lipids and/or carbohydrates.
1437/8	1, 4	$\delta(CH_2)$ in lipids/ Acyl chains/
1453	3	Protein bands/ Umbrella mode of methoxyl/ C-H bending mode of structural proteins/ Also,structural protein modes of tumors
1454-1468	2. 9	Overlapping asymmetric CH_3 bending & CH_2 scissoring (is associated with elastin, collagen, and phospholipids)
1484-1492	2, 3, 6, 8, 9	Amide II (due to a coupling of C-N stretching & in-plane bending of the N-H group)
1499-1501	4, 7	NH_3^+/ C=C stretching in benzenoid ring
1505	2	N=H bending
1508	10	C base
1528-1533	1, 5, 9, 10	Carotenoid -C=C-
1544-1594	1-10	Amide carbonyl group vibrations and aromatic hydrogens/ Amide II vibrations/ COO$^-$ vibrations
1582/1587/1602	3, 6, 7	δ(C=C) in F
1584	1	Olefinic protein C=C stretch
1608/9	3, 9	NH_2 in Cytosine
1625-1643	5, 7, 9	Amino Acid Y/ Amide I band of proteins due to C=O stretching/ Amide carbonyl group vibrations and aromatic hydrogens

Table S3: All assigned major peaks of primary HuAEC-MG exosomes from Figure 5.14, Chapter 5.

Raman Shift (cm^{-1})	Corresponding Spectrum on Figure 5.14, Chapter 5	Presumed Origin
406-599	1-10	Glycogen Fingerprint Region
447-453	1, 7, 9	Ring torsion of a phenyl group
508-546	3-9	S-S stretching (protein)
589	3	Symmetric stretching vibration of v_4 PO_4^{3-}/ Glycerol
613	10	Cholesterol (ester)
617/8	1, 7	Protein C-C torsion
622	4, 8	Aromatic ring C-C twist, most likely due to F
644	4	tw(C-C) mode of Y
631-669	3, 4, 6, 9, 10	v(C-S) *gauche* in amino acid M
726	1	C-S (protein)/ ρ(CH$_2$)/ A base
736-745	4, 7, 8	v(C-S) *trans* (amino acid M)
751	6	Symmetric breathing of W
604, 679-777	3, 5-10	Nucleotide conformation
803-808	2, 3, 5	General Protein band
816-818	2, 7, 10	C-C stretching in collagen
835/6	2, 5	v(C-C) stretch of amino acid P and/or its derivative hydroxyproline; Also a PO_4^{3-} vibration
841-845	8-10	Polysaccharide structure
865	7	Ribose Vibration
875	4	Antisymmetric stretch vibration of choline group N^+(CH$_3$)$_3$ (a phospholipid-characteristic)/ Also indicative of Phosphatidylcholine and/or sphingomyelin
881	1	δ(ring) of W
886	3	ρ(CH2) (in protein)
892	9	C-C skeletal backbone
916/7	7,8, 10	Ribose Vibration
918-920	1, 5, 6	C-C stretch Amino Acid P and/or its derivative Hydroxyproline/ Glycogen and lactic acid
909-947	4, 6, 8	General Protein band
964	4	Unassigned mode in protein structures/ CH'$_{2,6}$ out-of-plane bending

972	1	C-C backbone (in collagen)
976/7	7, 9	Ribose Vibration
979	2	β-sheet protein C-C stretching/ =CH lipid bending
988	3	Unassigned band but previously found and reported in exosomal-isolates
1001-1004	1, 5-10	Amino acid F, also aromatic C-C stretching
1024	3	Glycogen
1032-1034	1, 2, 5-10	F residues within collagen
1075-1078	1, 3, 4	PO_2^- stretching (in DNA/RNA)/ Chain C-C stretching (lipids)/ C-O, C-C stretching (carbohydrates)
1081	6	$\nu_1 CO_3{}^{2-}$, $\nu_3 PO_4{}^{3-}$, ν(C-C) skeletal of acyl backbone in lipid (*gauche* conformation)
1082	7	Carbohydrate residues of collagen/ also indicative of Nucleic acids
1084/5	5, 10	Symmetric PO_2^- stretching of DNA
1111	3	δ(Benzoid ring)
1114-1200	2-4, 7-10	ν(C-C) in lipids/fatty acids/ Amide III
1162-1166	2, 5, 7	Y (specifically in collagen type I)
1174	8	C-H bend in either Y and/or F
1177	4	C and G bases
1185	9	Anti-symmetric phosphate vibrations
1202-1338	1, 4, 5, 7, 8, 10	Amide III(C-N stretching and N-H bending vibrations)/ Alternatively indicative of nucleotides
1224	3	Amide III (β-sheet structure)
1250-1253	6, 8, 10	NH_2 in G and C bases
1253	3	Aromatic $C-O_4$ stretch
1270/1	2, 9	Typical phospholipid band/ Also an Amide III protein band (specifically caused by a C-N stretch in α-helix proteins)
1280	3	Amide III (α-helix)/ Amide III and CH_2 wagging vibrations from G backbone & P side-chains/ Collagen/ Nucleic acids and phosphates
1287-1292	4, 6, 9, 10	C base
1300/1	1, 7	Triglycerides (fatty acids) tw(CH_2) in lipids
1308	3	asymmetric C-N stretching in asymmetric aromatic amines
1311	7	CH bending
1345	10	CH_3, CH_2 wagging in collagen assignment

1391	1	ρ(CH)
1406	3	ν(C=O)O^{2-} (in amino acids D and E)
1424	8	Deoxyribose, (B,Z-marker)
1436-1442	5-7, 10	CH$_2$ scissoring vibrations (lipid band) CH$_2$ bending mode of proteins and lipids G, A bases (in DNA and/or RNA) δ(CH) in DNA/RNA & proteins, lipids and carbohydrates)
1438	1, 6, 8	δ(CH$_2$)
1457-1462	5, 8	Overlapping asymmetric CH$_3$ bending & CH$_2$ scissoring (is associated with elastin, collagen, and phospholipids)
1471-1477	3, 4	G and A bases in DNA, RNA/ δ(C-H) in DNA/RNA, proteins, lipids and/or carbohydrates.
1487/1497	3, 7	Amide II/ NH3$^+$
1511	9	A base (ring breathing mode)
1513/1515	2, 10	C base
1522	5, 6	Carotenoid -C=C-
1540-1595	1, 3-10	Amide carbonyl group vibrations and aromatic hydrogens/ Amide II vibrations/ COO$^-$ vibrations
1573	2	G and A bases/ TRP (protein)
1576	1	Nucleic acid mode(s)/ G base (in N$_3$ form)
1588/1590	5, 9	Amide carbonyl group vibrations and aromatic hydrogens/ Amide II vibrations/
1611	9	Amino Acid Y/ Amide I band of proteins due to C=O stretching/ Amide carbonyl group vibrations and aromatic hydrogens
1626	1	Cα=Cα stretch Amide C=O stretching absorption for the β-form polypeptide films
1623-1639	5, 7, 10	Amino Acid Y/ Amide I band of proteins due to C=O stretching/ Amide carbonyl group vibrations and aromatic hydrogens
1668	10	Amide I band (protein)
1704	3	ν(C=O)OH (in amino acids D and E)

L

C.3.0 Supplementary SERS Results

C.3.1 Primary HuAECs- NG
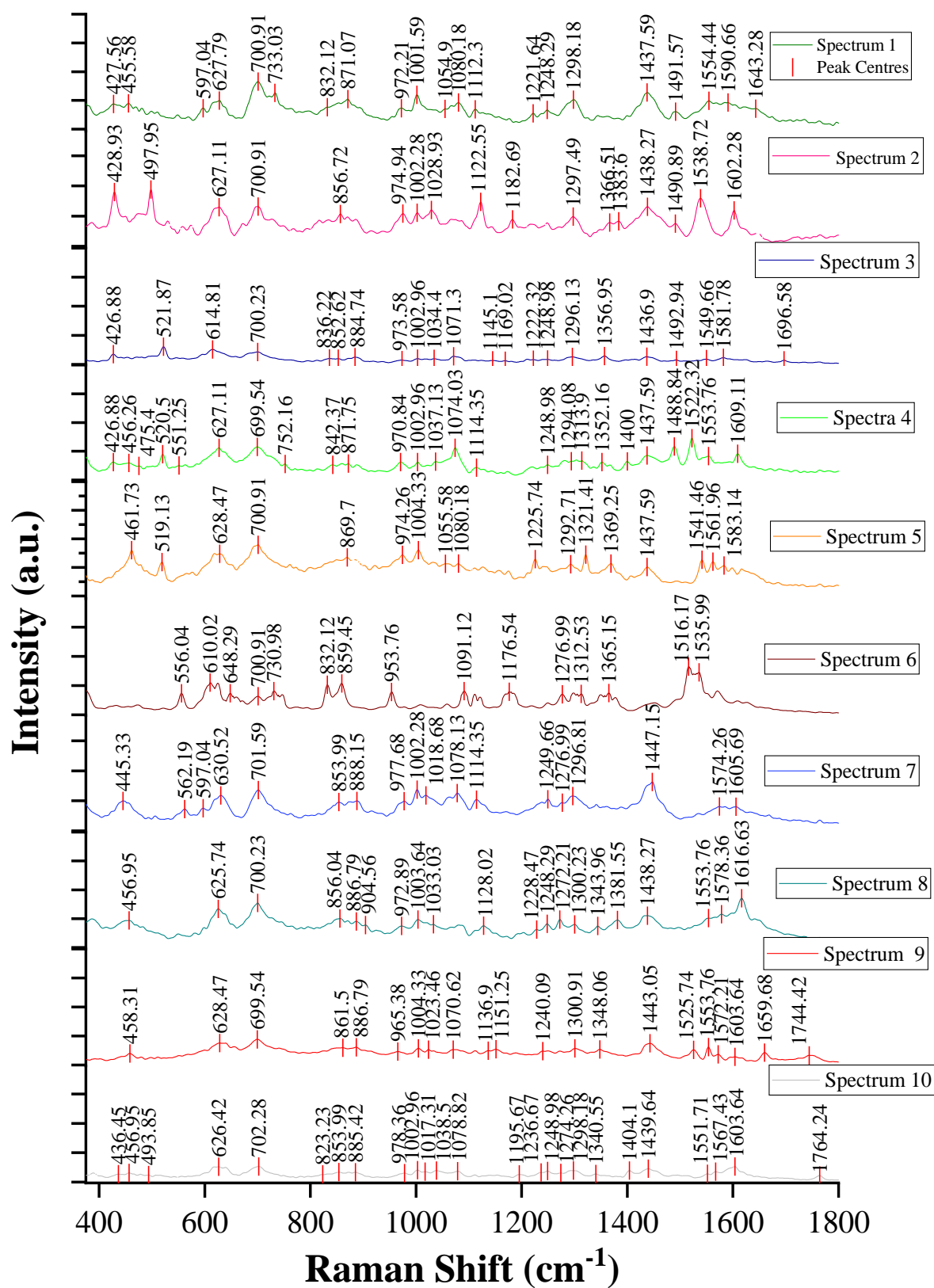
Figure S3.04: Ten representative SERS spectra of exosomes from primary HuAECs -NG within a SH-(c)-RGDFK functionalized Au micro array platform.
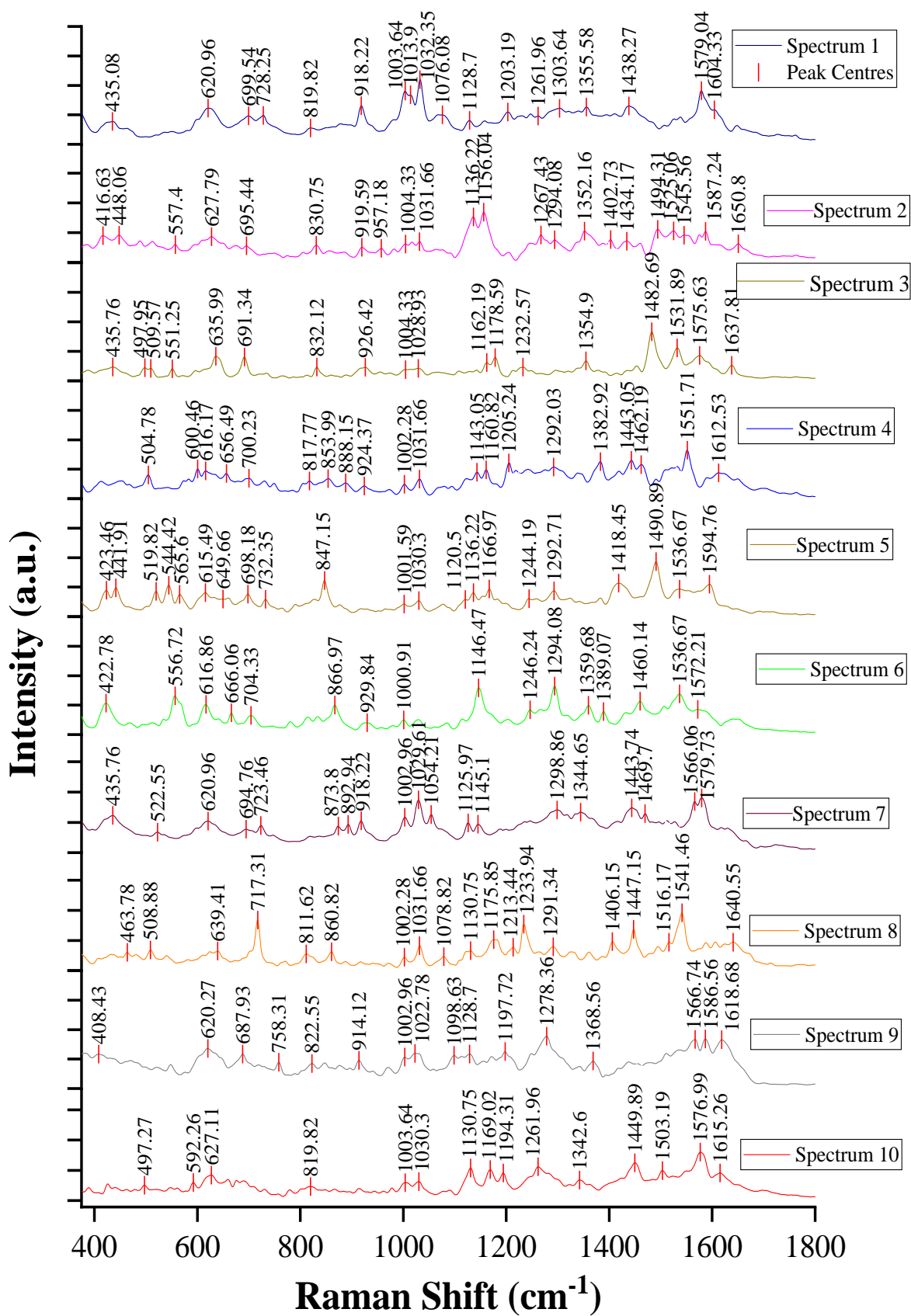
Figure S3.05: Ten representative SERS spectra of exosomes from primary HuAECs -NG within a SH-(c)-RGDFK functionalized Au micro array platform.
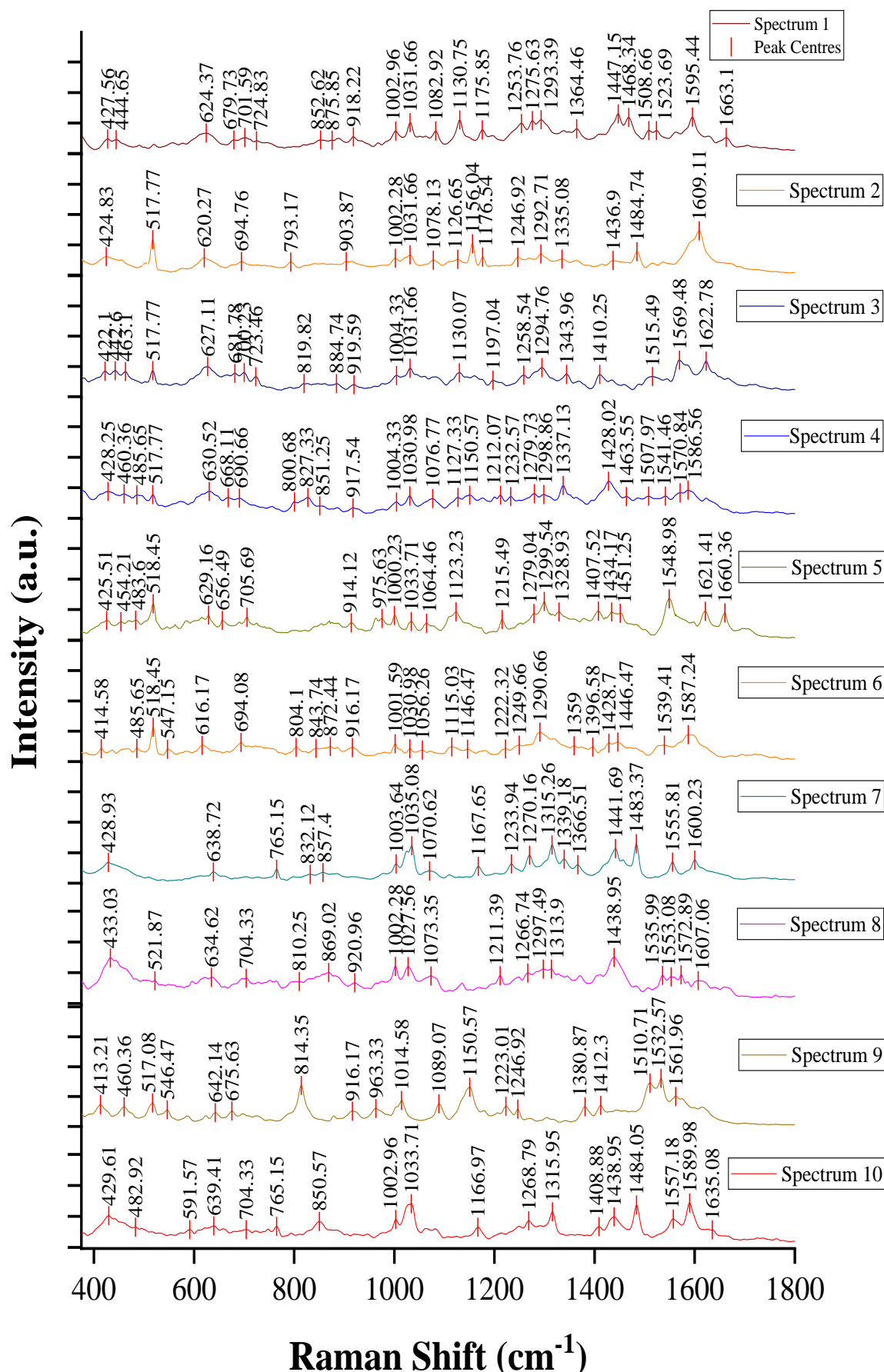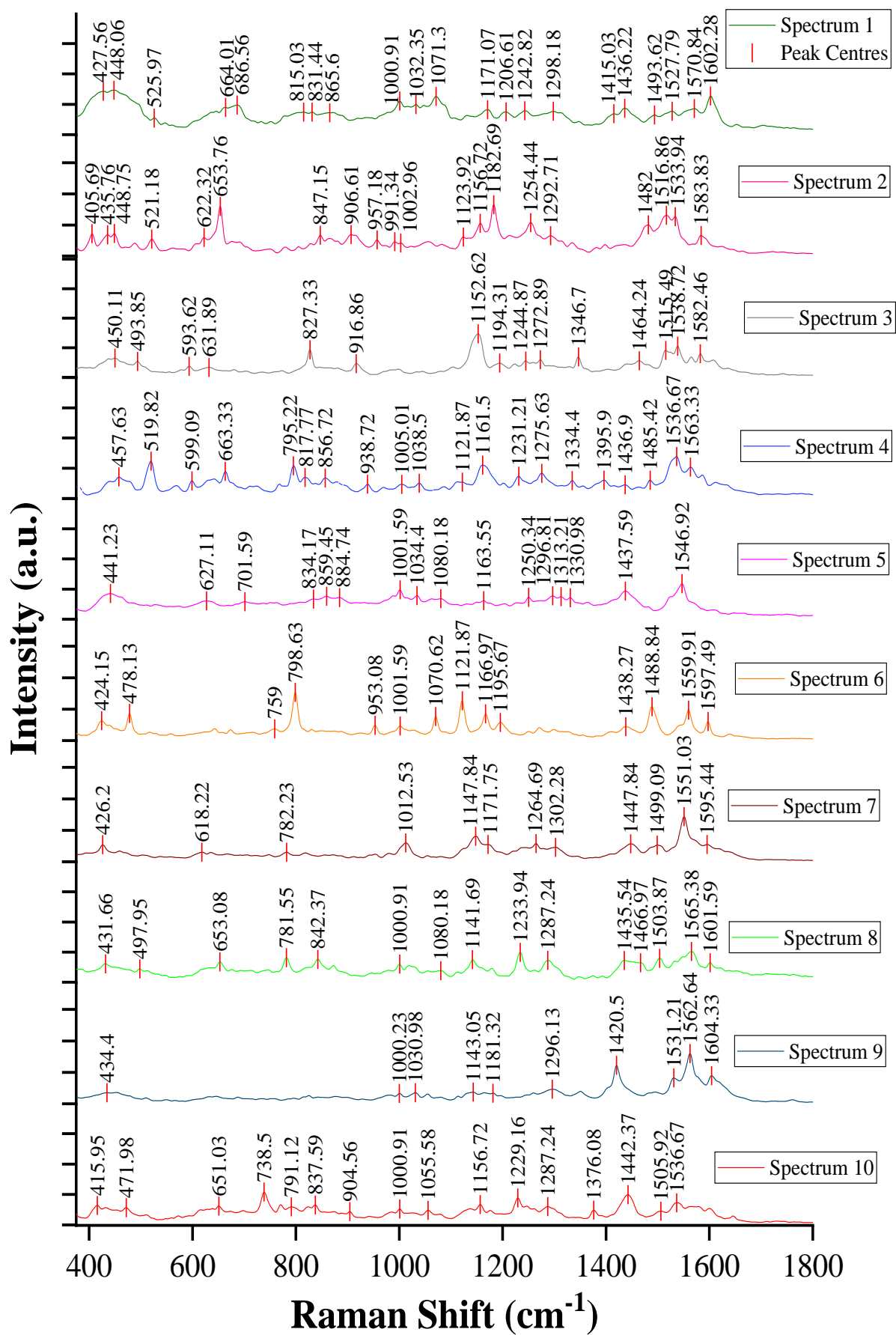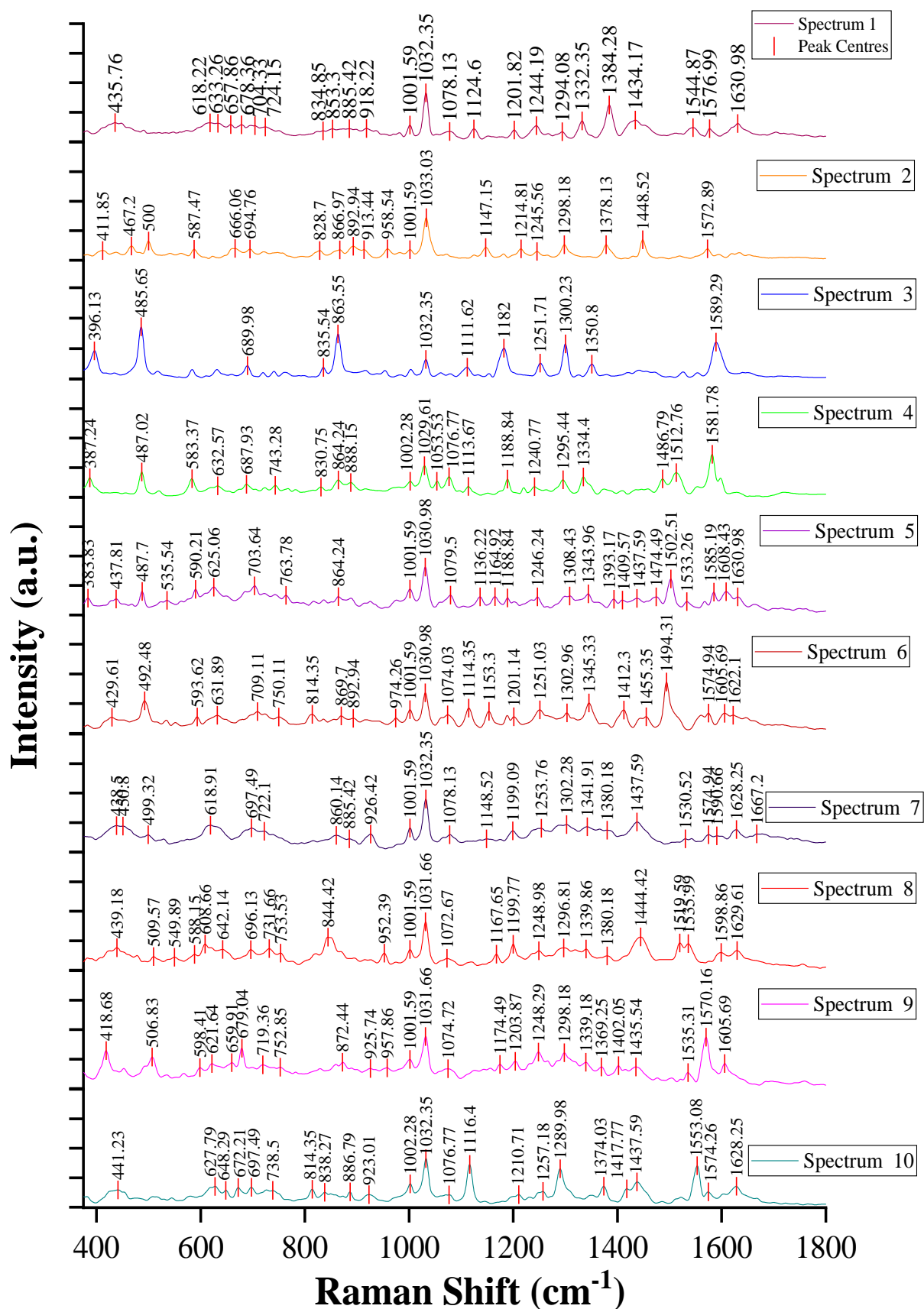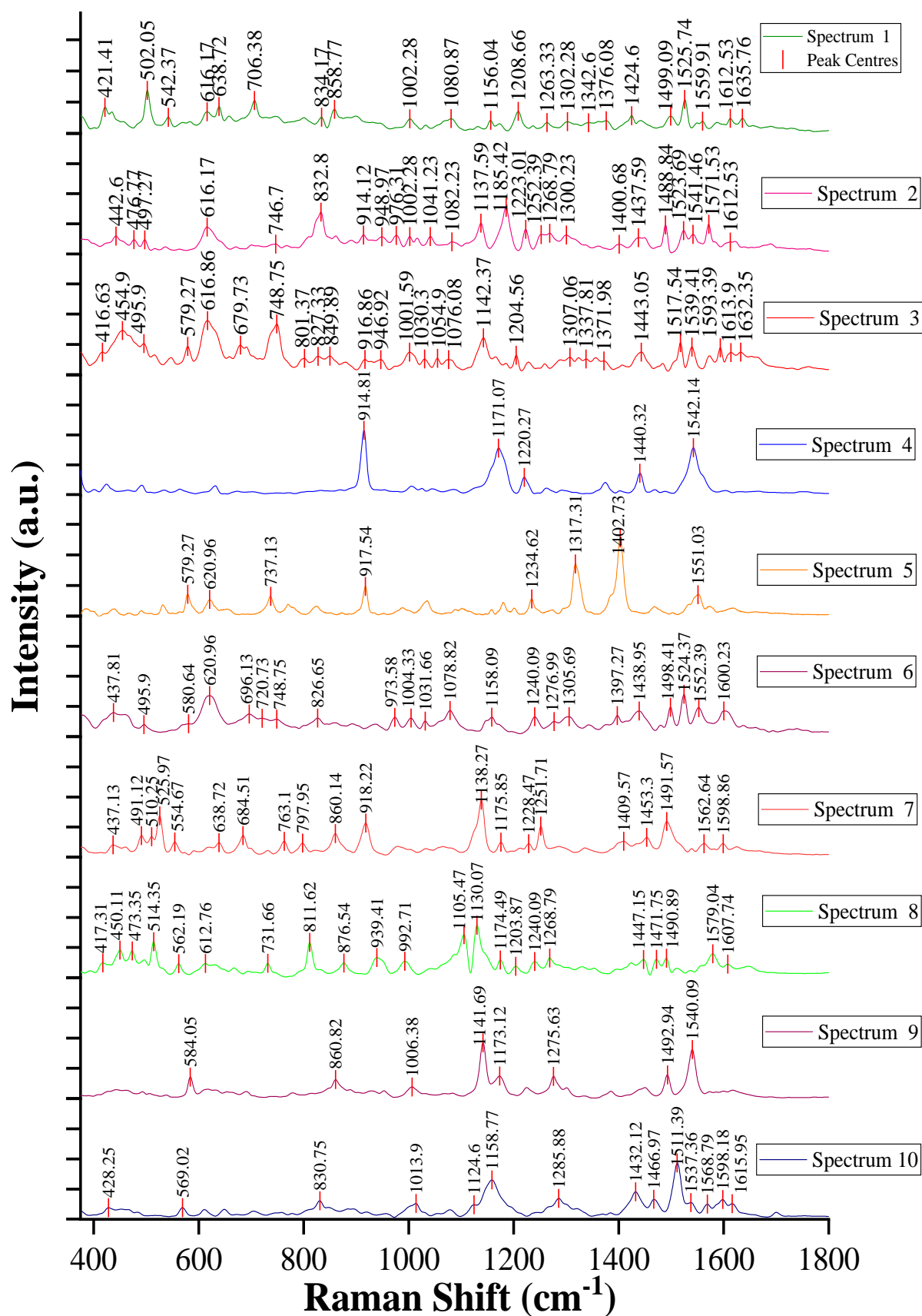
Figure S3.06: Ten representative SERS spectra of exosomes from primary HuAECs-NG within a SH-(c)-RGDFK functionalized Au micro array platform.
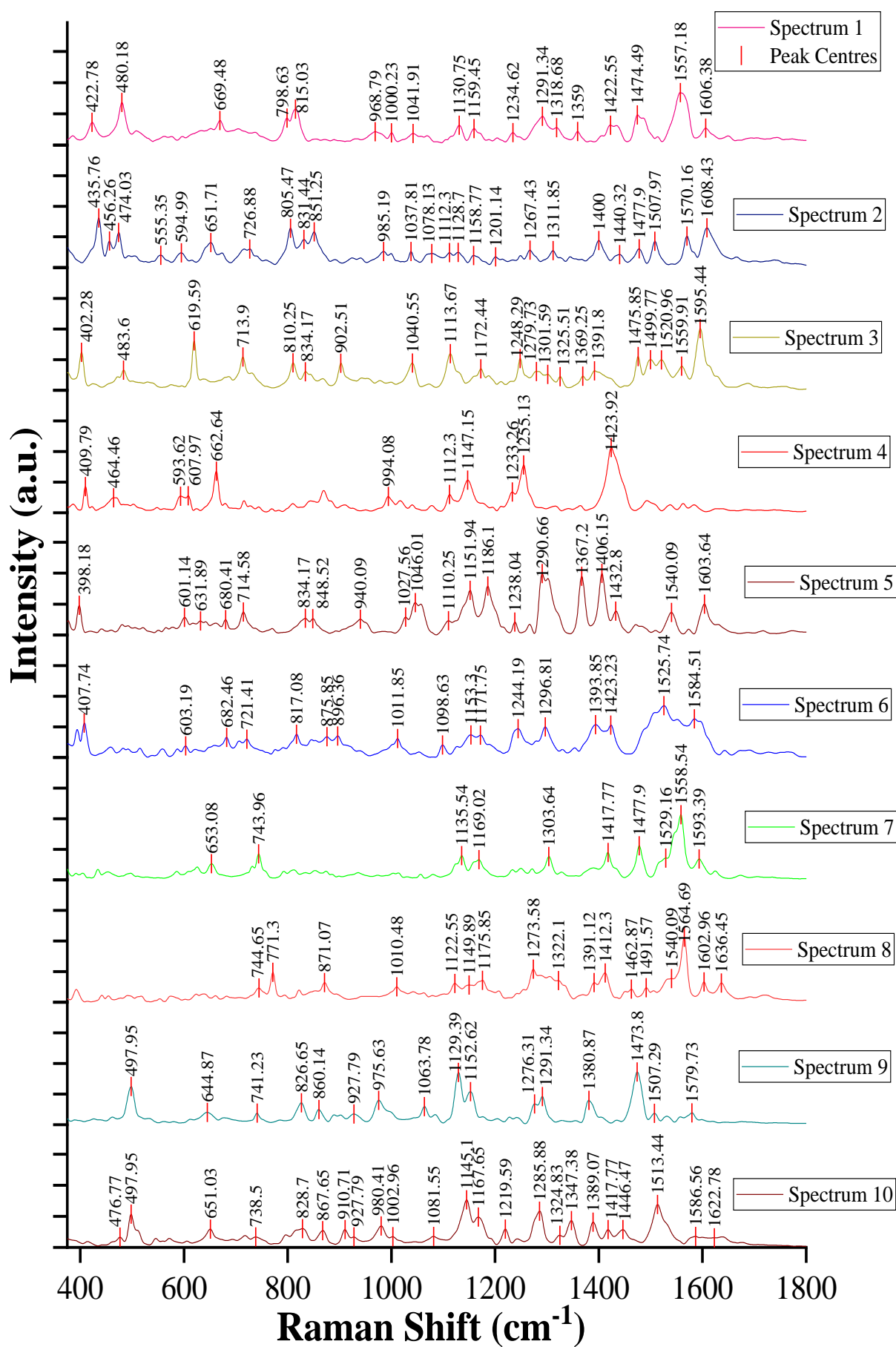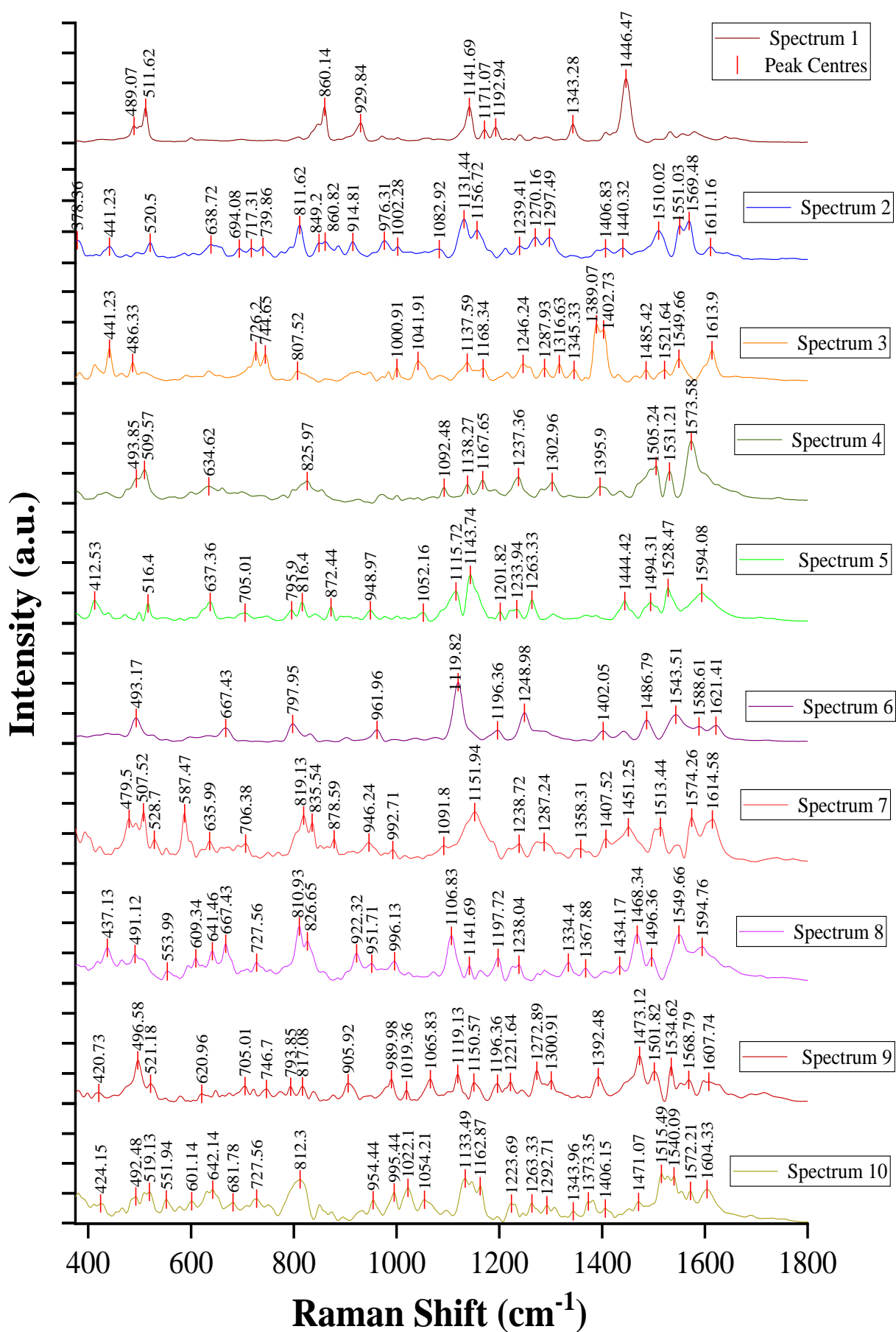
Figure S3.07: Ten representative SERS spectra of exosomes from primary HuAECs -NG within a SH-(c)-RGDFK functionalized Au micro array platform..

C.3.2 Primary HuAECs -HG

Figure S3.08: Ten representative SERS spectra of exosomes from primary HuAECs -HG within a SH-(c)-RGDFK functionalized Au micro array platform.

Figure S3.09: Ten representative SERS spectra of exosomes from primary HuAECs-HG within a SH-(c)-RGDFK functionalized Au micro array platform.
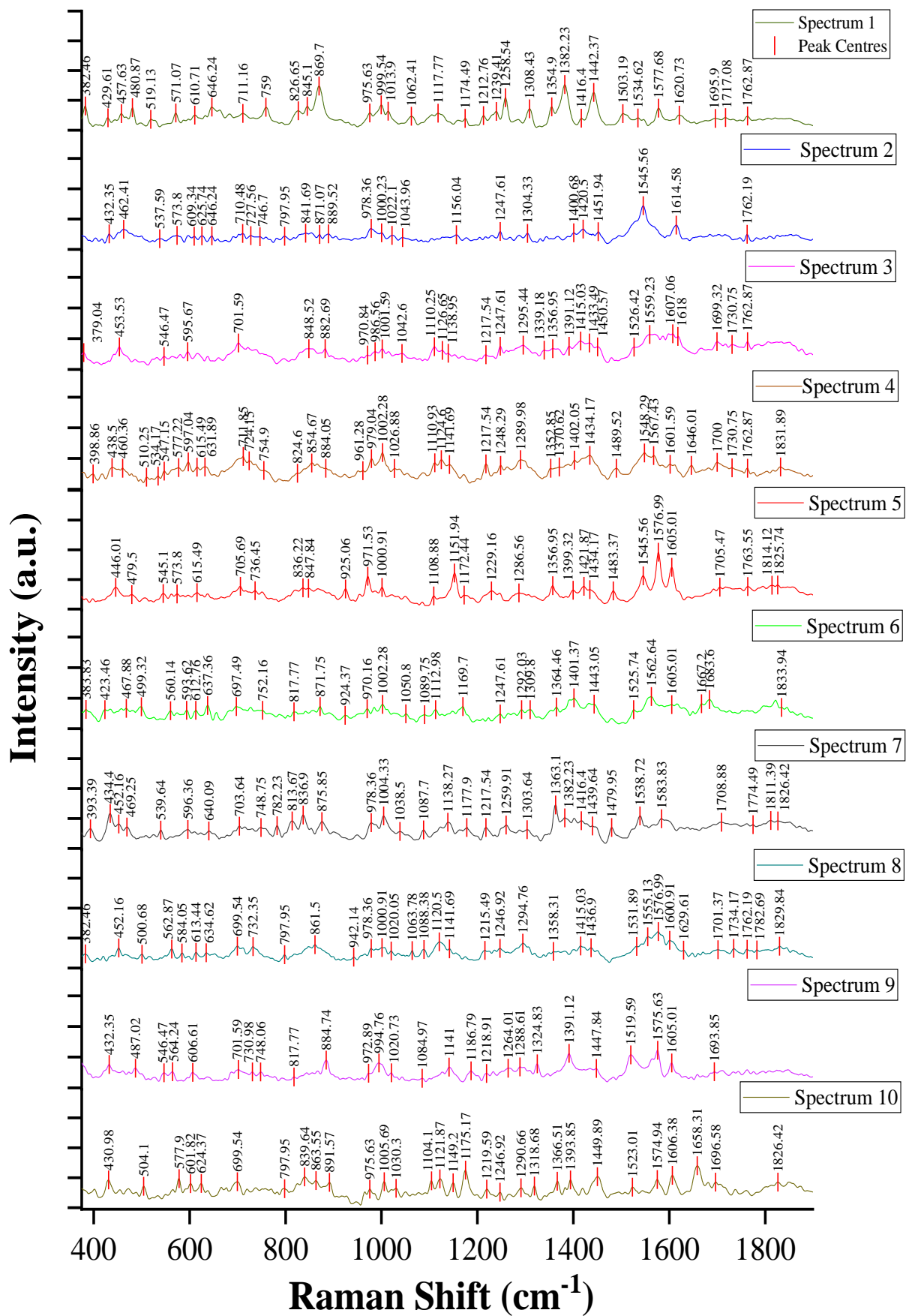
Figure S3.10: Ten representative SERS spectra of exosomes from primary HuAECs-HG within a SH-(c)-RGDFK functionalized Au micro array platform.

Figure S3.11: Ten representative SERS spectra of exosomes from primary HuAECs-HG within a SH-(c)-RGDFK functionalized Au micro array platform.

C.3.3 Primary HuAECs -MG

Figure S3.12: Ten representative SERS spectra of exosomes from primary HuAECs-MG within a SH-(c)-RGDFK functionalized Au micro array platform.
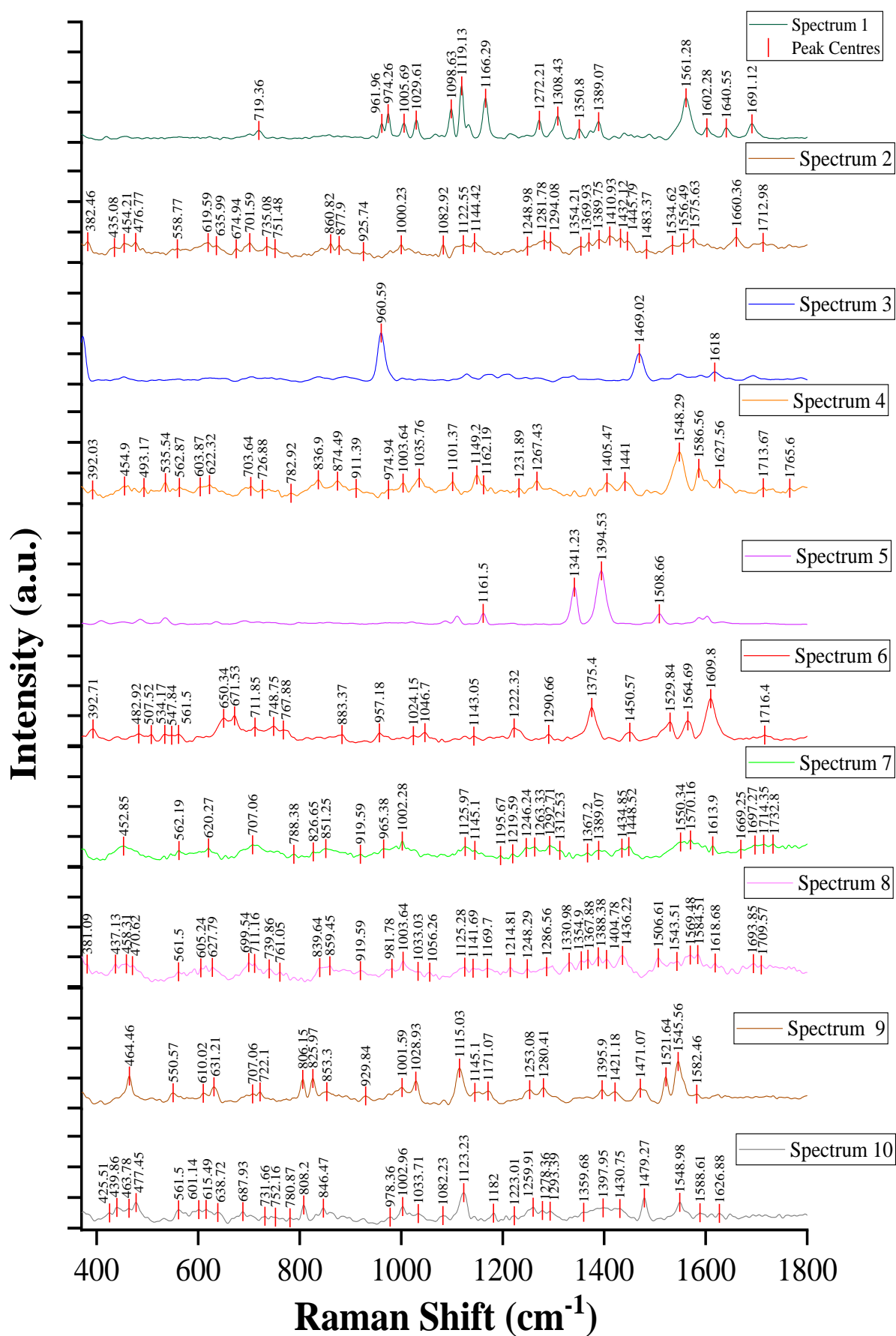
Figure S3.13: Ten representative SERS spectra of exosomes from primary HuAECs-MG within a SH-(c)-RGDFK functionalized Au micro array platform.
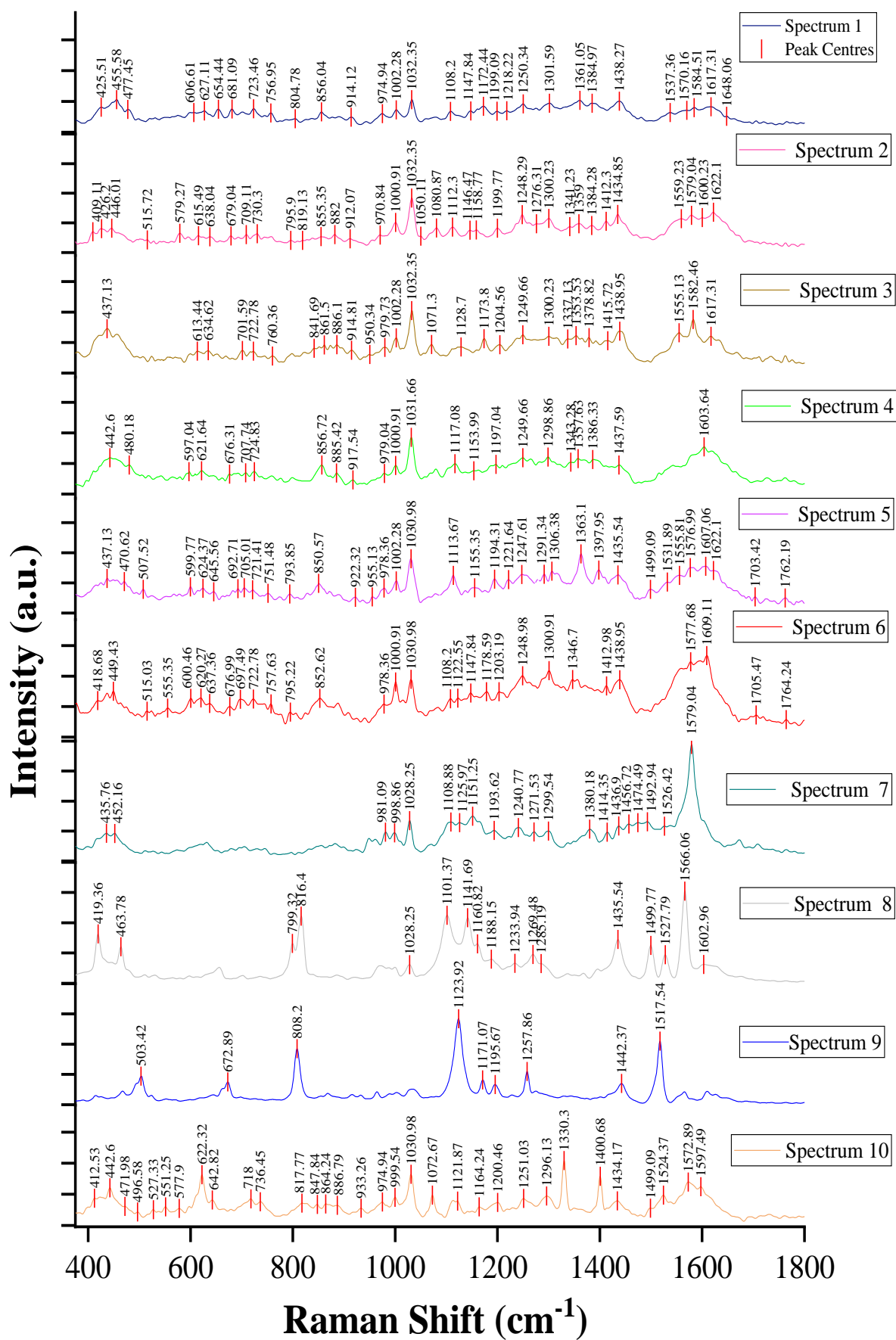
Figure S3.14: Ten representative SERS spectra of exosomes from primary HuAECs-MG within a SH-(c)-RGDFK functionalized Au micro array platform.
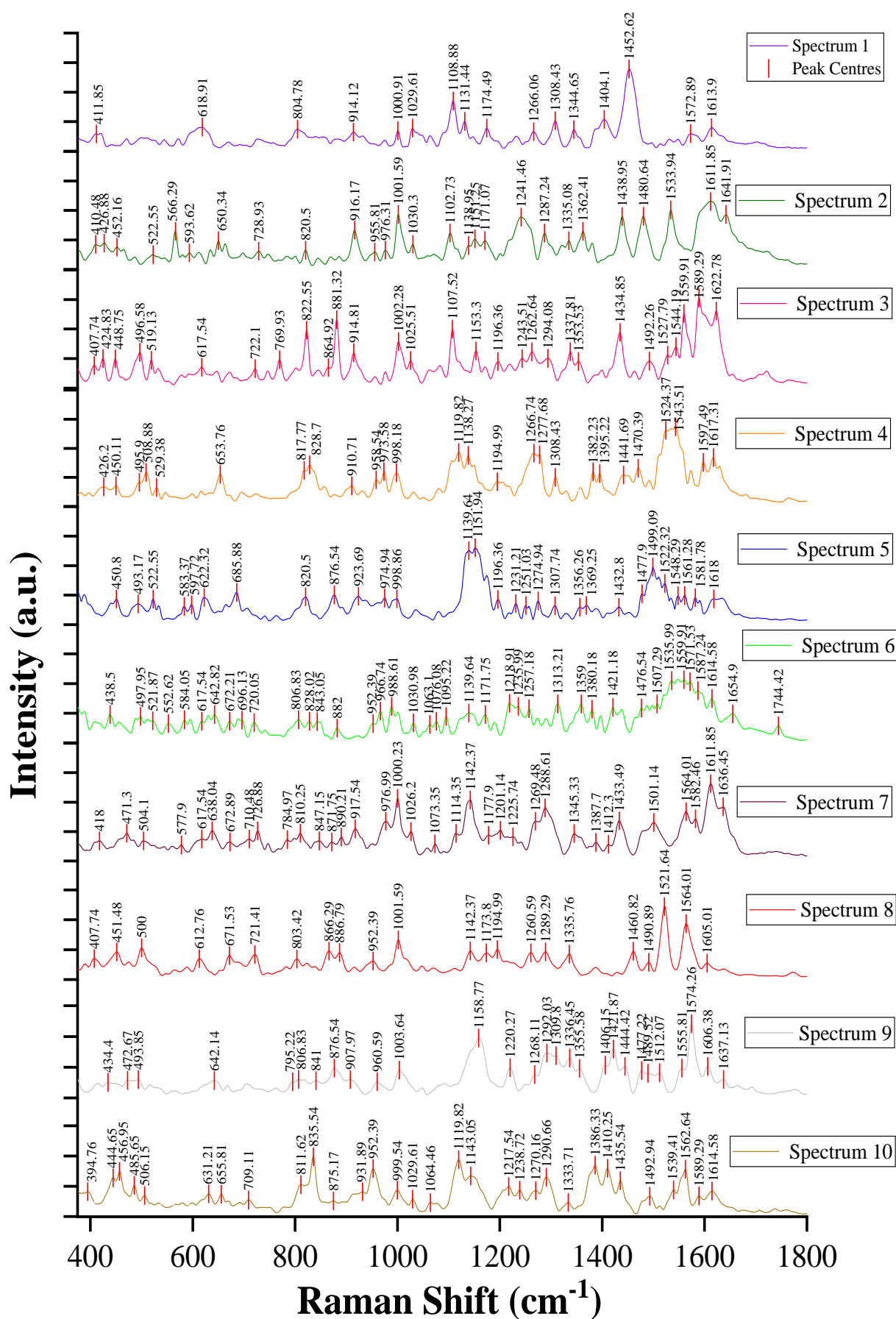
Figure S3.15: Ten representative SERS spectra of exosomes from primary HuAECs-MG within a SH-(c)-RGDFK functionalized Au micro array platform.

Y